MECHANICAL AND ELECTRICAL CHARACTERISATION OF ANISOTROPIC CONDUCTIVE ADHESIVE PARTICLES

By

Guangbin Dou

A DOCTORAL THESIS
SUBMITTED IN PARTIAL FULFILMENT OF THE REQUIREMENTS
FOR THE AWARD OF
DOCTOR OF PHILOSOPHY OF LOUGHBOROUGH UNIVERSITY
JUNE 2007

LOUGHBOROUGH UNIVERSITY
WOLFSON SCHOOL OF
MECHANICAL AND MANUFACTURING ENGINEERING

Dated: June 2007

Director of Research: _____
Jon Petzing

First Supervisor: _____
David C. Whalley

Second Supervisor: _____
Changqing Liu

External Examiner: _____
Helge Kristiansen

Internal Examiner: _____
David Williams

To my parents.

Table of Contents

List of Tables

List of Figures

List of Abbreviations

AFM	-	Atomic Force Microscope
ACA	-	Anisotropic Conductive Adhesive
ACF	-	Anisotropic Conductive Film
Au	-	Gold
Ag	-	Silver
BGA	-	Ball Grid Array
COG	-	Chip-on-glass
COB	-	Chip-on-board
COF	-	Chip-on-flex
Cu	-	Copper
CTE	-	Coefficient of Thermal Expansions
FPC	-	Flexible Printed Circuit
FWR	-	Four Wire Resistance
HSS	-	High Speed Steel
ICA	-	Isotropic Conductive Adhesive
LCD	-	Liquid Crystal Display
mm	-	millimeter
MEMES	-	Micro Electro Mechanical Systems
NCA	-	Non-conductive Adhesive
Pb	-	Lead
PCB	-	Printed Circuit Board
SEM	-	Scanning Electron Microscope
Sn	-	Tin
TCP	-	Tap Carrier Package
WSI	-	Wafer Scale Integration
W	-	Tungsten

Ti - Titanium

μm - Micrometer

Abstract

This thesis presents research into the mechanical and electrical characterisation of Anisotropic Conductive Adhesive (ACA) particles and their behaviour within typical joints. A new technique has been developed for study of individual ACA particle mechanical and electrical performance when undergoing deformation. A study of the effects of planarity variations on individual electrical joints in real ACA assemblies is presented firstly, followed by the research on the mechanical deformation and electrical tests of individual ACA particles undergoing deformation.

In the co-planarity research, experiments introducing deliberate rotation between a chip and substrate were designed and carried out to simulate planarity variations in ACA assemblies. There are two outputs from this part of the research. One is the planarity variation effects on individual electrical joints in ACA assemblies, and the other is the effect of bond thickness on the resistance of a real joint.

The mechanical deformation and electrical resistance of individual ACA particles undergoing deformation were measured using specially prepared punches in a nano-indentor. Information on various aspects of their mechanical deformation and electrical behaviour of a single ACA particle has been obtained through analysis of the experimental results. The mechanical aspects include the typical load/deformation relationship, viso-elasticity, presence of an adhesive resin, and multiple particles; the electrical performance aspects include the typical resistance of a single ACA particle, electrical stability, choice of punch materials and V/I behaviour. Four stages were identified in a typical particle deformation i.e. initial deformation, further deformation, crushing, and post crushing. The strain stress curve of the particle deformation indicated that the particle appears to soften in the first stage, and harden in the second stage but appears to soften again before crushing. The relationship between the joint resistance and deformation of a particle was found to be a exponential decay function affected by the conductivity and surface finish of the punch and base stage. Finally an individual ACA particle was found to exhibit ohmic conduction.

A comparison between the joint resistance versus deformation and individual particle versus deformation results shows good agreement between the two experimental techniques and demonstrates that the single particle experiments can be used to determine information relevant to the performance of actual ACA assemblies.

In conclusion, the planarity effects on individual ACA joints of ACA assemblies

has been analysed and a new/novel methodology for the mechanical and electrical testing of individual ACA particles has been developed in this research. A number of significant findings have resulted from these experiments. The technique could be used to test any kind of micro particles that are of a similar size to the ACA particles tested.

Key words: Anisotropic Conductive Adhesive (ACA), co-planarity variation, joint resistance, reliability, mechanical deformation, electrical test, punches, nano-indentor, visco-elastic, voltage and current (V/I).

Acknowledgements

I would like to express my sincere gratitude to my supervisors, Mr. David C. Whalley and Dr. Changqing Liu for their guidance, constant support during this research. And greatly thanks to Mr. David C. Whalley for proof-reading of the thesis and Dr. Changqing Liu for introducing me this research opportunity.

I would like to thank all the staff and students within the Interconnection Group who have contributed to various aspects of this thesis and to my knowledge. In particular Dr. Farhad Sarvar for his valuable suggestions on my Ph.D. study, Dr. Patrick Webb for helpful discussions on the electrical testing of the ACA particles, and Mr. Jicheng Gong for his help in the SEM sample preparation.

I would also like to extend my gratitude to all the technical staff in the Wolfson School who helped me during my research, but in particular to Mr. Andy Sandaver for his assistance and useful discussions in the sample preparation, and to Mr. Richard Price, Mr John Jones, Mr. William Veitch and Mr. Alan Wilkinson for their training and help in machining of experimental parts.

I would also like to acknowledge Prof. Y. C. Chan, based at City University of Hong Kong, for his support on the co-planarity experiments and to Conpart AS Company in Norway for supplying the ACA particles. Great thanks are also due to Dr. Chunyan Yin, The University of Greenwich, for the sharing of her experimental results as identified in the footnotes on pages 78 and 79.

I am deeply grateful to my wife Chunyan. It is her love and encouragement that have accompanied me through the most difficult times during my study. Without her understanding and full support, I would not have achieved this research. I would like to thank my parents and my sister and brother for their love and support over the years. Their belief that I can achieve my ambition, has been my incentive to work hard on this thesis.

Finally I would like to acknowledge the Wolfson School of Mechanical and Manufacturing Engineering of Loughborough University for their financial support which enabled me to undertake this research.

Loughborough, Leicestershire — Guangbin Dou
June, 2007

Chapter 1

Introduction

In this introductory chapter, the background to the research undertaken and the aims are introduced, followed by a discussion of the structure of the thesis and a summary of the achievements made.

1.1 Background

With technology advancing, electronic products are touching every aspect of human life with the potential to bring everyone around the planet into the digital age. It is hard to imagine a world without computers, cell phones, televisions, fax machines and other electronic products. The technologies behind all these electronic devices in space exploring, automotive, communication, computer and medical industries are all based on micro-devices and packaging technologies. The fundamental technological building blocks behind all these products are four technology waves: Microelectronics, RF/Wireless, Photonics and Micro Electro Mechanical Systems (MEMS) [1]. However, their exploitation is only possible with advanced packaging technology. In other words, it is system and device packaging that integrates these technologies into products. Therefore, electronics packaging plays an important role in all electronic products. Furthermore, developments in the semiconductor industry, along with consumer demand for cheaper, lighter, high-density information processing tools, have demanded revolutions in the entire electronics packaging infrastructure. Developments in semiconductor technology have resulted in very large scale integration devices with attendant feature sizes as small as a 0.3 to 0.2 microns and input/output (I/O) counts of hundreds or thousands [2].

Electronics packaging is defined as the bridge that connects the Integrated Circuit (IC) and other components to form a product [3][4]. Figure 1.1 shows schematically a typical packaging hierarchy for a complex system. The first interconnection occurs at the level where the input/output (I/O) pads on the IC are bonded to a substrate or package to form the first level of the packaging. This stage of packaging is referred to as an IC assembly. The second interconnection is achieved between the lead frame of the first-level package and the electrically conductive pads on the printed circuit board (PCB). This is referred to as a board assembly. The third level package is the system-level board, with components assembled on either or both sides, typically completing the system.

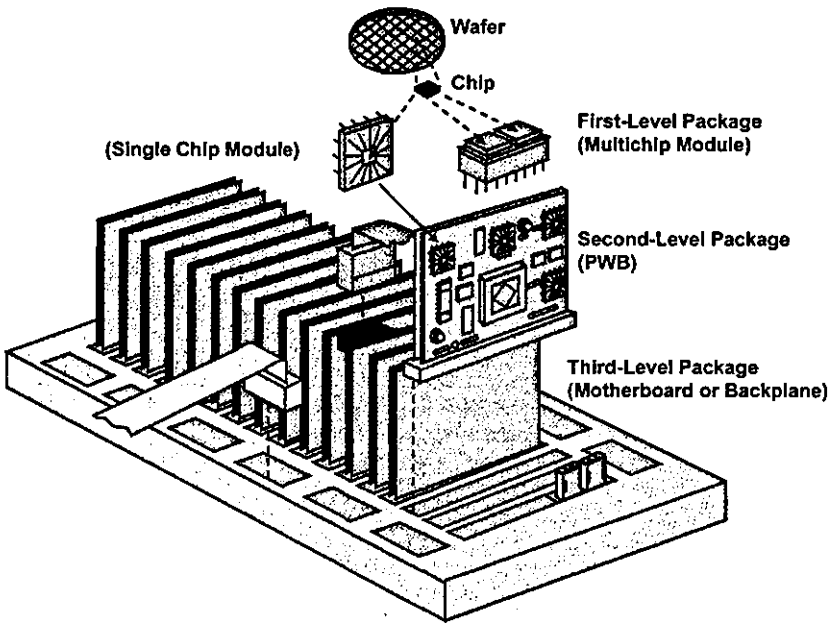

Figure 1.1: Packaging hierarchy [4].

Many packaging technologies and materials are used in IC devices and applications. High density, high reliability, high speed production and low cost as well as "green" packaging (e.g. lead free) are currently the main issues in designing and developing new electronics assembly technologies. Among these new technologies, anisotropic conductive adhesives (ACAs) first proposed 50 years ago is a novel packaging [5], which are capable of high density, low temperature bonding. They have been used in various niche applications in flip chip die-attach, smart cards and Liquid

Crystal Display (LCD) or other flat panel assembly [6]. Nowadays, ACAs are becoming popular bonding materials especially in the flat panel display, disk drive and smart card industries, where traditional soldering processes are unable to achieve both the fine pitch and low temperature assembly requirements. For example, high density I/Os have to be produced in LCD panels due to the high display resolution and more vivid colour quality achieved by today's technology. Such fine pitch connections of less than 100 μm are more suitable to be bonded by ACAs, where it is impossible to use traditional solder alloys [7]. Lower processing temperature is another strength of ACAs compared to solder alloys since many components are sensitive to heat and cannot survive the solder reflow process where for lead free alloys the peak temperatures can be as high as 250 $^{\circ}C$, which is far too high for many piezoelectric materials (e.g. ink jet printers) and board materials to survive.

ACA materials consist of electrically conductive particles within a polymer matrix. It can be placed between e.g. an IC and a substrate or a flex or a glass panel to form the electrical interconnections between them. These connections are anisotropic as the current can only travel through the thickness of the adhesive, but not between adjacent joints as shown in Figure 1.2. It can be seen in the figure that some particles are trapped between the chip bumps and the substrate pads. The particle deformation in the ACA joints is important, because the contact areas between the deformed particles and the component pads are decided by the particle deformation degree. The higher the deformation degree the trapped particles is, the bigger the contact areas and the lower the joint resistance are. Therefore, it is important to do some systematic research on the mechanical and electrical characteristics of ACA particles, multiple and individual.

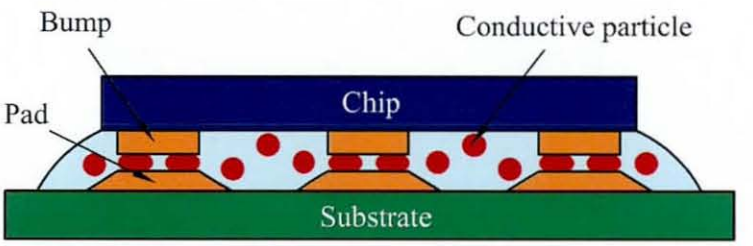

Figure 1.2: A typical ACA package.

Research on the mechanical and electrical characterisation of ACA particles will be presented in this thesis. These include the co-planarity research on the mechanical and electrical study of individual ACA joints in ACA assembles and the mechanical deformation and electrical tests of individual ACA particles undergoing deformation. The co-planarity research is the planarity variation and bond thickness study on individual ACA joints packaged with multiple ACA particles. And the research on the individual ACA particle compression is a systematic study on the mechanical and electrical performance of individual ACA particle. Therefore, in summary, the research presented in this thesis are firstly focused on the tests of multiple ACA particles and then the systematic research on individual particles.

In conclusion, electronics packaging using ACAs provides significant advantages for fine pitch connections and low temperature assembly. On the other hand, ACAs are also lead-free and hence satisfy many of the current environmental legislation restrictions stated in recent European directives or other national legislation [8][9]. However, the major concern with ACF materials is their yield and conductivity. The planarity variation effects on the ACA assemblies are the current research challenge that is needed to be examined before ACAs can be used in really high volumes for low-cost applications [6]. Compared with traditional metallic solder materials, especially tin-lead solders, ACAs are very new with little documented study on the mechanical and electrical characterisation of ACA particles available, especially individual particles.

1.2 Aims and Objectives of The Thesis

The research presented is dedicated to the exploration of the fundamental mechanical deformation and electrical conduction characteristic of individual ACA particles. The methodology used to undertake this research is a combination of novel experiments and mathematical analysis.

ACA particles are typically around 3 μm to 10 μm in the diameter, therefore it is very difficult to investigate their properties individually. The majority of published research on the mechanical deformation and electrical conduction of ACA particles are focused on the properties of ACA interconnections with multiple ACA particles,

normally hundreds or thousands per joint together. The advantage of this approach is the easy experiment setup and the subsequent analysis, however, on the other hand, whilst the experimental results can establish some properties of individual ACA particles, they are limited in their ability to reveal the fundamental characteristic of single ACA particle .

The yield of assemblies bonded by ACAs has been found very sensitive to the misalignment of the packaged parts and especially the non-planarity effect of the pad surface [10]. The non-planarity packaging or the planarity variation in the assemblies can be summarized that the bump surface and the pad surface in a joint are not parallel. Little published research [11] has been found on this topic, since it is very difficult to control the planarity of bumps on chip or pads on substrate due to the small bump surfaces, normally about 20 μm by 20 μm. One objective of this research is to design experiments and examine the planarity effects for an ACA bonded package from the experimental results. Therefore, co-planarity experiments for rotation errors were carried out and presented in this thesis. In the experiments, different no-planarity ACA joints were assembled by differing the amounts of the angled chip on the substrate, that is, the non-planarity joints were formed by the chip rotation; there were no non-planarity bumps on the chip or pads on the substrate. These non-planarity assembles were similar as the wedge experiment [11], however they were more flexible and not affected by adhesive flow restriction as there was no metal foil on the bonded edges. Another advancement of these experiments were the real chips and substrates, instead of two rigid planar surfaces, were used. The effects of rotated chip bonding (bond thickness effects) on the particle deformation have also been acquired from these tests. Furthermore, these experiments can also be considered as the research on the mechanical deformation and electrical conduction of ACA joints with about 20 particles, because different particle deformation degrees were packaged in the real ACA assemblies.

During the final stage of the bonding process, ACA particles are trapped between the component pads, become deformed to construct electrical paths between the two components. Once trapped the particle deformation degree is therefore very important in deciding the mechanical and electrical characteristic of bonding. Several electrical contact models for predicating contact resistance have been suggested

[17][18][19][20][21][22], and some experiments have been reported to support these models, but all the experiments were done with multiple particles (including the co-planarity research in the thesis), not individual particles. The mechanical and electrical properties of the individual ACA particles in a joint are fundamental to the overall properties of the ACA assembly. Successful research on these props of individual ACA particles will contribute to the basic understanding of ACA technology and establish the reasons for failure, thereby helping to further improve ACA bonding reliability and material manufacturing process.

The overall aims of this research are to use both experiments and mathematical analysis to investigate:

- The effect of co-planarity variation on ACA assemblies. In detail, it is the research on the planarity variation and bond thickness effects on the mechanical and electrical performance of individual ACA joints in ACA assembles.
- Individual ACA particle compression. In detail, it is the systematic research on the mechanical and electrical characteristics of individual ACA particles undergoing deformation.

The first task, investigation of non-planarity effects, was carried out through:

- Design an experiment to assembly the substrates and chips in certain tilted angle to simulate non-planarity assemblies, in which ACA particles were deformed in different deformation degree and cured in individual electrical joints.
- Statistical analysis of the experimental results.

The second task, the mechanical and electrical tests on individual ACA particles, was achieved by using novel experimental methods with a nano-indentor machine. The details are as follows:

- Experiment design, including the preparing of needle punches, base stages for mechanical and electrical tests and the test methodology by using $NanoTest^{TM}$ machine.
- Mechanical deformation of individual ACA particles undergoing deformation.

- Electrical tests of individual ACA particles undergoing deformation.
- Statistical and mathematical analysis of the experimental results.

1.3 Structure of the Thesis

In total there are 8 chapters in this thesis. The introduction to this research is presented in Chapter 1, and outlines the background, aims and original findings of this thesis. It illustrates the challenges in the electronics industry at present and explains why the research on ACAs is important.

In Chapter 2, a literature review of the early history and recent research related to ACA assemblies is presented. More than 90 academic papers are cited, which are classified into five major topics, which are ACA history and associated technologies, ACAs, ACA assembly process, ACA interconnections, and reliability of ACA assembly.

Chapter 3 details the co-planarity experiments, followed by the results and discussion in Chapter 4. In these two chapters, the research on the planarity variation and bond thickness effects on the mechanical and electrical performance of individual ACA joints in ACA assembles are presented and discussed.

In Chapter 5, the experiments on the mechanical deformation and electrical conduction of individual ACA particles are presented. Thanks to the novel methodology, including use of specially prepared punches and four wire resistance (FWR) measurement system, the whole history of particle deformation versus load force and deformation was recorded, as was the electrical performance of individual ACA particles undergoing deformation. In the following chapters 6 and 7, the experimental results for the mechanical deformation and electrical tests of individual ACA particles are summarized, analyzed and discussed.

Chapter 8 concluded the thesis with a summary of the achievements and potential further work is discussed.

1.4 Original Techniques and Findings

This is believed to be the first time that planarity effects in an ACA assembly have been studied using the methods in this research. It is shown that the performance of ACA bonding is sensitive to the rotation differing between the chip and the substrate. The joint resistance increased quickly in the less compressed side, however kept almost stable in the highly compressed side although bad reliability was expected if the particles were over deformed.

A novel experimental design to measure the mechanical and electrical properties of individual ACA particles undergoing deformation has been achieved in this research. This is the first systematic experiment of its kind that has been carried out in the world. The specially prepared punches manufactured by polishing the points of metal needles manually are the first tools that can both deform individual ACA particles and measure electrical resistance, no report of a similar achievement in the literature in the past 30 years has been found. After the mechanical deformation of single ACA particles and the electrical tests of individual ACA particles undergoing deformation were achieved, a clear understanding of the effects of the bonding force on the deformation of individual ACA particles and their resulting conductivity when in contact with an appropriate metallic surface was established. Deformation properties of individual ACA particles were built and the relationship between the electrical resistance and mechanical deformation of individual particles were acquired from the experimental results by using mathematical fitting. This research will contribute to the fundamental research of ACA technology and therefore help to find the optimum particle deformation degree and manufacture more efficient ACA materials.

So far, this research work has resulted in 5 international conference papers [12] [13][14][15][16], and some journal papers are under preparing.

Chapter 2

Literature Review

2.1 Introduction

The principal objective of this literature review is to provide significant insights into the basic characteristics of ACA materials including history and associated technologies, materials, assembly process, interconnections and reliability of ACA assemblies based on a review of previously reported scientific research, and to identify the current challenges and future prospects for this technology.

Initially, ACA history and associated technologies are introduced, including the material development history, flip chip assembly, soldering and the diverse conductive adhesive packaging.

Secondly, ACA materials are introduced, including ACA types and their typical composition, types of ACA particles and the conductive mechanisms in ACA materials.

Thirdly, a typical ACA assembly process is presented. These include the bonding tolerances in the alignment process and the bonding force, particle deformation, curing methods, resin flow and thermo-mechanical performance in the final bonding.

Fourthly, ACA interconnections are conducted in detail in the section, which is structured in the sequence of a current path where five types of component resistance can be identified from the chip bump, the contact between the chip bump and the particle, the particle, the contact between the particle and the substrate pad, to the substrate pad.

Finally, reliability of ACA assembly is presented. This chapter is ended by the

current challenges and thesis tasks.

2.2 ACA History and Associated Technologies

Flip chip assemblies by soldering are still the leading packaging method in electronics industry. However, such assemblies have limitation on their fine pitch outer lead bonding. ACA assemblies are devised as next generation technology to achieve fine pitch interconnections. Compared to the traditional soldering connection, ACAs are good at fine pitch, low temperature and low cost electronics packaging, suitable in fine pitch flip chip bonding for LCD driving ICs, such as digital watches, viewfinders, and personal Palms or laptops, where the classic soldering flip chip technology are not capable of high density packaging in small size. ACAs are widely using in flip chip bonding to connect chips onto Flexible Printed Circuit (FPC), Printed Circuit Boards (PCB), and ITO coated glass. Chip-on-glass (COG), Chip-on-boards (COB) and Chip-on-flex (COF) are three kinds of ACA flip chip packaging in the interest of product miniaturization, multiple connectivity, and low cost. On the other hand, ACAs are also widely used for high density interconnection between LCD panels and tap carrier packages (TCPs) to replace the classic soldering and rubber connecting.

2.2.1 ACA History

Extensive research and development have taken place since the earliest concept of ACA was introduced in the 1950s [23]. In the early 1980s, some companies, such as Sheldahl in the United States and Sony in Japan, were facing problems connecting low temperature materials unable to withstand the high temperatures of soldering processes. At this time, Sheldahl and other flexible circuit manufacturers focused many resources on the problem of connecting ICs to the circuit boards unable to withstand the high temperatures of soldering processes, whilst a concerted effort in solving the connection problem for substrates used for LCDs was made in Japan. The Japanese company, Sony, first introduced samples of an interconnect film that contained carbon fibres which were oriented in parallel and acted as the electrical conductors. Almost at the same time, companies in the United States suggested

that the conductors within the polymer matrix should be spherically-shaped metal particles and both Sheldahl and Amp produced ACAs using silver particles in 1985. Since then, considerable research has been undertaken around the world to develop improved ACA materials.

2.2.2 Flip Chip Assembly

The popular interconnect methods to connect the chips on the substrate are wire bonding, TAB bonding and flip chip bonding. Among these methods, flip chip provides the shortest possible leads, lowest inductance, highest frequency, best noise control, highest density, greatest number of I/Os, smallest device footprints, and lowest profile. Flip chip assembly is to mount the flip chip on a substrate or board using various interconnect materials and methods, as long as the chip surface (circuit) is facing (oriented in the direction of) the substrate [24]. Flip chip assemblies have been successfully applied in electronics packaging to make smaller, more compact products and high density for high-speed circuitry since one of the earliest flip chip technologies was introduced by IBM in the early 1960s. During these years, electronics product are getting smaller and smaller and I/O leads is getting finer and finer due to the developing of modern flip chip technology, as well as new development in electronics assembly. Flip chip assembles by soldering are still the major assembly technique in electronics industry, however flip chip assembles by conductive adhesives are getting popular nowadays, especially in some niche area where soldering is incapable.

2.2.3 Soldering Assembly

Soldering is one of the oldest methods of metal jointing that is using in electronics packaging. When used properly with today's improved methods and materials, it can solve many design and production problems reliably and economically. The vast majority of solder used in electronics assembly have traditionally been based on the binary system of tin and lead, with possibly small additions of silver and antimony. They offer advantages of low cost and ease of use, allowing relatively low soldering temperatures and a wide choice of soldering techniques. However, there has long been concern over the toxicity of the lead and has since been worldwide environmental

concern over the fate of obsolete electronic and electrical equipment when eventually discarded. Therefore, tin-base alloys containing some copper, silver and bismuth are now widely used. Actually, there are already some lead free electronics products available in the market during recent years.

The widely used soldering method is SMT and BGA packaging, they still can not be replaced by other kinds of interconnect methods, such as adhesive packaging, because their joint reliability are still better than the adhesive joints. However, the adhesive package has been used to replace soldering in some area where the soldering is not suitable or impossible. The direct drive forces towards using and developing new joint material and method are the demand of portable and high capacity electronics products. It is also clear that lead will have to be phased out of electronics assembly on a global basis and within a relatively short time. In an effort to minimize the risks and the impact on the environment and human health, the European Union (EU) has passed new directives and legislation restricting the use of hazardous substances including use, treatment and disposal of waste electrical and electronic equipment. Introduced in 1998 by the European Union, WEEE (Waste Electrical and Electronic Equipment) is a directive (law) that bans the selling and/or import of all electronic/electrical equipment containing lead interconnect by January 1, 2004 [8]. Adopted by the EU on June 13, 2000, RoHS (Restriction of Hazardous Substances) is a European Union initiative to ban *six hazardous materials*[1] including lead and mercury from electronic products by July 1, 2006. Products sold in the EU after July 2006 must contain less than a maximum concentration value of 0.1% by weight in homogeneous materials for lead, mercury, hexavalent chromium, polybrominated biphenyls (PBB) and polybrominated diphenyl ethers (PBDE) [9].

The most promising tin-based alloys have successfully used in some packages. However, more work still need to do to find more lead-free solders to replace the lead alloys for green electronics packaging. Adhesive is one of the promising alternative.

[1]Cadmium (Cd), mercury (Hg), hexavalent chromium (Cr (VI)), polybrominated biphenyls (PBBs) and polybrominated diphenyl ethers (PBDEs), as well as lead (Pb)

2.2.4 Conductive Adhesive Packaging

Adhesives have a significant processing advantage over solder, which exposes components and circuits to harsh temperature environment during packaging. It is no wonder that adhesives play a great role in electronics packaging. The adhesives used in electronics are basically synthetic polymer-based adhesives, versatile, compatible and easy to synthesis and customize. They are so important for electronics industry that most of our modern electronic products would be impossible without them. Adhesive packagings are intrinsically clean, simple, and logical solution for all other kinds of electrical interconnect challenges. Adhesives are not only lead free, ideal alternative to solder, but also highly compatible materials which are proposal solution to problems where solder is totally inadequate. Their low assembly temperatures induce lower thermal shock in the components and circuits than high soldering temperature. Electronics industry can thus pay less attention on the components' thermal properties and accordingly cost less than those in solder assembly. Three types of conductive adhesives can be identified as their conduction mechanisms are considered. They are none-conductive adhesive, isotropic conductive adhesive and anisotropic conductive adhesive.

A. None-conductive Adhesive (NCA)

It may sound impossible, but it is true that selective adhesives are used to create mechanical connection between opposite component pads. They can be used to make it because their Coefficient of Thermal Expansions (CTEs) are much lager than the metal pads', thereby locking compressive stresses around the joints after curing to provide pressure contact between the pad surfaces. The insulation barrier between contact interfaces is not avoidable, the thicker the barrier is, the larger the contact resistance. The successful NCA joints are accomplished by applying enough force to displace adhesive from between electrical contact areas to make the insulation layer as thin as possible. Such assemblies has been used in circuit-to-circuit mating, circuit-to-LCD and bare die to circuit interconnections [25].

B. Isotropic Conductive Adhesive (ICA)

ICAs consist of a polymer matrix filled with conductive metal particles, normally silver flakes, conduct equally well in all directions [26]. Similarly to NCA, it is the epoxy that provides the mechanical adhesion. The conduction paths are from a component pad to flakes, and flakes to flakes, ended at the opposite pad. Obviously, the higher metallic content contributes to higher conductivity, however, higher metallic content lowers adhesive strength, therefore, the optimum volume ratio of metal filler is very important to the conductive and mechanical properties of ICA joints [26]. There are two kinds of ICAs as for the adhesive formula, thermoset ICAs and thermoplastic ICAs. Thermoset ICAs are chemically cured during the thermosetting temperature and not reverable after bonding. The advantage characteristic of thermoset ICAs is higher strength than thermoplastic ones. Thermoplastic ICAs could be applied as solvent-containing pastes, dried to solids and then melted for assembly. They have been referred to as 'organic solders', as they are much more akin to solders. Different from thermoset ICAs which change chemically during thermosetting, the thermoplastic ICAs can be re-melted for re-bonding [27].

The problems with using ICAs as bonding material are the long duration and high curing temperature, and junction instability [27]. New designed fast curing and infrared (IR) curable ICAs have successfully used in the traditional SMT line without modification or adding equipment, fast and low temperature. Even though very stable adhesives were used, the junction between the component and circuit often showed a large increase resistance after reliability test, such as humility and temperature aging [27]. The instability may be resulted from the formation of insulating oxide on the component leads, especially on the flakes, and the water absorption in the adhesives. However, oxide-reducing hardeners, such as anhydrides and carboxy acids, have been introduced to stable ICA joints. Much more work is being done in the ICA area to increase their performance and reliability [27].

C. Anisotropic Conductive Adhesive (ACA)

Compared to NCAs and ICAs, ACAs are designed to achieve even more complex packaging system by simple methods. It is to disperse conductive particles in a

dielectric adhesive while the loading is kept low enough so that the material is not made conductive by contact between particles.

2.3 Anisotropic Conductive Adhesives (ACAs)

ACAs consist of a polymer adhesive matrix containing fine conductive particles dispersed either randomly, or more rarely in an ordered way [28]. They have been significantly applied in surface mount applications for many years, although originally designed for applications such as the joining of edge connectors to flat panel displays [29]. Beside the extensive use in LCD assembly, ACAs have gained popularity as a potential replacement for solder interconnections, especially for fine pitch flip chip bonding. During the bonding process, some ACA particles are trapped between each chip bump and the associated substrate pad, and become deformed sufficiently to achieve electrical interconnections between the chip and the substrate. A typical ACA flip chip assembly is shown in Figure 1.2. After bonding, the deformed particles are held between the bump and the pad by the compressive force, induced by the cured adhesive around the joints, resulting in high quality, fine pitch electrical interconnections.

Considerable work has been carried out in many laboratories to better exploit the fascinating concept of uni-directional conductivity [30]. Figure 2.1 shows an ACA material consisting mainly of an adhesive layer containing a random dispersion of fine conductive particles [13]. In general, ACA materials are prepared by dispersing electrically conductive particles in an adhesive matrix at a concentration far below the percolation threshold. The concentration of particles is controlled such that enough particles are present to provide conduction in the Z-direction while too few particles are present to achieve percolation conduction in the X-Y plane [31]. Therefore, the conductivity of these materials is restricted to the Z-direction (perpendicular to the plane of the board) with electrical isolation provided in the X-Y plane.

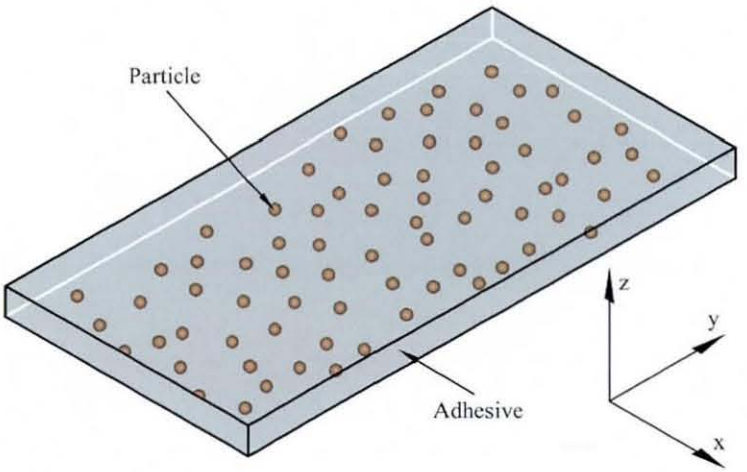

Figure 2.1: Schematic of an Anisotropic Conductive Adhesive [13].

2.3.1 ACA Types and Their Typical Composition

Figure 2.2 shows the main categories of ACA materials. There are two forms of ACA, films (ACFs) and pastes (ACPs). These two kinds of ACAs typically have similar compositions, but are delivered to the user in a different form. Paste materials are applied by either printing (screen and stencil) or dispensed with a syringe, and film materials are typically supplied by the adhesive manufacturer in a reel and the end-user must have dedicated equipment to cut, align and tack the adhesive into

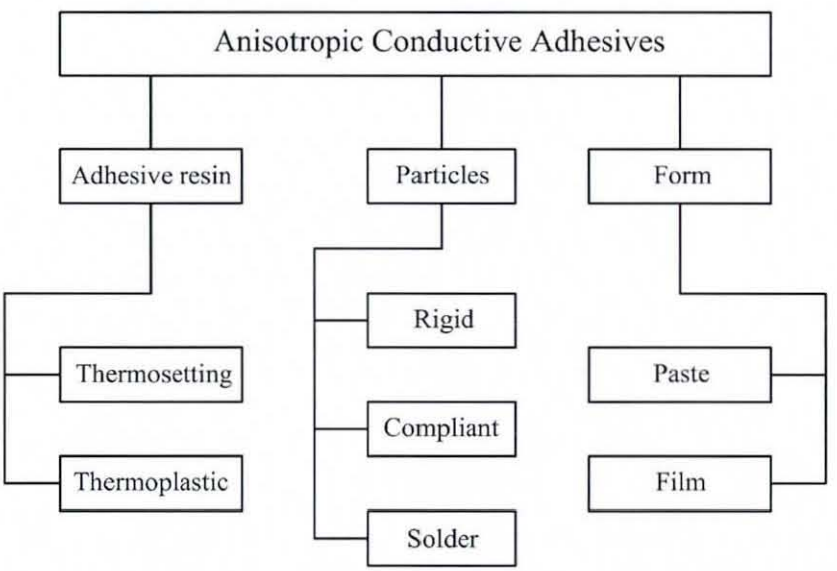

Figure 2.2: ACA types and their typical compositions.

position on the substrate. Two types of adhesive matrix are available: thermoplastic and thermosetting. Thermoplastic adhesives are thermally reversible, and therefore have good rework-ability since they melt if re-heated. Thermoset adhesives, however cross link during cure and are not thermally reversible. Thermosetting adhesives are typically cured either through application of heat or UV radiation. Thermoset adhesives are more durable than thermoplastic ones due to the stronger chemical bonds in cured thermoset adhesives, therefore are more mechanically stable in service temperature. Therefore, thermoset adhesives are more commonly used in electronics packaging nowadays. The conductor particles are generally dispersed randomly in the resin/polymer at a low density, however, ACFs have been developed where the particles are uniformly separated in the same non-conductive plane [28]. The material has been designed in such a way to maximise the loading of particles and eliminate particle-particle interactions to provide a uniformly separated array of conductors. The typical density in the research was 1800 particles per mm^2 for the relatively coarse (200 μm) pitches. These two types of material are referred to as random ACAs, and ordered ACFs respectively. Several materials are used to make the particles, including solid metals and metal coated polymers and solders. Metal particles can be used directly to make ACA particles, such as silver, gold, and nickel, however, for nickel, gold coating is normally necessary to prevent them from oxidizing. Silver, nickel and gold coating on polymer cores are the most common types of ACA particles. Plated polymer particles have lower densities and therefore are less prone to settling and are easy to be deformed to make better contact with bonding surfaces. The preferred metals for polymer particles are nickel under a thin layer of gold [32]. The typical particle size is from 3 to 10 μm. The particle size selection is importance in the ACA packaging since adequate particles are needed in each joint to provide electrical conduction, therefore smaller particles are needed in the fine pitch applications where higher particle densities are necessary. Bigger particles, more than 10 μm, were used in the old days, however fine particles, around 4 μm, are popular in fine pitch applications.

2.3.2 Types of ACA Particles

Considered the mechanisms of ACA joints, there are three types of particles used in ACAs, rigid particles, compliant particles and solder particles [33] as shown in Figure 2.2.

Rigid particle systems and compliant particle systems were studied by Liu [5]. The schematics of the joint of a single particle system are shown in Figure 2.3(a) and (b) respectively. Rigid particles are hard relative to the substrate and component metallisations, therefore there is almost no particle deformation in packaging. Compliant particles are plastically deformed during assembly and make contact over an area greater than their initial diameter. Solder particles can alternately be used to form metallurgical bonds through a reflow process to both the substrate and component metallisations, therefore there is no need of the polymer adhesive to maintain the particles under a compressive load for solder particles [33]. Compliant particles are the most widely used conductive fillers for ACAs and are typically composed of gold and nickel plated polymer spheres, which are the main interests of this research.

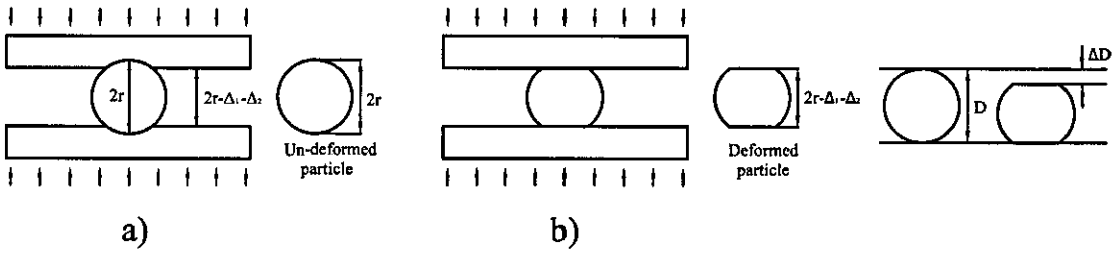

Figure 2.3: (a) Schematics of a rigid particle system; (b) Schematics of a compliant particle system [33].

There has also been some research on solder particles. Much of the work on flip chip interconnections with solder filled ACAs had been reported by Solvolainen and Kivilahti [34][35][36]. They found that *SnPb* as well as *Pb*-free *Sn* alloys form intermetallic with copper and nickel based small solder particles, leaving a layer of relatively pure bismuth or lead, the most commonly used alloying elements.

The compliant type, nickel and gold coated polymer particles are the best choice

for fine pitch ACA interconnections because the distribution of the diameter of particles is fairly uniform, and the particles can be dispersed uniformly into the adhesive compared to the rigid based particles due to the light weight of the polymer. On the other hand, the more easily deformed polymer particles are much cheaper than the noble metal particles.

2.3.3 Conductive Mechanism in ACA Materials

Electrical conduction through non-solder particle ACAs is achieved by the mechanical deformation of the conductive particles contained within the cured adhesive. As described by Whalley et al. [37], ACA joints rely upon the trapping of the conductive particles between the conductive pads on the two parts being connected, followed by the solidification of the adhesive thereby locking in residual stresses to ensure retention of sufficient contact force to create stable and low resistance electrical connections. In order to understand the electrical and mechanical behaviour of ACA materials, three key issues require to be considered. First, sufficient conducting particles must be trapped during the bonding process to guarantee electrical contacts with both conductor surfaces. Second, the degree of deformation of the particles determines the contact area between the particles and metal pads and therefore the electrical characteristics of the interconnections. Last, the residual stress state after assembly significantly influences the mechanical performance under testing conditions and in service [38].

ACA conduction mechanisms are highly depended upon the type of conductive particle that is formulated into the adhesive matrix, and the particle type determines the nature of the electrical contacts between the particles and the component parts. During ACA assembly, the applied pressure is not only required to displace excess adhesive such that single particles span the gap between component and substrate metallization surfaces, but is also required to deform some ACA particles to a sufficient degree. After assembly, the cured adhesive supplied compressive force to hold the particles between the component pads. The contact resistance of ACA joint is dependent on the contact area between the particles and the pads. Such kinds of mechanical contact resistance are similar to the stationary contact resistance between

two metal parts in pairs as studied by Holm [39] as will be discussed in the section of ACA interconnections.

2.4 ACA Assembly Process

ACA assemblies require dedicated bonding machine due to the fine pitch pads on the components. There are a number of key steps identifiable in the ACA assembly process [40]. They are described as Pre-assembly, Component placement, Heating, Assembly pressure application, Resin flow and particle compression, Resin cure, Assembly pressure release, and Cooling. Generally, they can be catalogued into three processes, pre-bonding, alignment and final bonding as shown in Figure 2.4.

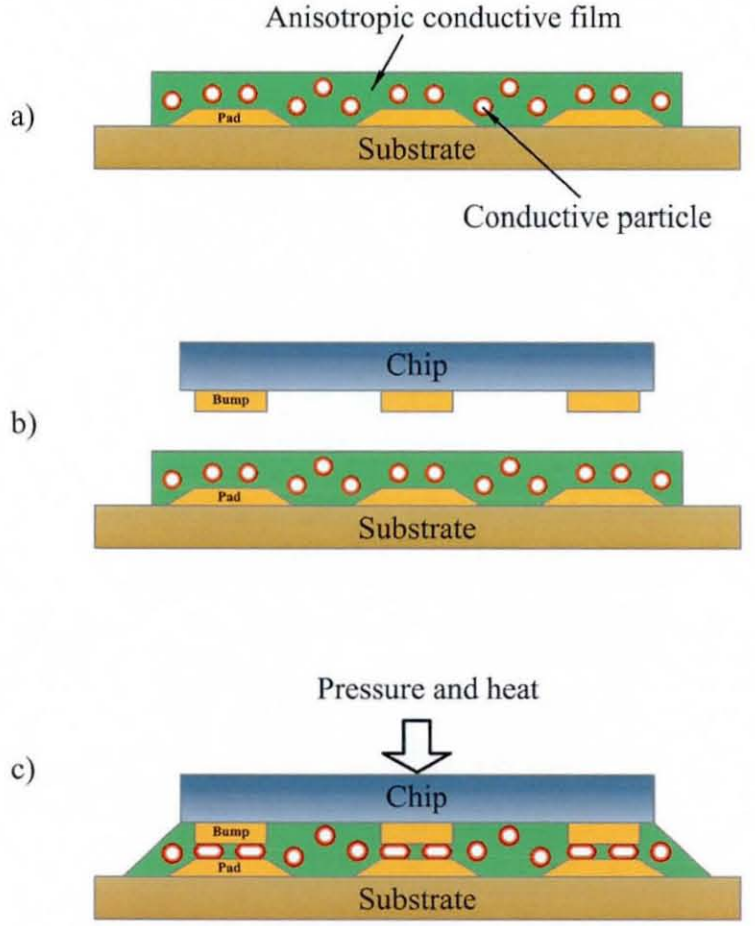

Figure 2.4: ACA bonding process, a) pre-bonding; b) alignment; c) final bonding [14].

- Initially, pre-bonding as shown in Figure 2.4-a is to laminate the prepared ACA

on the substrate by low pressure and low temperature. The aim of pre-bonding is to dispense or print pastes or placement and tack film materials.

- Subsequently, the chip is accurately aligned to the pre-bonded substrate by a dedicated machine as shown in Figure 2.4-b, where the alignment accuracy is very important to the final bonding.

- Finally, the final-bonding is achieved by applying pressure and heat on the chip as shown in Figure 2.4-c, and then the assembly is finished by properly cooling.

2.4.1 Alignment

There are many factors that affect the yield and performance of electronics packaging. Bonding parameters are often critical factors during adhesive bonding processes as far as final assembly quality and reliability are concerned. They are even more important in ACA packaging due to the complex mechanical, rheological and chemical properties of ACA materials. In addition to the bonding parameters, mechanical tolerances resulting from bonding process variations or component dimensional variations are other critical factors, which may be difficult to control.

The alignments of chip to the substrate significantly affect ACA assemblies. The alignment could not be 100% accurate due to the bonding tolerances. There are two kinds of bonding tolerances in ACA packaging, in plane misalignment between the chip and the substrate, which may be translational or rotational, and co-planarity variations between the joint planes. Experimental research on the in plane misalignment of components in ACA assemblies had been carried out in previous research [41]. Misalignment can be caused by chip placement errors, uneven assembling pressure, bump height variation and lack of flatness of the bump pads, and non-uniformity of the ACA thickness. The joint resistances are very sensitive to the alignment of chip bumps with substrate pads that some of them are too large to be used in some cases [41].

However, to our knowledge, there has been no previously reported detailed research into the effects of co-planarity variations. Bad co-planarity ACA packaging can be caused by the rotated chip alignment, distorted components and different

height pads. There is a research on the effects of gap height on conduction within ACA assembly, which explores the effect that compression of the conducting particles in ACA assemblies has on the resistance of the joints. This research can be considered as one kind of non-planarity, but the spacer foil on the package edge affected the adhesive flow during the bonding and also the metal pieces were used instead of chip or electronic components. Co-planarity effects remain one of the most important issues to be understood before ACAs can be used in really high volumes for low-cost applications [6]. Experimental research on the co-planarity variation of ACA assemblies will be presented in Chapters 3 and 4.

2.4.2 Final Bonding

There are many subsequences happened to the assembly in the final bonding. These include resin flowing, particle deformation, resin cure, pressure releasing and cooling down. Many research e.g. [40] have been put on the resin flow and thermal mechanical process by using Finite Element Analysis (FEA) to find more reliability data of ACA assemblies. It has been the subject of many recent studies.

A. Bonding Force

Bonding force, bonding temperature and bonding time are the main parameters in an ACA assembly process. Bonding force is a significant parameter that affects the ACA particle distribution and determines the particle deformation degree, and the resulting contact area between the particles and the component pads [42][43][44]. Moreover, selection of a suitable bonding force is important to achieve a reliable assembly, because the deformation of the conducting particles affects the reliability of the ACA joints [45][46]. Bonding temperature and bonding time are other critical parameters for the ACA joint reliability, since they affect the curing degree of the adhesive resin [47][48]. Furthermore, the temperature affects the adhesive flow process, consequently determines the thermo-mechanical mechanisms of ACA bonding process [38][49]. Therefore, a set of optimum ACA bonding parameters will contribute to high quality and reliable electronics assemblies. Nowadays, computational modelling of the ACA assembly process can lead to a better understanding of the

assembly process and facilitate establishment of design rules for different applications [37][40].

The effect of bonding force on the conducting particles with different sizes has been studied by Yeung et al. [42]. Finite Element (FE) analysis was used to model the transient heat transfer problem and the mechanical influence of the conducting particle in the ACF assembly. The result shows that a larger bonding force and a smaller particle size would lead to a larger stress concentration which would be a preferential site for the crack initiation and propagation. Moreover, the stress concentration was located at the edge area especially for the gold coating layer.

B. Particle Deformation

In the final assembly process, the deformation degree of the packaging, or particle deformation degree, is a very important factor for the joint resistance and the reliability of the connection. Too much deformation may make ACA particles crushed and too low deformation may cause large constrict contact resistance. The resistance of the contact rises to intermediate levels when the gap height after compression is reduced to 80% of the original particle diameter, while open circuit result when the particles are compressed to a height less than 66% of their original size. In another word, the contact resistance are stable when the particle deformation is between 20% to 34% of their original particle size [11]. The most stable values of the deformation degree was reported for 40% for metal coated particles [50][51]. Research using mathematical model of ACA particle assumes that the deformation degree in a safety region (30%—60%) has successfully predicated the characteristics of ACA particle conduction [12][43].

C. Curing Methods

There are three kinds of curing methods for ACA assembly, thermal curing, UV curing and microwave curing. Much of ACA assemblies are finished by thermal curing and much of assembly reliability has been tested for thermal curing joint. Recently developed UV ACA has been suggested for use in temperature sensitive electronics packages. In order to optimize the bonding conditions for fabrication of UV curable

ACA, smart card packaging research has been carried out [52][53]. By comparing the experimental results in curing degree, shear strength of the ACA joint and the reading distance of the smart card samples, a set of parameters which gave better performance of the COF bonding were determined. The reliability research has contributed to a better understanding of the failure mechanism of ACA joints of the smart card using UV curing.

Microwave heating significantly speeds up the curing process of polymer and polymer-based composites. Single mode microwave cured adhesives for electronics packaging application has been developed [54]. Recently theoretical work has studied the microwave transmission through the electrically conductive adhesive ECA (including ICA and ACA), heat generation and transfer inside the ECA and subsequently the microwave heating rate of the ECA. It has been shown that the penetration depth of the skin effect in the metal filler is significantly smaller than the one of a bulk metal material. The heat generation (microwave power absorption) is negligible in the metal filler due to its large electric conductivity [55].

D. Flow Analysis of ACA Assembly

In order to design an optimum process for ACA assembly, or to understand the origin of process defects, it is necessary to establish models of the process steps and to study how they interact to achieve the final geometry and material properties. One of the critical phases in the process is the adhesive flow and how the conductive particles are compressed. For the adhesive flow analysis, FE models as well as the computational fluid dynamics (CFD) modelling have been used to study this process. The Scott equation is commonly used in computational modelling to analyze the compression rate and the Newtonian or non-Newtonian flow behaviour of the adhesive. Some useful results have been found that there are many parameters affect the flow process such as the chip geometry, the chip distortion during the bonding process and the temperature gradient which were usually ignored by the early research. The flow analysis including the heat conduction during the bonding process with a domain geometry has been done successfully using Physica software, the typical work about this analysis can be found in the literature of the Loughborough University in the

UK [37],[40].

FEM Modelling on flow characterization of ACFs was mainly reported by Dudek et. al. [38]. In this study, the transient temperature analysis shows that the heat immediately spreads over the whole chip, when an initial temperature jump is assumed as shown in Figure 2.5. The temperature at the bottom of the chip reaches almost the upper chuck temperature within a few milliseconds. After 50 ms, the temperature at the bottom of the adhesive layer is about 90% of its stationary value, while the solution becomes almost stationary after 0.5 s. The fully stationary state of an overall temperature is reached after about 10 s. Analytical model is shown in Figure 2.6, where the investigations are focused the squeezed flow of adhesive occurring in the gap underneath one bump. Based on this model and from Navier-Stokes equations, a formula is obtained as:

$$x(t) = x_0[\frac{h(t)}{h_0}], \tag{2.4.1}$$

where $h(t) = h_0 - V_A t$ is the height of the gap, V_A is the vertical velocity of the bump and assumed as a constant in the modelling [38] although it is not the case in a real assembly. This analytical techniques of fluid mechanics are used to predict the flow of the conductive particles during bonding, treated as dimensionless points embedded in a viscous matrix. It allows to estimate the number of conducting particles on a bump of a chip after bonding.

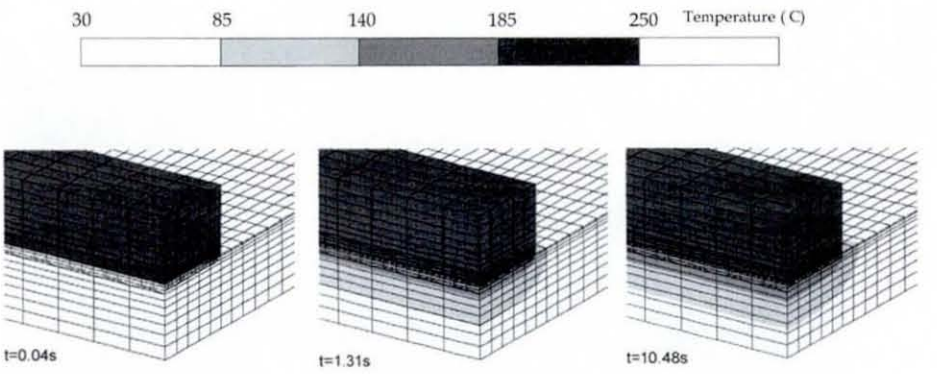

Figure 2.5: Temperature isosurfaces during bonding at different times of the process [38].

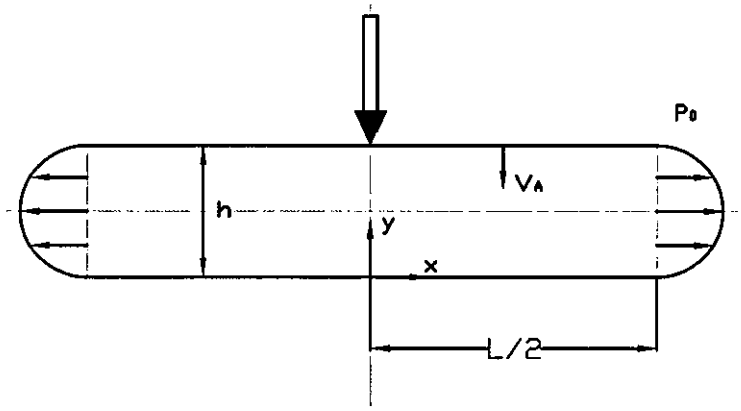

Figure 2.6: Schematic of the analytical model for the squeezing flow investigation [38].

The influence of viscosity gradients on the particle flow is characterized based on the analytical description. The stress development and stress relaxation process within the assembly are also investigated by FE modelling.

Conventional ACF has one layer of adhesive material in the sheet form with randomly distributed particles. But other proposals are known for the development of advanced ACF's with a bilayer structure [56]. The conducting particles layer is thin, similar to the diameter of the particles, and is made of a high-viscosity thermosetting material, in which the particles are arranged as a monolayer. The thick adhesive layer consists of a low viscosity pure thermosetting resin. In order to estimate the effects of viscosity changing in the flow field, a series of numerical simulations with an in-house FE-code for flow and transport problems ("CF2D" see [57] for algorithmical issues) has been accomplished. Both non-isothermal and isothermal flow situations have been studied.

Flow process during ACA particle compression was studied by Ogunjimi et al. [49]. The compression/flow of the adhesive resin is divided into two distinct steps. These are: Type I flow, where the bumps on the substrate of components penetrate into the adhesive and the adhesive flows into the gaps between the pads; and Type II flow, where all of the space between the pads has been filled and the adhesive must then flow out from under the component. A typical situation of the particle flow is given in Figure 2.7. Ideally the bond pad sizes and heights and the adhesive thickness should be chosen such that Type II flow just occurs, however limitations

on the choice of these parameters often result in significant Type II flow being necessary. This study approximated the components as being circular, with a purely radial adhesive flow, and used the Scott equation to model the rate of compression of the adhesive during Type II flow. Dudek et al. [38] also modelled the adhesive compression process analytically using a 2D representation rather than the rotationally symmetric approximation. The 2D approximation of this equation is likely to be more approximate for assemblies where the pads have a high length to width ratio, such as LCD to flex connections, but less appropriate for more conventionally shaped IC pads such as those used in smart card applications. Also the equation neglects the effects of shear thinning of the adhesive, which significantly affects the resin flow and it can not therefore be safely used for Type II flow if the adhesive resin flow is non-Newtonian.

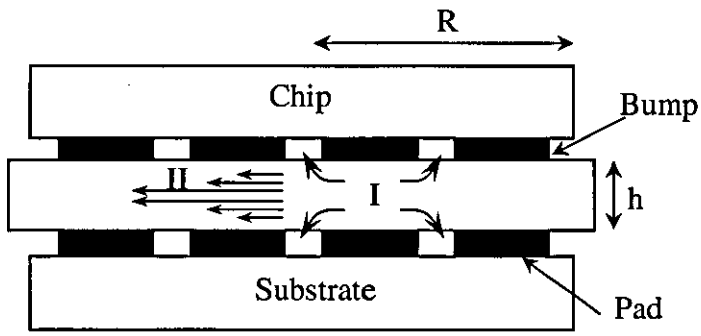

Figure 2.7: Schematic drawing of the ACA flow during the bonding [49].

There have been several other reported studies of modelling on the flow process. Mannan et al. [58] modelled the initial stages of ACA joints assembly process and predicted the time required to squeeze out the adhesive from beneath the chip with the ignoring of the presence of the conducting particles in the adhesive. The Scott equation was also used and a non-Newtonian power law model is assumed for the adhesive viscosity, the chip is modelled as circular rather than square and the temperature is assumed to ramp up linearly with time. The squeezing time is found to be affected by various process parameters and geometry, the chip size may have a large effect on process time. In the later report [59], Mannan et al. studied the ACF squeezing process using the CFD software package: Fidap 7.52. This CFD modelling

has successfully taken into account the detail geometry of the assembly and showed the paths taken by infinitesimally small conducting particles. Real conducting particles of finite size will affect the flow of fluid around them, and hence the CFD models will not be able to track the movement of particles exactly, just lead to insight as regards the case when the particles are present. It was concluded in this paper that the flow out from the centre of the chip will be much weaker than the corners, and the central regions of the chip, resulting in enhanced particles numbers in these regions.

Whalley et al. [37] successfully discussed the effect of heat conduction during the flow process for an ACA using Physica software to model a simple domain geometry. The results showed that it is important to include non-Newtonian flow behaviour in models of an ACF, as the combined effect of shear thinning and a temperature gradient is much higher than for a temperature gradient alone, presumably because the reduction in viscosity due to the combined effects of increased temperature and shear thinning were sufficient to exceed the effect of the flow being constrained into a much thinner layer. Also in another paper [60], the substrate/component distortion during processing is predicted with FE modelling. The result shows that the compression of the adhesive layer is unlikely to be uniform.

E. Thermal Mechanical Analysis of ACA Assembly

Another point interested is the thermal mechanical analysis during the bonding process and the relationship between the conductive particle compression and the electrical property. The stress and strain distribution on the particle and I/O pads during the bonding process has been reported before. While, owing to the phase change of the polymer foil from viscous to solid, the effect of the adhesive matrix on the stress generation of conductive particles during the bonding process is normally ignored by the early research. Also the heat conduction analysis is neglected in most mechanical research. However, a complete analysis of the effect of bump height on the stress distribution can be found in the literature of Wu et al. [61]. For the relationship between the particle compression and the electrical property, some experimental and theoretical results have been reported, the typical work has been done by Yim et al. [19] and Wang et al. [62].

The consequence of the bonding pressure during the ACA bonding on the stress generation is evident. This stress generation is probably the reason for catastrophic failure [10]. Owing to the phase change of the polymer foil from viscous to solid, it is a little complicated for this analysis. There have been several reported studies of modelling of the assembly process. Most of the literature has neglected the effect of the polymer on the stress generation of conductive particles.

Buratynski [63] modelled the transient heat flows occurring during the curing process and the resulting residual stress of following assembly pressure removal and cooling. These models provide some extremely valuable insights, but assume that the adhesive flow has completely finished and that all of the assembly force is therefore carried by the conductor particles before resin curing commences. However, it is likely that this assumption is often invalid. Dudek et al. [38] and Chiang et al. [64] have also modelled the residual stresses within the assembly after curing, but have made the similar assumptions. Dudek et al. demonstrated very clearly how temperature gradients significantly affect the adhesive flow, a result supported by the experiment results in [65] where the temperature ramp rate was shown to significantly affect the process.

Wu et al. [66] also simulated the stress generation during the bonding process using FE modelling, they have found that both for rigid and deformable particles, significant stress is built up in the interface between the two contacts, as shown in Figure 2.8. They have offered a useful insight of the stress distribution during the boning process, but only a very simplified finite element analysis of the problem of a particle embedded in a bonding system is used, also the polymer effect on the mechanical property is neglected.

Pinardi et al. [67] and Wu et al. [61] have made a complete analysis on the effect of bump height on the stress and strain distribution on the ACF joints during the compression process, cooling and thermal cycling test. The results showed that the residual stress is larger on rigid substrate than on the flexible substrate after bonding, the thermal stress increased with the thickness of the bump, also the bigger volume strain is found for higher bump. But in these two papers, the particle is looked as infinitely small and ignored in the research.

In order to provide a first hand approximation and insight of the thermal behaviour

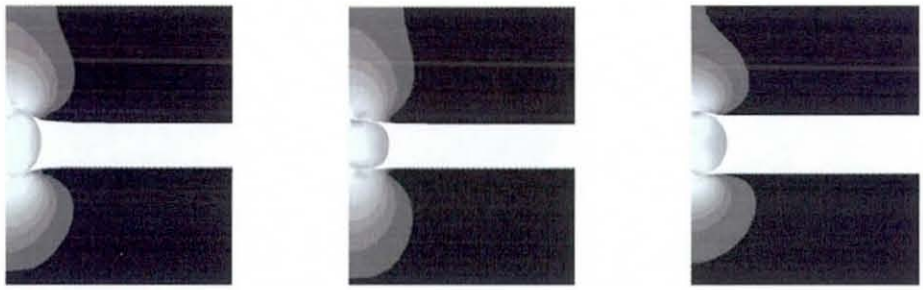

a) b) c)

Figure 2.8: Deformation distribution of different particle systems, (a) rigid system, (b) deformable particle system and (c) fully deformable system [66].

of the ACA assembly and ACF film during bonding process, the actual assembly and manufacturing process was simulated by Chiriac et al. [68]. Results from the detailed process modelling indicated that during initial ramping, within 0.02 s, the die and nozzle head experienced a small temperature drop due to the cooling effect of the ACF material and substrate. The ACF material also displayed a steep increase in temperature after contacting the die, followed by a short decay, then ramped again. At the end of the 10 s ramping process, the ACF reached a temperature of almost 230 ^0C. During the 5 s of curing, all parts reached steady state in less than 2 s.

2.5 ACA Interconnections

A single ACA connection includes three parts: the component bump, ACA particles, and the substrate pad, as schematically shown in Figure 1.2. A cross-section profile of an ACA joint including one particle is shown in Figure 2.9, which shows the real scale of a typical particle in relation to its surrounding joint parts in a typical flip-chip application. Conductive path through the bump, the single particle, and the pad can be divided into five parts, which can be represented as five independent resistors, bump resistance, two contact resistances, particle resistance, and pad resistance, as shown in Figure 2.10 [43].

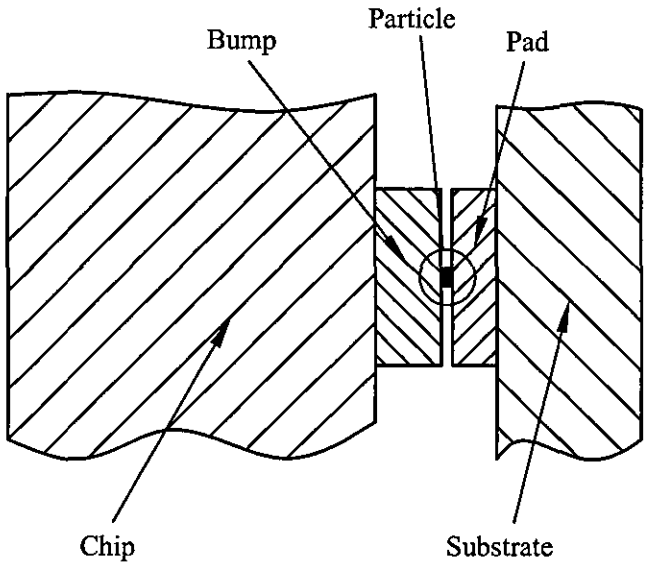

Figure 2.9: A single current path in an ACA joint [13].

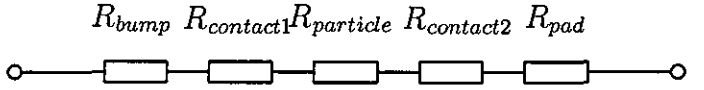

Figure 2.10: The five resistances in a DC current path [43].

2.5.1 Chip

Basically, all single chips are made from crystalline silicon wafer. The fundamental building blocks in a chip are transistors. Theoretically, wafer scale integration (WSI), which builds the entire system or subsystems on a single wafer, is the most ideal electronics assembly. However, wafers are usually broken up into individual chips due to the poor yield of WSI. The connections that link the functional blocks in the chip to other electrical traces are square metal electrodes, which are bumped on the chip surface, side by side in daisy-chain pattern. The material used in bumping are *Al*, *Cu*, *Ni* and *Au*. The basic layer in the bump is *Al*, then *Cu* or *Ni*, then *Ni/Au* coating, the *Au* layer is coated outside to make better mechanical contact and protect the bump from oxidizing. Therefore, there is resistance resulted from chip bumps if the chip is packaged by ACAs.

2.5.2 Contact Area

There are two kinds of contacts in ACA assemblies as two kinds of ACA particle system, rigid and compliant, are considered. In Figure 2.3(a) [33], it is assumed that the particle indentation does not change the resistance of the pad metallization. Given the indentation depths of Δ_1 and Δ_2 in the upper and lower metal pads, respectively, the resistance of the interconnect with the particle radius r is:

$$R = \int_{-(r-\Delta_1)}^{r-\Delta_2} \rho \frac{dl}{A} = \frac{\rho}{2\pi r} \ln\Big[\Big(\frac{2}{\varepsilon_1} - 1\Big)\Big(\frac{2}{\varepsilon_2} - 1\Big)\Big], \tag{2.5.1}$$

where ρ is the particle resistivity, $\varepsilon_1 = \Delta_1/r$ and $\varepsilon_2 = \Delta_2/r$. ε_1 and ε_2 measure the magnitude of deformation in the pad, and can be interpreted as an overall particle strain. For small strains, where $\varepsilon_1 \ll 1$ and $\varepsilon_2 \ll 1$, we have:

$$R = \frac{\rho}{2\pi r} \ln\Big(\frac{4}{\varepsilon_1 \varepsilon_2}\Big). \tag{2.5.2}$$

For the case where lower and upper pads have the same amount of deformation, $\varepsilon_1 = \varepsilon_2 = \varepsilon$, and therefore:

$$R = \frac{\rho}{\pi r} \ln\Big(\frac{2}{\varepsilon} - 1\Big). \tag{2.5.3}$$

And for the symmetrical and small deformation case:

$$R = \frac{\rho}{\pi r} \ln\Big(\frac{2}{\varepsilon}\Big). \tag{2.5.4}$$

In the case of deformable particles Figure 2.3(b), Equations (2.5.1) to (2.5.4) will still be valid if Δ_1 and Δ_2 now represent the particle deformation in the lower and upper interfaces, respectively. It should be noted that the cross-sectional area of the particles is enlarged due to the Poisson's ratio effect in the compressed conducting particles. The extent of this area enlargement depends on the cross-sectional location. For the purpose of bulk resistance calculations, it is assumed that area enlargement follows an average Poisson's law. The deformed area at the location x becomes:

$$A = \pi(r^2 - l^2)\Big[1 + \frac{\nu(\varepsilon_1 + \varepsilon_2)}{2}\Big]^2, \tag{2.5.5}$$

where ν is the Poisson's ratio of the particle. Accordingly, Equation (2.5.1) is modified to account for the effect of Poisson's ratio on the resistance, giving:

$$R = \frac{\rho}{2\pi r\Big[1 + \frac{\nu(\varepsilon_1+\varepsilon_2)}{2}\Big]^2} \ln\Big[\Big(\frac{2}{\varepsilon_1} - 1\Big)\Big(\frac{2}{\varepsilon_2} - 1\Big)\Big]. \tag{2.5.6}$$

For the symmetrical case, where lower and upper particles are compressed by the same amount:

$$R = \frac{\rho}{\pi r(1+\nu\varepsilon)^2} \ln\left(\frac{2}{\varepsilon} - 1\right). \tag{2.5.7}$$

Equations (2.5.1) and (2.5.6) depict the closed-form resistance-deformation relationships for the rigid and the deformable particle systems. Under a deformation-controlled scheme, these equations can be used to estimate how much deformation is required to attain a desirable level of contact resistance.

2.5.3 Contact Resistance

The conductive abilities of ACA assemblies are dependent on the pad materials and the type of particles that are trapped between the pads. In other word, the materials of ACA particles and component parts determine the interface properties of the electrical contact and the extent of particle deformation. In order to provide a concise, structured overview of this topic, some detailed conductive models, mathematical solutions and research methodologies are presented in this section based on the reviewed literature. These models can partially explain the conduction mechanisms for an ACA particle, but make a number of important simplifying assumptions. The prediction of electrical contact resistance for ACA assemblies, has also been reported by Chin et al. [69]. This study shows that important issues generally not considered in existing models are tunnelling resistance, multi-material layers, edge effects, surface roughness, elastic recovery and residual forces, contact interaction between nearby particles and particle size distribution.

A. Hertz Contact Stress

Hertz theory of elastic contact can be used to evaluate the contact between a sphere and a flat surface. It has been used to model the contact and reliability of electronic interconnections [70], although Hertz equations are only appropriate to small and elastic deformations.

The first satisfactory analysis of the stresses at the contact of two elastic solids is due to Hertz [71]. Hertzian contact stress refers to the localized stresses that develop

as two curved surfaces come in contact and deform slightly under the imposed loads. This amount of deformation is dependent on the elasticity of the material in contact, i.e., its modulus of elasticity. It gives the contact stress as a function of the normal contact force, the radii of curvature of both bodies and the modulus of elasticity of both bodies. In ACA assembly, the formula can be expressed as:

$$\sigma = (\frac{6PE^{*2}}{\pi^3 R^2})^{\frac{1}{3}}, \tag{2.5.8}$$

where σ is the contact stress, P is the normal contact force, R is the radius of the ACA particle, and E^* can be calculated by:

$$\frac{1}{E^*} = \frac{1-\nu_1^2}{E_1} + \frac{1-\nu_2^2}{E_2}, \tag{2.5.9}$$

where E_1 and E_2 are the Young's modulus and ν_1 and ν_2 are Poisson's ratios of the two contact parts respectively. Hertz contact is considered as apparent contact in the following Holm's theory.

B. Holm's Stationary Electrical Contact Theory

The surface topography of a typical gold coating chip bump, taken by Atomic Force Microscope (AFM) (*Dimension*^{TM} 3100), is shown in Figure 2.11. Even by excellent polishing or plating, the micro-topography of such a metal surface cannot be perfectly smooth. The contact area between two metal surfaces is therefore not as large as it appears because of the asperity of the metal surfaces.

Holm's *stationary electric contact* theory [39] is widely recognized as being applicable in this area. The term *electric contact* means a no-permanent junction between two conductors, which is apt to carry electric current and a *stationary contact* is where the two metal conductors are held in contact via an external load. The load that presses the contact members together is the mechanical load or simply the *load*, P, or normal force. If the contact members were infinitely hard, the load could not bring them to touch each other in more than three points. However since actual materials are deformable, the contact points become enlarged into small areas and simultaneously new contact points may occur. As shown in Figure 2.12, the sum of all these areas and *spots* is the *load bearing area*, A_b. The whole covered area is called the *apparent contact area*, A_a, upon which the pressure is finite. A_b can be generated

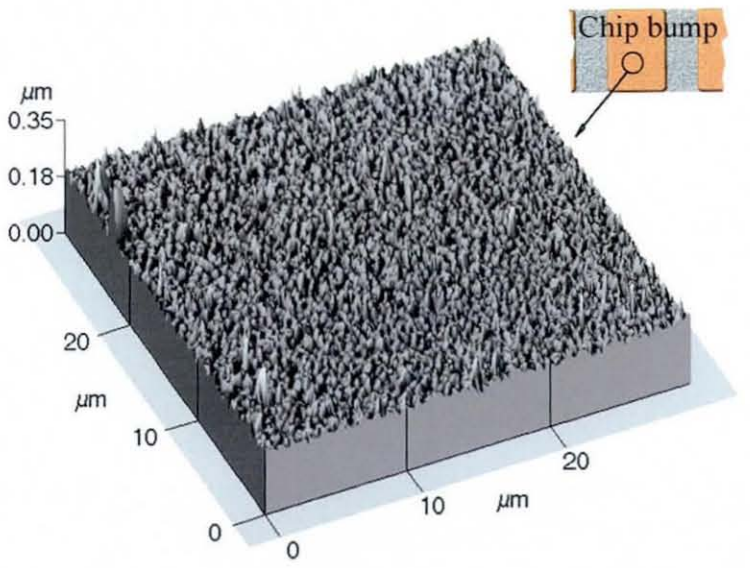

Figure 2.11: The surface topography of a gold coated chip bump.

merely by elastic deformation. But, because of the unevenness, the contact members, even though they may be nominally flat, actually touch each other in areas that are more or less plastically generated. They then satisfy the following:

$$P = \xi H A_b, \tag{2.5.10}$$

where usually $0.2 < \xi < 1$ (ξ is a factor affected by the asperity of the metal surface) and H is the contact hardness (N/mm^2). A_b may be of much smaller magnitude than the apparent contact area.

The contact resistance due to current having to crowd into this restricted contact area is known as the constriction resistance, R_C, which is the consequence of the current flow being constricted through the small conducting spots as shown in Figure 2.12. The term *a-spot* is usually used for the conducting contact areas, referring to the radius a of a circuit contact area. In addition to this constriction resistance, an isulating film between the particles and pads may give rise to an additional film resistance, R_f. The surface A_b usually is partly covered by insulating tarnish films and then only a fraction of A_b has metallic or quasi-metallic contact, producing a relatively small film resistance because of the tunnelling effect. Thus, the total contact resistance, R, is the sum of the constriction resistance R_c resulted from the two contact

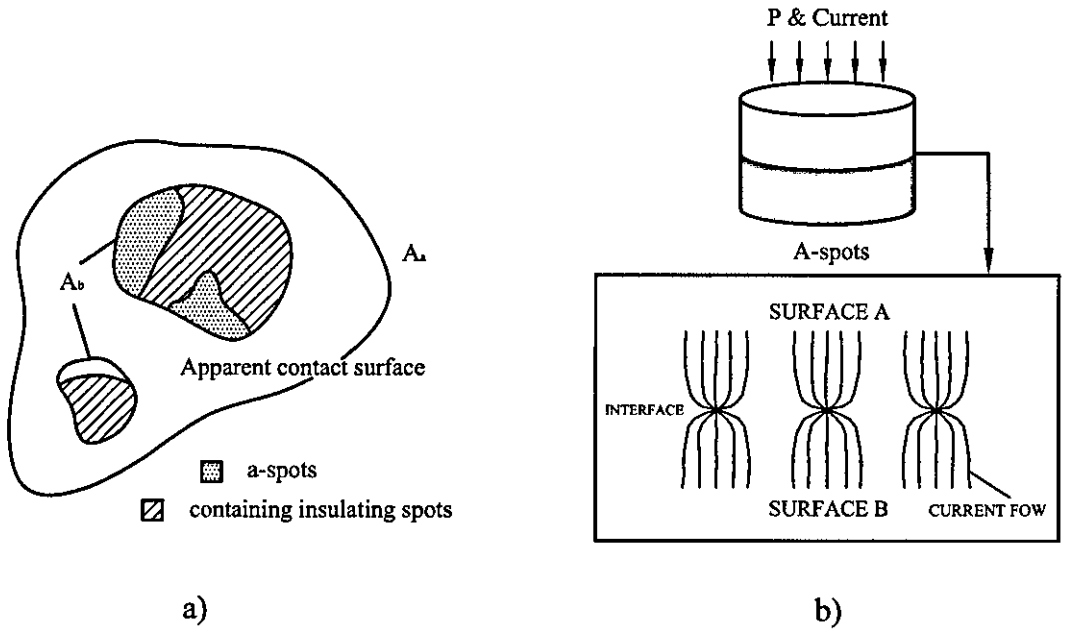

Figure 2.12: Apparent contact surface A_a; load-bearing contact area A_b, containing insulating spots (shaded) and conducting spots, i.e., a-spots (dotted) [39].

members and the film resistance R_f:

$$R = R_c + R_f \tag{2.5.11}$$

C. Stationary Electrical Contact of ACA Interconnections

The contacts in an ACA joint are stationary electric contacts, except that they are retained by the surrounding cured or solidified polymer instead of external mechanical means. Some authors have suggested that the stationary electric contact resistance is the major proportion of the whole ACA joint resistance [5][21]. Liu [5] assumed that all particles touching both substrate and component surfaces make electrical contacts, then A_b is equivalent to the area of the electrically conducting spot such that:

$$A_b = \pi n a^2 \tag{2.5.12}$$

where a is equivalent to the area of the electrically conducting spot (i.e., the radius of the spot formed at the substrate/particle interface) and n is the number of spots. If the particle concentration is sufficiently low, then each particle contributes to R_c independently and from Holm's theory:

$$R_c = 2(\frac{\rho}{4na}) \tag{2.5.13}$$

where ρ is the resistivity of the particles.

In reference [5], it is assumed $\xi = 1$. By combining Equation (2.5.10), (2.5.12) and (2.5.13), it is seen that:

$$R_c = 0.0886\rho(H/nP)^{\frac{1}{2}} \tag{2.5.14}$$

From Equation 2.5.14, it can be seen that for a certain particle, if $\xi = 1$, the contact resistance is determined by the normal force, P (per particle).

As already noted, ACA assembly creates a form of stationary electric contact where a non-conductive adhesive maintains the contact force. Kristiansen [72] reported the characterization of such electrical contacts using Holm's contact theory. Several factors that may affect the ACA electric contacts were explored in his study. The indentation in an isotropic semi-infinite body, produced by a spherical indenter is schematically shown in Figure 2.13. The heavy line represents the indentation before removal of the force on the indenter ball. The dashed line represents the final remaining deformation in the surface. The space between the two lines represents the elastic (load bearing) deformation of the indentation. The stress is most inhomogeneous at the rim, and the plastic deformation starts in this area. In this way, the 'mouth' of the indentation remains visible. The mouth area πa^2 is practically equivalent to the load bearing area, which means Equation (2.5.10) can be written as:

$$P = H\pi a^2 \tag{2.5.15}$$

However, in a real contact not all the contact spots will experience a stress above the yield stress of the material. The total area of the contact spots during pressure will therefore be somewhat larger than expected from the contact force. Whereas the observable area of indentation after the load has been removed will be smaller.

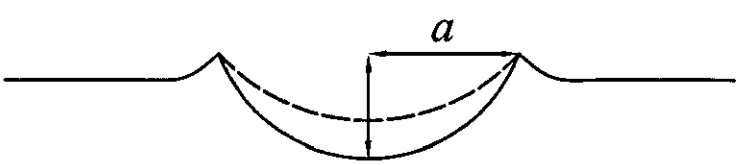

Figure 2.13: The indentation in an isotropic semi-infinite body, produced by a spherical indenter [72].

Kristiansen [72][73] explained the effect of contact films present in the bearing area, A_b. In an ACA connection, films of different composition may be present:

- Pre-tarnish film, which typically is a chemisorbed monolayer of oxygen on the metal surface. This can be presented on any types of ACA particles.
- Tarnish, where one constituent of the film is the matrix metal, as a metal oxide. This may be found on Ni and Ag ACA particles.
- Alien films, comprised of 'foreign' materials such as water, hydrocarbons, etc. A thin layer of adhesive may also be trapped in the ACA contact area.

The thickness of the tarnish film can be a monolayer, a thin protective or passivating film, which stops growing at a certain thickness. Other films can grow continuously, but diffusion processes will often inhibit their growth rate. The film resistance can be controlled by the tunnelling resistance. In such cases, the current will be able to penetrate the thin insulating layers by tunnelling due to the wave like properties of the electron, however, when the film in the contact area is very thin then the constriction resistance, and not the tunnelling resistance, dominates the contact resistance in the quasi-metallic contact area.

The chemisorption of oxygen was also discussed by Kristiansen [72][73]. Chemisorption is a more complicated phenomenon, where oxygen is often involved. Initially the oxygen molecule may be physisorbed, but within a fraction of a second, the molecule is dissociated into atoms which become chemically bonded to the dangling bonds on the metal surface. The oxide layer will continue to grow when the bond energy between the oxygen and metal represents a larger energy than the sum of the metal-metal bond and the oxygen-oxygen bond in the oxygen molecule. This results in a parabolic rate of oxidation [72].

During the curing/setting of the ACA assembly, tarnish films may be broken due to the asperity of the contact surface. When one member of the contact is deformed plastically, groups of atoms on the surface will be moved relative to each other. The result is that the tarnish layer is ruptured, creating spots of bare metal surface [72]. Figure 2.14 shows a model of a possible deformation of the oxide. The model shows that it is the initial pointed spike that causes the most significant thinning of the oxide,

whereas a blunt elevation causes a much smaller reduction in the oxide thickness.

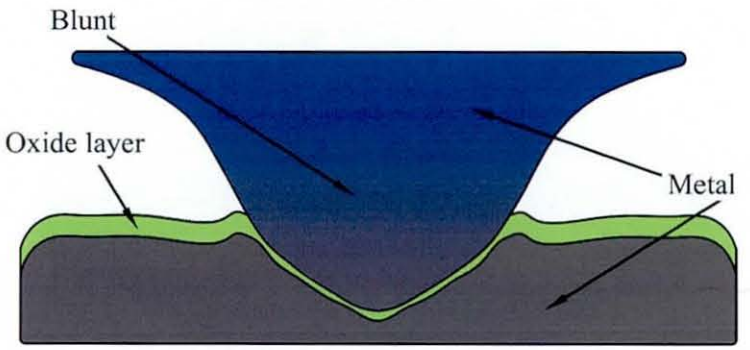

Figure 2.14: A schematic model of a possible deformation of the oxide [72].

D. Stationary Electric Contact Model

Yim et al. [19] derived an analytical model based on Holm's theory and Hertz's classic elastic theory, which describes the interconnection resistance of an ACF in terms of sample geometry, particle size and applied pressure. In the model, the constriction resistance, R_{CR}, has been shown to be:

$$R_{CR} = \frac{\rho_1 + \rho_2}{2d}, \tag{2.5.16}$$

where ρ_1, ρ_2 are the intrinsic resistivity of the metal conductive particles and substrate respectively, and d is the diameter of the contact spot area [39]. The magnitude of the deformation for a given pressure is determined by the number, the contact hardness and the diameter of the conductive particles. In considering these factors, the radius of the contact area between conductive particles, with number of n, and a flat substrate under an applied force F, can be obtained using elasticity theory [71]:

$$a = \left(\frac{3FD}{n8E^*}\right)^{1/3}, \tag{2.5.17}$$

where D is the diameter of curvature of conductive particles and E^* is the elastic modulus. Substituting Equation (2.5.17) into Equation (2.5.16), we get the constriction resistance [19]:

$$R_{CR}(elastic) = 0.347(\rho_1 + \rho_2)\left(\frac{nE^*}{FD}\right)^{1/3} \tag{2.5.18}$$

The behaviour of the contacts in an ACA assembly was studied in a similar way by Chiang et al. [64]. Figure 2.12-*b* shows the surface contact mechanism and the electrical behaviour of metal to metal stationary contact. The *a-spots* instead of the entire nominal contact surface constrict the electrical current between these two objects. Since the conductive particles in an ACA assembly are very small (diameter of around 5 μm), one approach that has been used is to assume that each of the conductive metal particles can be treated as an *a-spot*. Therefore, after considering classic elastic theory, the constriction resistance is the same as in Equation 2.5.18, which indicates that the electrical resistance can be estimated if the material properties of the two contact bodies, the contact pressure and the radius of the deformed surface are known.

Two kinds of ACA contact conduction, single-particle conduction and multiple-particle conduction, were studied by Shi et al. for solid particles [20].

- Single-particle conduction

If a single particle is placed between two conductors as shown in Figure 2.9, the total resistance of the system can be written as (see Figure 2.10):

$$R = R_{bump} + R_{contact} + R_{particle} + R_{contact} + R_{pad} \tag{2.5.19}$$

Shi et. al. extended this to:

$$R = R_{pu} + (R_{cu} + R_{tu}) + R_{blk} + (R_{tb} + R_{cb}) + R_{pb} \tag{2.5.20}$$

where R_{pu} and R_{pb} are the two constriction resistances of the plates, R_{cu} and R_{cb} are the constriction resistances between the plates and the particle, R_{tu} and R_{tb} are the tunnelling resistances, and R_{blk} is the bulk resistance of the particle. Both the upper and lower conductors can be considered to be circular, with finite diameters of b_u and b_b, respectively. The equipotential surfaces around each plate are then hemispherical, with the centre being the centre of the plate. The current flows radially, normal to the equipotential surfaces as schematically shown in Figure 2.15. The constriction resistance of R_{pu} is then readily given by:

$$R_{pu} = \int_{bu}^{\infty} \frac{\rho d\xi}{2\pi\xi^2} = \frac{\rho}{2\pi b_u}, \tag{2.5.21}$$

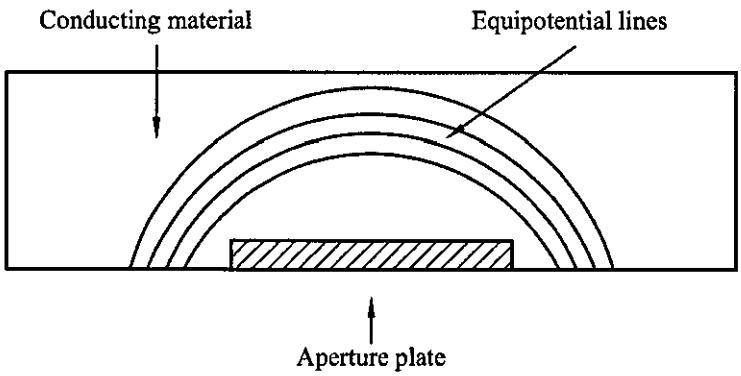

Figure 2.15: Schematic for the calculation of the constriction resistance of a conducting plate of finite size [20].

and similarly:

$$R_{pb} = \frac{\rho}{2\pi b_b}. \tag{2.5.22}$$

In a similar way, the constriction resistance of the contact is given by:

$$R_{cu} = \int_{ru}^{b_u} \frac{\rho d\xi}{2\pi\xi^2} = \frac{\rho}{2\pi}\Big(\frac{1}{r_u} - \frac{1}{b_u}\Big), \tag{2.5.23}$$

where r_u is the radius of the contact between the particle and the upper plate. Similarly, the constriction resistance of the contact between the particle and the lower plate is:

$$R_{cb} = \frac{\rho}{2\pi}\Big(\frac{1}{r_b} - \frac{1}{b_b}\Big), \tag{2.5.24}$$

where r_b is the contact radius.

Using Figure 2.16 as a reference, one can obtain the bulk resistance of the particle R_{blk}:

$$R_{blk} = \int_{-\sqrt{r^2-r_b^2}}^{\sqrt{r^2-r_b^2}} \frac{\rho dx}{\pi(r^2 - x^2)} = \frac{\rho K(r, r_u, r_b)}{2\pi r}, \tag{2.5.25}$$

where:

$$K(r, r_u, r_b) = \ln\Big[\frac{(r + \sqrt{r^2 - r_u^2})(r + \sqrt{r^2 - r_b^2})}{(r - \sqrt{r^2 - r_u^2})(r - \sqrt{r^2 - r_b^2})}\Big]. \tag{2.5.26}$$

By substituting Equations (2.5.21)-(2.5.26) into Equation (2.5.20), the total resistance of a single-particle system can be written as:

$$R = \frac{\rho}{2\pi r_u} + \frac{\rho}{2\pi r_b} + R_{tu} + R_{tb} + \frac{\rho K(r, r_u, r_b)}{2\pi r}. \tag{2.5.27}$$

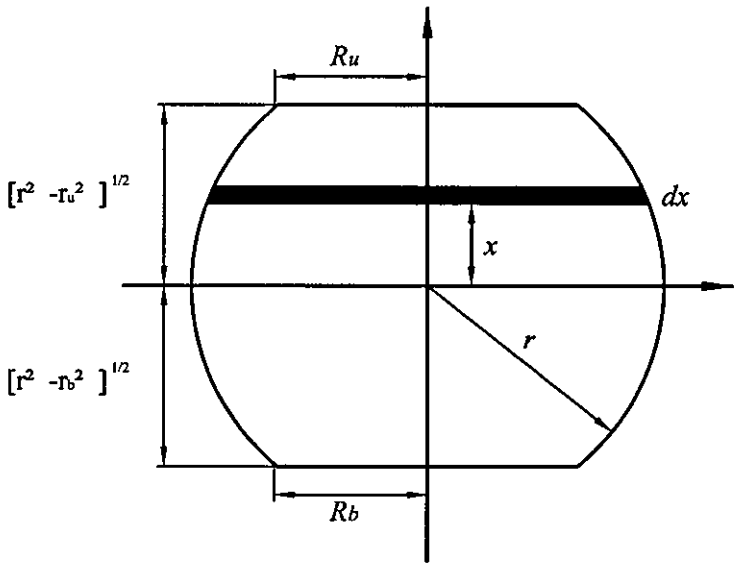

Figure 2.16: Schematic for the calculation of the bulk resistance of a particle [20].

- Multiple-particle conduction

When multiple particles are placed between the conducting plates, as schematically illustrated in Figure 2.17, the total resistance for all the particles placed between the plates R_2 can be obtained by using the fact that the particles are arranged in parallel.

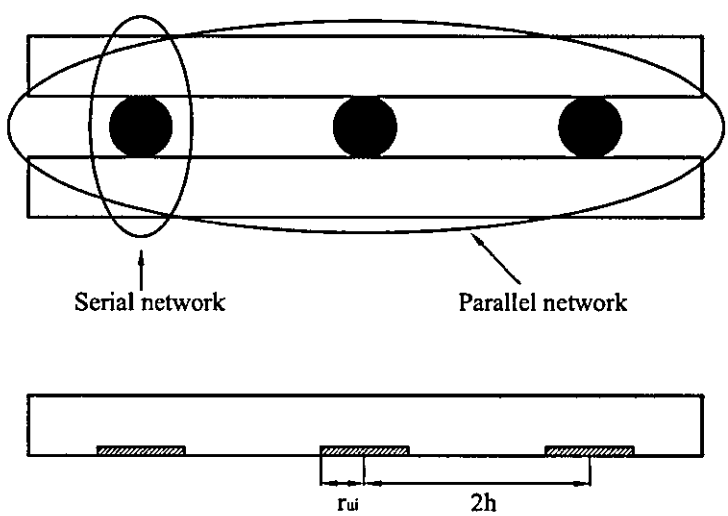

Figure 2.17: Schematic of electrical conduction when multiple particles are placed between the plates [20].

Hence $1/R_2 = \sum 1/R_1$, where R_1 is a sum of the constriction resistance and the tunnelling resistance of an isolated particle. On the other hand, the resistance of the entire system, R, is given by $R = R_2 + R_{pu} + R_{pb}$, since the particles and the plates are arranged in series. In a similar way to that for single particle conduction, Shi et al. [20] calculated the total resistance of the entire system. It can be expressed as:

$$R = [\sum_{i}^{N} \frac{1}{R_{1,i}}]^{-1} + \frac{\rho}{2\pi b_u} + \frac{\rho}{2\pi b_b} \tag{2.5.28}$$

To sum up, the electric contact models reviewed here are proposed to explain the resistance of the stationary contacts in ACA joints, and they are all based on the assumption that the $a-spot$ is equal to the whole apparent contact area, which is different from Holm's theory, where the total $a-spot$ area is much smaller than the apparent contact area. Such discussion can be found in reference [17][74]. There is insufficient experimental data in the literature to conclusively demonstrate whether this approach is adequate, but there is some evidence to suggest that in practice the resistances are higher [21][74].

2.5.4 Particle Resistance

Määttänen [44] calculated the particle resistance as a function of particle deformation degree using a conduction model.

Starting from Ohm's law, the resistance of a conductor, R_P, is given by:

$$R_P = \rho \frac{l}{A}, \tag{2.5.29}$$

where, ρ is the resistivity of the metal coating, l is the length of the conductor and A is the cross sectional area of the conductor.

The degree of deformation, $Deformpercent$, is described by the formula:

$$Deform\ percent = 100\Big[1 - \Big(\frac{h}{2r}\Big)\Big], \tag{2.5.30}$$

where h is the distance between the contact surfaces and r is the undeformed radius of the metal coating polymer particle.

If it is assumed that the area of the metal coating remains constant during the deformation, the following results can be derived from the geometry as shown in

Figure 2.18. The area of the spherical cap forms the metallic contact area of the particle and, therefore, the metallic contact area, A, is given by:

$$A = 2\pi R^2\left(1 - \frac{h}{2r}\right). \tag{2.5.31}$$

And the length of the conductor, l, is given by:

$$l = \frac{\pi h}{2}. \tag{2.5.32}$$

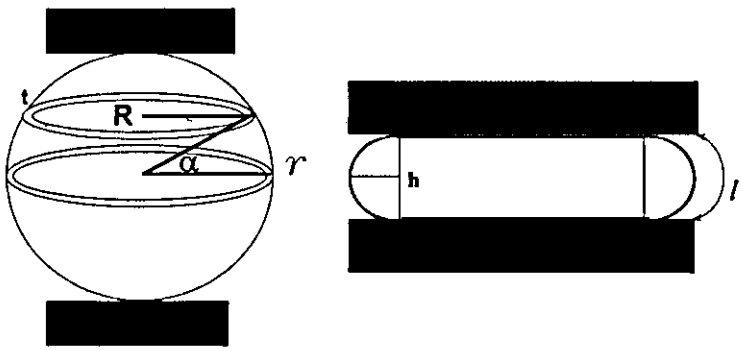

Figure 2.18: Deformation model of the particle [44].

The average cross sectional area of the current is the average area of the thin metal 'rings' around the polymer particle (Figure 2.18). Because the resistance is inversely proportional to the cross sectional area of the conductor, the average area can be calculated as follows:

$$\left(\frac{\widetilde{l}}{A}\right) = \frac{\int_0^{\frac{\pi h}{4}} \frac{dS}{2\pi t r\cos\alpha}}{\int_0^{\frac{\pi h}{4r}} ds} = \frac{2}{\pi^2 h t}\ln\tan\left[\frac{\pi}{4}\left(1+\frac{h}{2r}\right)\right], \tag{2.5.33}$$

where $R = r\cos(\alpha)$ (Figure 2.18), $S = r\alpha$, $dS = rd\alpha$ and t is the thickness of the metal layer on the particle.

Since there is spherical symmetry, an approximation can be made and the problem is solved using Ohm's law and the formula for the resistance of the deformed particle, R_p, is written as follows:

$$R_P = \rho\frac{\pi h}{2}\left(\frac{\widetilde{l}}{A}\right) = \frac{\rho}{\pi t}\ln\tan\left[\frac{\pi}{4}\left(1+\frac{h}{2r}\right)\right]. \tag{2.5.34}$$

An important observation that can be made from this is that the resistance is independent of the particle size, but depends on the resistivity of the particle (ρ), the thickness of metal layer (t) and the degree of deformation ($h/2r$).

For the solid metal particle the following approximate formula can be used [75]:

$$R_P = \frac{\rho}{\pi r}\ln\left(\frac{2}{\varepsilon} - 1\right) = \frac{\rho}{\pi r}\ln\left(\frac{1+\frac{h}{2r}}{1-\frac{h}{2r}}\right), \tag{2.5.35}$$

where ε is the average degree of deformation.

It can be seen from Equation 2.5.35 that for a solid particle the resistance increases when the particle size becomes smaller. The pressure does not affect the degree of deformation of hard particles, for example nickel, as much as for softer particles like gold or silver. The main results obtained from Formulas 2.5.34 and 2.5.35 are presented in Figure 2.19, where the particle size is $10\mu m$. Figure 2.19 shows the large difference in particle resistance between the Au/Ni coating particle and the solid metal. In conclusion, the thickness of the metal coating has a direct influence on the resistance. This means that there is a large difference, depending on particle type, in the number of particles estimated to be needed for a good contact. Solid gold and silver particles give a much smaller resistance compared to the nickel coating polymer particle.

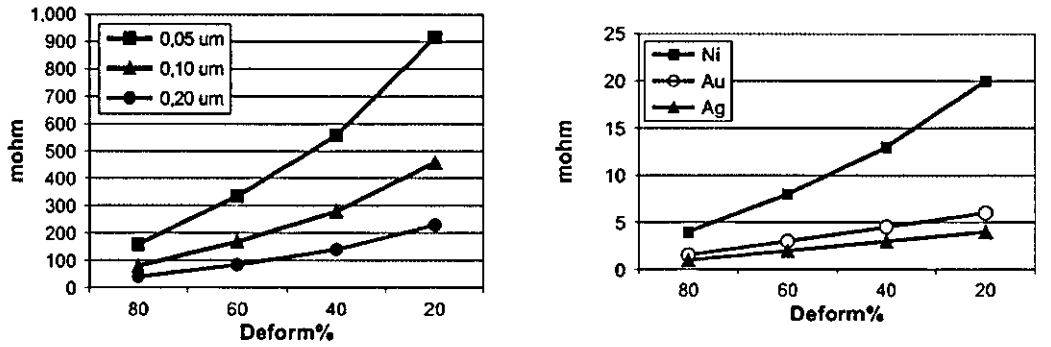

Figure 2.19: Predicted particle resistance for different degree of deformation (a) for Au/Ni-polymer with various metal thicknesses, (b) for solid metal particles [44].

Another model for the electrical conduction characteristics of metal coating ACA particles, was derived by Dou et al. [43]. According to the numerical solutions, the greater the level of particle deformation, the thicker the metal coating layer and the

greater the resin diameter, the lower the particle resistance is. It was shown that the ACA particle resistance is determined by the particle deformation and the particle geometries, however it is more sensitive to the deformation degree and the nickel layer thickness than the resin diameter and the gold layer thickness.

An ACA particle, consisting of a nickel layer, a gold layer and a resin core, is shown schematically in Figure 2.20. The particle resistance can be considered as being the resistance of the Ni layer in parallel with the Au layer:

$$\frac{1}{R_{particle}} = \frac{1}{R_{nickel}} + \frac{1}{R_{gold}}. \tag{2.5.36}$$

The resistance of a single ACA particle is a multi-parameter function, i.e. it is a function of resin sphere diameter d, deformation degree k, nickel layer thickness t_1 and gold layer thickness t_2. During the deformation process, if the particle volume is not changed, hence the original resin sphere volume V_{sphere} is equal to the deformed resin solid volume $V_{deformed}$:

$$V_{deformed} = V_{sphere} = \frac{4}{3}\pi(\frac{d}{2})^3. \tag{2.5.37}$$

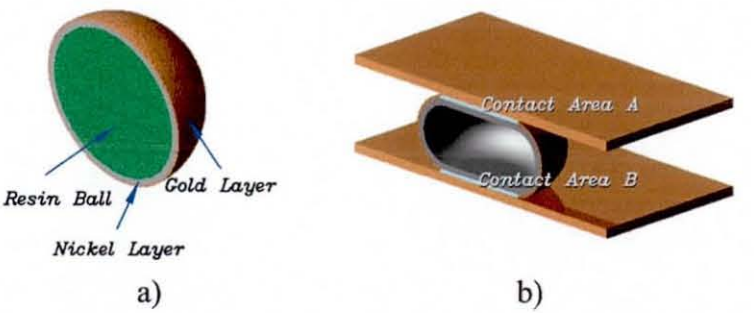

Figure 2.20: An ACA particle and its connection [43].

By Applying mathematics on the geometry of the deformed particle, an equation for $R(k,d)$ is obtained:

$$R(k,d) = \frac{-3\pi(1-k)^2}{24(1-k)} + \frac{\sqrt{[3\pi(1-k)^2d^2]^2 - 48(1-k)[2(1-k)^3d^2 - 2d^2]}}{24(1-k)}. \tag{2.5.38}$$

For the particle, resin coated with nickel layer and gold layer, the nickel layer is schematically shown in Figure 2.21. In the z direction, the increment in electrical resistance dR^* over a distance dz is given by:

$$dR^* = \frac{dz}{\sigma S^*}, \tag{2.5.39}$$

where

- σ nickel conductivity, $(m\Omega)^{-1}$;
- S^* ringlike region area or circle area, μm^2;
- dz the height of the integral unit, μm.

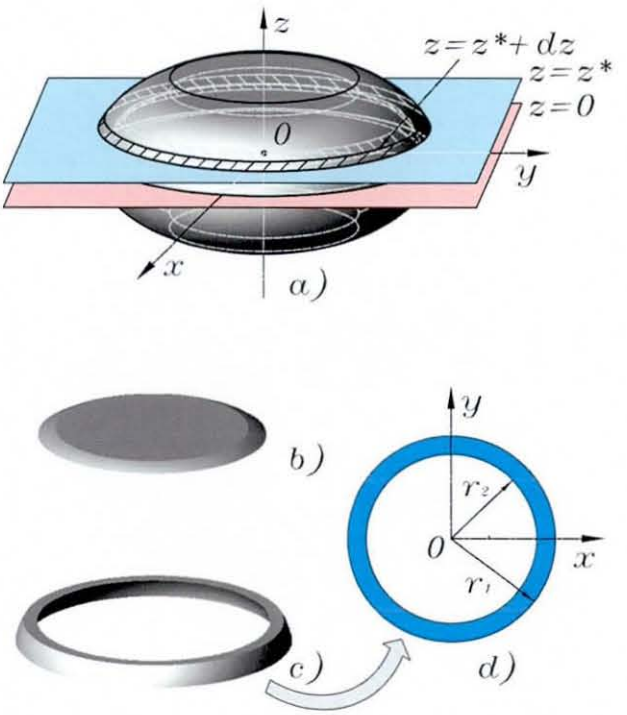

Figure 2.21: Deformed nickel layer of an ACA particle [43].

For $-(\frac{h}{2}+t_1) \le z \le +(\frac{h}{2}+t_1)$, the resistance of the Ni layer is:

$$R_{nickel}(k,d,t_1) = R^1_{nickel} + R^2_{nickel} = \frac{2}{\sigma\pi}\int_0^{+\frac{h}{2}} \frac{dz}{\left[\sqrt{(\frac{h}{2}+t_1)^2-(z)^2}+R\right]^2 - \left[\sqrt{(\frac{h}{2})^2-(z)^2}+R\right]^2} + \frac{2}{\sigma\pi}\int_{+\frac{h}{2}}^{+(\frac{h}{2}+t_1)} \frac{dz}{\left[\sqrt{(\frac{h}{2}+t_1)^2-z^2}+R\right]^2}. \tag{2.5.40}$$

Similarly, the Au layer resistance can be obtained:

$$R_{gold}(k,d,t_1,t_2) = \frac{2}{\sigma\pi}\int_0^{+(\frac{h}{2}+t_1)} \frac{dz}{\left[\sqrt{(\frac{h}{2}+t_1+t_2)^2-(z)^2}+R\right]^2 - \left[\sqrt{(\frac{h}{2}+t_1)^2-(z)^2}+R\right]^2} + \frac{2}{\sigma\pi}\int_{+(\frac{h}{2}+t_1)}^{+(\frac{h}{2}+t_1+t_2)} \frac{dz}{\left[\sqrt{(\frac{h}{2}+t_1+t_2)^2-z^2}+R\right]^2}. \quad (2.5.41)$$

Substituting Equation (2.5.40) and Equation (2.5.41) into Equation (2.5.36), we obtain the total particle resistance:

$$R_{particle}(k,d,t_1,t_2) = \frac{1}{[R_{nickel}(k,d,t_1)]^{-1} + [R_{gold}(k,d,t_1,t_2)]^{-1}}. \quad (2.5.42)$$

By using same method, the electrical conduction of solid ACA particle was also studied by Dou et al. [12]. The paper presented the method to calculate the contact area and electrical resistance of a solid metal conductor particle as a function of the particle diameter and deformation degree. The formula can be described in Equation:

$$R_{particle}(k,d) = \frac{2}{\sigma\pi}\int_0^{+\frac{h}{2}} \frac{dz}{\left[\sqrt{(\frac{h}{2})^2-(z)^2}+R(k,d)\right]^2}. \quad (2.5.43)$$

It suggested that the degree of particle deformation has a greater affect than the particle diameter on the particle resistance. The larger the conductor particle is, the lower the particle resistance is. However, if the particle diameter is more than 10 μm, it does not significantly affect the particle resistance at any acceptable degree of particle deformation.

2.5.5 Substrate

Substrates are designed as a bridge to interconnect chips and the functional circuits. There are many kinds of substrates available in the market, such as PCB (organic/ceramic), ITO coated glass, and FPC. Compared with widely used PCBs in flip chip bondings, ITO coated glass and FPC are well suitable for ACA assemblies.

ACAs can be used on several kinds of substrates, such as glass substrate, flex substrate, ceramic substrate and organic substrate. They are widely used in high density

LCD's, surface mount leaded devices and flip chip attach. The conductivity and yield of ACA assemblies using ceramic substrate and organic substrate were previously studied[76][77]. It suggested that the optimum process conditions and adhesive material choice are important for using these substrates. Glass substrate is idea for ACA packaging as glass substrate is flat. A review of the use on the glass substrate has been done earlier [78]. Flex substrate is flexible material that is widely used to connect LCD to LCD drive chips. Such assembly needs dedicated machine to align and cure special ACFs accurately. Most experiment research using flex substrate can be found in the literature of Department of Electrical Engineering, City University Hong Kong, e.g. [79]. Ceramic substrate and organic substrate were studied by Ogunjimi et al. [80]. In this study, uniform conductivity and high yield are more readily obtained with ceramic substrate than the organic substrate, however, improvements to the organic substrate pad geometries may increase substrate performance. Bumpless substrate can also be applied in ACA assembly due to the flat surface of the *Al* surface. Bumpless die has been tested to have high performance after considering the influence of bonding pressure, bonding temperature and humidity on the adhesion strength of bumpless die (aluminium surface) with two kinds of Anisotropically Conductive Films (ACFs) [81]. Strength between the ACFs and aluminium is not affected seriously by bonding pressure but it increases when bonding temperature increases. In addition, the oxidation reaction can provide a fresh rougher surface that may enhance adhesion strength.

Different kinds of pads and circuit traces can be found from different types of substrates. There is no metal pads or metal circuit traces on ITO substrate. The metal pads and circuit traces are found on PCB and FPC. The material used in the pads/traces are *Cu* or *Ni* and *Au*. The basic layers in a typical pad/trace are *Cu* or *Ni*, then *Ni/Au* or *Au* coating, the *Au* layer is coated outside to make better mechanical contact and protect the bump from oxidizing.

2.6 Reliability of ACA Assembly

Reliability of electronics packaging is a big issue that needs more research to make electronics production more reliable. Reliability in ACA assembly has been a big

challenge to use it to replace traditional soldering. The moisture effect on ACA packaging has been taken as a main reliability mechanism. Besides moisture, there are some other factors that affect ACA assembly reliability. The effects of bump height on the reliability of ACF in flip-chip was studied by Wu [61]. The high stress level in the ACF was found at the position in contact with the top edge of the copper pad, which may be a favourable site for crack initiation and propagation. Impact of temperature excursion is one of the failure mechanism of ACF packages [82]. From failure initiation point of view, the response of ACF packages to environmental (temperature and humidity) exposure is very different from standard underfilled packages. These difference cause the ACF package to fail in different ways from an underfilled packages.

Electrical opening and bridging between component pads are another issues that have been modelled [29]. As ACA particles are randomly distributed in the adhesive, there is possibility that no particles are trapped in the component joint. Williams et al. [29] tried to estimate this possibility assuming that particle distribution charged by Poisson distribution theory. Bridging is also possible because there are too many particles in the fine pitch gaps [83]. In this study, ACA particle volume fraction range is determined using statistical model, generally used for commercial ACA manufacturing nowadays.

2.6.1 Modelling of the Moisture of ACA assembly

Moisture induced failure is an important issue with ACF material. A lot of experimental works have been done. But few literatures were published based on the modelling work. It is an important reliability issue before and after electronic productions are under service.

The diffusion of moisture into a material can be described by Fick's Law. That is, the process is governed by the following differential equation [84]-[85]:

$$\frac{\partial C}{\partial t} = D(\frac{\partial C}{\partial x^2} + \frac{\partial C}{\partial y^2} + \frac{\partial C}{\partial z^2}) \tag{2.6.1}$$

where D is the coefficient of moisture diffusion (mm^2/s). C is the moisture concentration (g/mm^3).

However, unlike heat flux, which is continuous in nature, moisture diffusion poses a new challenge in that the concentration is discontinuous across a bi-material interface. Significant moisture diffusion may also take place along the interface between materials. A new variable that could enforce field continuity is required for modelling of moisture diffusion in a multi-material system such as IC packaging.

Wetness fraction approach [84]-[86] was introduced to remove this discontinuity due to the different saturated concentration of different materials that is:

$$W = C/C_{sat} \tag{2.6.2}$$

where W =wetness faction and C_{sat} =saturated concentration of moisture in the body. Then, we can get the Equation

$$\frac{\partial C}{\partial t} = D_c(\frac{\partial C}{\partial x^2} + \frac{\partial C}{\partial y^2} + \frac{\partial C}{\partial z^2}) \Rightarrow \frac{\partial W}{\partial t} = D_c^*(\frac{\partial W}{\partial x^2} + \frac{\partial W}{\partial y^2} + \frac{\partial W}{\partial z^2}) \tag{2.6.3}$$

In the presence of moisture and changes in temperature, hygroscopic stresses and thermal-induced stresses are generated due to the mismatches in coefficient of material moisture expansion (CME) and thermal expansion (CTE) [86]. Both kinds of stresses within the package can be determined through the following governing Equation [87].

$$\epsilon_{ij} = \frac{1+\nu}{E}\sigma_{ij} - \frac{\nu}{E}\sigma_{kk}\delta_{ij} + (\alpha\Delta T + \beta C)\delta_{ij} \tag{2.6.4}$$

where β stands for CME, α for CTE, ΔT for temperature change, C for moisture concentrations and E and ν for material's modulus and passion ratio respectively.

Zhou et al. [87] has studied the moisture diffusion and moisture induced stress inside ACF assembly under $121C100RH2atm$ condition. The three-dimensional transit moisture diffusion model was built up and the moisture gain versus the time was drawn. A two-dimensional model for performing stresses analysis was also created. The stress pattern in the vicinity of joint showed that the stress are high along the interface between the ACF and metal joints (bump and copper pads) where crack has high chances to initiate.

Caers et al. [88] has studied the moisture induced failures under $85C/85\%RH$ condition using experimental and modelling methods. The two-dimensional model of the moisture ingress is illustrated and shows that the adhesive can be fully saturated with moisture after 1.5 hours at such condition.

Moisture absorption in uncured underfilled materials was reported by Lou et al. [89] recently. In their study, the influence of absorbed moisture on curing properties, thermomechanical property, and adhesion property of underfill after curing has been investigated. The absorbed moisture can catalyze the curing reaction between acid anhydride and epoxy. The glass transition temperature of the cured samples is reduced after the underfill absorbs the moisture before curing. The adhesion strength decreases dramatically after the underfill absorbs the moisture before curing. Should the same problem happen in ACA assembly? More research needs to be done in this area.

Moisture-induced ACF swelling and delamination was reported as the major cause of ACF swelling and delamination by Mercado et al. [82]. The simulation results showed that, with moisture absorption, the loading condition at the interface is tensile-dominant, which corresponds to lower interface toughness (or fracture resistance). This condition is more prone to interface delamination. Therefore, the reliability of ACF packages is highly dependent on the ACF materials. The paper suggests a new approach toward material selection for reliable ACF packages. This approach has very good correlation with experimental results and reliability testing of various ACF materials.

2.6.2 Reflow Process Effects on the Reliability of ACF Interconnections

Owing to the respective advantages of the ACF and traditional soldering technologies, there is an increasing demand to use these two interconnection technologies together. The electronics manufacturing industry is very interested in firstly using ACF materials to achieve high accuracy for fine pitch placement of devices, and then to use standard solder reflow to interconnect other components. This approach would allow the advantages of both technologies to be exploited. However, the ability of ACFs to survive the solder reflow has been a major concern in this combination process [90].

Yin et al. [91]-[93] has studied the effect of the solder reflow process on the reliability of ACF interconnections based on experimental and modelling results. In the experiments, the contact resistance has been used as the criterion to evaluate

the reliability performance of ACF joints. It was found that the subsequent reflow process has a significant effect on the reliability of ACF joints. The contact resistance was found to increase up to 40 percent after the subsequent reflow process, and the magnitude of this increase was strongly correlated to the peak temperature of the reflow profile. Modelling results has shown that due to the CTE mismatch between the materials in the ACF flip chips, the stresse at the interface between the particle and its surrounding materials is significant and is highest at the interface between the particle and the adhesive matrix , this interfacial stress could release the contact pressure caused by the elastic/plastic deformation of the particles during the bonding process and cause the loss of contact area between the conductive particles and metallisations. The limitation of this research work is the assumption of stress free at the beginning of the modelling analysis, which means the residual stress created during the flip bonding process has been ignored, also only elastic property of ACF material was considered in this research.

Yeung et al. [94] has studied the effect of voids in the ACF assembly during the subsequent reflow process. The results showed that different reflow profiles and location of voids could affect the stress level and hence the reliability of ACF in flip chip assembly. The suggestion is the more to minimize the number and size of the voids inside the ACF, the more to maximize the mechanical strength of ACF assembly.

2.7 Current Challenges and Thesis Tasks

ACAs have been widely used in modern electronics packaging, especially portable devices and high resolution LCDs. However, there are still challenges to overcome the co-planarity variation in the packaging and to investigate the mechanical and electrical characterisation of individual ACA particles undergoing deformation.

Locking in the correct deformation degree of the conductive particles to produce highly conductive joints is an essential factor in achieving reliable ACA assemblies. The contacts in the joints are similar in nature to the stationary contacts present in separable electrical connectors, but in an ACA the normal force is maintained by the cured adhesive resin rather than by external mechanical means. Although the complex

effects of the mechanical contact on the stationary contact resistance between the pads and the particles have been briefly addressed in a number of papers [17]-[22], no systematic understanding of these effects has been achieved. There are still significant gaps in the existing understanding of other factors governing the achievement of stable and low resistance interconnections in an ACA assembly. As far as electrical conduction is concerned, the complex behaviour of stationary electric contacts is very different to metallurgical bonds, such as solder joints, especially at such small scales, and is one of the main drawbacks to the use of ACA bonding. Therefore, mechanical and electrical characterisation of individual ACA particles undergoing deformation are currently challenges in achieving fundamental understanding of ACA assemblies. These have therefore been identified as the main topics for my Ph.D. research presented in this thesis.

It is difficult to measure the deformation of individual ACA particles due to their small size and the roughness of the contact area. When considering the function of the particles, two kinds of deformation properties can be identified, i.e. micro properties and macro properties. Micro properties relate to the hardness of the materials constituting the ACA particles, i.e. the particle micro mechanical properties, whilst the macro properties relate to deformation properties of the whole particle [16]. Previous research on the micro-properties using a nano-indenter on cross-sections of ACA samples assembled at different pressures showed that ACA particle deformation resulted in a reduction in hardness of the polymer core with increasing particle deformation. It also showed that the particle hardness after assembly varied within the particle, due to the non-uniform plastic strain within the particles [95]. The macro-properties of the ACA particles are critical to the ACA material performance, because they determine how the particle deforms and the resulting contact forces with it. However, little research has been conducted into the macro properties of ACA particle deformation, especially for a single particle e.g. [96]. The reason for this is that the particles are too small to be deformed in normal material testing machines and are also very fragile. Experiments on an individual ACA particle have been conducted [96]. In this experiment, the load versus deformation behaviour was partially measured, however only a modest level of deformation was achieved due to the use of a large punch with a 100 μm square flat tip, i.e. about 400 times the area of the particles tested. This

resulted in the deformation being insufficient to allow the crushing behaviour to be measured. However, these measurement of the deformation properties of individual ACA particles were achieved in this research due to the use of a smaller, specially prepared punch.

Measurement of the electrical resistance of individual ACA particles undergoing deformation is another challenge of this research. Many supporting experiments have been performed in order to measure the resistances of ACA joints, but these experiments are generally not able to measure individual particle resistances to support the models reviewed in this report. The measurement of the resistance of a single ACA particle for different degrees of the particle deformation will be a significant part of this thesis. Undertaking such an experiment for an individual particle is an big challenge. Furthermore, accurate measurement of the resistance during the particle deformation process is hard to achieve.

The mechanical joints of ACA assemblies are affected by the surface planarity between the joint components. Therefore, the co-planarity effects on an ACA assembly due to component or substrate planarity and packaging accuracy are another important issue that requires further study. This challenge was introduced by Liu [10]. Research about co-planarity issue in ACA packagings will be reported in this thesis.

Chapter 3

Experiments on Co-planarity Effects on Anisotropic Conductive Adhesive Assemblies

3.1 Introduction

This chapter is committed to investigating how co-planarity variations affect the joints in an ACA assembly. This issue isn't easy to investigate because the individual connections are in micro scale. Therefore, carefully designed experiments are needed. That is why an experiment deliberately introducing co-planarity variations into ACA assemblies was introduced.

The ACA assembly process is very different from soldering, since the adhesive does not generate surface tension forces to drive the self-alignment process that allows misplaced chips to be pulled into the correct position relative to the substrate electrodes in soldering. Therefore, it is possible to investigate the effects of co-planarity variation on conduction in ACA assemblies by rotating the chip plane relative to the substrate plane, and then thermally locking/curing these rotations in place. The purpose of this study was to understand the possible effects of non-uniform bond thickness due to non-planarity of the component or substrate terminations on the joint resistances in ACA assemblies. There were two kinds of chip rotations as, for a rectangular chip, rotation along the long chip side and rotation along the short chip side have different effects. These were called α-rotation and β-rotation respectively in this study. At the end, the bonding force distribution between the individual ACA particles is qualitatively analyzed.

3.2 Materials

Bare *Si* chips with *Au* coated *Ni* bumps together with FPCs were used in these experiments. The component bumps and pads used in ACA assembly were planar array leads, which are extending from the components, all lying in the same plane for surface mount applications [97]. The chips and the FPC substrates were designed by City University of Hong Kong [98], and the chips were made by Hong Kong University of Science and Technology [99] and FPCs were manufactured by Compass Technology Company Limited [100].

3.2.1 Chips

The chips used in these experiments were dummy components with no active circuitry. An interconnected bump pattern was designed to allow measurement of the electrical resistance of individual joints once assembled using an ACA. The specifications for the chips used in this study are listed in Table 3.1. The width and length of the chip bump are shown in Figure 3.1. The bump pitch is the distance from one bump centre to the adjacent bump centre, and the bump spacing refers to the gap between each adjacent bumps as shown in the figure. The chips used in this research were bumped along their four sides as shown in Figure 3.2. The bumps on the long sides of the chip were interconnected so that the joint resistance of some of the ACA joints coulcd be measured using the FWR measurement. This bump pattern on the chips couples with the pad pattern on the substrates. The bumps are in groups of five, in which three bumps are connected and the other two are not, as shown in the figure. One bump in each group is used to make FWR measurement and the unconnected bumps are for short circuit detection, and were not used in this experiment.

Table 3.1: Specifications of the Dummy Chip

	Materials	*Thickness*	*Length*	*Width*	*Pitch*	*Spacing*
Unit	− − −	(μm)	(μm)	(μm)	(μm)	(μm)
Chip	*Silicon*	500	11000	3100	− − −	− − −
Bump	*Ni*	4	70	50	70	20
Coating	*Au*	0.4 − 0.5	− − −	− − −	− − −	− − −

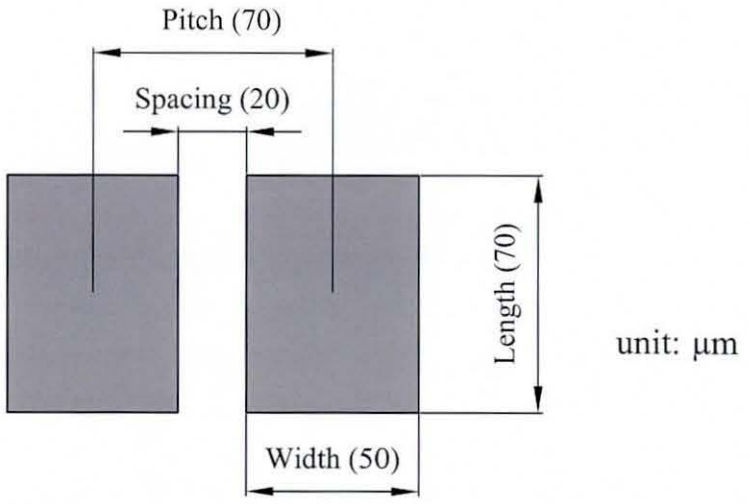

Figure 3.1: Pitch and spacing.

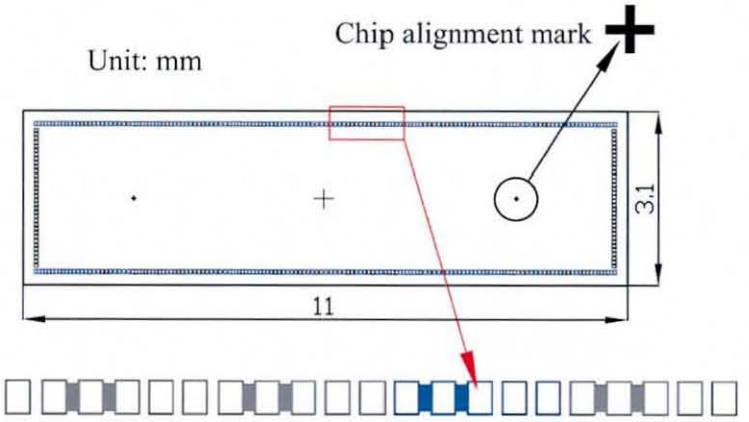

Figure 3.2: Chip pattern.

There are also two small chip alignment marks as shown in the figure, which are used to help align the chip to the substrate.

3.2.2 Substrates

The FPC substrates, 25 *um* in thicknesses, were specially manufactured for the FWR measurement from a Upilex laminate. The specification provided by the manufacture is summarized in Table 3.2. The Upilex material is made from high temperature resistance polyimide film, so that it can survive the solder reflow process when soldered components are also required to be packaged on the substrate.

Table 3.2: Specification of Flex Substrate

	Materials	*Thickness*	*Length*	*Width*	*Spacing*
Unit	$---$	(μm)	$\mu m)$	(μm)	(μm)
Flex	*Upilex*	25	37500	37500	$---$
Trace	*Cu/Ni/Au*	16.5	$---$	$20-25$	$25-30$
Pad	*Cu/Ni/Au*	16.5	70	50	20
Ni Coating	*Ni*	$4-5$	$---$	$---$	$---$
Au Coating	*Au*	$0.4-0.5$	$---$	$---$	$---$
Note:	Upilex:High temperature resistant polyimide film				

The layout of the substrate pattern is as shown in Figure 3.3. The metal pads on the substrate are about 16.5 μm in height, which consists of a Cu layer, a Ni layer and a Au layer. The metal traces including pads on the substrate were specially designed to match the chip's bump pattern, in order to achieve the measurement of electrical resistance of some of the ACA joints. There are two substrate alignment marks and two small chip alignment marks on the substrate, as shown in the figure. The substrate alignment marks were used to help align the substrate on the base stage of the bonding machine, and the chip align marks were used to help align the chip onto the substrate.

3.2.3 FWR Measurement

After all the samples were bonded, they were tested by the micro-ohmmeter used FWR measurement. A schematic of a joint group for FWR measurement is shown in Figure 3.4, where only the joint designed for FWR measurement was tested. Trace 1 and 2 were connected to the voltage sense input of the micro-ohmmeter, where trace 2 was connected with the HI terminal. Trace 4 and 5 were connected to the current source of the micro-ohmmeter, where trace 5 was connected to the HI terminal. In the test, the electrical current flowed from the trace 5 to the trace 4 as the arrows illustrate, the voltage was measured by the sensor through trace 2 and 1. Due to this specially designed circuit, there was no trace resistance introduced in these experiments, only the pad, the bump and the deformed particles contributed to the measured value of the joint resistance. This joint resistance can be divided into 5 parts, as shown in Figure 2.10.

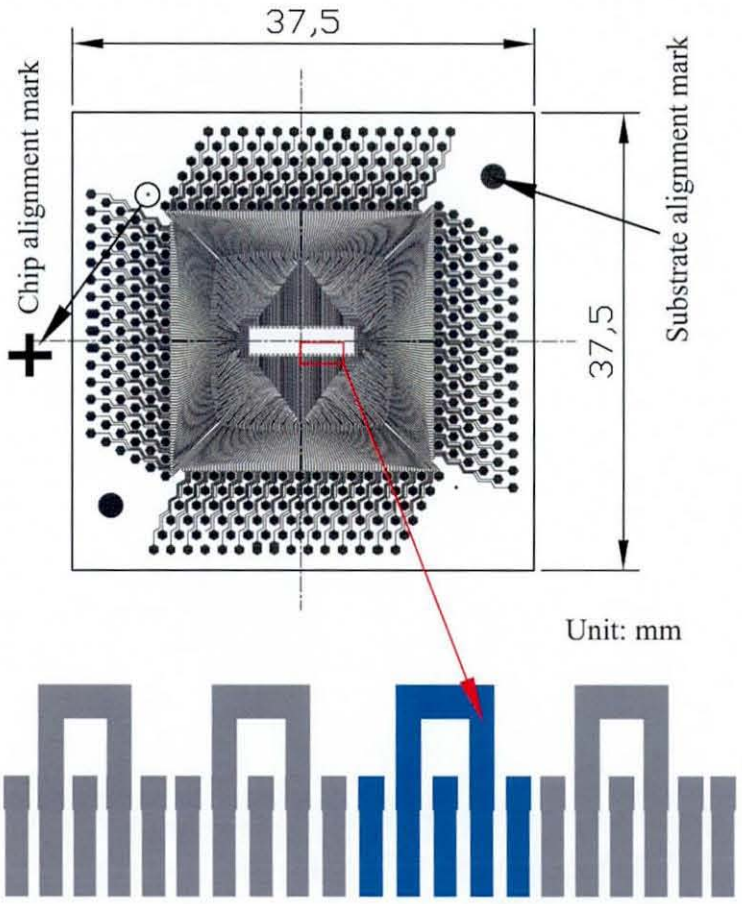

Figure 3.3: Substrate pattern.

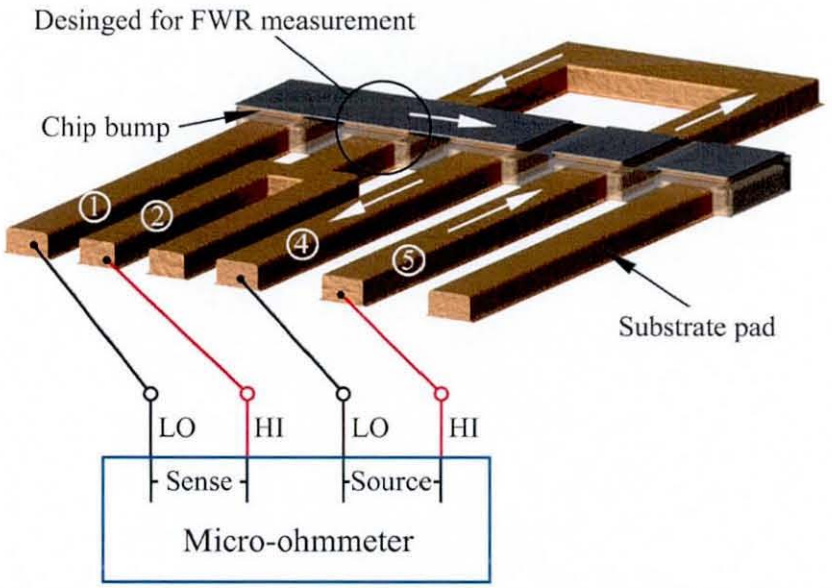

Figure 3.4: 5 joints for FPP measurement.

3.2.4 ACF

A commercial ACF, Sony FP1508E, was used to assembly the bare chip onto the flex substrate. Sony FP1508E is a product developed for fine pitch COF packaging. It is designed with a binder which improves the characteristic to the reflow condition to assume lead free mounting of capacitors and resistors after the chip is mounted further. The structure of the ACF material and the conducting particle is shown in Figure 3.5. Its specifications are listed in Table 3.3. There is a cover film and separator on each sides of the film as shown in the figure. This ACA is thermosetting adhesive, with the compliant polymer cored conductive particles randomly dispersed. This particle resulted in a particle density on the pads of about 5000 per mm^2. The cover film and the separators are made of PET (Polyethylene Terephthalate) plastics, which are generally clear, tough, and a good barrier to gas and moisture, and have a good resistance to heat. They protect the covered adhesive from moisturizing and can survive during the pre-bonding process.

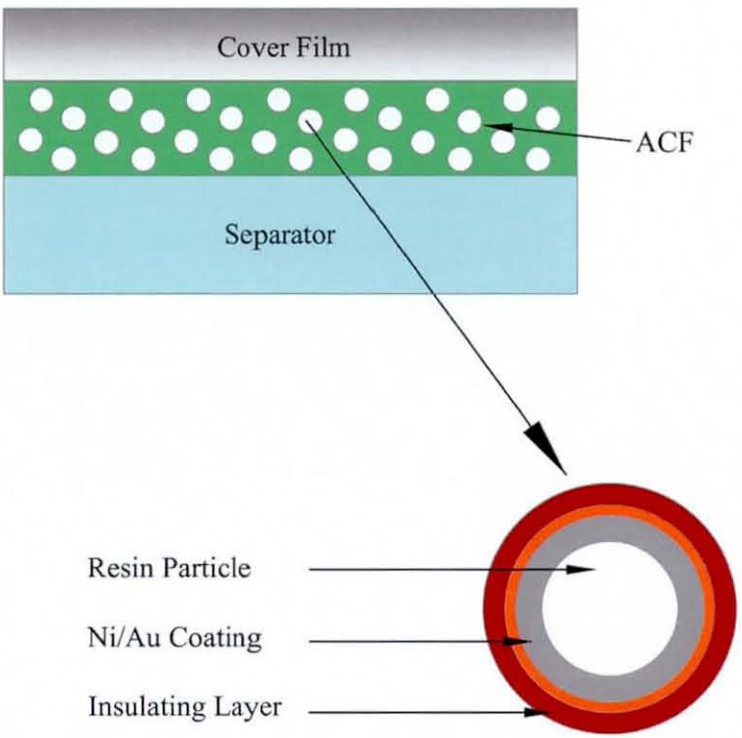

Figure 3.5: ACA-configuration.

Table 3.3: Specifications of Sony FP1508E

	Materials	*Thickness*	*Density*
Unit	$---$	(μm)	$(million/mm^3)$
Cover film	*Transparent PET*	25	$---$
Adhesives	*Thermoset polymer*	35	$---$
Particle	$Resin + Ni/Auplating + insulated$	$\phi 3.5$	3.5
Seperator	*White PET*	50	$---$
Note:	PET:Polyethylene Terephthalate		

3.3 Apparatus

ACA assembly of fine pitch devices requires a specialised bonding machine due to the fine placement tolerances and the specific bonding force and time/temperature requirements. Two flip chip bonding machines, a Karl Suss 9493 Mauren and a Toray (FC1200-2k-#95) were used for pre-bonding and final bonding respectively as shows in Figure 3.6. The bonding parameters used are summarized in Table 3.4, which were selected according to the ACF manufacturer specifications.

a) Karl Suss 9493 Mauren

b) Toray FC1200-2k-#95

Figure 3.6: Assembly machines.

The Karl Suss bonding machine is good for pre-bonding, since it is a simple machine without automatic control alignment, but unsuitable for the final-bonding. In the Toray machine that was used for final-bonding, there are twin stages with a high precision optical alignment system, where the alignment accuracy is ± 2 μm along the chip sides. The chip placement head is schematically shown in Figure 3.7.

Table 3.4: Bonding Parameters for the ACA Assembly

Process	*Temperature*	*Pressure*	*Time*
$---$	$(°C)$	(MPa)	(s)
$Pre-bonding$	80	10	5
$Final-bonding$	180	100	15

Basically, there are the high accurate heating block on the head, vacuum devices and a ceramic attachment. In the experiment, the ceramic attachment was sucked on the nozzle head, then the chip was vacuumed on the ceramic attachment to achieve high-speed temperature profile and fine pressure control for various bonding conditions application. For the experiments here, the head vacuumed on the nozzle was tilted in certain angle before the bonding, for example 1×10^{-4} rad in each rotation increment. Thus the chips rotated in different degree can be cured in the final assembly. The rotation of the chip head is thought to be accurate without any play or deflection during the boning.

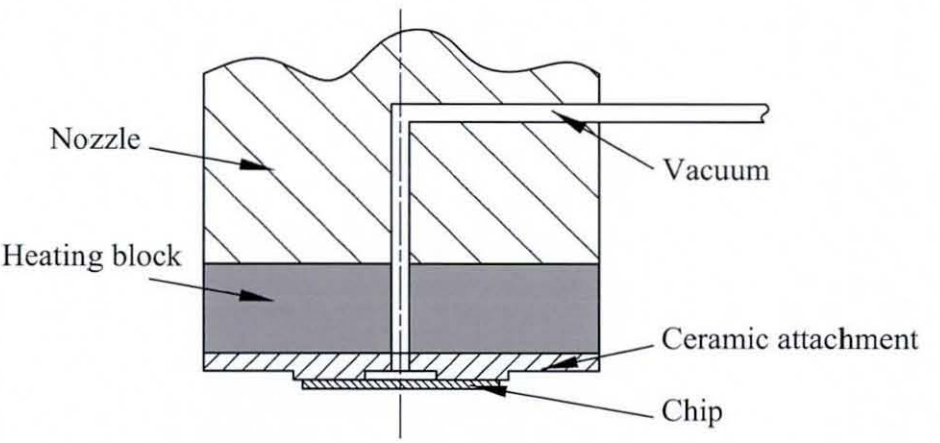

Figure 3.7: Chip placement head.

In order to measure the electrical resistance of individual ACA joints accurately by the method of FWR measurement, a Keithley 580 Micro-ohmmeter was used in these experiments. This meter also provides correction for the effects of any thermoelectric electromotive forces (EMFs) on the measurement.

3.4 Non-planarity in ACA Assemblies

3.4.1 Sources of non-coplanarity

In this research on ACA assemblies, co-planarity refers to the uniformity of bond line thickness. Co-planarity issues in an ACA assembly are complex, since there are many factors that can cause poor planarity connections, such as manufacture errors and assembly faults. In this section, five sources of non-coplanarity will be discussed as the pads on the components not lying in the same plane, the variation of pad height, the roughness finish of the pads on the components, the distortion of the components, and the incorrect alignment.

A. Pads on the Components Not Lying in the Same Plane

This kind of of non-planarity is caused by their manufacture errors or assembly faults. The top surface finish of the pads are smooth, but the surfaces are not in a same plane as shown in Figure 3.8, where the top surface of the pads in the chip and substrate can be a tilted surface, a convex surface or a concave surface. The bump in the centre chip is unlikely in the real packaging, but the others happened although they are not as serious as shown in the figure.

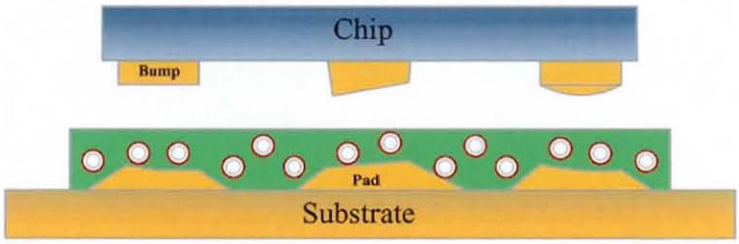

Figure 3.8: Sources of non-coplanarity A.

B. Variation of Pad Height

The variation of component pad height is normally caused by the manufacture errors. The schematic of this kind of no-planarity is shown in 3.9. The variation of pad height is normal in an ACA assembly, and is controlled in fairly low level. The

serious variation can result in large joint resistance and cause reliability problem during service [61].

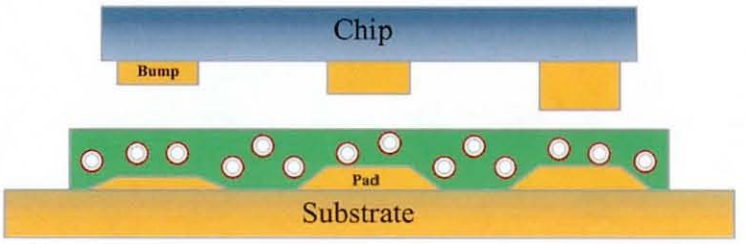

Figure 3.9: Sources of non-coplanarity B.

C. Roughness Finish of the Pads on the Components

A rough or wavy finish to the pads is where there are a lot of convex and concave surfaces on the tops of the pads. ACA particles are trapped between the uneven surface of the coupled pads on the chip and the substrate as shown in Figure 3.10, where the co-planarity situation is much more complex than the sources of non-planarity 1. The particles are apt to be trapped in the concave spot [41][101].

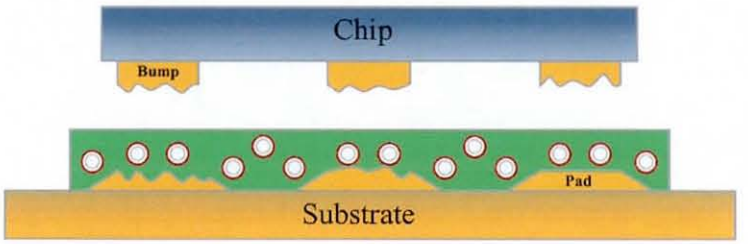

Figure 3.10: Sources of non-coplanarity C.

D. Distortion of the Components

The distortion of the components is another kind of co-planarity source in an ACA packaging. The distortion could be from the bonding condition, the thermal shrinkage of the adhesive after boning and the manufacture errors. This kind of distortion is illustrated in Figure 3.11. It happens in all ACA assemblies due to big CTE difference between the component and substrate globally and the components and adhesives

locally. The global CTE mismatch has more effect on component distortion than the local mismatch.

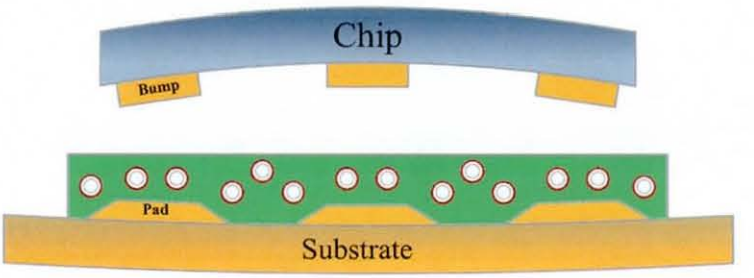

Figure 3.11: Sources of non-coplanarity D.

E. Incorrect Alignment

The fourth kind of non-coplanarity source is the incorrect alignment due to the bonding machine errors as show in Figure 3.12. The experimental design of this research is based on deliberately introducing this kind of non-coplanarity. It is a model that the rotation degree can be easily controlled during the ACA assembly. It can represent the models of other sources of thickness variation if only the particle deformation degree is considered, especially in the case of the variation of pad height and the distortion of the components.

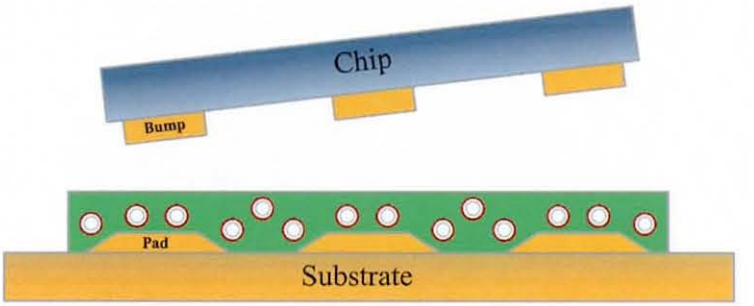

Figure 3.12: Sources of non-coplanarity E.

3.4.2 Simulation of Non-coplanarity through Chip Rotation

In this study, it was assumed that all the component and substrate pads were coplanar [97], the co-planarity assembly experiment was designed to use the rotation of the chips through a small angle, as shown in Figure 3.13. The substrate pad surface is a horizontal plane and the bonding machine used is able to present the chip parallel to this. Different levels of non-planarity in the assembly are then obtained by rotating the chip through different small angles and locking them in this position by the final bonding procedures. Two kinds of rotations were defined in this research, α-rotation or β-rotation where α-rotation is rotated around the long chip side and β-rotation is around the short chip side.

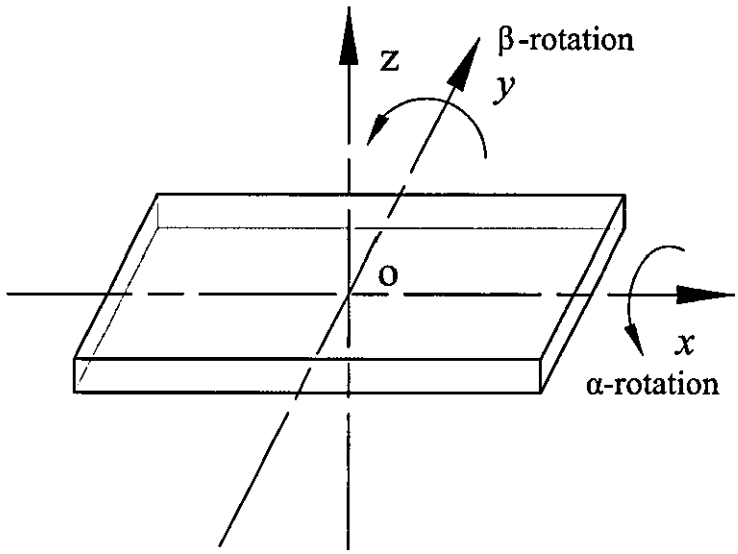

Figure 3.13: Definition of chip rotations.

As mentioned earlier, although the chips used in this research were bumped along their four sides, only the two long sides were capable of FWR measurement. If the chip is rotated around the x axis, one of the long chip sides is lifted up and the other is moved down in relation to the x-y plane, as illustrated in the cross section of α-rotation in y-z plane in Figure 3.14. All bumps in the same long side of the chip are at the same level of rotation. If the chip is rotated around the y axis, one of the short chip sides is lifted up and the other is moved down in relation to the x-y plane as illustrated in the cross section of β-rotation in the x-z plane in Figure 3.15,

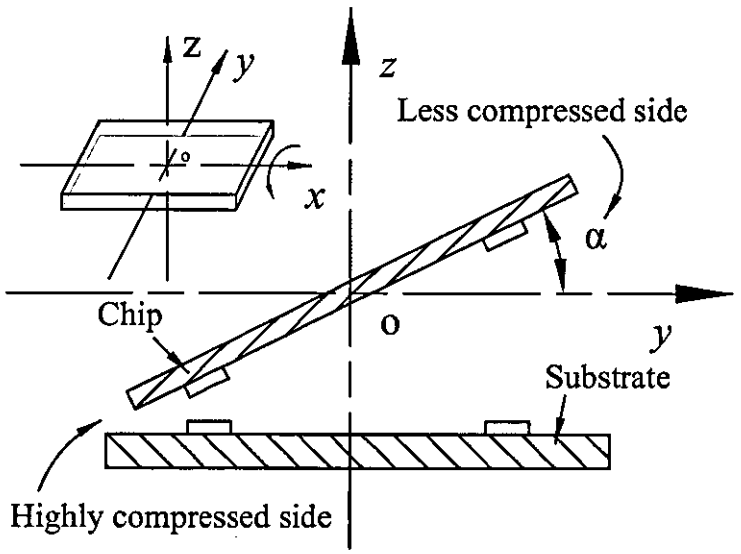

Figure 3.14: α-rotation.

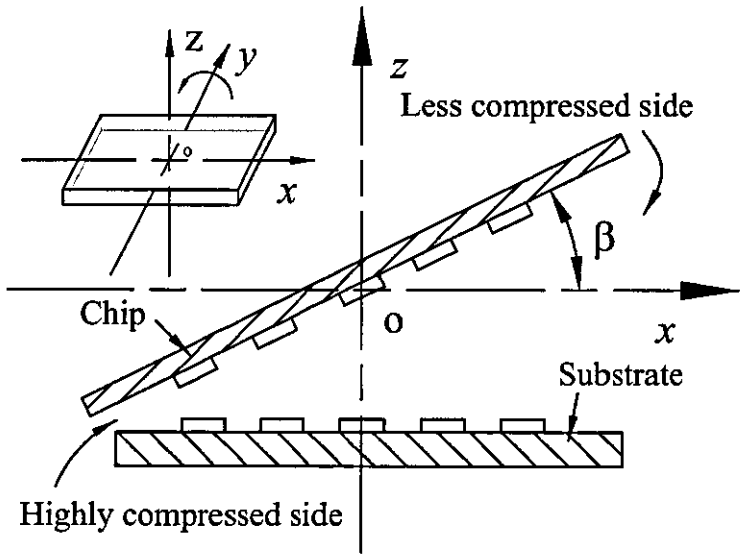

Figure 3.15: β-rotation.

so the bumps in the same long side of the chip are not at the same level of rotation. There is no movement along the centre line of the chip, but the movement gradually increases on either side of the centre line, y, and arrives at its maximum shift at each end of the chip.

All the chip bumps in the α-rotation assemblies are in the same rotation level, however the bumps in the β-rotation assemblies are not in the same level. Therefore, more consistent increment of particle deformation can be acquired along the long chip sides in a β-rotation assembly than those from different α-rotation assemblies. α-rotation and β-rotation are different co-planarity issues, which are ideal situations in these experiments. All the co-planarity issues in the practical assembly should be the mixture of these two kinds of rotations, and may also include the other kinds of non-planarity as discussed in the last section.

3.5 Experimental Methodology

3.5.1 Co-planarity Experimental Methodology

The ACF reel, 5 mm in width, used in these experiments must be stored at a low temperature (-20 $°C$) to prevent premature curing, and should be returned to ambient temperature for at least half an hour before the bonding process. The chips and FPC substrates were cleaned using Acetone and dried using lint free cotton cloths to remove any contamination. In the pre-bonding process, the ACF was cut into small pieces, 15 mm long, and then the PET cover was removed. In the next stage, the ACF was adhered to the substrate such that all of the substrate pads were covered by the adhesive. Finally, the ACF was pre bonded by the Karl Suss bonder using the bonding parameters as listed in Table 3.4. In the final-bonding, the pre bonded substrate was put into the Toray bonding machine by visually aligning the two substrate alignment marks to the matching marks on the base stage. After proper setup in the bonding machine, the cleaned chip was picked up by a vacuum bonding head (made of ceramic) in the machine automatically from a chip tray fixed in the machine. The chip was then aligned to the substrate using the chip alignment marks on the substrate and chip through the dual cameras in the machine. Finally the assembly is accomplished

by ACF heating by the ceramic head, the particle deforming, thermosetting process, and cooling process using the bonding parameters listed in Table 3.4.

The bonding parameters for all of the co-planarity experiment assemblies were kept constant, except that the ceramic head of the Toray bonding machine was rotated through different angles as illustrated in the last section. Samples, labeled 1, 2, ..., 10, were assembled for each of 10 levels of α-rotation, where α=$1 \times 10^{-4}, 2 \times 10^{-4}, ..., 10 \times 10^{-4}$ rad. The shift in the height of the centre of the bonding pads from the x-y plane was 0.135 μm for each increment of rotation. 16 samples, labeled 1, 2, ..., 16, were used in β -rotation, where β=$1 \times 10^{-4}, 2 \times 10^{-4}, ..., 16 \times 10^{-4}$ rad. The shift in height of the centre of the bonding pads at the edge of the chip from the x-y plane was increased by 0.525 μm for each increment of β-rotation. There were two unrotated samples assembled in each type of the experiments, and their mean value was taken as rotation 0.

3.5.2 Sample Analysis Methods

After all the samples were prepared, the α-rotation samples were divided into two groups. One group, including samples 2, 4, 6, 8 and 10 was used for analysis of their less compressed sides, and the other, including 3, 5, 7 and 9 was used for analysis of their highly compressed sides. Only the highly rotated sample 16 of β-rotation was selected for the analysing of rotation effects on the joint resistance.

Conventional optical microscopy and Scanning Electron Microscopy (SEM) were both used. A SEM provides high depth of field images at much higher magnification than is possible with an optical microscope. The SEM used in this research was a LEO 440. The optical microscopy was used to check the sample cross-sections during the sample preparation. Sample preparation for SEM analysis consisted of the following three steps:

- Epoxy Moulding: The ACF samples were firstly cut into a suitable size and put into a mould which was then filled with an 2 part epoxy resin and then the mould was left for several hours until the resin solidified.

- Grinding and Polishing: The moulded sample was then ground to remove material to expose the face of the sample that was of interest. Care needs to be

taken in this process to ensure that not too much material is removed, thereby loosing the features of interest. Once the surface of interest was captured, it was then polished using micro powders to remove any surface roughness.

- Gold Coating: Since a SEM illuminates the surface with electrons, the sample must be able to conduct electricity or the sample will charge up, distorting the image. To achieve this, the sample surface was coated with a very thin layer of gold using a sputter coating machine. Finally, the samples were attached onto a mount using a conductive tape and were then ready for the SEM analysis.

Figure 3.16 shows a typical SEM cross-section where a chip bump, substrate pad and a deformed particle surrounded by cured adhesive can be clearly seen. Figure 3.17 is the schematic of Figure 3.16, where d is the diameter of the original particle and Δd is the particle deformation. The distance between the bump and the pad is referred as to the bond thickness Bt. The particle deformation degree, k, is defined as $\Delta d/d$.

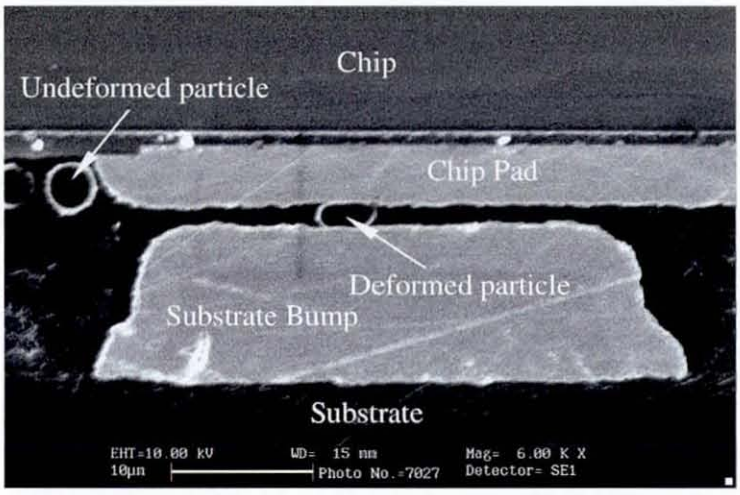

Figure 3.16: SEM of a typical ACA joint.

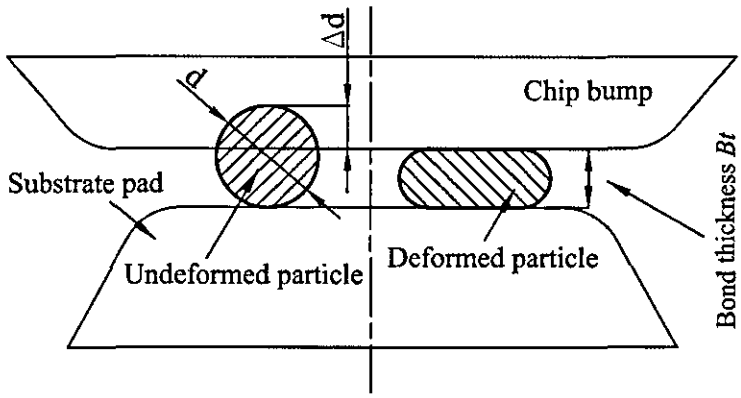

Figure 3.17: Schematic of a typical ACA joint.

3.6 Physical Model of Rotated Assemblies

In order to gain a better understanding of the effects of α-rotation and β-rotation on the electrical performance of ACA interconnections, a simply physical model based on some assumptions was developed to analyze the load on each individual ACA particle. This model confirms the vertical displacement rather than the angle.

3.6.1 Assumptions

Three main assumptions have been made. The first assumption is that the effect of gravity on the particles can be ignored. This is a reasonable assumption since the particles have a very small mass and are suspended in a viscous medium. The second assumption is that the surfaces of the bumps and the pads in the components were smooth and flat if the asperity of the micro scale surfaces is ignored. It is also assumed that the same number of conducting particles would be caught within each ACA joint during the bonding process.

3.6.2 Force Effect on a Single ACA Particle

The actual bonding force applied to an ACA particle in a rotated assembly is slightly different from the assembly without rotation, due to the angle between the bump and

the pad. The actual bonding force applied to the particle is an elastic force, F_p, as shown in the Figure 3.18-a, where two forces were found on the particle applied by the bump, besides the bonding force, there is friction, f_p. There are three forces can be identified in the bump applied by the bonding machine and the particle, the bonding force from the bonding machine, F_{single}, the friction, f_p', caused by the particle and the elastic force applied by the particle, F_p', as shown in 3.18-b. Considering the force vectors, the actual bonding force can be calculated from the following equation:

$$F_p = F_p' = F_{single} \cdot cos\alpha, \tag{3.6.1}$$

for the longest angle used in the experiments, $\alpha = 10 \times 10^{-4}\ rad$, then $F_p \approx 0.99999 F_{single}$, and it can be seen that the rotation has little effect on the actual bonding force. Therefore the bonding force was taken to be the actual bonding force in these experiments.

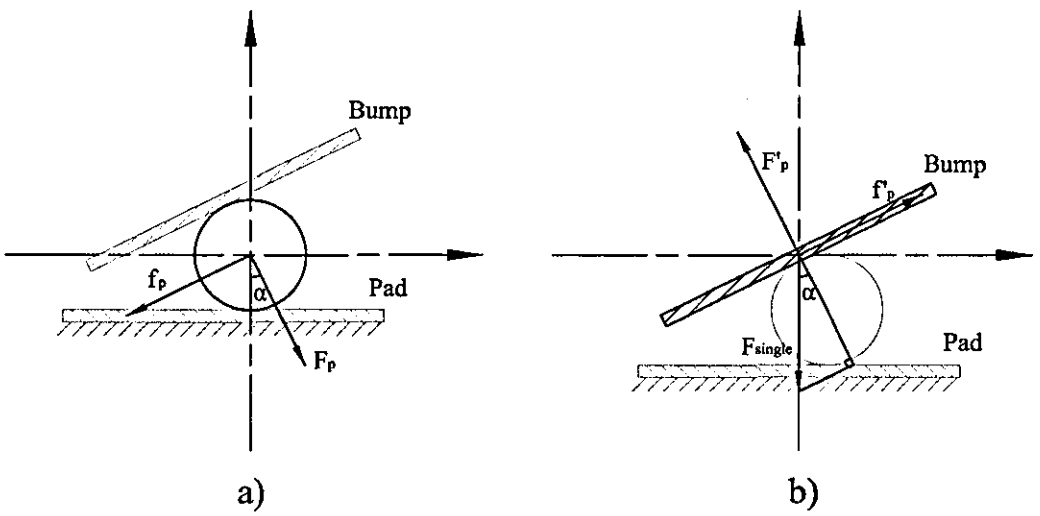

Figure 3.18: Force vector diagram for a single ACA particle.

3.6.3 Physical Model

Despite the assumptions mentioned above, the actual situation for rotation of the assemblies is still very complex. The numbers of particles trapped in different ACA joints will not be same, and their positions within the joint are unpredictable. In this study, it is assumed that each trapped particle will equally share the bonding force

in an ACA assembly joint. The force applied on each particle is therefore F/n, where the total bonding force is F and there are n particles trapped in the ACA assembly. This makes an assumption none of the force is borne by the fliud. However, in the rotation assembly, the bonding force in the less compressed side and the highly compressed side are different. In order to evaluate the distribution of the bonding force, a simplified model is adapted here as shown in Figure 3.19. It is assumed that there are only two ACA joints in a rotated assembly. The bump and the pad in each joint have the same size, and there is only one particle trapped in each joint. A more deformed particle would be expected to be found in the highly compressed side than in the less compressed side, as shown in the figure.

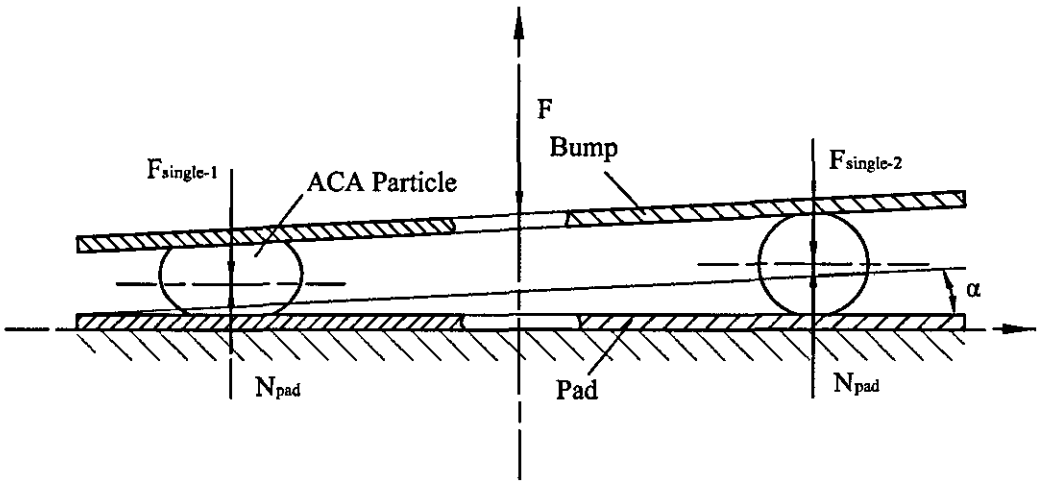

Figure 3.19: Simplified model of α-rotation.

To simplify the model further, the particles are represented as two springs as shown in Figure 3.20. The particle deformation is non-linear, as there is both elastic and plastic deformation and the spherical geometry of the particle leads to geometric non-linearity as discussed in section 2 of Chapter 2. However, representing them as a linear spring is an easy way to analyze the bonding force distribution on the particles qualitatively.

The mechanism of the particle deformation and bonding force distribution in the model is schematically shown in Figure 3.21, where Δl_1 and Δl_2 are the spring movements from their free level to their final bonding positions respectively, F is the total bonding force, $F_{single-1}$ is the bonding force applied on spring 1 and $F_{single-2}$ is

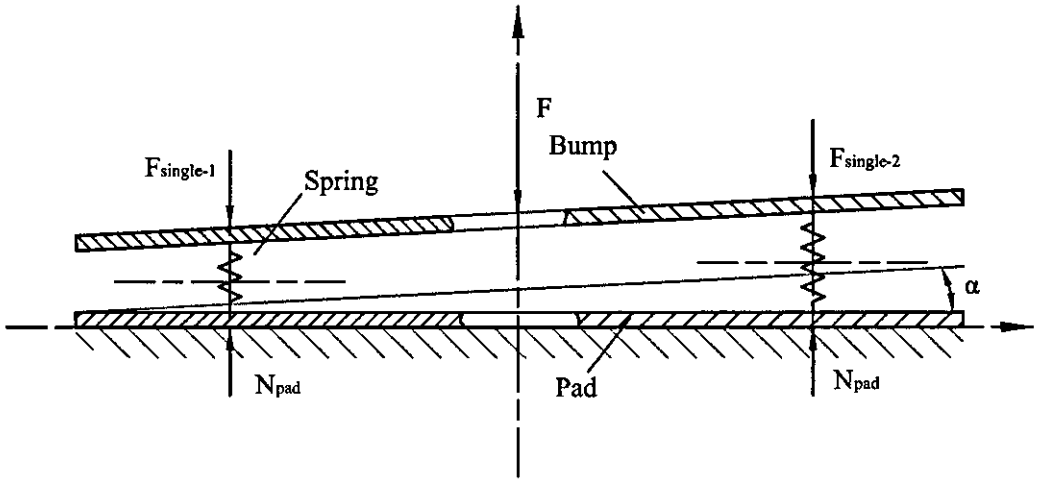

Figure 3.20: Spring model of α-rotation.

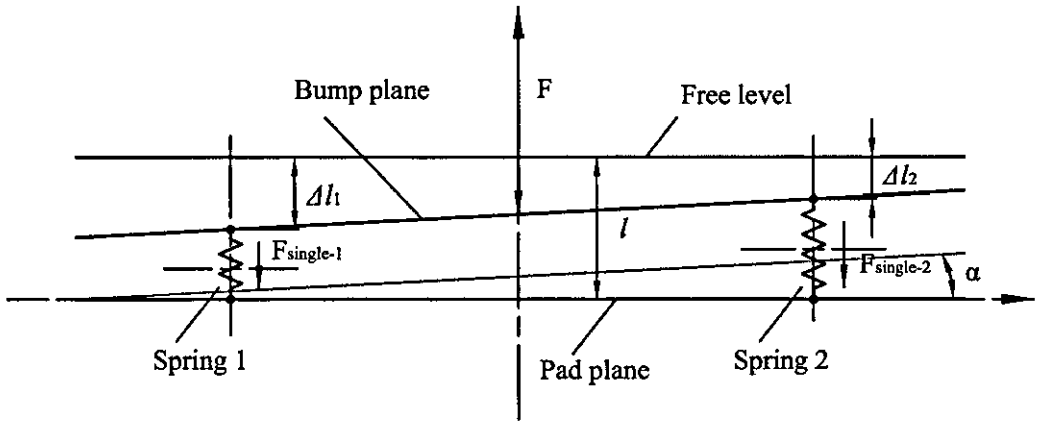

Figure 3.21: Spring model analysis of α-rotation.

the bonding force on spring 2. If k is the elastic spring constant, the bonding forces are:

$$F_{single-1} = k\Delta l_1,$$

$$F_{single-2} = k\Delta l_2.$$

It can be seen from the figure that $\Delta l_1 > \Delta l_2$, therefore:

$$F_{single-1} = k\Delta l_1 > F_{single-2} = k\Delta l_2 \Rightarrow F_{single-1} > F_{single-2},$$

Considered that $F = F_{single-1} + F_{single-2}$, thus:

$$F_{single-1} > F/2 > F_{single-2}. \tag{3.6.2}$$

If there are n particles trapped in an ACA assembly and equally deformed particles in every joint, Equation 3.6.2 can be written as:

$$F_{single-1} > F/n > F_{single-2}, \tag{3.6.3}$$

where $F_{single-1}$ and $F_{single-2}$ are the bonding forces applied to each particle in the less compressed side and highly compressed side respectively.

From Equation 3.6.3, it can be concluded that, firstly, the bonding force applied on each particle in the highly compressed side is higher than in the less compressed side, secondly, the bonding force applied on each single particle in the highly compressed side is higher than the average bonding force F/n, and the force in the less compressed side is lower than F/n. Therefore, there was more particle deformation in the more compressed side than in the less compressed side, and the deformation in the more compressed side was bigger than in the unrotated assemblies and the deformation in the less compressed side was smaller than in the unrotated assemblies.

Chapter 4

Results and Discussion of Co-planarity Effects on Anisotropic Conductive Adhesive Assemblies

4.1 Introduction

In this chapter, the results of co-planarity variation on ACA assemblies presents firstly. Then the effects of the co-planarity variation experiments are analyzed and discussed based on the resulting electrical properties of the ACA joints. There are two outputs from these experiments. One is the non-planarity effects on the ACA assemblies and the other is the bond thickness effects on the joint resistance in the ACA assemblies. The bond thickness refers to the height of the deformed particles in the ACA joints. This is different from the research of individual ACA particles undergoing deformation that will be presented in the following chapters, because about 20 to 30 particles, not individuals, were deformed together in these experiments. Finally, the electrical performance of individual ACA joints bonded with different co-planarity variations are discussed according to the rotation degree of the chip on flex.

4.2 Experimental Results

4.2.1 Deformation Degree Effects on the Particle Crush

Crushed particles are difficult to identify using the sample analysis methods discussed in section 3.5.2. However clear deformation of the contact areas and a characteristic

pattern in the crushed particles can be seen in assemblies manufactured using a glass substrate through an optical microscope. Four such images are selected to detail the deformation degree effects on particle crushing as shown in Figure 4.1[1], where the particle deformation degree can be calculated using Equation 2.5.38, as listed in Table 4.1,

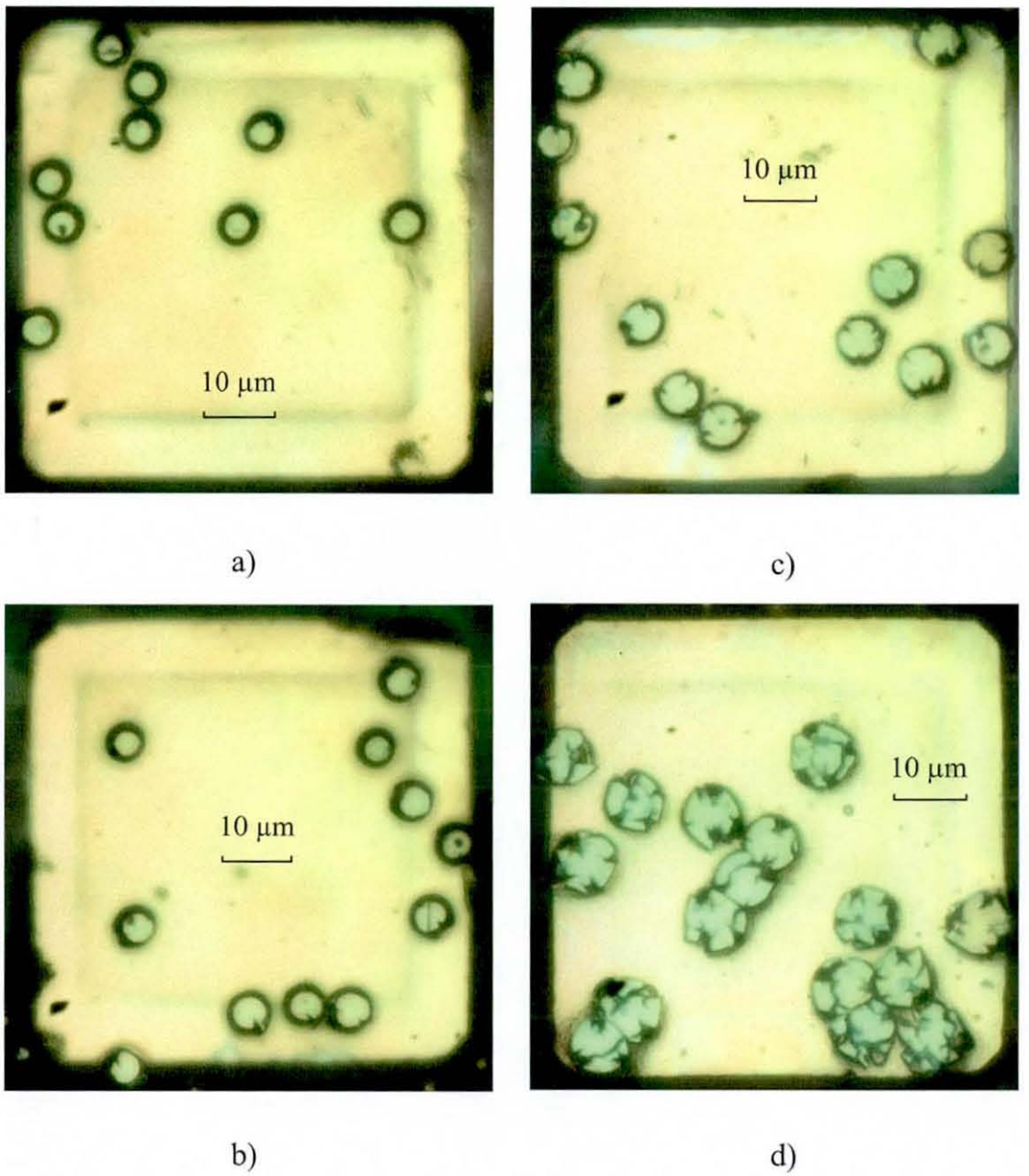

Figure 4.1: Effects of deformation degree on particle crushing[1].

[1]Samples prepared and imaged by Dr. Yin using the same ACA as used in the co-planarity experiments.

Table 4.1: Measured Contact Radii and Their Deformation Degrees

Sample	$R(\mu m)$	$k(\%)$	*Avg no. of cracks/particle*
1	1.33	51	0/9
2	1.58	57	8/11
3	2.13	69	30/12
4	3.46	85	N/A
Notes:	R: Average contact radius		
	k: deformation degree		

and plotted in Figure 4.2, against the average contact radius measured from Figure 4.1.

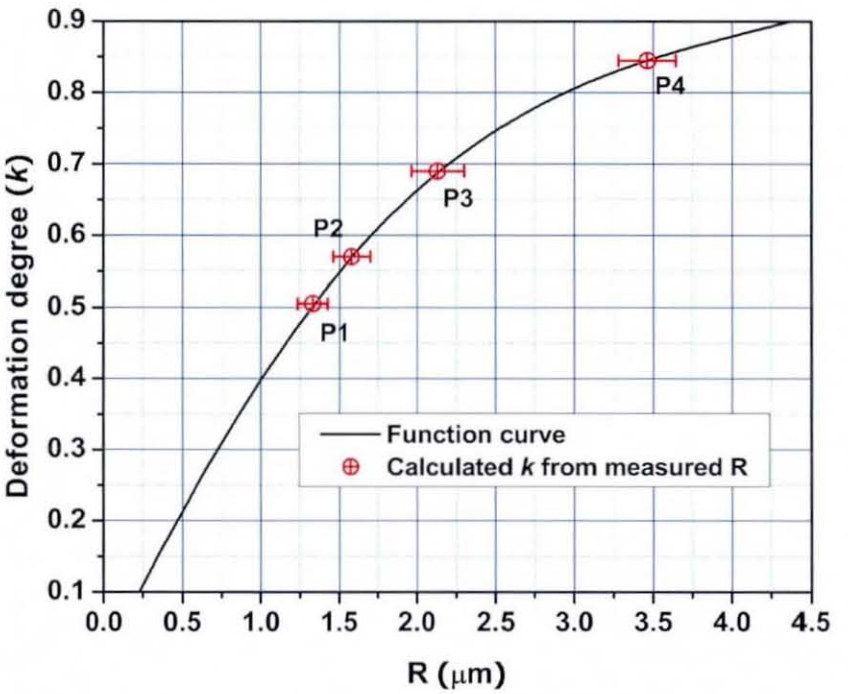

Figure 4.2: Calculated deformation degree versus the measured contact radius.

It can be seen from Figure 4.1 that there are no visible cracks in the particles for the deformation of 51%, one crack had initiated when the deformation degree had reached 57%, three cracks were found in the particles when the deformation degree reached 69%, and all particles were crushed by a deformation of 85%. Therefore, it can be concluded that the particles begin to crush at between 51% and 57% deformation, although it can not be detected using the methods discussed in section 3.5.2.

4.2.2 α-rotation

The output of these experiments is the variation in joint resistance for different rotations. The experimental results for α-rotation are shown in Tables 8.1 and 8.2 in appendix I. 30 joint resistances were measured from the less compressed side of each chip and another 30 joints resistances were measured from the highly compressed side of each assembly.

The joint resistance versus joint number/postion along the long chip side are shown in Figure 4.3 and 4.4, where the horizontal axis in each figure represents the measured joint number/postion. Sample 0 is the normal assembly without any rotation, while samples 1 to 10 are the 10 samples with increasing rotation angle. As expected, these results show that the joint resistances are higher in the less compressed side (Figure 4.3) than in the highly compressed side (Figure 4.4).

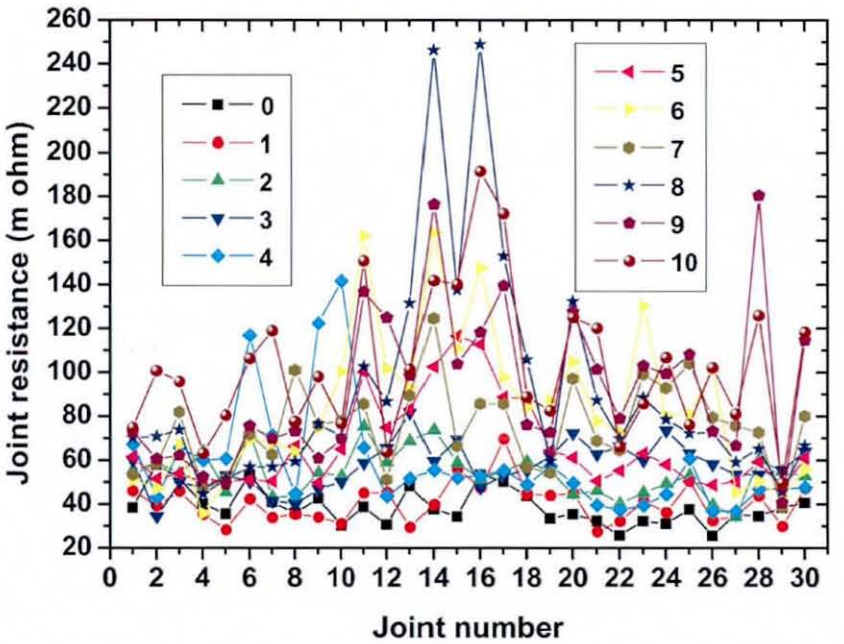

Figure 4.3: Effects of α-rotation for the joint resistance of less compressed side.

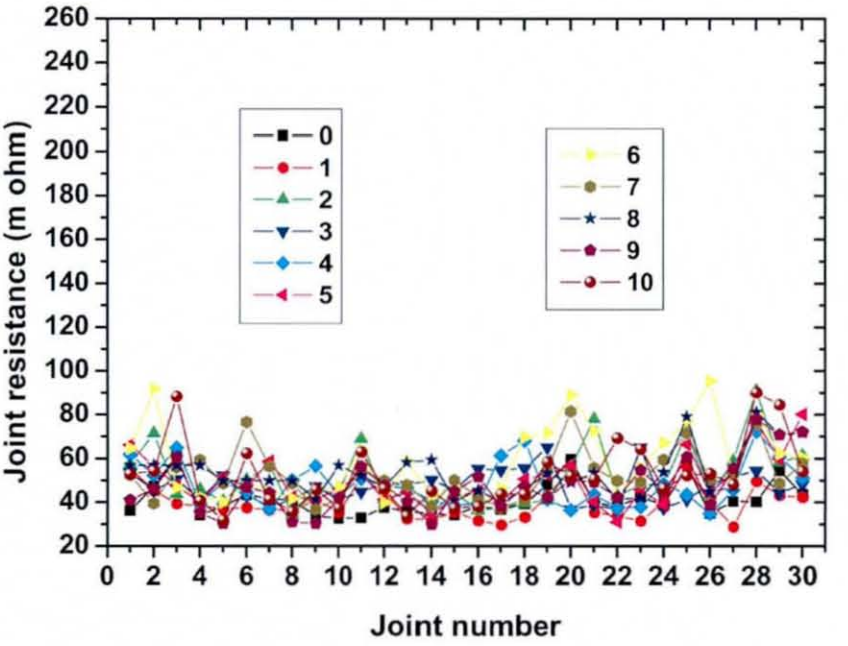

Figure 4.4: Effects of β-rotation for the joint resistance of highly compressed side.

4.2.3 β-rotation

In the β-rotation assemblies, pairs of joints on opposite long sides of the chip in each assembly had the same level of compression as shown in Figure 3.15. Therefore, the mean value of the two opposite joints along the long side of the chip were examined together to evaluate the assemblies with β-rotation. 60 joint resistances were measured from each of 16 samples, and the 30 mean values of these results are plotted in Figure 4.5, where the horizontal axis is for different joint number/position along the long side of the chip. The more compressed ends is for joint numbers from 15 to 1, whereas the less compressed ends is where the joint numbers/postions were from 16 to 30. The mean joint resistances, a total of 510 points as shown in the figure, are mostly concentrated in the range from 30 $m\Omega$ to 90 $m\Omega$, therefore, it is not easy to identify a tread in the resistance variation for each joint location over the 16 tested samples. However, the tread is very clear if the results of joint resistance versus rotation angle are considered as shown in Figure 4.6. In this figure, the horizontal axis is for the rotation angle, which increases from sample 0 to 16, and the vertical line represents the joint resistance. It can be seen that the joint resistance measured for

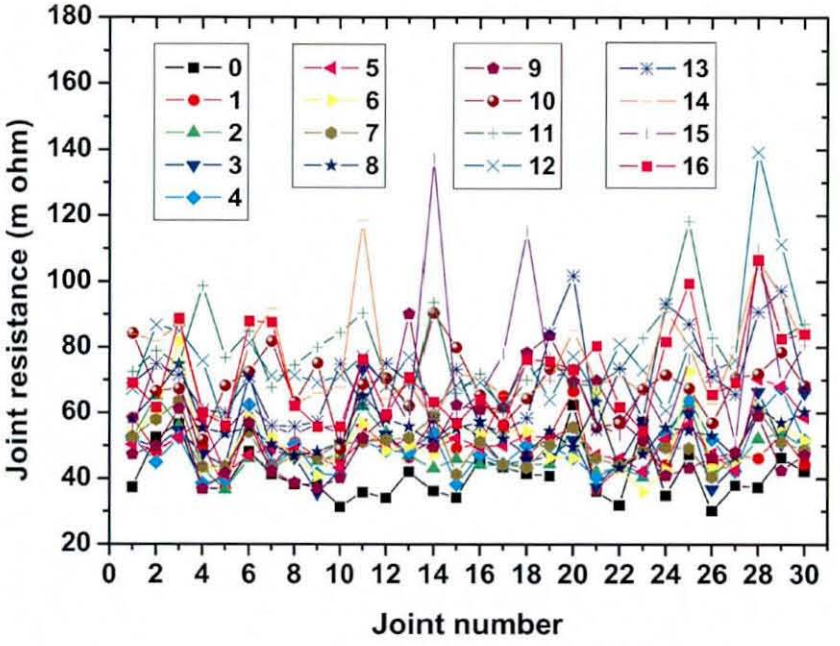

Figure 4.5: Joint position effects of β-rotation on resistance.

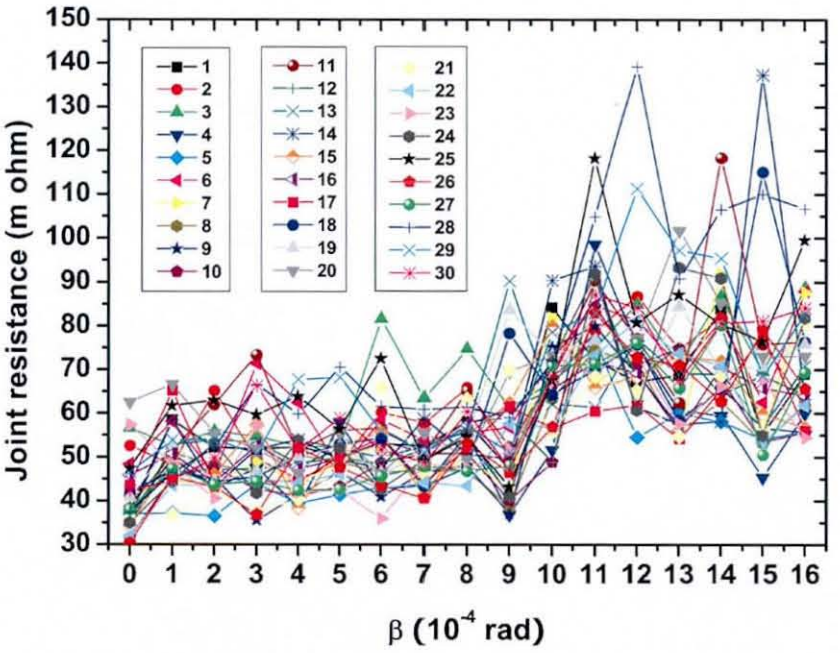

Figure 4.6: Effects of β-rotation on resistance

the same joint position in a different sample increases as the rotation angle increases from sample 0 to the highly rotated sample 16.

4.3 Analysis and Discussion of α-rotation Results

The raw resistance results from the experiment as shown in Figure 4.3 were difficult to interpret, because there are so many factors that can affect ACA joint resistances. ACA joint resistances for the same bonding conditions and same bonding machine, but assembled at different times, can vary significantly due to other uncontrolled factors. The deviation of the joint resistances from the mean/normal value must be within an acceptable range, otherwise the process cannot be used in electronics products. Therefore a quality control concern in the electronics industry is the achievement of consistent joint resistances.

The results shown in this section are the mean values of the joint resistances for the same level of compression from the same samples, together with results for the standard deviation of the resistances and the numbers exceeding the acceptable level of resistance (defined here as 100 $m\Omega$).

4.3.1 Less Compressed Side of α-rotation

The results presented in Figure 4.7 are the mean values for the less compressed side of samples with different imposed rotation angles, where the horizontal axis is the rotation angle, where each increase is a tiny angle, 1×10^{-4} rad, and the vertical axis is the mean joint resistance. Each value in the figure is the average (arithmetic mean) of the results for the 30 joint resistance measurements from the less compressed side of a sample, except that for an angle of 0, which is the mean value of the 120 joints measured from 2 samples without rotation, so it can be taken as a standard value. The error bars show the standard deviation of resistance, giving an indication of the consistency/spread of the resistances.

It can be seen that the mean joint resistance increased reasonably linearly from about 40 $m\Omega$ to more than 100 $m\Omega$ as the rotation angle increased, although the joint resistances did not change significantly for the smallest level of rotation. The spread in

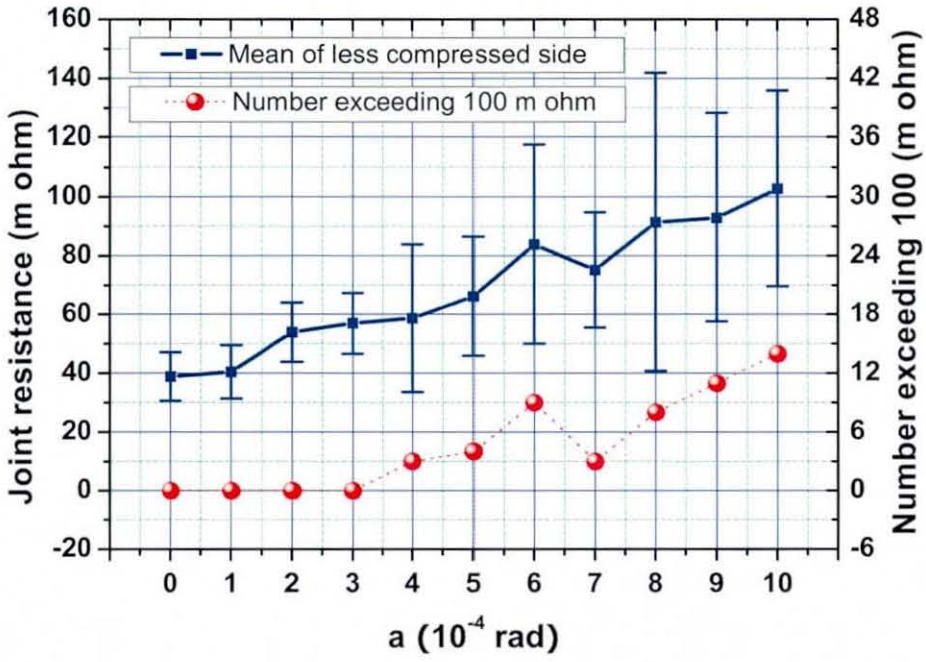

Figure 4.7: Less compressed side.

resistance values also tended to increase with increasing rotation angle, although not in such a linear way. These increases in resistance may be attributed to the reduced compression of the conductor particles and may also be due to a reduced number of trapped particles caused by the greater flow of ACA resin over the pads during the final bonding, due to the tilted chip forcing all of the resin out of that side of the chip as shown in Figure 4.8. Flow of the adhesive over the pads has previously been shown to reduce particle density by Mannan et al. [59]. Furthermore, the variation of the mean joint resistances for large rotation angles indicated that the joint yield may be significantly reduced. For instance, the highest joint resistance in sample 8 was more than 240 $m\Omega$, and some high resistance joints (defined here as more than 1000 $m\Omega$) were found in the less compressed side in some of the samples with larger rotations (samples 8, 9 and 10), i.e. there were 3 high resistance joints in sample 8, 1 in sample 9 and 2 in sample 10. The resistance variations in samples 0, 1, 2 and 3 were all relatively small, but from sample 4 to sample 10, the spread increased dramatically, reaching their maximum for sample 8. These results show assemblies with large rotation angles would definitely cause yield problems because some joint resistances, are too large to be used. It is not clear why the mean joint resistance for

sample 7 was smaller than for sample 6, however it is probably a random effect due to variability in the materials and bonding process.

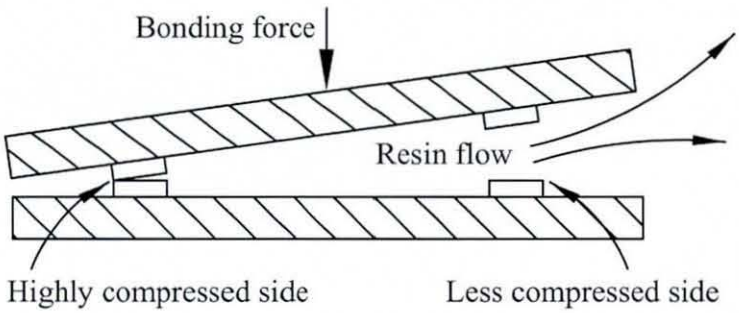

Figure 4.8: Resin flow.

Figure 4.7 also shows the numbers of joints in each sample with a resistance exceeding the acceptable threshold of 100 $m\Omega$. The numbers showed that some of the joints in the samples were not acceptable after angle 3, and the larger the angle was, the more joints exceeded the threshold. For example, in sample 10, 14 joint resistances were more than 100 $m\Omega$.

To sum up, there were types of behaviours identified for the less compressed side in this experiment. Stage I, the stable stage, was identified as being for samples 0 and 1 as for as the mean joint resistances were concerned. It can be seen there was almost no difference in joint resistances within this small amount of small rotation. A typical joint and the level of particle deformation in this stable stage is shown in the SEM cross-section Figure 4.9-a. As for stage II, from sample 2 to 6, the mean joint resistances increased gradually due to the decreased deformation of the ACA particles and contact areas as the rotation angle increased step by step. The particle deformation in this stage can be seen in Figures 4.9-b, c and d, where the particle deformation decreases as the rotation increases from sample 2 to 6. In stage III sample 7 to 10 variability of the mean joint resistances was found. In this stage, besides the large resistances resulting from the smaller deformated ACA particles as shown in Figures 4.9-e and f, the conductivity of the mechanical contacts reduced due to the dramatically reducing area of contact between the particles and the pads. The probably lower number of particles trapped between the bumps and the pads, due to the increased ACA matrix flow over the pads as the rotation increased,

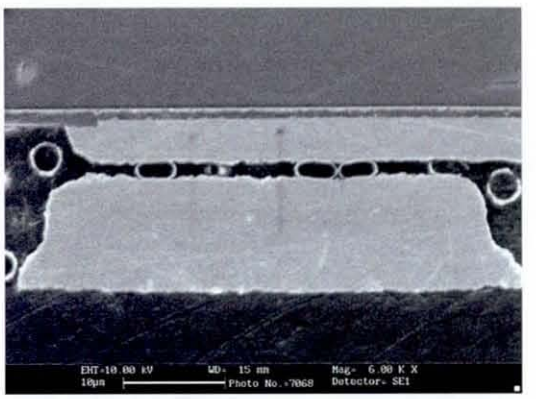

a) Standard sample (Bt=1.590 μm)

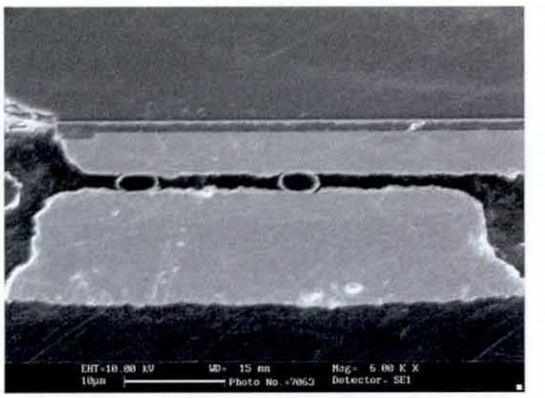

d) Sample 6 (Bt=2.096 μm)

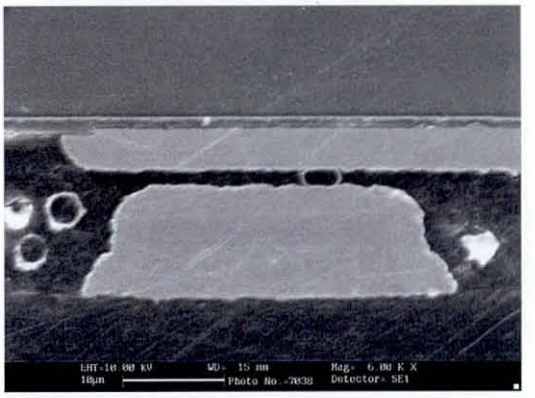

b) Sample 2 (Bt=1.788 μm)

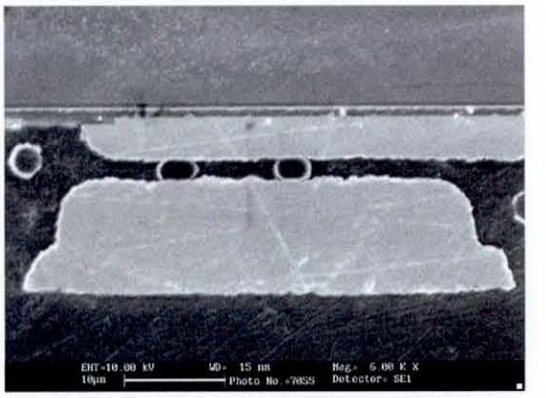

e) Sample 8 (Bt=2.384 μm)

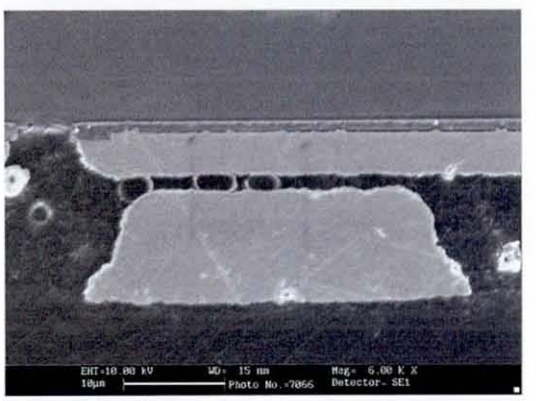

c) Sample 4 (Bt=1.901 μm)

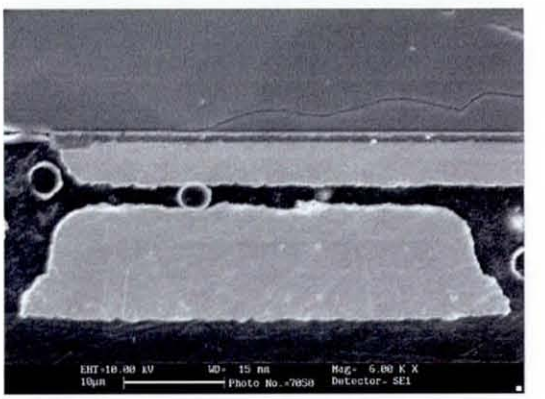

f) Sample 10 (Bt=2.721 μm)

Figure 4.9: SEM cross-sections of less compressed side of α-rotation.

is another factor that could have contributed to the large and variable joint resistances, but this has not been quantified. There are no SEM cross-sections of the less compressed sides of samples 1, 3, 5, 7, and 9, since they were polished and scanned for the demonstration of the highly compressed sides in the following section.

4.3.2 Highly Compressed Side of α-rotation

Compared to the less compressed sides of the same samples, the mean results for the highly compressed side were much more consistent. The results are presented in Figure 4.10, to the same scale as in Figure 4.7. The the joint resistances in the highly compressed sides were more consistent than the opposite ones in the less compressed sides, as the resistance profile shown in the figure. All of the mean resistance values were between 40 $m\Omega$ and 60 $m\Omega$ and none of the resistances exceeded the acceptable threshold of 100 $m\Omega$, indicating that the highly compressed side joints were more uniform than those in the less compressed sides.

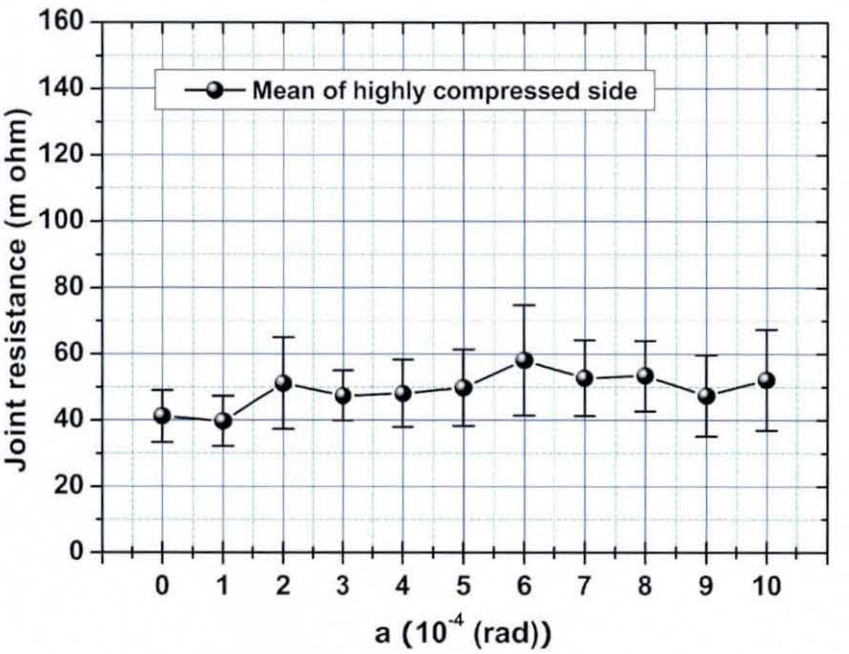

Figure 4.10: Highly compressed side.

In order to achieve a detailed understanding of the effect of high levels of compression on the ACA assemblies, the results for the highly compressed side were also

divided into three stages according to the resistance pattern shown in Figure 4.10. As for the less compressed side, the three identified stages are:

Stage I: sample 0—1;
Stage II: sample 2—6;
Stage III: sample 7—10.

However, the behaviour that they demonstrate are different.

Stage I: The mean joint resistances as shown in the figure dropped a little, which is believed to be because the particles trapped between the bumps and the pads in sample 1 were deformed a little more than in sample 0, increasing the contact area. However, there is no visible difference between the joints of sample 0 and sample 1, and are similar to those shown in Figure 4.9-a.

Stage II: As the rotation increased, the trapped particles between the bumps and the pads started to become over compressed and were considered to be therefore crushed, as shown in the SEM cross-sections of sample 3 and 5 in Figure 4.11-a and b. Therefore the interconnection resistances increased slightly above those in stage I. Crushed particles result in low conductivity, because of the cracks in the particles and also the reduced mechanical contact areas between the particles and the pads. The worst situation in this stage was that most of the particles were crushed, and there were few apparent mechanical contacts between the bumps and the pads. In such cases, the joint resistances may be quite high, some of them were as high as 95.2 $m\Omega$ in sample 5.

Stage III: The ACA particles were crushed deeply in this stage due to the large pressure caused by high levels of compression along the long chip side as the SEM cross-sections of sample 7 and 9 shown in Figure 4.11-c and d. In this stage, there was a significant direct mechanical contact area between the bumps and pads, where the situation became similar to that in NCA assembly, however the pieces of crushed resin coated particles may reduce the area of direct mechanical contact between the metal pads, resulting in a worse conductivity than for a NCA assembly.

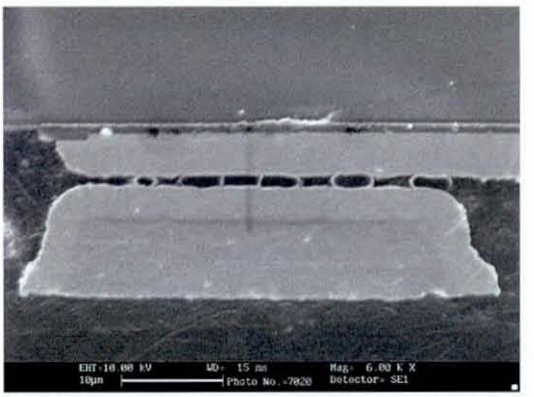

a) Sample 3 (Bt=1.394 μm)

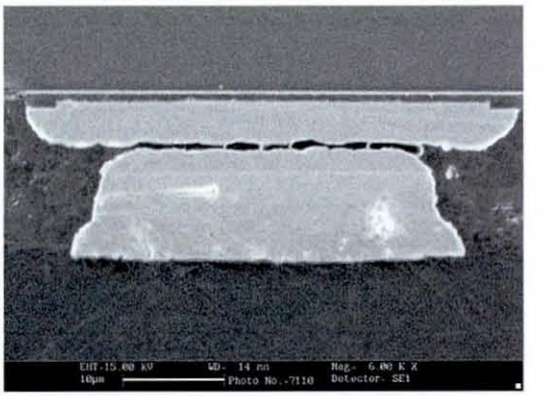

c) Sample 7 (bt=0.894 μm)

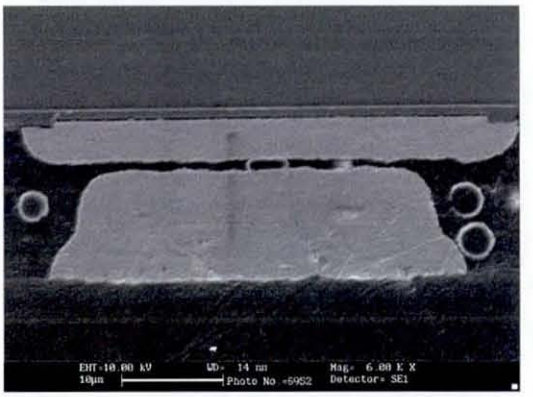

b) Sample 5 (Bt=1.197 μm)

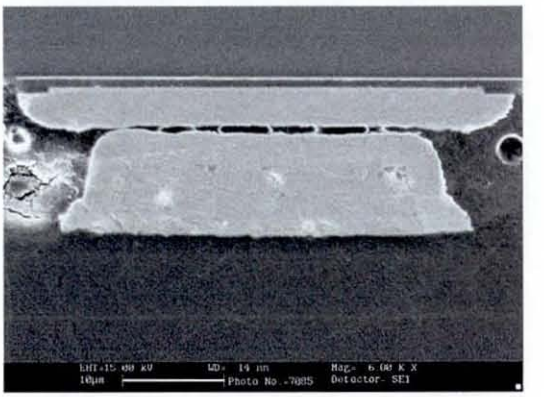

d) Sample 9 (Bt=0.761 μm)

Figure 4.11: SEM cross-sections of highly compressed side of α-rotation.

4.4 Bond Thickness Effects of α-rotation on Joint Resistance

The actual bond thicknesses for the α-rotation samples were measured using the SEM for comparison with those calculated for the pre-set rotations. Four bond thicknesses were randomly measured along each long side of the rotated sample. The calculated and measured bond thickness are listed in 4.2.

Table 4.2: Bond Thicknesses due to α-rotation.

	Rotation (rad)									
− − −	−9	−7	−5	−3	0	+2	+4	+6	+8	+10
	Calculated thickness (μm)									
− − −	0.375	0.645	0.915	1.185	1.59	1.86	2.13	2.4	2.67	2.94
	Measured thickness (μm)									
$Bt01$	0.76	0.90	1.20	1.39	1.59	1.79	1.90	2.10	2.39	2.72
$Bt02$	0.71	0.78	0.91	1.45	1.41	1.69	1.65	1.95	2.19	2.9
$Bt03$	0.86	0.96	1.25	1.29	1.71	1.83	1.86	2.32	2.41	2.46
$Bt04$	0.72	1.05	1.38	1.42	1.66	1.85	2.15	2.19	2.55	2.81
$Avg.$	0.763	0.923	1.19	1.388	1.593	1.790	1.890	2.140	2.385	2.723
$S.D.$	0.069	0.113	0.198	0.069	0.131	0.071	0.205	0.155	0.148	0.189
Note:	highly compressed sides				NR	less compressed sides				
Note:	Avg:average of 4 measurements; S.D.:standard error.									
Note:	NR:no roation.									

These measurements and calculated thicknesses are plotted in Figure 4.12, where the measured bond thickness is the mean of the four measurements with one standard deviation error bars. In the calculation, it is assumed that the bond thickness is 1.59 μm, if there is no rotation, which is the average bond thickness of the unrotated samples. The measured bonds are thinner in the less compressed sides and thicker in the highly compressed sides than the calculations. This indicates that the real rotations are smaller than the calculations. It can been seen that the plot of the measured bond thickness is not a straight curve, indicating that the particle deformation is not linear.

The particle deformation degree can be calculated from the measured bond thickness. Then, together with the measured joint resistance, the relationship between the the joint resistance and deformation can be built, as plotted in Figure 4.13.

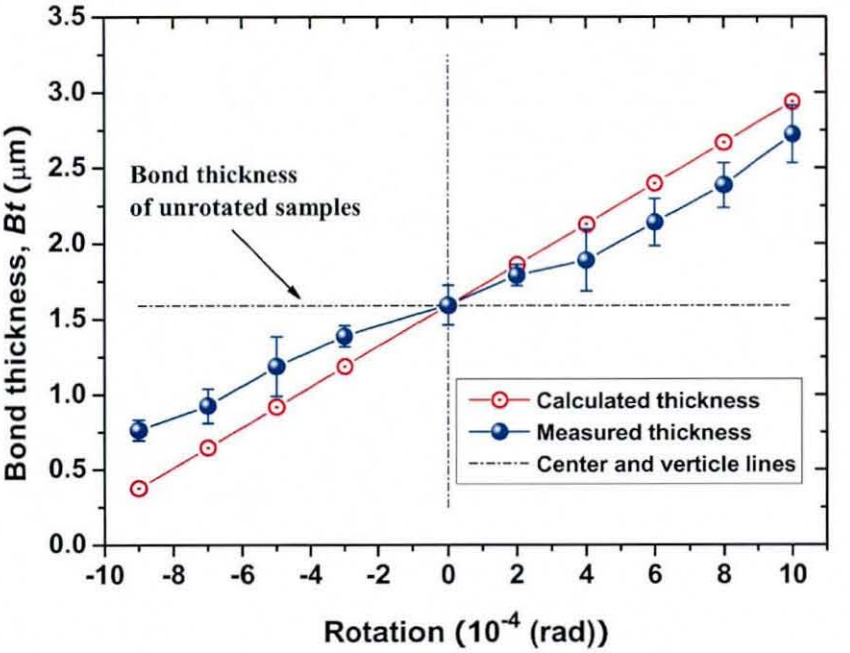

Figure 4.12: Bond thicknesses for α-rotation.

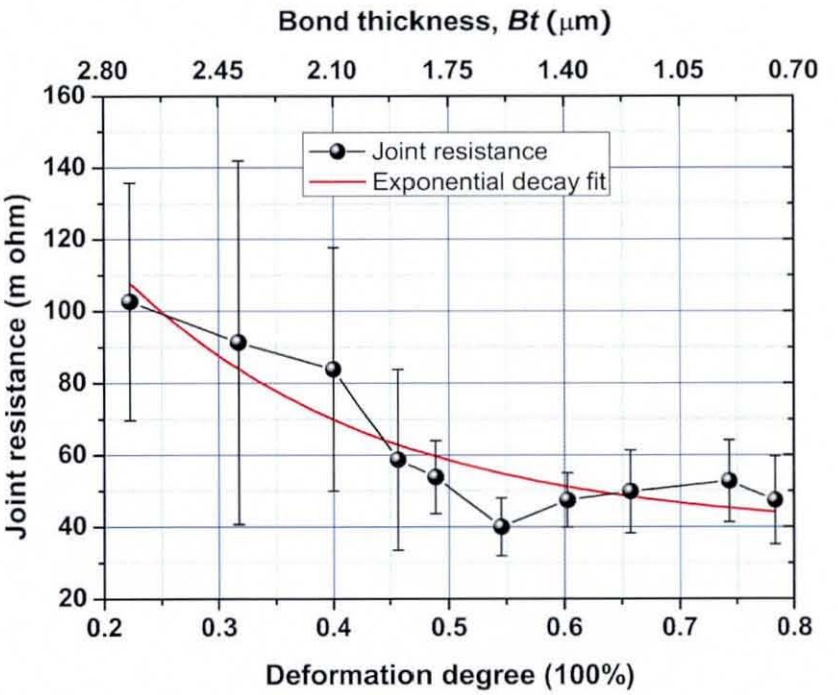

Figure 4.13: Joint resistance versus deformation for α-rotation samples.

In this figure, the joint resistances are the same as those shown in Figures 4.7 and 4.10. The deformations up to before the deformation degree, 55%, occurred in the less compressed sides of a-rotation, while those greater than 55% are for the highly compressed sides. It can be seen that the joint resistance reduced as the particle deformation increased up to 55% deformation, but then the joint resistance had relatively little further change for the deeper deformations, although there is some evidence of a slight increase in resistance. On the other hand, the results suggest that the joint resistances are getting more consistent as the standard error is reduced up to about 10 $m\Omega$ as also shown in Figure 4.13. This indicates that for individual ACA particles: *their joint resistance reduces as the deformation increases until reaching a stable value after a certain deformation degree.* Furthermore, the data can be interpreted as indicating that the joint resistance reduces continuously as the particle deformation increases, as indicated by the exponential decay function ($e^{-\lambda t}$) fitted to the data in Figure 4.13. This exponential decay function also fits well with the relationship between joint resistance and particle deformation, will be established in the following chapters.

It can be seen that the average joint resistances in the rotated samples are all bigger than those measured in the unrotated samples. This raises the question: *as to whether the joint resistances of ACA assemblies are more significantly affected by other affects of non-planarity than just by its effect on bond thickness.* In Figure 4.13, the smallest joint resistance is that for the unrotated samples. This trend can also be seen in the β-rotation results presented in Figure 4.5, where the lowest joint resistances were measured for sample 0, the unrotated assembly. However, before the conclusion is arrived, more research need to be done to check if this trend happens if different load is used in the bonding.

In summary, systematic research into the relationship between mechanical deformation and electrical behaviour of ACA particles, especially individual particles,is necessary to further understand the particle deformation effects on the joint resistance. Research on individual ACA particles will be presented in the following chapters. Such single particle experiments will separate load/deformation effect from other effects, e.g. particle sweep and contribute to the fundamental understanding of ACA technology.

4.5 Analysis and Discussion of β-rotation Results

The joint resistances of the different joints samples that assembled with β-rotations, results of 5 samples, 0, 4, 8, 12 and 16, are typically selected as plotted in Figure 4.14, where the horizontal axis represents the joint position along the long side of the chip. Sample 0 was the assembly without any rotation and samples 4, 8, 12 and 16 were assembled with angles, 4×10^{-4}, 8×10^{-4}, 12×10^{-4} and 16×10^{-4} *rad* respectively. The more compressed end is located from joints 1 to 15 and the less compressed end is located from 16 to 30. It clearly shows that all the joint resistances in an individual sample increase as the rotation angle increases. Another tendency is that the joint resistances near to the short edge are higher than the ones near to the middle of the chip, especially the joint resistances in the less compressed end which are much bigger than the others as shown in sample 12 and 16. Almost all the joint resistances were higher than those measured in the standard assembly, no matter where the joints were located. This is similar to the results for α-rotation; where all the joint resistances increased if there was any non-planarity in the assembly.

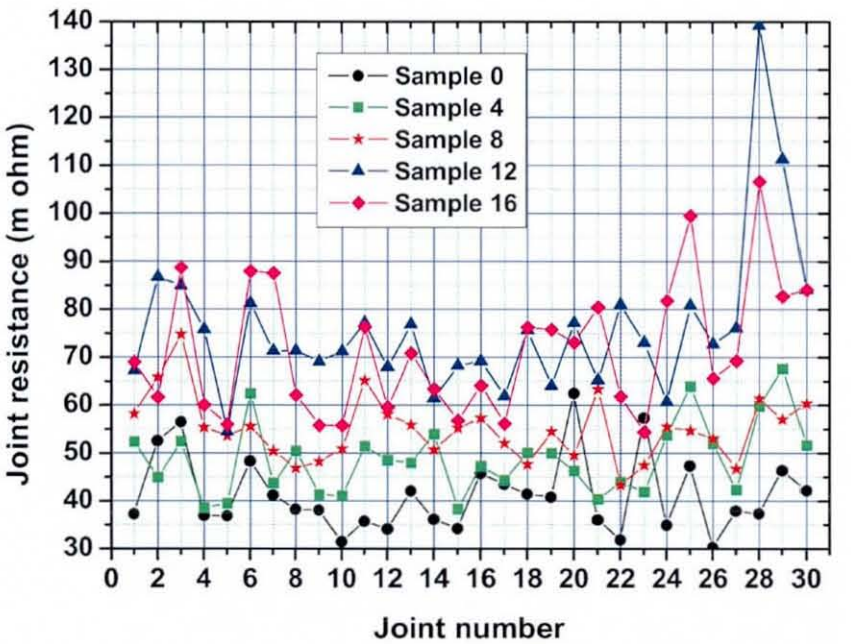

Figure 4.14: Joint resistance versus joints of β-Rotation samples 0, 4, 8, 12.

On the other hand, in order to have a clear picture of how the joint resistance at any specific joint location depends on the rotation angle, the results for 7 joint

locations, 1, 6, 12, 15, 18, 24 and 30, are selected and plotted in Figure 4.15, where the horizontal axis represents the rotation increment. It can be seen that all the 7 curves have a similar trend in that the joint resistance increases as the rotation angle increases. However, there is no clear difference between different joints locations for the same β-rotation.

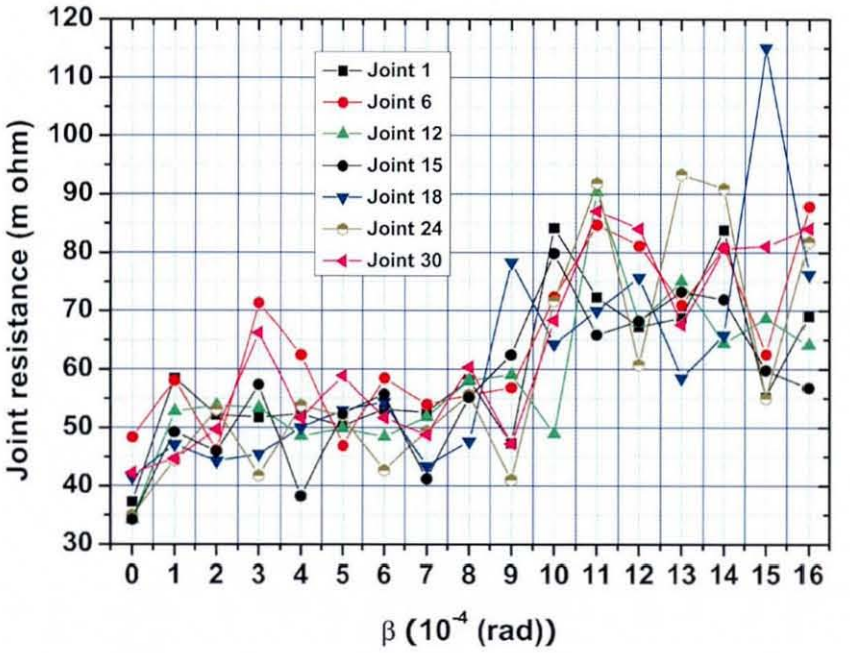

Figure 4.15: Joint resistance versus rotation angle for samples 1, 6, 12, 15, 18, 24 and 30.

The average joint resistance of each chip is shown Figure 4.16, where the horizontal axis represents rotation increment and the vertical axis is the mean joint resistances of each test chip. All the mean joint resistances for rotated samples were higher than for the standard sample, but remained around 50 $m\Omega$ for rotation angles up to 7×10^{-4} *rad*. They then increased more significantly from a rotation angle of sample 8, up to sample 11, rotation angle 11×10^{-4} *rad* and then and kept almost stable again.

4.5.1 Highly Compressed Side of β-Rotation

The joint resistances for the highly compressed side of the β-rotation samples increase as the rotation angle increases, as shown in Figure 4.15. This is considered to be due to the same reasons discussed for the different stages for the highly compressed side

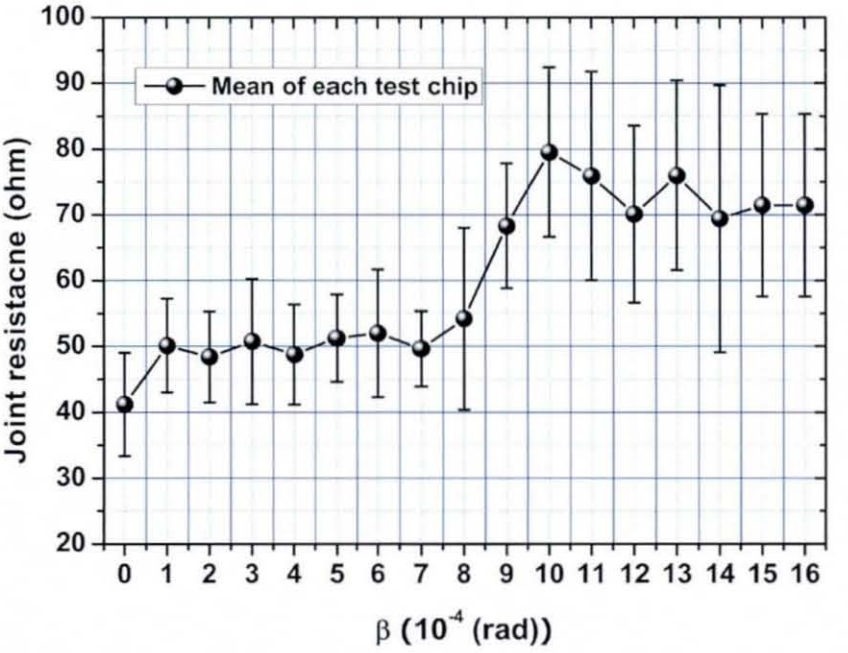

Figure 4.16: Mean joint resistance versus rotation angle of β-rotation.

in α-rotation. The trapped particles between the bumps and the pads were becoming over compressed as the rotation angle increased and therefore crushed as the rotation increased, therefore the interconnection resistances became slightly higher than those in the un-rotated assembly. This tendency became greater for the joints further away from the centre of the chip. The highest resistance was always found near to the short edge of the chip, joint 2 or 3. The electrical resistance of joint 1, the nearest to the short edge, was higher than the ones near to the centre of the chip, but smaller than those in joint 2 or 3. This is considered to be caused by the uneven flow of melted adhesive in the edge area during the high temperature bonding. All the joint resistances in the highly compressed side were kept almost consistent as shown in Figure 4.14, although they were higher than the standard one. Different deformation stages, as discussed in the highly compressed side of α-rotation, could be performed in the highly compressed side of β-rotation samples. The conclusion is that the joint quality reduces as the rotation angle increases. The SEM cross-section of joint 2 in sample 16, shown in Figure 4.17-a, where it can be seen that the particles were completely crushed. The assemblies with highly crushed particles, as discussed for Stage III α-rotation were expected unreliability performance if under service.

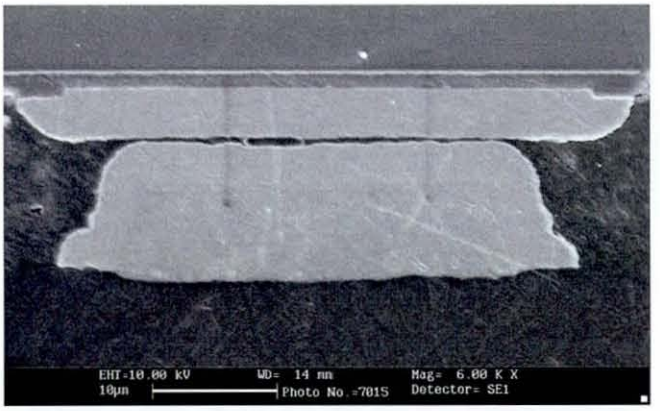

a) Joint 2 (Bt=0.782 μm)

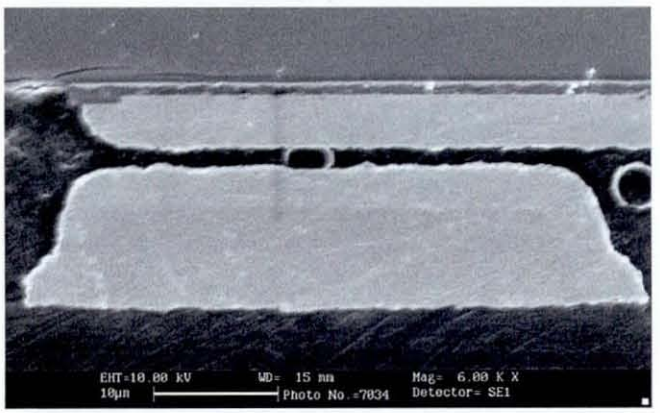

b) Joint 15 (Bt=1.866 μm)

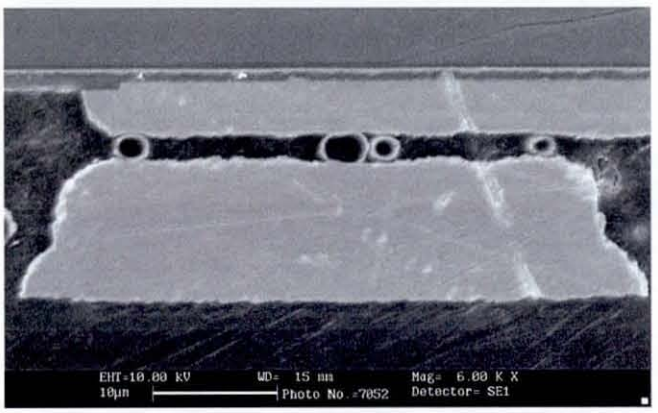

c) Joint 28 (Bt=2.593 μm)

Figure 4.17: SEMs of joints 2, 15 and 28 of β-rotation sample 16.

The particle deformation in joint 15 was much better than joint 2 as shown in 4.17-b, where the deformation was similar to the unrotated sample joint shown in Figure 4.9-a.

4.5.2 Less Compressed Side of β-rotation

The joint resistances of the less compressed side for β-rotation also increased as the rotation angle increased , as shown in Figure 4.14. The resistances of the joints near to the short edge of the chip were higher than those near the centre of the chip. This trend was similar to that for the highly compressed side of β-rotation, except that the joint resistances in the less compressed side were higher than those joints the same distance from the centre on the highly compressed side. For example, it can be seen that the resistances of joints 28 and 29 were much higher than those of joints 3 and 2 in the highly rotated samples 12 and 16. In each sample with β-rotation, the measured resistances increased from joint 16 to joint 30, due to the increasing bond thickness cured in the assembly. This tendency is much clearer in the samples with highly rotations, as the curve for sample 16 shows in Figure 4.14, where the resistances of joints 28 and 29 near the short edge were very much higher than those in the less compressed side. These resistance values were similar to those for stage III of the less compressed side of α-rotation. This is considered that similar deformation degree was performed in these joints as the SEM cross-section shown in Figure 4.17-c. These large resistances resulted from the small deformation of the ACA particles, and small area of contact between the particles and the pads.

4.6 Summary

This set of trials has generated an understanding of the effects of co-planarity variations on ACA joint resistances. It has been confirmed that poor co-planarity can result in low conductivity joints. The effects are dominated by height difference rather than the orientation.

4.6.1 α-rotation

Three stages of particle deformation were identified from the α-rotation experiments as the rotation angle of tested samples was increased, as shown in Figure 4.18.

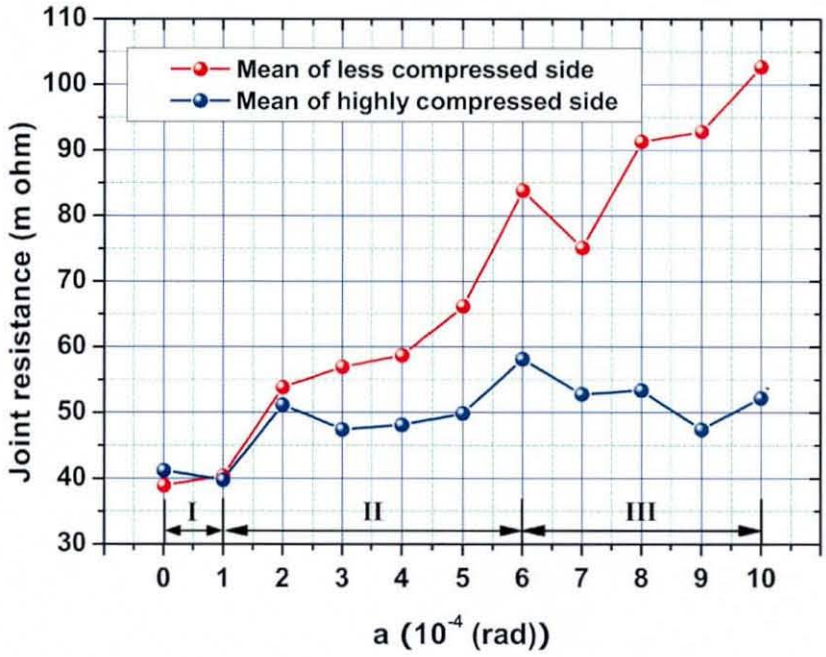

Figure 4.18: Mean resistance of α-rotation.

In stage I, low and uniform resistances were found. In stage II, the joint resistances of the less compressed side increased, due to the decreased deformation of the ACA particles. In contrast to the less compressed side, the lower conductivity joints in the highly compressed side resulted from the crushed particles and the reduced area of mechanical contact between the particles and the pads. In stage III, highly variable ACA joints were found in the less compressed side, because the ACA particle deformation was dramatically decreased and the mechanical contact between the particles and bumps/pads were very limited. A smaller number of particles trapped in the joints may be another factor that resulted in non-uniform conductivity in the less compressed side. In Figure 4.18, it suggests that the joint resistances in the highly compressed sides are stable compared to the ones in the less compressed sides, however such joints will suffer reliability problem under service, since that ACA particles were crushed in this stage and stationary contacts between the bumps and pads were initialled between the pieces of the crushed particles.

4.6.2 β-rotation

It can be concluded that the larger the rotation angle was, the higher the joint resistance in the less compressed side of β-rotation samples, and the nearer the joints to the centre of the chip was, the smaller the joint resistance in the less compressed side of each β-rotation samples. The joint resistances in the less compressed side increased from joint 16 to joint 30, and different stages as discussed in the less compressed side of α-rotation could be performed in these samples. In the less rotated samples, only the Stage I was performed, however, three stages are supposed to be found in the same sample with highly rotation as the joint resistances were quite high as shown in Figure 4.16.

In the highly compressed side of β-rotation, the joint resistances increased from joint 15 to joint 1 in each rotation, and the increase tendency became strong when the rotation angle was increased. It can be seen that the particles in joint 2 were crushed in the highly compressed side of sample 16 as shown in Figure 4.17-a. The particle deformation in sample 16 decreased from joint 1 to joint 15 because the compression decreased from the short edge to the centre of the of the chip. In joint 15, the particle deformation was similar as in the joints of standard ACA assembly as shown in Figure 4.17-b.

Assemblies with co-planarity variation, such as β-rotation, will suffer reliability problem under service due to the uneven joints near to the short edges of the chip, where similar failure mechanics as discussed in the α-rotation are expected.

Chapter 5

Individual ACA Particle Compression Experiments

5.1 Introduction

As discussed in previous chapters, ACA particle deformation is a critical factor that decides the mechanical and electrical performance of ACA assemblies. Significant research has been focused on the average mechanical and electrical properties of multiple ACA particles, however there has been little systematic research into the individual particle deformation behaviour. Research on the behaviour of multiple ACA particles, such as the non-planarity effects in the last chapter, is limited in its ability to reveal the particle deformation process, the strain and stress status during the deformation and the relationship between particle deformation and the electrical performance of ACA assemblies. This is why the systematic research on the mechanical deformation and electrical behaviour of individual ACA particles is introduced in the following chapters. This chapter describes the materials, equipments and experimental procedures for measurement of the deformation behaviour of individual ACA particles and their electrical resistance during deformation. The materials and apparatus are described first, followed by an explanation of the experimental methodologies and some discussion.

Due to the very small size of the particles, extreme accuracy is required to deform individual ACA particles and simultaneously measure their electrical resistance. Rather than design and build from scratch a suitable test system with the required accuracy, an existing nano-indenter machine was adopted and dedicated punches were

designed and prepared to achieve these experiments. Many materials were investigated for manufacture of these punches for the deformation tests. Punches with a small circular tip were used to deform single ACA particles on a base stage, as schematically shown in Figure 5.1. In the electrical tests, the particle deformation process also required specially configured punches and base stages to allow the FWR measurements.

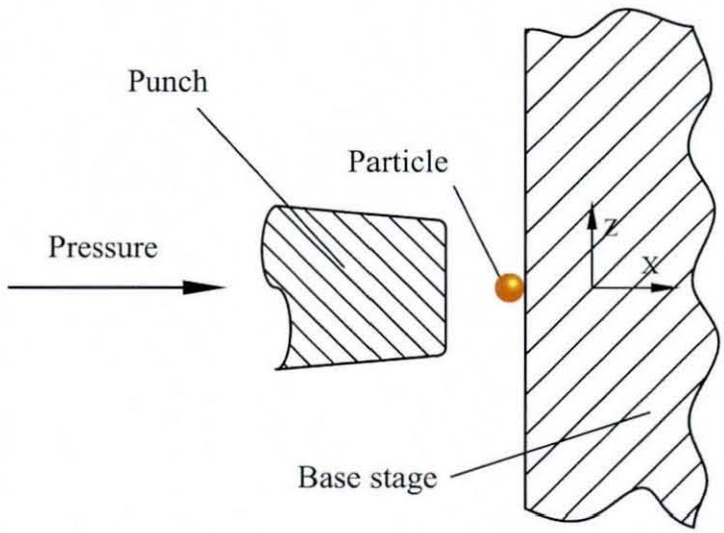

Figure 5.1: Individual ACA particle deformation.

In addition, the mechanical deformation of multiple ACA particles was also conducted using the same equipment to gain a more detailed understanding how a single ACA particle performs within an ACA joint containing multiple deformed ACA particles. The purpose of these experiments was to determine: *if the deformation of multiple ACA particles is simply the sum of the individual particle deformations.*

5.2 ACA Conductor Particles

The ACA particles used in these experiments are two types of commercially manufactured and available particles, Conpart AU-4 and Sekisui Micropearl AU-20575, which will be referred to as Type I and Type II respectively. The two kinds of particles are specifically designed for use in ACA/ACF applications and have similar structures, although they differ in detail, including lightly different polymer core composition,

different metal coating thicknesses and probably different manufacturing processes. The structure of the particles used in these experiments is shown in the schematic cross-section in Figure 5.2. The structure is mainly a polymer core coated firstly by a Ni layer and then a Au layer. There is an insulating layer over the Au layer to further prevent the ACA particle from conducting with the adjacent particles. These types of particles are widely used in LCD assembly and flip chip device mounting, since these Ni/Au coated high precision fine particles have high conduction and excellent reliability. The material properties of these two types of ACA particle are summarized in Table 5.1.

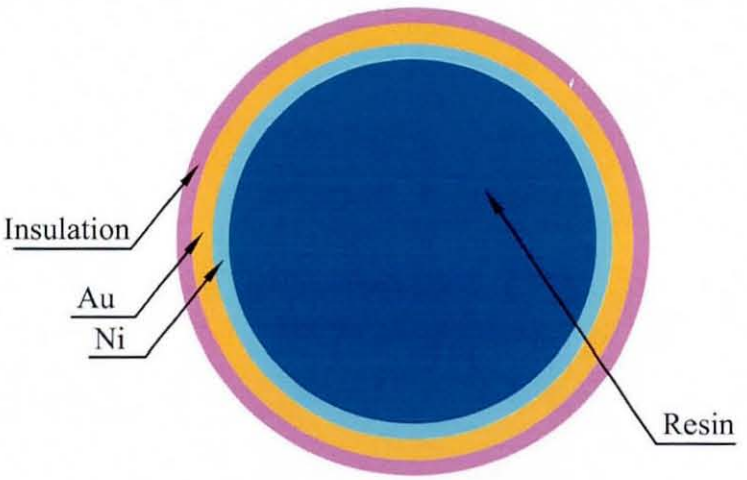

Figure 5.2: Configuration of a typical ACA particle.

Table 5.1: Properties of the ACA Particles.

Type	*Diameter* (μm)	*Compostion*	*Ni layer* (nm)	*Au layer* (nm)
I	4	*Styrene/Acrylate/DVB*	~ 10	$30 - 50$
II	5.75	*DVB*	~ 50	< 30
Note:		DVB:Di-vinyl-benzene		

The Conpart ACA particles can be supplied with diameters from 1 μm to 30 μm and can have their mechanical and chemical properties specially tailored due to the unique polymerization process is used in the manufacturing, which also results in near mono-sized spheres. The metal coating layers on the ACA particles are not homogenous as shown in Figure 5.3.

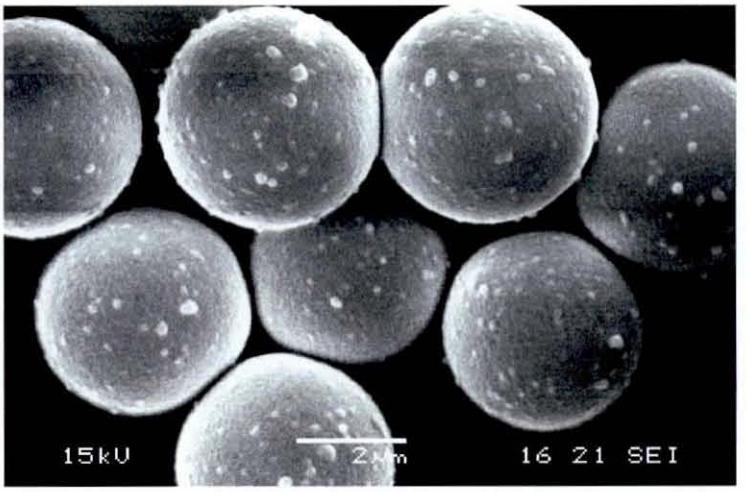

Figure 5.3: Type I particle.

The Sekisui Micropearl particles are also supplied in different sizes and different compositions for different applications. The metal coating layers on this kind of ACA particles are also not homogenous as shown in Figure 5.4.

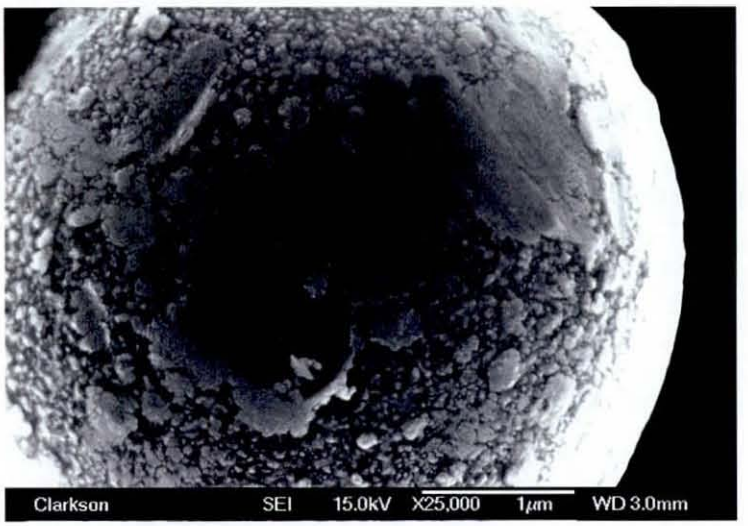

Figure 5.4: Type II particle.

5.3 Apparatus

5.3.1 Load Application and Displacement Measurement Machine

This experimental research was accomplished by using a Micro Materials $NanoTest^{TM}$ machine, which is normally used to measure micro materials properties, such as in nanoindentation testing, nano-scratch testing and nanotribometry [9]. However, this machine has been adapted specially in this experiment to deform the ACA particles using flat tipped punches.

Basically, this kind of nano-indenter consists of three main parts, voice coil actuator, capacitor plates for displacement measurement, and the pendulum which connects the actuator and capacitor plates to the indentor. The load force is applied by the voice coil actuator at the top end of the pendulum, while the punch is fixed to the bottom side of the pendulum, opposite to the capacitor, as shown in Figure 5.5-a. A frictionless pivot is used to allow the pendulum to rotate around the X-axis. The limit stop is to prevent the bottom side of the pendulum from moving too far towards the capacitor side.

The indenter and sample stage are schematically shown in Figure 5.5-b, where a flat tipped punch instead of the usual pointed diamond indenter was used. The machine is computer controlled and has a sample stage that can move in 3 directions to a positional accuracy of 0.1-1 μm. The load resolution of this machine is up to 100 nN, and the indentor displacement resolution is 0.1 nm.

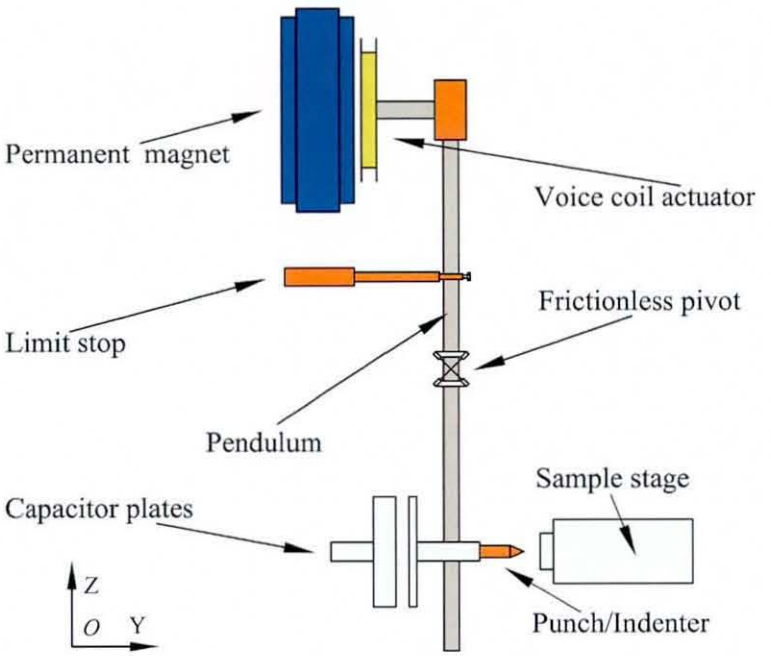

a) Schematic nanoindenter

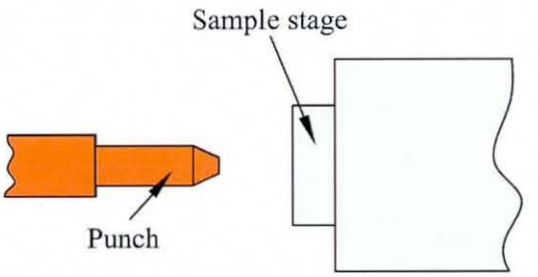

b) Puch and base stage

Figure 5.5: Schematic diagram of the nano-indenter.

5.3.2 Punches

Three kinds of materials were investigated for manufacture of the punches used in this study. These were High Speed Steel (HSS), a Titanium alloy ($Ti90Al60V4$) and a Tungsten/Copper alloy ($W80Cu20$). The material properties are listed in Table 5.2. Some other materials, such as ruby, diamond and silica, were also considered. Ruby was tried to make punches, however it was too hard to be shaped by available facilities. The ideal material should be diamond for the punches used for the mechanical deformation, but not tried due to the cost and the difficulty of manufacturing by available facilities. The silica was not tried because it was thought easy to be broken by the base stages.

Table 5.2: Selected Punch Materials.

Materials Composition	*Hardness Rockwell*	*Resistivity* ($\mu\Omega cm$)	*Corrosion Resistance*	*Polished Surface*	*Round Edge*
HSS	$80-82$	8.9	*Good*	*Excellent*	*Excellent*
W/Cu	82	3.2	*Average*	*Average*	*Average*
Ti	$35-39$	168	*Excellent*	*Good*	*Good*

A. HSS Punch

The term 'high speed steel' is derived from the fact that this material is capable of cutting metal at a much higher rate than carbon tool steel and continues to cut and retain its hardness even when the cutting tip of the tool is heated to a low red temperature. Besides iron and carbon, tungsten is the major alloying element but it is also combined with molybdenum, vanadium and cobalt in varying amounts. It is widely used for the manufacture of taps, dies, twist drills, reamers, saw blades and other cutting tools. The reason for selecting this material to make punches is that HSS is hard, and may be readily available, such as a small drill from which a flat tip with relatively sharp edges could be achieved and it has a relatively low electrical resistivity. A HSS punch made for mechanical deformation of individual ACA particles is shown in Figure 5.6, where the diameter of the tip is about 30 μm.

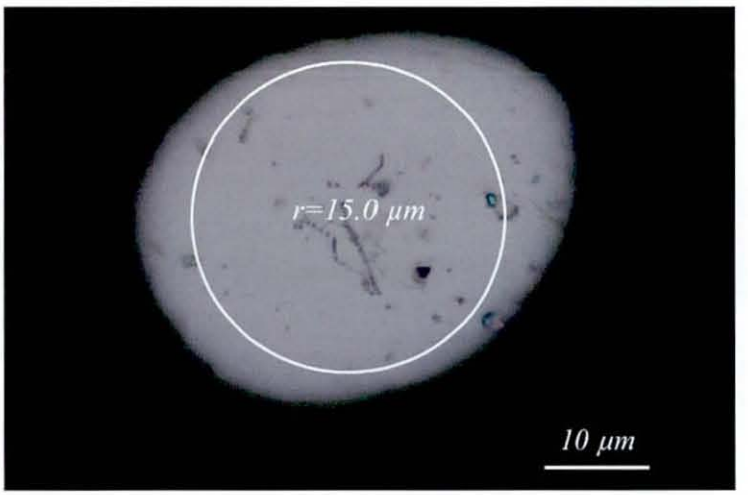

Figure 5.6: Surface of a HSS punch.

B. W/Cu Punch

A tungsten alloy ($W60/Cu40$) is typically used as an electrode material for spark erosion electrodes and electrical contacts, due to its excellent resistance to mechanical wear and electrical erosion. Therefore, by using this material a lower contact resistance as well as average mechanical properties can be achieved compared to the HSS and Ti punches, although the quality of polished surface achievable is not as good as for HSS or Ti. A W/Cu punch used for electrical testing of individual ACA particles is shown in Figure 5.7, where the diameter of the tip is about 20 μm.

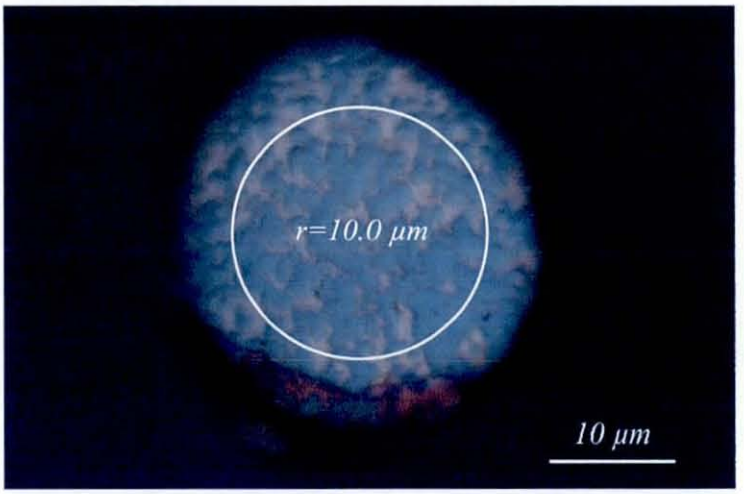

Figure 5.7: Surface of a W/Cu punch.

C. Ti Punch

A titanium alloy ($Ti90/Al6/V4$) was also chosen to make punches in this experiment, because it is a unique material with excellent corrosion resistance and mechanical properties. Although its resistivity and hardness is not as good as HSS or the W/Cu alloy, it is still a choice to make punches only for mechanical deformation.

5.3.3 Punch Manufacture

The punches used in these experiments were polished from sharp needles that were manually ground from a wire, 1 mm in diameter. Polishing a sharp needle into a flat tip punch requires a carefully designed and controlled process.

The starting material for punch manufacture is a length of a metal wire, 1 mm in diameter and 16 mm in length as schematically shown in Figure 5.8-a. This wire is ground into a sharp needle, as shown in 5.8-b. A mill machine, *Bridgeport Series I*, and abrasive papers were used to make needles. In the process, a fine abrasive paper (#4000 grit) was fixed in the mill with a angle of about 15° between the surface of the abrasive paper and the centre axis of the wire that was fixed in the mill vertically as shown in Figure 5.9, where the vice can move along Z axis automatically. The running speed of the mill was set at 4000 rpm, and the feed speed of the vice was set at fairly low rate, about $1mm/s$. Tapping oil was used as lubrication instead of suds. After grinding, the points of the ground needles were checked using an optical microscope to check they were smaller than 5 μm. If not, grinding continued. It should be mentioned that a smaller needle tip was better for the next step process.

For the next step, a turned brass bar, 25 mm in diameter and 25 mm in length, was turned by lathe and a 1 mm diameter hole along its axis was used as a jig. One end of this jig was finely polished using abrasive papers followed by a grinding pad with 1 micro diamond powder. By using this method, the finished surface was perpendicular to the centre line of the hole.

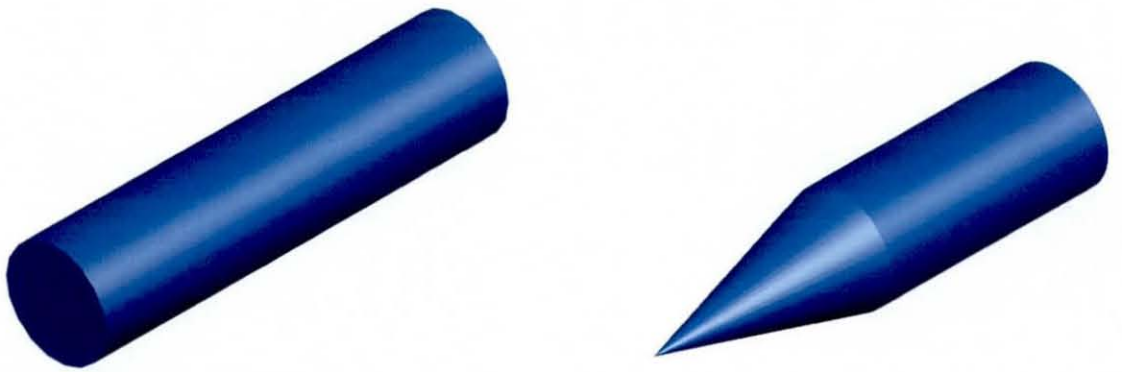

Figure 5.8: Needle production: a) original wire; b) ground needle.

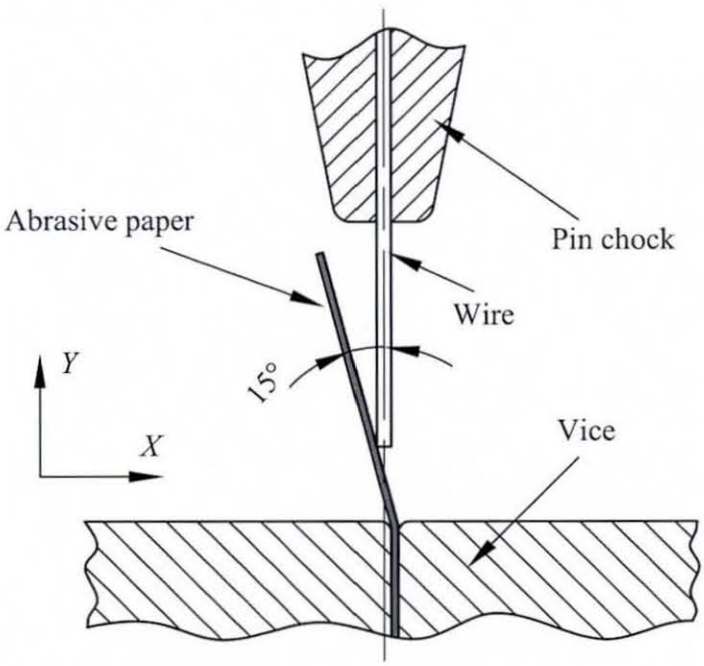

Figure 5.9: Wire grind setup in the Mill.

The next process step is to feed the polished needle into the hole in the jig and align the needle tip to the jig surface by gently pressing against a microscope slide, since the tip is easily broken by the glass side if it is pushed too hard as shown in Figure 5.10. Then, the needle was fixed in the hole using a drop of super glue, $LOCTITE_{®}$, applied from both sides, as shown in Figure 5.11-a. After the super glue had cured, the top surface was polished using a polishing pad loaded with 1 μm diamond powder until the tip surface was about 3-5 times the ACA particle diameter. The punch size was checked at regular intervals using a microscope about every minute to avoid over polishing the needle tip. After polishing, the punch, still fixed in the cylindrical jig, was as shown in Figure 5.11-b.

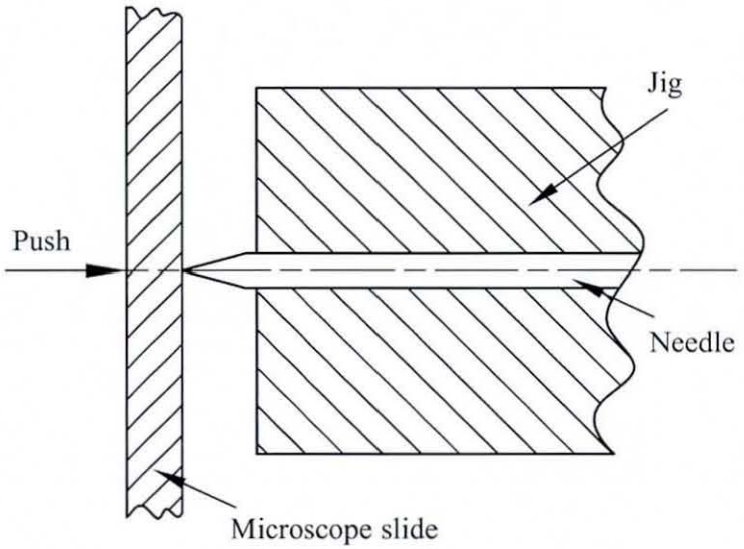

Figure 5.10: Needle tip alignment.

In the final process, the jig was placed in a beaker filled with Acetone. The cured super glue was removed by the Acetone after about 6 hours at room temperature, however it only took about 20 minutes if the beaker was put in an ultrasonic cleaning tank. After the super glue was dissolved from the jig, the polished punch as shown in Figure 5.12-a could be taken out from the hole. Figure 5.12-b shows a typical example of the finished surface of a W/Cu punch tip with a circular area about 20 μm in diameter, which was used in the electrical tests on single particles.

The process flow for punch production can be summarized as shown in Figure 5.13.

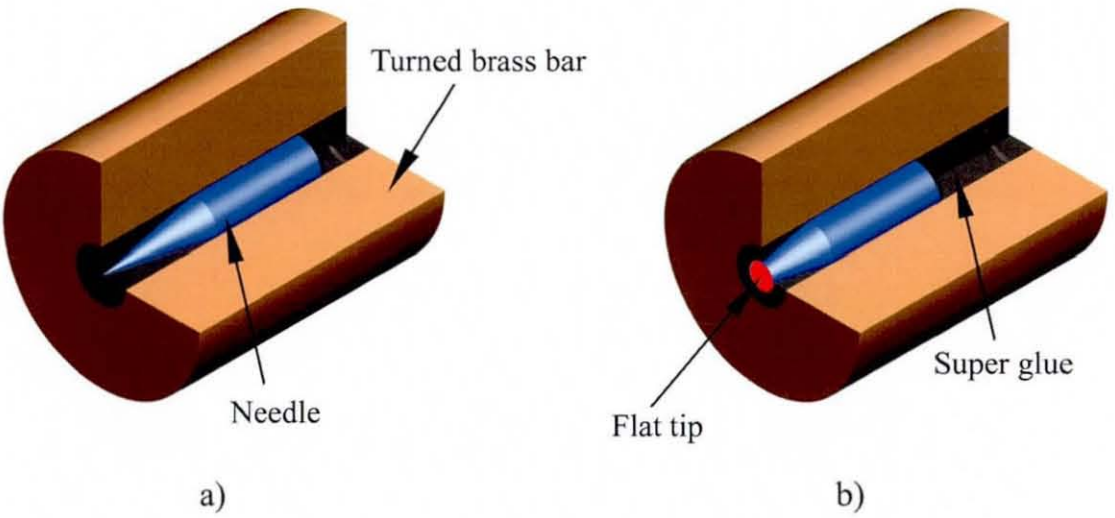

Figure 5.11: Punch grinding: a) needle fixed in jig; b) polished punch fixed in the cylinder.

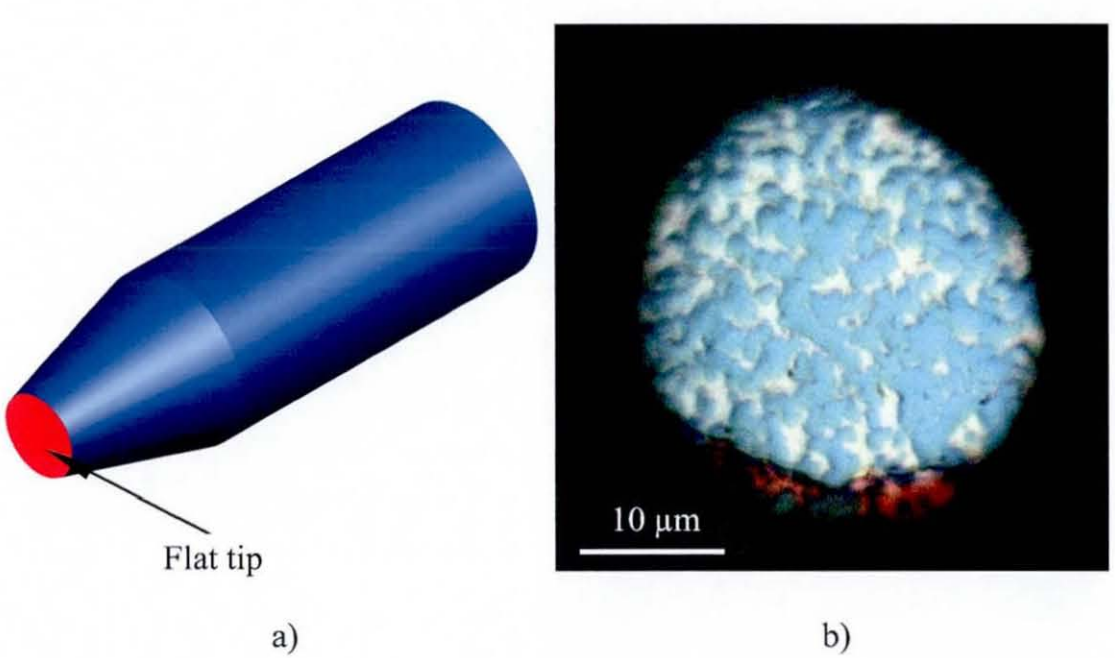

Figure 5.12: Completed punch: a) punch schematic; b) microscope image of a W/Cu punch.

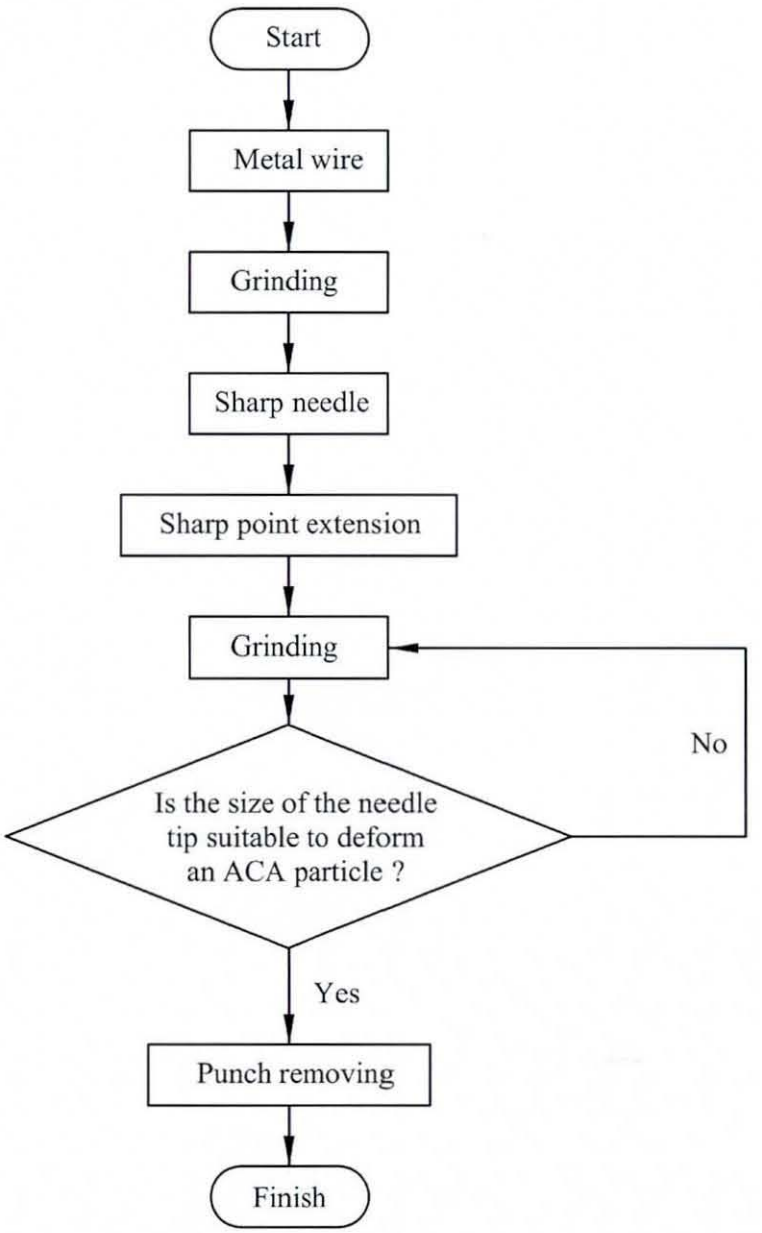

Figure 5.13: The punch production process.

5.3.4 Punch Assembly

Normal nano-indentor tip is a diamond indenter glued onto a machined metal indentor holder. Therefore, it is important that the punches used for these experiments are mounted in a similar holder that it can be fitted in the $NanoTest^{TM}$ Machine. Therefore, in order to use the punches within the $NanoTest^{TM}$ Machine, a modified indenter holder is needed. The indenter holder is also used to balance the pendulum, therefore the weight of the holder fixed punch should be similar to a standard indenter. The holder designed is shown in Figure 8.3 in Appendix 2. The punch assembly process is to insert the punch through the centre hole of the punch holder and tighten the M2 grub screw to fix it, keeping about 1.5 mm of the punch head protruding out of the hole. An assembled punch for the mechanical deformation of individual ACA particles is shown in Figure 5.14.

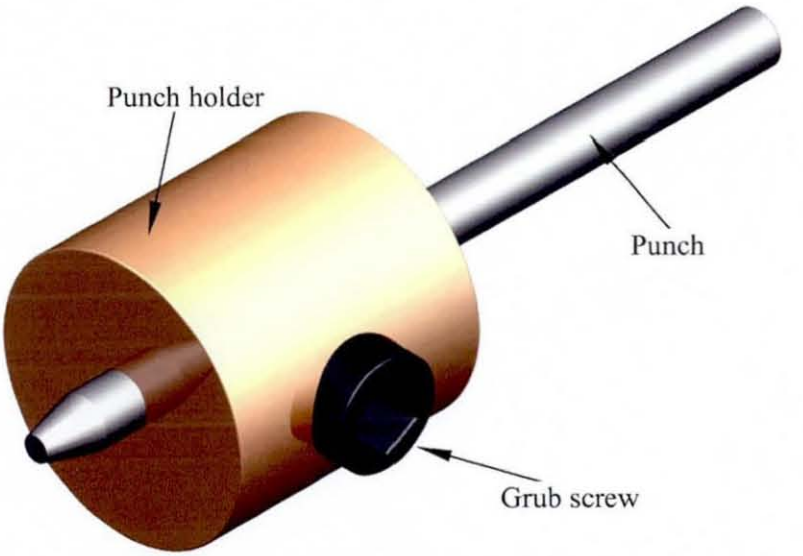

Figure 5.14: An assembled punch for mechanical deformation.

In the electrical resistance measurement experiments on individual particles, a more complex punch holder is needed to allow FWR measurement as two electrical connections are required to the punch as shown in Figure 5.15. One is a wire connected to the point near to the flat tip surface, since the nearer this point is to the tip, the better the measurement, since the resistance of the metal part between the connection point and the tip is added in series with the measurement. In order to achieve a good

contact between the wire and the punch, silver coated copper wires were used to make the connections. As shown in the figure, the electrical wire is twisted around the punch tip and is connected to it by soldering or application of a conductive silver paint. The wire is also glued to the side of the brass holder to prevent the sliver paint from loosing. It was found that the silver paint was better than soldering due to the oxidization of the tip surface resulting from the high temperatures of soldering compared to the painting at room temperature. The oxidized punch tip surface resulted in a high contact resistance between the deformed particle and the punch, such that there was no conduction measured in the experiment if the connection was made by soldering. The other electrical wire is soldered to the punch holder as shown in the figure. The wire was soldered before the punch was fixed into the holder to prevent the punch from oxidizing.

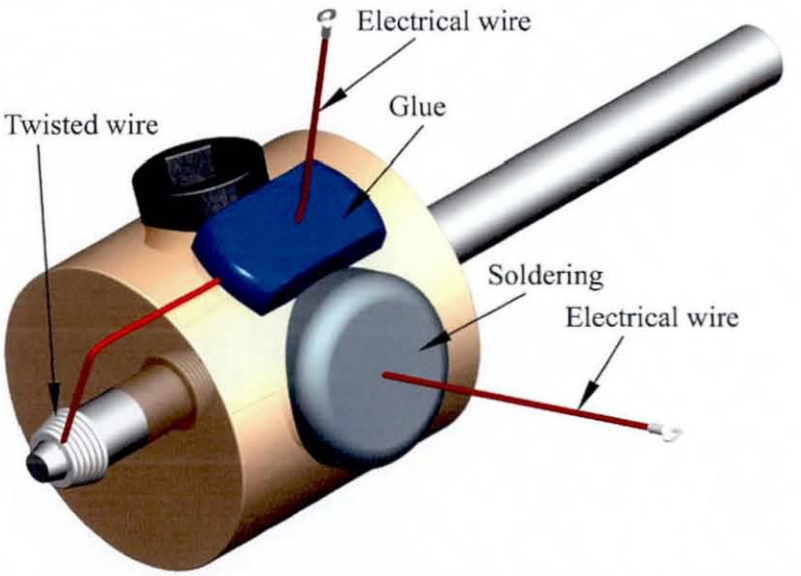

Figure 5.15: An assembled punch for electrical measurement.

5.3.5 Base Stages

Three materials were investigated for use to make the base stages for these experiments. They can be divided into three types, base stages for alignment, base stages for mechanical deformation of ACA particles and base stages for the electrical tests.

A. Alignment Stage

As soft metal, copper is an idea choice to make the base stage holder to centre and align the punch without damaging its flat tip. A piece of copper, 30 mm in length, 15 mm in width and 3 mm in thickness, was glued on an aluminum base stage holder after the top surface was polished and finished by 0.5 μm diamond grinder pad.

B. Mechanical Deformation Stage

The size of the base stages for mechanical deformation was 75 mm in length, 25 mm in width and 1 mm in thickness. Glass is a rigid material with a smooth and flat surface which is ideal for deforming the ACA particles against. Glass microscope slides, manufactured by MENZEL-GLÄSER, were used. The microscope slides used were purchased pre-prepared with an extra positive electrostatic charge on the top surface. This resulted in strong adhesion of the particles onto the slide.

C. Electrical Test Stage

Brass was used in the tests. Brass is the term used for alloys of copper and zinc in a solid solution. The brass used in this research was $C360$, a machinable brass which has very good resistance to corrosion. Excellent conductivity, on the other hand, is the idea choice to make base stages for the electrical measurement of deforming ACA particles. The size of the base stages for the electrical tests was 46 mm in length, 20 mm in width and 2-3 mm in thickness. Holes in the base stage 2 mm in diameter and 36 mm apart from the centre were used for the attachment of the base stage on the base stage holder. A finely polished surface is needed and was prepared for the electrical measurements during the deformation tests.

5.3.6 Base Stage Holder

Three types of base stages was adopted in this research to achieve the alignment, the mechanical deformation of ACA particles and the electrical measurement of individual ACA particles undergoing deformation. Accordingly, three kinds of base stage holders with different base stage retaining mechanisms, were designed and manufactured to

hold the base stages within the nanoindentor. The base stage holder for alignment is a turned aluminum, and super glue was used for the retaining mechanisms. It is not as complex as the stage holders for the mechanical deformation and the electrical tests although they have the same connection part used to hold them within the nanoindentor.

In the mechanical deformation experiments, a glass of the microscope slide is used as the base stage. In order to readily change between slides coated with different particles, a custom base stage holder was made to hold the microscope slide as shown in Figure 5.16, where the slide can be clipped on the top surface between the fixed jaw and the movable jaw by turning the fastener. The soft copper bar glued to the edge of the fixed jaw is used to prevent the glass slide from breaking.

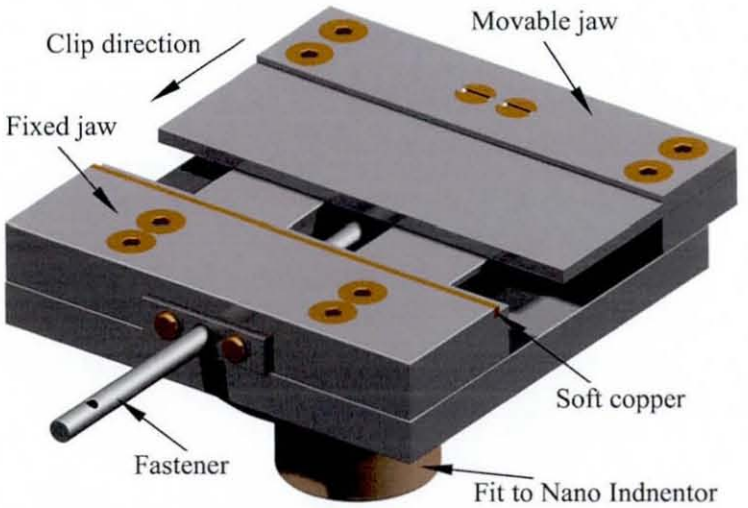

Figure 5.16: Base stage holder for microscope slide.

In the electrical measurement experiments of ACA particles undergoing deformation, in order to measure the joint resistance, a conductive material was demanded for the base stage, and the base stage holder had to provide electrical connections to the base stage for the tests. A base stage, as designed in map 8.4 in Appendix 2, was used to hold the metal base stage as shown in Figure 5.17, where two tapped holes are used to fix the metal stage onto the top surface by M2 screws. Two wires were soldered on the two gold plates that are fixed on the metal base by the screws as shown in the figure. To prevent the wires from moving and damaging the soldering connection, a metal part was made to fix the two wires on the side of the base holder

using a M2 screw.

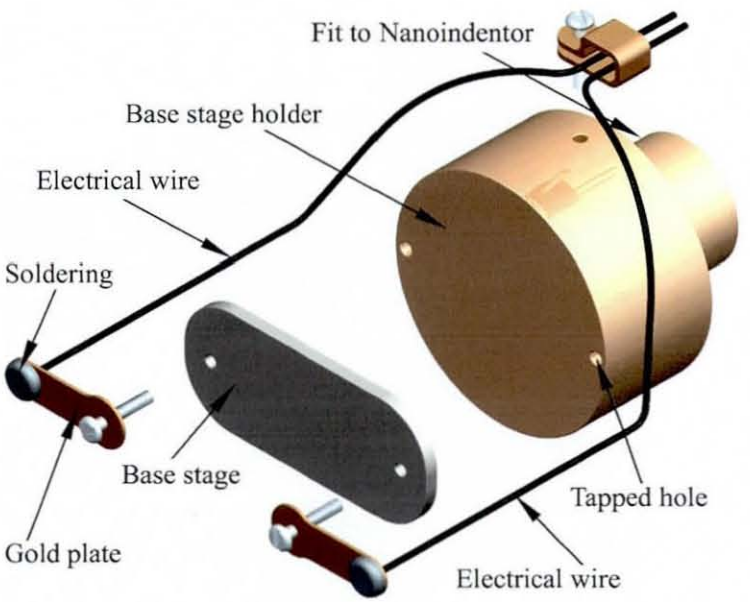

Figure 5.17: Base stage holder for metal base stage.

5.3.7 Data Acquisition

The load and deformation can be recorded by the control computer in the nanoindentor, however which is not capable of measuring the electrical tests. There is no more data acquisition needed for the mechanical deformation, however, additional data acquisition system is needed to record the mechanical deformation and electrical resistance together in the electrical tests.

In the electrical test, an Agilent 34970A Data Acquisition system with an Agilent 34901A A/D switching module were used to record the load force and deformation depth from analog outputs of the $NanoTest^{TM}$ Machine. In addition, Agilent 34901A module also has FWR measurement capacity which can be used to measure the electrical resistance of individual ACA particles undergoing deformation. The logger has a 60 channel/second scan rate and when making FWR measurements automatically compensates for thermoelectric EMFs. Using this data acquisition system, the electrical resistance was measured simultaneously with the load force and deformation depth and were automatically recorded by the Agilent BenchLink data logger software in a computer connected to the logger through the RS-232 interface.

A Keithley 580 Micro-ohmmeter was also tried to measure the electrical resistance using FWR method, however it was found the measurement was not consistent if the measurement varied from one range to another range. Therefore, only the Agilent 34970A Data Acquisition system was used in the electrical tests.

5.4 Methodologies

5.4.1 Mechanical Deformation of ACA particles

Experiments on the mechanical deformation of individual and multiple ACA particles using the nanoindenter involved force controlled deformation of the particles, where the force was increased linearly with time and the resulting deformation monitored. The load force and the deformation were recorded by the nano tester in control computer. Several major steps can be identified in the procedure for these experiments. They are punch alignment, sample preparation, and particle deformation.

Punch alignment: The punch must be aligned before it can deform the particles accurately, because each different punch has a different tip diameter, and also the same punch can not be re-fixed into the same position on the machine for different experiments. There is a cross-hair on the TV screen in the $NanoTest^{TM}$ Machine, where a video image of the base stage surface acquired by a video camera in the microscope is displayed. The alignment process, that is, the microscope cross-hair positioning, is to firstly make an indenter mark on a soft copper base stage, and then locating the mark by using the microscope. Then the cross-hair is moved to the mark centre and the position saved in the computer. After this process, the cross-hair can be used to accurately locate the position of an individual ACA particle on the base stage.

Sample preparation: Sample preparation involved spreading the ACA particles onto the base stages at a low enough density to ensure individual particles can be selected. In order to evenly spread the particles on the slide, three methods were tried. One was to spread the particles using pure water and then dry them at room temperature. Another was to blow the particles over the slide using an air duster at a distance of half a meter from the slide. The last method was to use a lens cleaning

paper to spread the particles gently and an air duster to reduce the particle density. The reason to use the lens cleaning paper is that the cleaning paper is soft and made of long fibers, which avoids damaging the particles or leaving fine fibers on the glass during the spreading. After some practice, each method worked perfectly, but the last method was mostly used in the experiments because it is easy to be controlled.

Particle deformation: In the experiment on the mechanical deformation of an individual ACA particle, the base stage holder with glass base stage was fixed into the indenter machine in stead of the copper base stage and the base stage surface is moved into the microscope focal plane. The ACA particles were then located on the base stage and an individual one was selected using the cross-hair. A test is then started after moving the base stage to the indenter position. The mechanical deformation process of an individual ACA particle is schematically shown in Figure 5.1. The base stage with the selected ACA particle moves at a high speed until close to the indenter, and then moves at a much lower speed until it touches the punch. It then moves back a short distance, a few micro meters, where the surface of the base stage with an ACA particle is fixed and then the punch moves from left to right to deform the particle. For multiple ACA particle deformation, a similar process is used, but a larger punch with a tip about 45 μm in diameter is used, and the cross-hair is positioned in the centre of a group of particles.

5.4.2 Electrical Resistance of Deforming ACA Particles

The procedure for electrical resistance measurement of individual particles undergoing deformation is basically the same as for mechanical deformation. However, in the experiment of the mechanical deformation, the deformation data is saved directly in the nanoindentor control computer, whilst for the electrical tests, the electrical properties as well as the mechanical deformation must be measured by four channels, carrying the electrical resistance, the load force and the deformation respectively simultaneously. Therefore, four channels of the Agilent 34970A Data Acquisition system were used and connected to the analogue outputs of the indentor and the electrical test system for the measurements. Two channels are for the FWR measurement and the other two are for the load force and deformation respectively. The time between the

start of each scan is 0.01 s.

The test configuration for electrical measurement is as schematically shown in Figure 5.18, where it can be seen that an ACA particle is deforming between the base stage and the punch. The wires on the punch and the metal base stage are for the electrical measurement using the FWR method. The connections of the FWR measurement to the 34901 A module are shown in Figure 5.19, where R is the measured resistance.

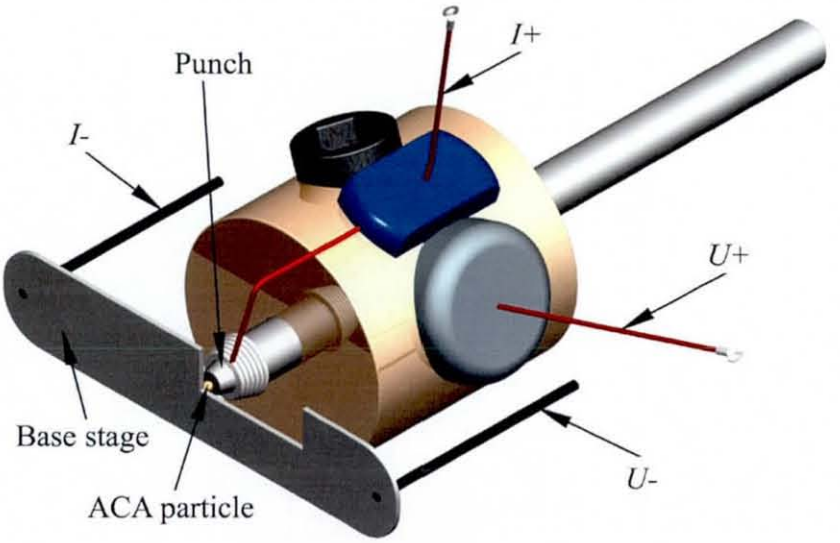

Figure 5.18: Electrical measurement.

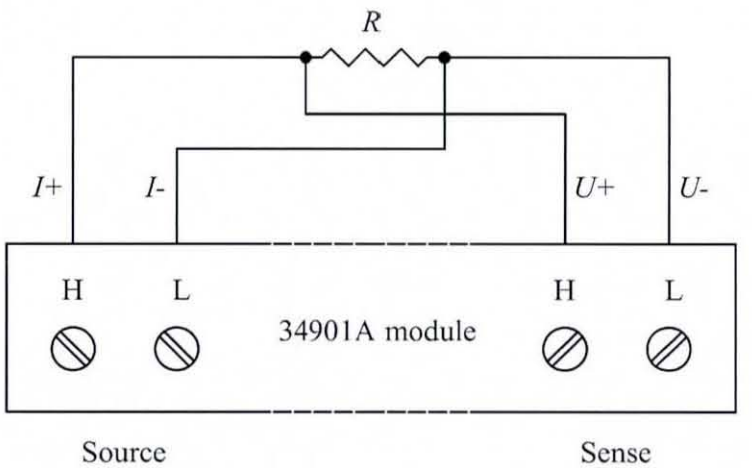

Figure 5.19: Connections of the FWR measurement.

In order to have a detailed analysis on the configuration of the electrical measurement, schematic cross-sections of the electrical connections are considered as shown in Figure 5.20, where R represents the resistance of the deforming ACA particle and the contact resistances between the particle and the contact metal surfaces. In the figure:

- P_1 refers to the silver paint connection near to the punch tip.
- P_2 is the solder connection on the punch holder.
- P_3 represents an electrical node.
- R_1 is the resistance of the base stage and the connecting wires ($U+$ and $U-$) between the joint area, where the particle is deformed on the base stage, and the sense of the measurement system.
- R_2 is an equivalent resistance to R_1, but in series with the source section of the measurement system.
- R_3 is the resistance of the punch between the electrical node and the bottom surface of the punch tip.

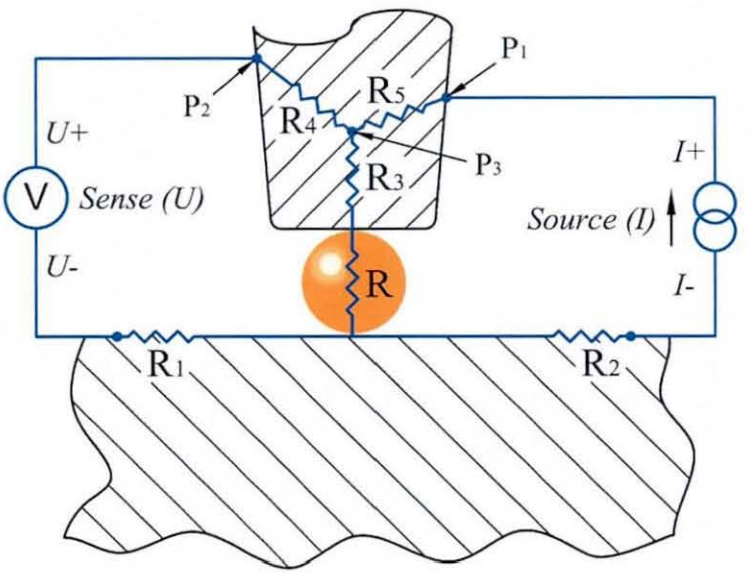

Figure 5.20: The schematic cross-sections of the electrical connections.

- R_4 is the resistance between the electrical node and the wire $(U+)$.
- R_5 is the resistance between the electrical node and the wire $(I+)$.

The equivalent circuit of Figure 5.20 is as shown in Figure 5.21, where it can be seen only R3 affects the electrical measurement. The formula of the equivalent circuit for R is:

$$R = \frac{U}{I} - R_3. \tag{5.4.1}$$

The length, l, of the metal part of the indentor tip that results in R_3 is about 400 μm, the radius of the tip surface is 10 μm, and the electrical resistivity, ρ, of W/Cu is 32 $\mu\Omega cm$. For the indentor tip taper angle of approximately 15°, R_3 can be calculated as:

$$R_3 = \frac{\rho l}{\pi\left[\frac{r + r + l tan(15°)}{2}\right]^2} \approx 1\ m\Omega. \tag{5.4.2}$$

Therefore, the effect of R_3 on the resistance measurements is negligible if the measured resistance is more than 100 $m\Omega$.

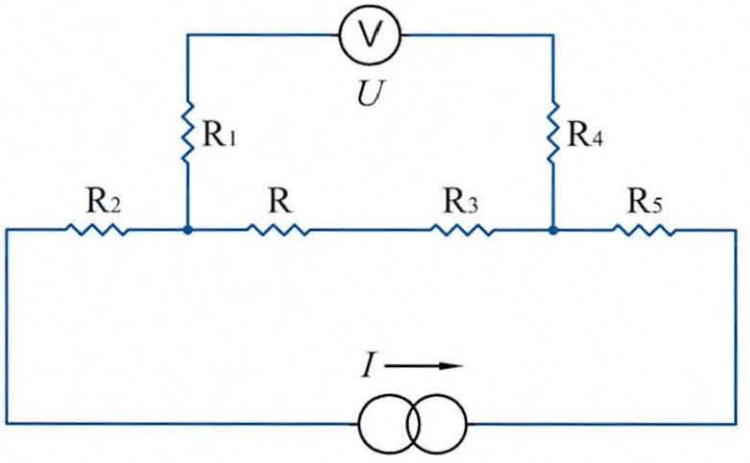

Figure 5.21: Equivalent circuit of the circuit configuration.

In theory, there is another kind of configuration where the positions of the source and the sense of the 34901 A module as shown in Figure 5.20 are swaped. However, the large contact resistance resulted from the silver paint at point P_1 may affect the sense accuracy. Therefore, it is not used in this research.

Chapter 6

Results for the Particle Deformation Experiments

6.1 Introduction

In this chapter, the results from the mechanical deformation and resistance measurement are introduced. These involve different series of tests on individual ACA particles. The purpose is to present the systematic research on the mechanical and electrical characteristic of individual ACA joints undergoing deformation.

In the mechanical deformation, the typical results for mechanical deformation of individual ACA particles are presented, followed by the effects of load rate, cycling load (dwell), and the presence of adhesive on the deformation. Compared with the individual particle deformation, results of mechanical deformation of multiple ACA particles are also presented.

In the resistance measurements, the results of typical electrical resistance of individual particles undergoing deformation are given. The measurements also include the results for the tests of different punches, resistance stability and voltage and current properties of a deformed ACA particle.

6.2 Mechanical Deformation Results

6.2.1 Typical Results for Mechanical Deformation of Individual ACA Particles

In order to gain a basic understanding of the mechanical deformation of individual ACA particles, typical experiment results are presented in this section as examples. As stated in Chapter 5, *HSS* and *Ti* punches were manufactured for the studies on the mechanical deformation of ACA particles. However, there was almost no difference between the results from initial tests comparing the *HSS* and *Ti* punches, and therefore only *HSS* punches were used for all of the mechanical deformation results presented in this thesis.

There were several initial user defined test parameters for the $NanoTest^{TM}$ machine that affected the final experiment results, which were load rate, maximum load, dwell, initial force and depth gain. *Load rate* is the amount the load force increases in each second, which remains constant during each particle deformation test. The nano tester used in this research can only work in a load controlled mode, where the load increases/decreases at a constant rate during the test. *Maximum load* is the preset maximum load force that the load machine applies to the test samples. *Dwell* is the time for which the load is kept constant after the maximum load is reached. *Initial force* is the load force at which the machine starts to record the experimental data. *Depth gain* is a machine constant, and is the preset maximum distance that the machine can move the punch forward. The machine stops increasing load force when either the load force reaches the maximum load or the deformation exceeds the depth gain. It was found that mechanical deformation at the same load rate was not affected by the other test parameters, if they were previously set to optimum values, although it took several tests to find their optimum values for each kind of particles.

Two particle deformation results, one for Type I and one for Type II particles were selected as typical experiment results and compared with the direct indentation of the punch on the microscope glass. The parameters for these typical experiments are listed in Table 6.1. In a typical experiment, taking Type II particles as an example, the load/unload force versus time is as shown in Figure 6.1. Similar load and unload

processes were used for all of the mechanical tests, although different load rates and maximum loads were used, for example, a 0.5 mN/s load rate and 20 mN maximum load were used for the Type I samples and 40 mN maximum load for the indentation on glass.

Table 6.1: Experimental Parameters for Typical ACA Particles

	Load rate (mN/s)	*Maximum force* (mN)	*Dwell* (s)	*Initial force* (mN)	*Depth gain* (μm)
On glass	1	40	5	0.2	6.378
Type I	0.5	20	5	0.35	6.378
Type II	1	50	5	0.35	4.783
Note:	On glass: direct indent on the glass without particle				

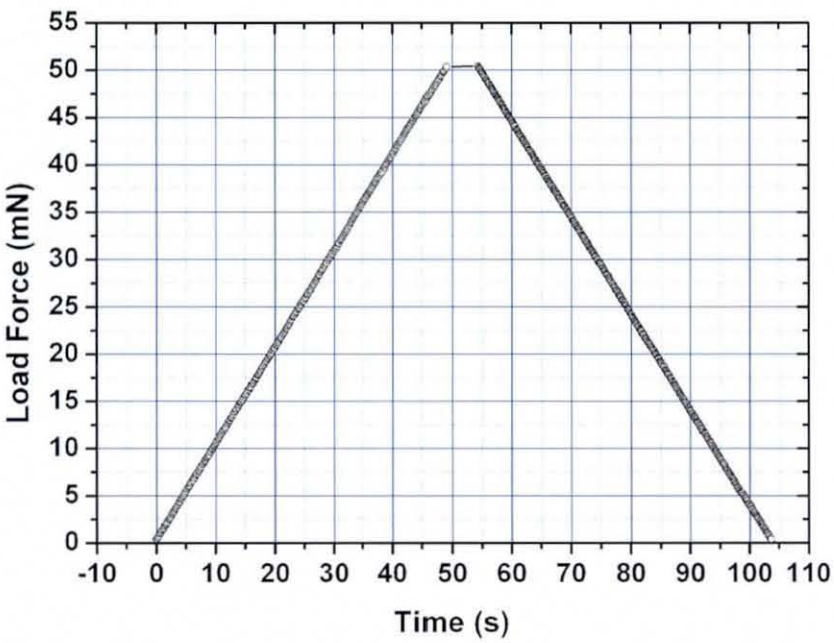

Figure 6.1: Load versus time.

Figure 6.2 compares the indentation of the punch directly on the glass slide with deformation tests on Type I and II particles. It shows that the indentation of the punch on the glass was much stiffer, and more linear than the deformation of the particles, for example the particle deformation, Δd, was more than 3 μm for the Type II particle and the indentation on the glass was only 0.75 μm when the load force was 30 mN. This suggested that the selection of the HSS punch and the microscope

slide was suitable for deforming the ACA particles. The deformation profile of the Type II particle in the figure showed that the deformation increased gradually as the load force increased, but the stiffness (load force/deformation) was initially low, i.e. for deformation up to 2 μm, and then increased for deformations greater than 2 μm. There was a sudden increase in deformation after the deformation, Δd, reached 57% of the original particle diameter, i.e. from 3.2 μm to about 4.2 μm, at which the load force was 32 mN. Although the deformation rapidly increased by about 1 μm, there was almost no recorded change in the load force, resulting in the horizontal line seen in the figure. It is assumed that the left end of the horizontal lines in the load profiles indicate the start of particle crushing, and this is referred to as the crush point in this work. However, since the machine was operating in a load controlled mode, the load may have actually dropped during the crushing process, but this would have been hidden by the inertia of the pendulum. The load then ramped up until the load force reached its set maximum, followed by the unloading process.

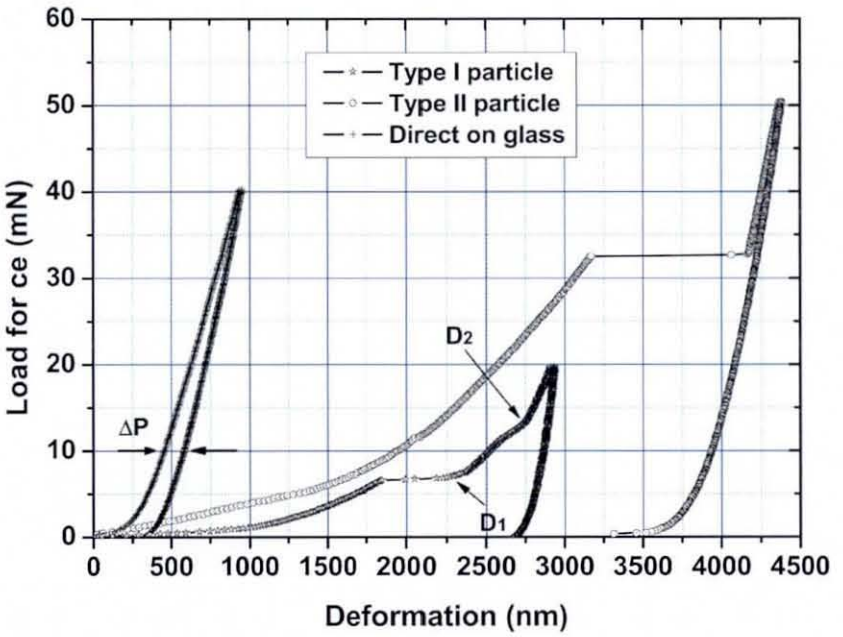

Figure 6.2: Comparison of indentation of the punch directly on the glass slide with particles.

Similar deformation processes for a Type I particle can be seen in the figure, however the crush point of the Type I particle is much lower than the Type II particle because the Type I particle is smaller in diameter than the Type II particle and also the material composition is different. Another difference identified is that there was more plastic deformation from points D_1 to D_2 after the Type I particle was crushed as shown in the figure.

There are two load ranges in the nanoindenter, high load model and low load model. High load model was used to deform Type II particles, however it was not good to deform type I particles because very limited deformation data can be acquired in the shorter deformation. It will take long time to test Type I particles in the low load model because more accurate deformation performs than in the high load model. Therefore, only Type II particles were used for the following single particle mechanical deformation experiments, but Type I particles were used for some other experiments as explained later.

6.2.2 The Effects of Load Rate on the Mechanical Deformation of Individual ACA Particles

In the mechanical deformation of individual ACA particles, the particle deformation behaviour was found to be significantly affected by the load rate. In order to give a detailed understanding of the effects of load rate on the particle deformation, three different load rates, 0.5, 1 and 2 mN/s, were used in the experiments. In total 27 experiments were conducted, as listed in Table 6.2, where 8 tests were for 0.5 mN/s, 11 tests were at 1 mN/s, and 8 tests were at 2 mN/s. The same initial load force, 0.35 mN, was used throughout, but different maximum forces and depth gates were used in the experiments as detailed in the Table 6.2.

Table 6.2: Experimental Parameters for the Different Mechanical Tests

Sample No./ID	*Load rate* (mN/s)	*Maximum load* (mN)	*Depth gain* (μm)	*S or F*
$T05-1$	0.5	50	6.378	S
$T05-2$	0.5	50	6.378	S
$T05-3$	0.5	50	6.378	S
$T05-4$	0.5	50	6.378	F
$T05-5$	0.5	40	6.378	S
$T05-6$	0.5	40	4.783	S
$T05-7$	0.5	40	4.783	F
$T05-8$	0.5	40	4.783	S
$T10-1$	1	40	4.783	S
$T10-2$	1	40	4.783	S
$T10-3$	1	40	4.783	F
$T10-4$	1	40	4.783	S
$T10-5$	1	40	6.378	S
$T10-6$	1	50	6.378	S
$T10-7$	1	50	6.378	S
$T10-8$	1	50	6.378	S
$T10-9$	1	50	6.378	S
$T10-10$	1	50	6.378	S
$T10-11$	1	50	6.378	S
$T20-1$	2	50	6.378	F
$T20-2$	2	50	6.378	S
$T20-3$	2	50	6.378	S
$T20-4$	2	50	6.378	F
$T20-5$	2	50	6.378	S
$T20-6$	2	50	6.378	F
$T20-7$	2	50	6.378	F
$T20-8$	2	50	6.378	S
Note:	S:Experiment succeeded; F:Experiment failed.			

A number of tests were considered to be unsuccessful, as the results were radically different to the majority of results. For example, two results (T05-4 and T05-7) out of the 8 tests for the load rate of 0.5 mN/s were very different from the rest as shown in Figure 6.3. For one result, T10-3, in the tests at 1 mN/s, reults characteristic of indentation directly on the glass were recorded. Four tests, T20-1, T20-4, T20-6 and T20-7 at 0.5 mN/s, also failed , since only indentation on the glass was found. These five results may be due to the particle slipping out of the punch.

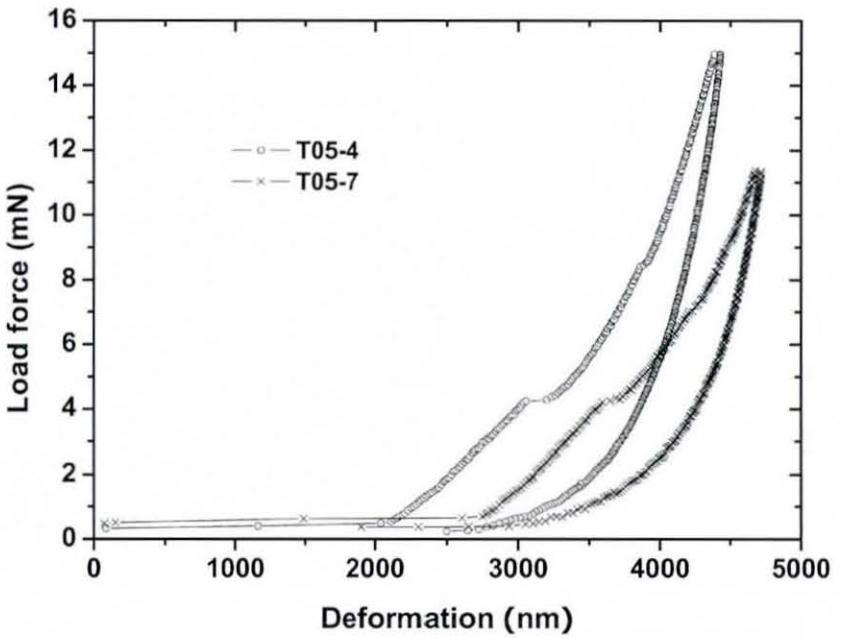

Figure 6.3: Results of T05-4 and T05-7.

The successful test results are plotted in Figure 6.4. These results show that the deformation behaviour of the particles was different when different load rates were used. For each load rate, the load curves vary significantly in terms of the average load/displacement at which crushing occurs, although there was substantial variation between individual results.

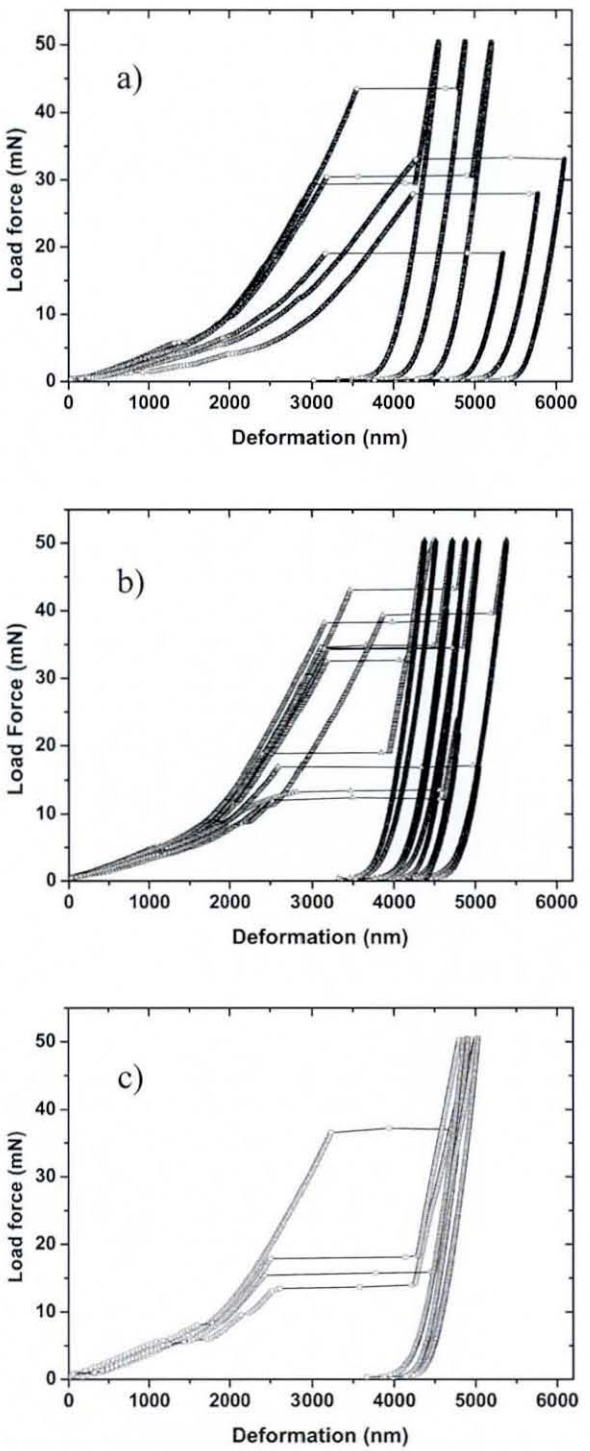

Figure 6.4: Succeeded test results. a) load rate at 0.5 mN/s; b) load rate at 1 mN/s; c) load rate at 2 mN/s.

6.2.3 Dwell Effects on the Mechanical Deformation of Individual Particles

Metal coated polymer ACA particles have been previously shown to have visco-elastic properties [23]. However there are little detailed studies reported on the visco-elastic properties of ACA particles, especially individual ACA particles. Therefore, experiments were carried out to examine the visco-elastic properties of individual polymer cored ACA particles. The experimental parameters for the experiments are listed in Table 6.3.

Table 6.3: Experimental Parameters of Dwelling

Particle type	*II*
Maximum load	15 mN
Initial load	0.35 mN
Load/unload rate	1 mN/s
Numbers of load cycles	10
Unloading percentage	40%, 60%, 80%
Dwell period at maximum load	60 s
Dwell period at % unload	60 s

Figure 6.5 schematically shows the loading history for a dwell test, where unloading percentage refers to the value of $(minimum\ dwell\ load)/(maximum\ dwell\ load)$.

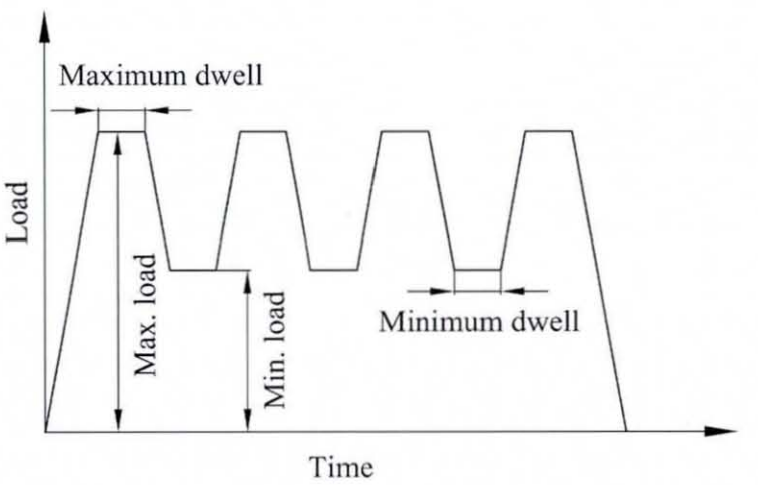

Figure 6.5: Schematic dwell load.

Typical results for unloading percentage at 40%, 60% and 80% are plotted in Figure 6.6, where the left vertical axis is for the deformation and the right is for the load force. The dashed black line is 60% unloading, the solid black line is the deformation for 60% unloading, the blue dotted line is the deformation for 40% unloading and the red dashed line is for 80% unloading. Taking the results cycled with 60% unloading as example, it can be seen that the deformation cycled with the load, although the deformation response in each dwell at maximum and percentage load was slightly different as illustrated in the figure. The maximum deformation was about 2660 nm at the end of the maximum load dwell in the sixth cycle, while the lowest deformation during unloading was at the end of the first cycle dwell and was about 2455 nm. The experiments with different unloading levels cycled in a similar way, although the cyclic change in deformation was higher for the 40% unload and smaller in the 80% unload.

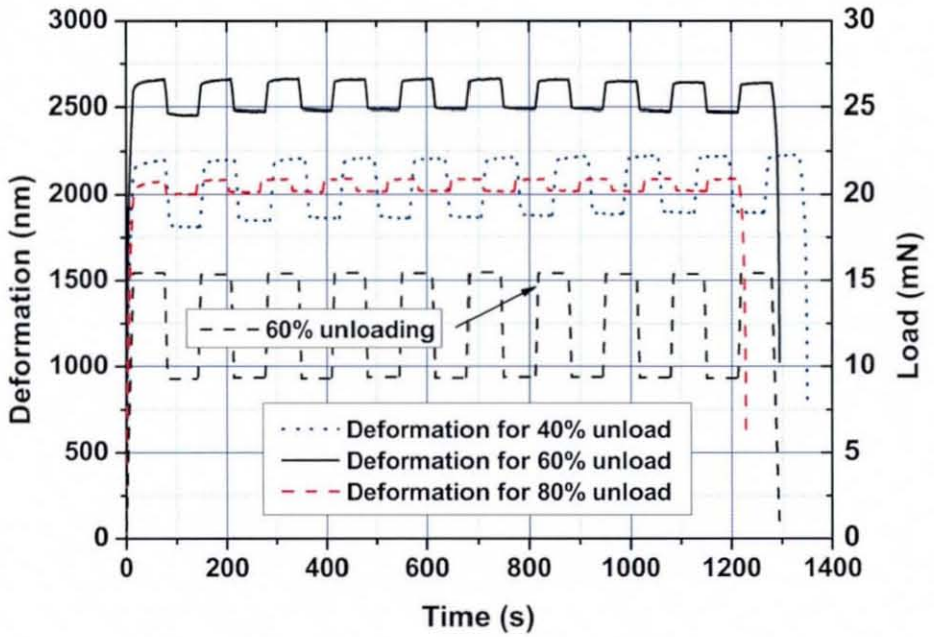

Figure 6.6: Results for load cycling to different unloading percentage.

The deformation during the maximum load dwell for the 10 cycles are plotted in Figure 6.7, for 60% unload, where the numbers indicate the cycle number of the maximum load dwell. The 9 cycles of deformation during the minimum dwell are plotted in Figure 6.8.

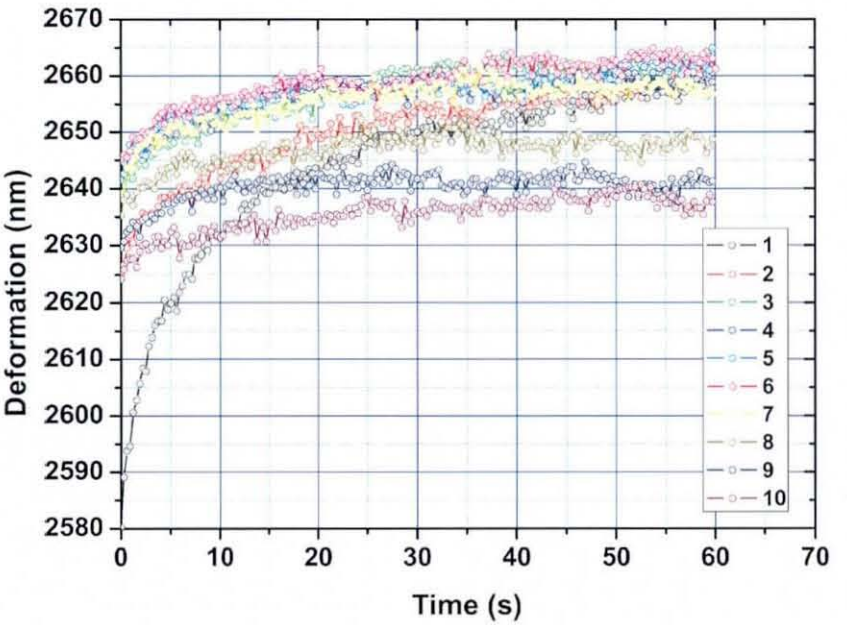

Figure 6.7: The 10 cycles of deformation during the maximum load dwell.

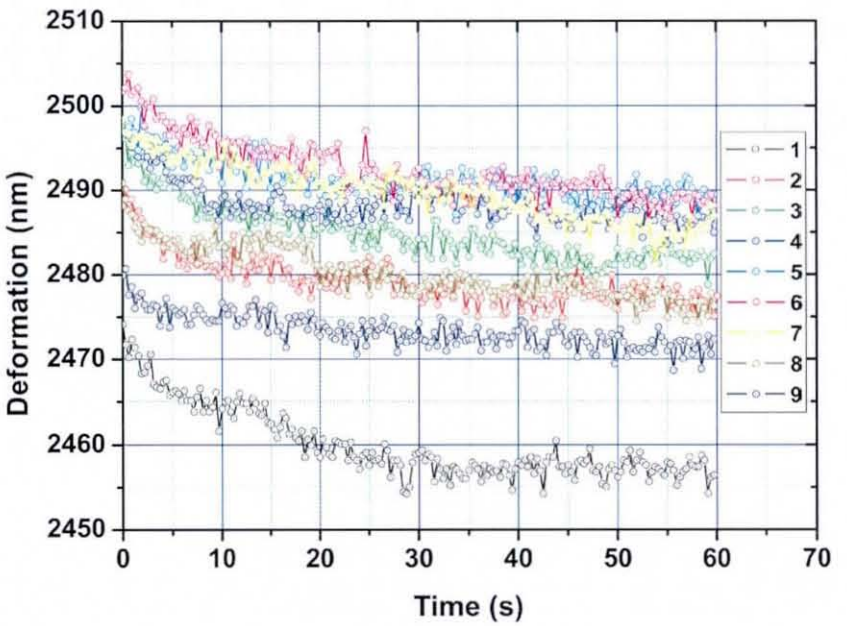

Figure 6.8: The 9 cycles of deformation during the minimum load dwell.

They show that the deformation increased during the maximum load dwell and decreased during the minimum load dwell. The largest differences in the dwell deformation were between the first cycles and the other cycles as shown in the figures. In the other word, the cycles except the first cycles were deformed almost in the same ways.

6.2.4 The Effects on the Mechanical Deformation of Particles of the Presence of Adhesive

In the bonding process for ACA assemblies, the particles are surrounded by liquid adhesive resin while being deformed between the bumps and pads. Therefore, it is important to understand whether the deformation of the particles is affected by the liquid adhesive, e.g. by its lubricating effect on contact between the particle and bump/pad or the deformation effect on the particle crush. In a real assembly process, both particles and resin will typically be heated and the adhesive viscosity will change rapidly with temperature due to cure. However, at this time the facilities are not ready for performing a high temperature test, although it is possible to deform the particles in liquid adhesive at room temperature. This has the advantage that the viscosity will not change significantly over the time of the experiment. Bis[glycidyloxphen]methane adhesive resin supplied by ALDRICH was used for this experiment. This kind of adhesive is the basic material in epoxy resin based ACA adhesives. It is a visco liquid at room temperature if not blended with hardeners. The molecular formula is $C_{19}H_{20}O_4$, and its chemical structure is shown in Figure 6.9. The viscosity of this material at 25 $^{\circ}C$ is 2000-3000 $mPa \cdot s$. In the experiments, the adhesive was spread in a thin layer on the microscope slide after the particles were coated on

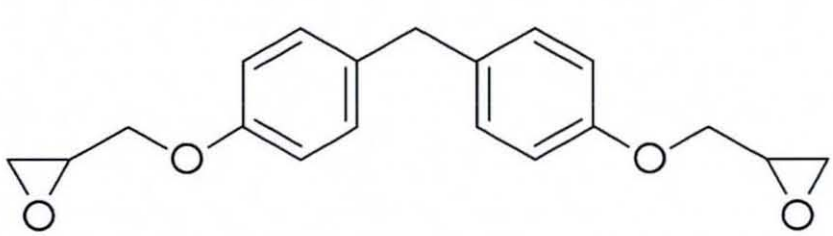

Figure 6.9: Resin chemical structure.

the surface using a small piece of glass. It was best to prepare the samples just before the experiment, since the adhesive was found to harden after a couple of hours if exposed to air.

In order to investigate the adhesives effects on the particle deformation, fifteen samples were tested, all at a temperature of 25 $^{\circ}C$. The experimental parameters are listed in Table 6.4. A successful experiment was considered to have occurred if the crush process was detected, therefore it was labelled as S if crushing was recorded in the experiment, otherwise it was labelled as F. Of the first four tests at a max force of 50 mN, three failed as no crush points was found in the results. This shows that the adhesive coated particles appear much stronger than those deformed dry i.e. without the adhesive coating as can be seen in Figure 6.4-b all samples without adhesive crushed at force less than 50 mN. Therefore, higher maximum load forces of 60 mN, and 80 mN were used in the subsequent experiments. Some further experiments were found to be unsuccessful due to no particle deformation being detected. Hence, the experiment results can be divided into three catalogues: seven successful tests, three unsuccessful tests including particle deformation but no crushing, and five unsuccessful tests due to failure to deform the particle.

Table 6.4: Parameters for the Adhesive Effects Experiments

Samples	*Load rate* (mN/s)	*Maximum force* (mN)	*Initial force* (μm)	*S or F*
$T-R01$	1	50	0.4	S
$T-R02$	1	50	0.4	F
$T-R03$	1	50	0.4	F
$T-R04$	1	50	0.4	F
$T-R05$	1	60	0.4	S
$T-R06$	1	80	0.4	S
$T-R07$	1	80	0.4	S
$T-R08$	1	80	0.4	F
$T-R09$	1	80	0.4	S
$T-R10$	1	80	0.4	F
$T-R11$	1	80	0.4	S
$T-R12$	1	80	0.4	F
$T-R13$	1	80	0.4	S
$T-R14$	1	80	0.4	F
$T-R15$	1	80	0.4	F
Note:	S:Experiment succeeded; F:Experiment failed.			

The results for the seven successful experiments are plotted in Figure 6.10. It can be seen from the figure that the crush forces were higher than for the dry experiments shown in Figure 6.4-b, although the profiles are similar. The highest crush point was about 60 mN. The deformation at the crushing point was also found to be bigger than the results without adhesive coating on the base stage. The three unsuccessful tests including particle deformation are plotted in Figure 6.11. It shows that the deformations were as opposed to be smooth, however no crushing can be seen. Figure 6.12 shows the other five unsuccessful experiments from the following nine tests. The green curve plotted is for indentation on the microscope slide directly without adhesive coating. Compared to the green curve, the five tests were similar, but much stiffer, with almost no plastic deformation during loading and unloading except for test B (the red plot), which is almost same shape as the green curve, although a higher load was applied. Three very similar results, C, D and E were acquired as shown in the inset figure in the figure. These results were believed to be caused by indentation on the adhesive coated microscope glass directly or indentation on the glass after missing the particle, because their load profiles were almost same as result A, blue plot in Figure 6.12, if not considering the initial force.

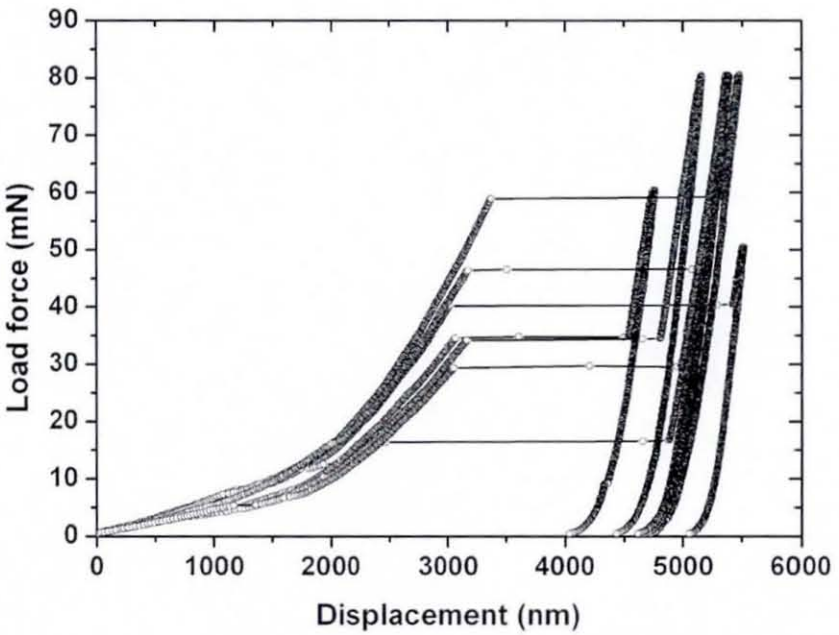

Figure 6.10: Mechanical deformation of particles within adhesive resin.

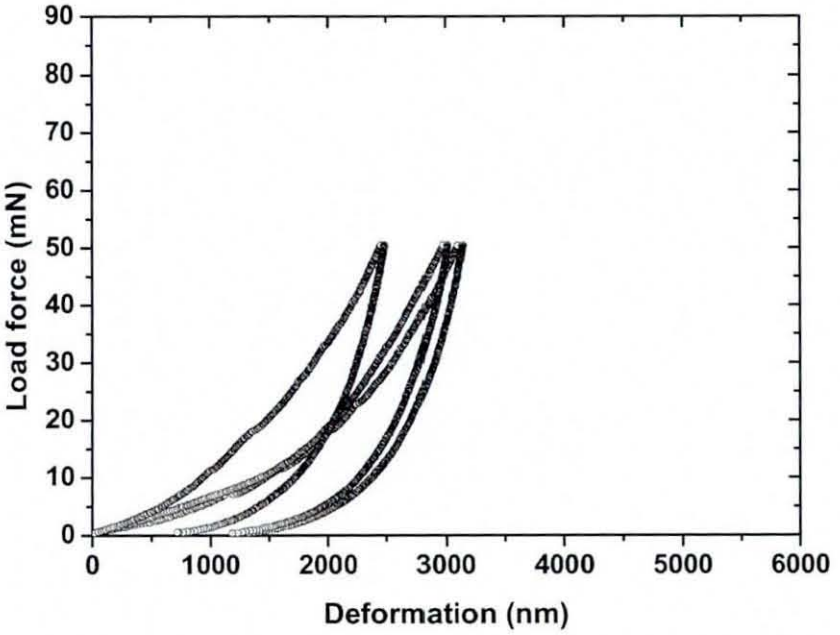

Figure 6.11: Unsuccessful particle deformation tests with adhesive.

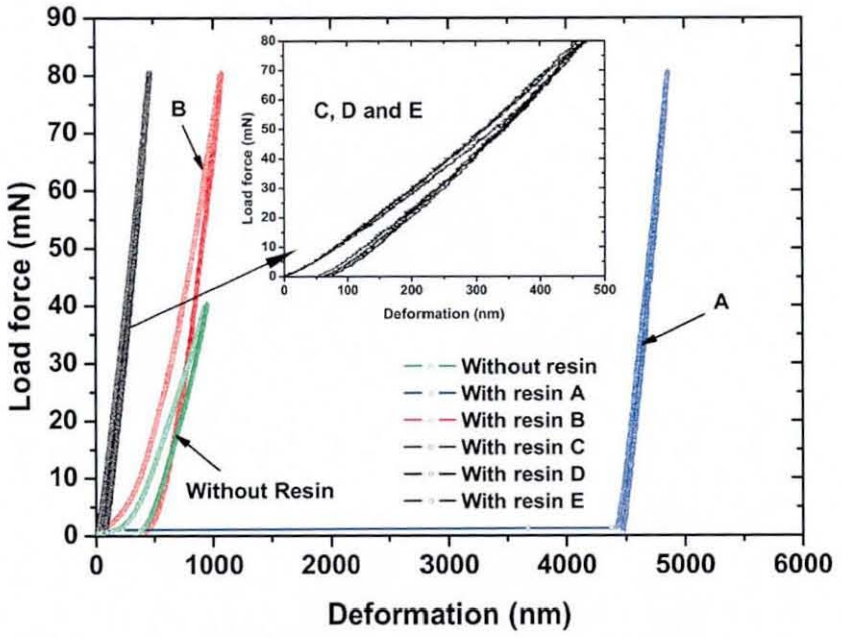

Figure 6.12: Unsuccessful tests without particle deformation.

For test A it is believed that the particle to be tested moved out from under the punch tip after the initial force was reached as the punch moved forward against the glass base stage, and consequently the punch then moved quickly by about 4.5 μm to indent on the glass in the adhesive. Experiments C, D, and E could be the same process as experiment A, however the nano-indenter machine failed to record the particle moving from under the punch tip since it moved before the load reached the initial load force of 0.4 mN.

6.2.5 Mechanical Deformation of Multiple ACA Particles

Mechanical deformation of multiple ACA particles was carried out in this study to compare the mechanical deformation of individual and multiple particles. In order to catch more than one particle using the HSS punch, the smaller Type I particles were used in this experiment and one particle, two, three and four particles were tested. The experiments are listed in Table 6.5. A maximum load of 20 mN was used in the one particle test, 50 mN was used in the experiments on two and three particles, and 60 mN was used in the four particle experiments. The experiments were quite successful except the two particles experiments, in which, two tests failed.

Table 6.5: Experimental Parameters for Multiple Particle Deformation Experiments

No. of particles	*Load rate* (mN/s)	*Maximum force* (mN)	*Intitial force* (mN)	*No. of tests*	*No. of failed tests*
1	0.5	20	0.35	5	0
2	0.5	50	0.35	5	2
3	0.5	50	0.35	5	0
4	0.5	60	0.35	5	0
Note:	Same HSS punch was used; the load was total load on particles				

In order to compare the deformation of multiple particles with the deformation of individual particles, five experiments were firstly completed for the mechanical deformation of one particle and the results are plotted in Figure 6.13. It can be seen that the particles were crushed when the deformation was between 1700 nm and 2000 nm, that is between 42% and 50% of the original particle size, and the crush load force was smaller than 10 mN in all of the experiments.

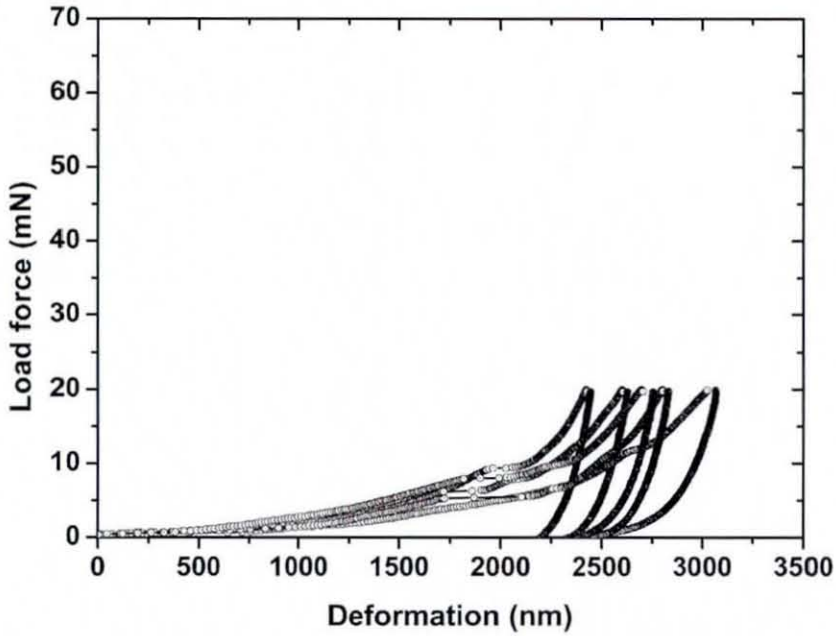

Figure 6.13: Deformation of one particle.

Compared to individual particles found in the one particle experiments, multiple particles, i.e. two particles or more, were rarer to be found on the microscope slide close enough together to fall under the punch tip, but separated from other particles sufficiently that there was no risk of the punch inadvertently pressing on additional particles. Therefore, it took significant time to find a suitable group of particles. In the five experiments on two particles, two tests were considered to have failed, as shown in Figure 6.14. In the inset figure, it can been that the profiles of the two failed tests were similar to the curves for single particle deformation shown in Figure 6.13. Therefore, the failure was considered to be caused by only one particle being deformed due to one particle sliding out from under the punch tip. The other three results were believed to be the deformation of two particles together. Compared to the single particle deformation, it can be been that crushing occurred at a higher load force and were not as distinct as in the single particle deformation.

The experimental processes for three particles were similar to two particle deformation. The difference was the need to find three particles close together in a triangular pattern, instead of two particles side by side, to minimise the risk of particles from pushing out from under the punch during deformation. The results for

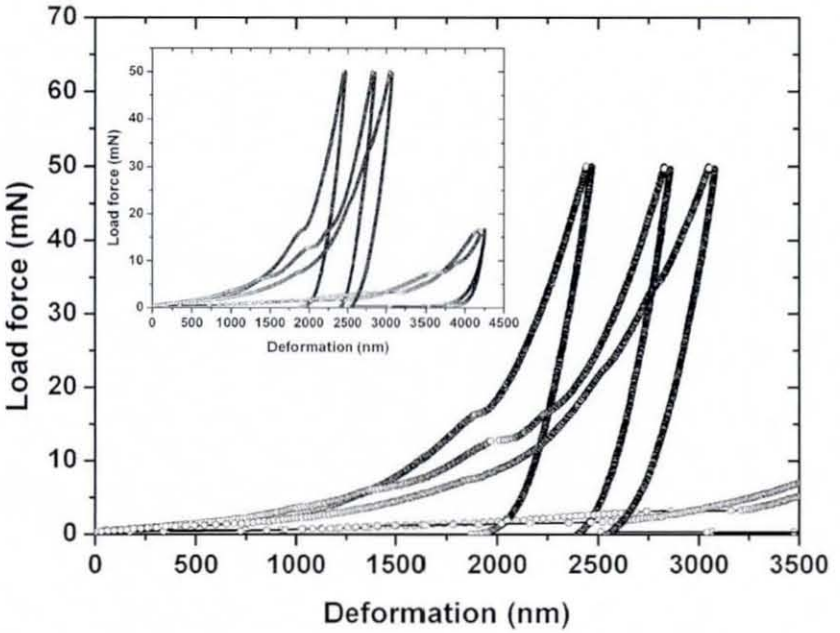

Figure 6.14: Deformation of two particles.

three particle deformation are shown in Figure 6.15. All five three particle deformation experiments succeeded. Compared to the one and two particle deformation, the crushes occurred at a much higher load force and the curve shapes were similar to those for the two particle deformation. The highest crush force in the plot is about 25 mN when the deformation was more than 2000 nm, 50% the original particle size. This suggested that both a higher load force and a deeper deformation were needed to crush particles if more particles were caught and deformed in the multiple particle experiments, however it may be an effect of scatter in the particle size.

For the four particle deformation experiments, four particles in a quadrilateral pattern were selected, and the deformation centre was pointed at the centre of the quadrilateral. All five tests were successful and the results are plotted in Figure 6.16. The curves are similar to the results for the three particle deformation except that the crush points are even less distinct, as shown in Figure 6.15.

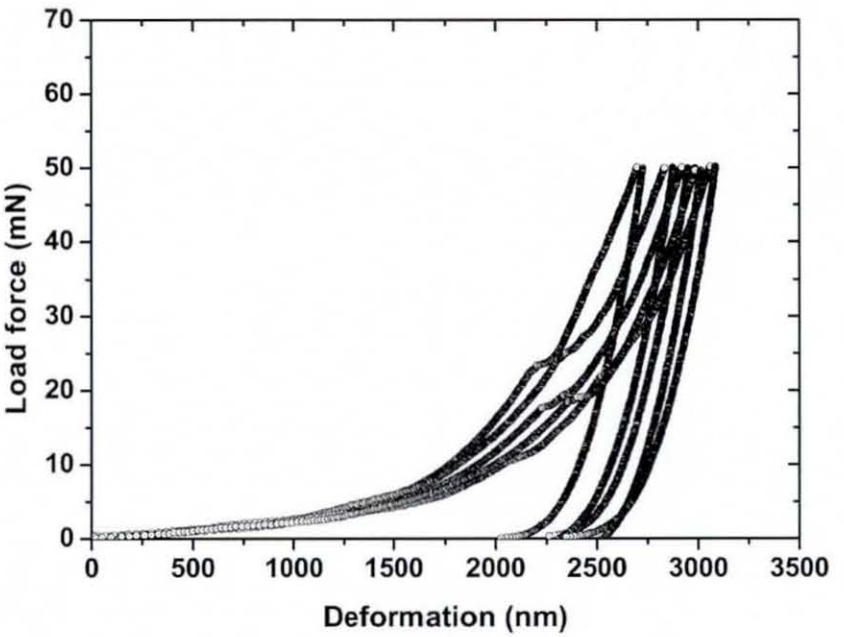

Figure 6.15: Deformation of three particles.

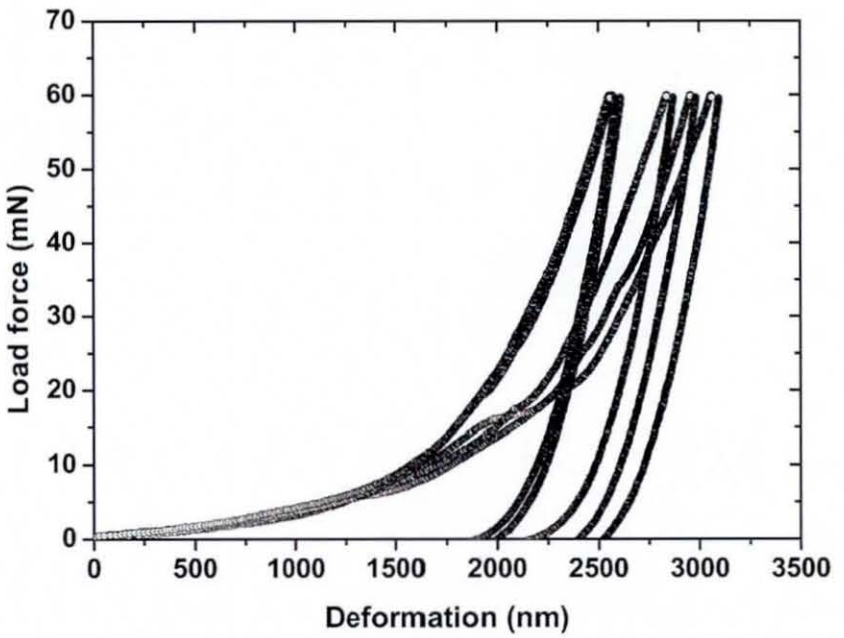

Figure 6.16: Deformation of four particles.

In conclusion, the test results show that the deformation behaviours of the multiple particle deformation were different. For each experiment, the load curves vary significantly in terms of both the load and displacement at which crushing occurs. The stiffness per particle also varied for higher deformations, particularly in the four particle experiments. Typical loading and unloading curves for multiple particles tests are shown in Figure 6.17, which compares the different experiments where the results selected are for where the deformation is near to the mean value for the respective multiple particle experiment and the load force is divided by the particle numbers. The results for the two particle experiments were not plotted in the figure due to the inconsistent results acquired. It can be seen that for higher numbers of particles, the greater the deformation before the particles were crushed. In addition, the crushing became less abrupt as the number of particles deformed increased, and particularly in the four particle experiments, the crushing was very indistinct.

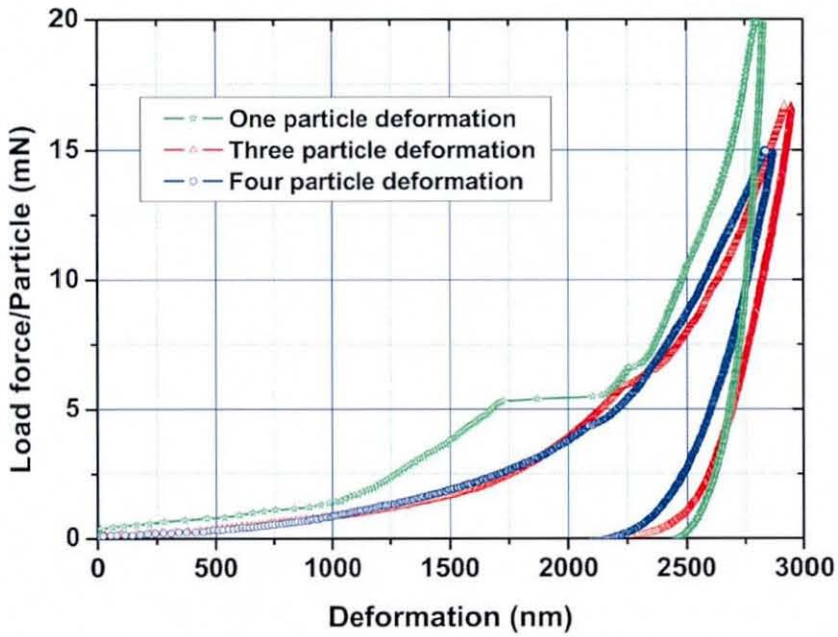

Figure 6.17: Results for multiple ACA particle deformation experiments.

6.3 Results of Electrical Tests

6.3.1 Typical Electrical Resistance of an Individual Particle Undergoing Deformation

In this experiment, a W/Cu punch and HSS punch, the brass base stage, and the Agilent data logger, were used as described in the previous chapter and the electrical configuration of these tests was also as described in that chapter. In order to establish the typical electrical resistance of individual ACA particles undergoing deformation, five tests were performed. The load force versus time for the tests is shown in Figure 6.18. It can be seen that the load and unload rate was 1 mN/s, the maximum load force was 60 mN, and the dwell time was at the max force 5 s.

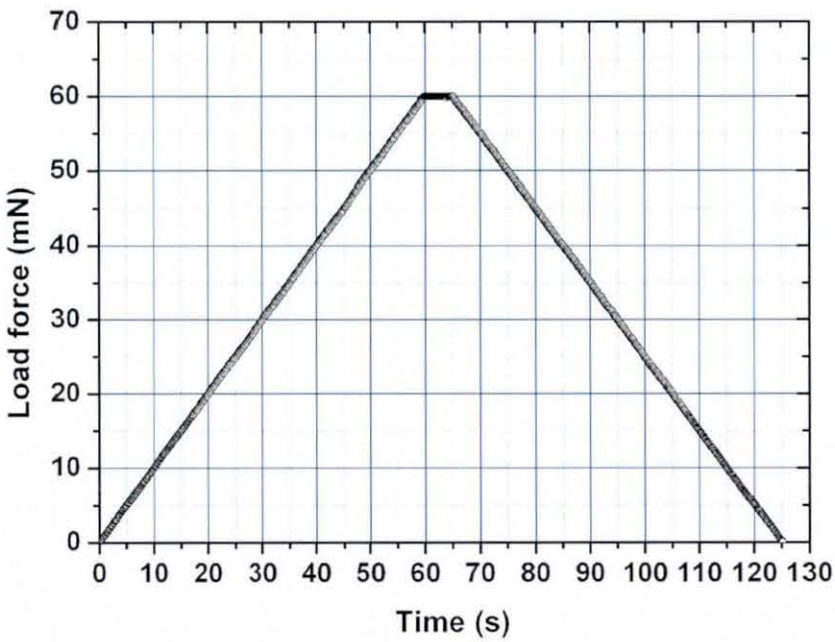

Figure 6.18: Load cycle for electrical tests.

In order to provide a detailed understanding of the electrical test results, one test is selected as an example to be presented in detail. The load force versus deformation is shown in Figure 6.19, where the mechanical deformation is similar to the results measured in the mechanical deformation experiment although W/Cu punch was used to achieve the electrical test. It can be seen that the particle started to crush when the deformation reached about 2750 nm, i.e. 48% of the original particle size. There

appears to have been another small crushing event or perhaps initiation of cracks when the load force was about 45 mN and the deformation was about 2600 nm, where the 'crushing deformation' was about 125 nm, much smaller than typical crushing deformations of about 1000 nm. It was found generally in the electrical experiments that the deformation process included a main crushing deformation with or without evidence of smaller crushing or cracking events detected from the load curve. This is similar to a typical mechanical deformation experiments on individual ACA particles.

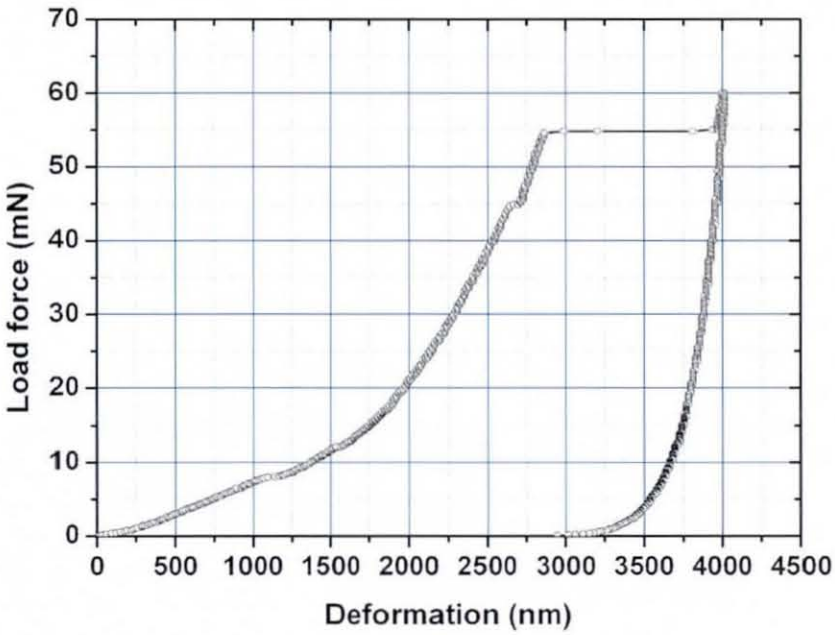

Figure 6.19: Load force versus deformation for an electrical test.

The results of the deformation versus time and the resistance versus time results are plotted in Figure 6.20, where the left vertical axis is for the deformation and the right axis indicates the joint resistance of the test particle. It can be seen that up to 55 s the particle deformation increased in a non-linear way with time whilst the joint resistance reduced. The small jump in the deformation visible in Figure 6.19 can be seen to have occurred when the time was about 45 s, and clearly there was no effect on the joint resistance when this small jump happened. However, an abrupt increase in the joint resistance occurred when the time reached about 55 s. This abrupt increase in the joint resistance was due to the particle crushing, where

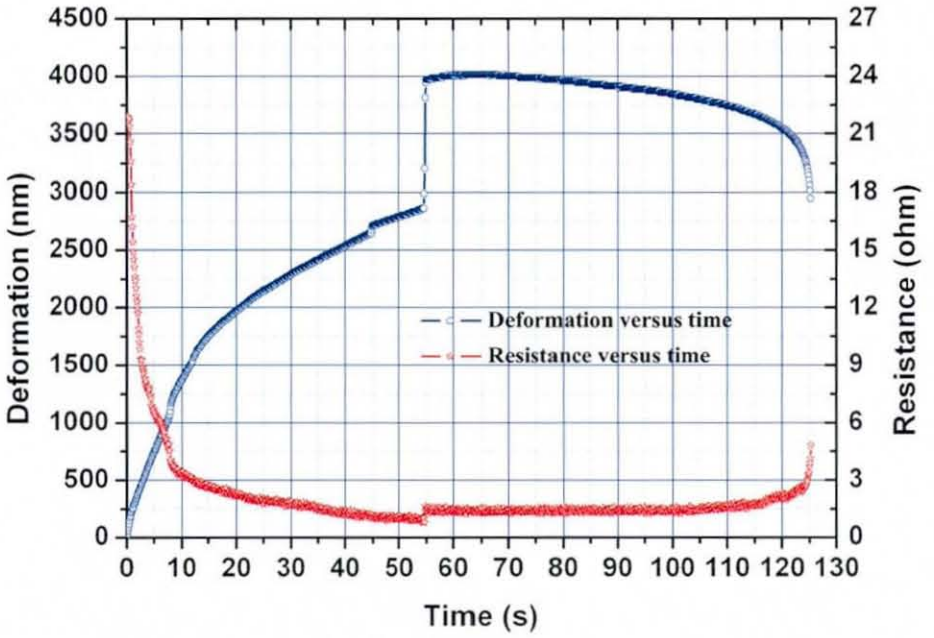

Figure 6.20: Deformation and joint resistance versus time.

the pressure between the metal base stage/punch surfaces and the deformed particle was released suddenly. The deformation reached its highest level when the load was at its maximum 60 mN, no joint resistance variation was observed during the 5 s dwell at maximum load. In the unloading process, commencing at 65 s, the particle deformation reduced as the time increased and the joint resistance increased at fairly low rate until the final stage of the unloading process.

The resistance versus deformation is shown in Figure 6.21. It can be seen that the joint resistance reduced as the deformation increased until the lowest resistance was measured when the deformation was about 2750 nm, the crush point as shown in Figure 6.19, after which the joint resistance increased slightly during the crushing deformation. The joint resistance then increased gradually during unloading.

The results of the five electrical tests are shown in Figure 6.22, where test 2 was the one selected as the typical result shown above. These results are from the point of first contact up to the deformation at the crush point or the maximum load if no crushing was detected. It can be seen that generally similar resistance versus deformation behaviour was measured, although the start points and the end points were different.

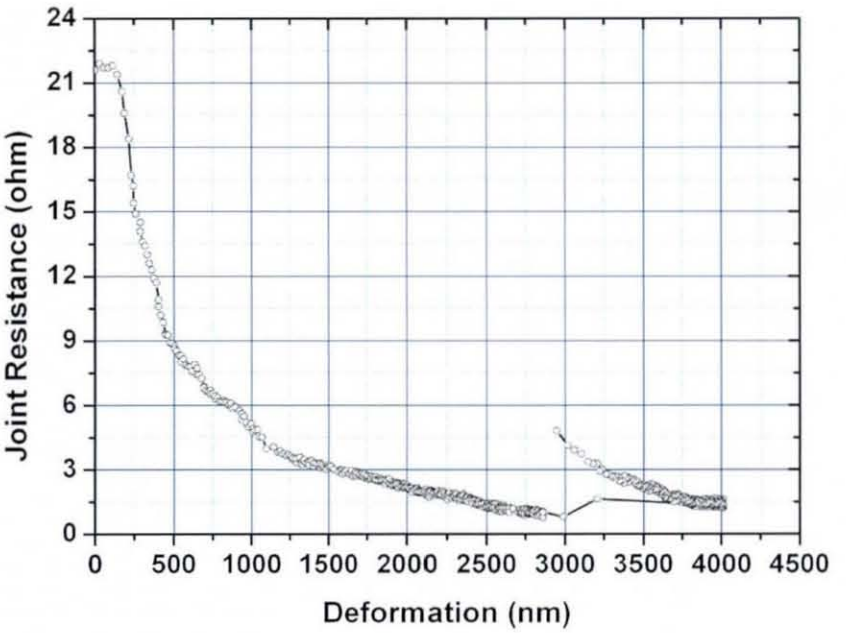

Figure 6.21: Joint resistance versus deformation.

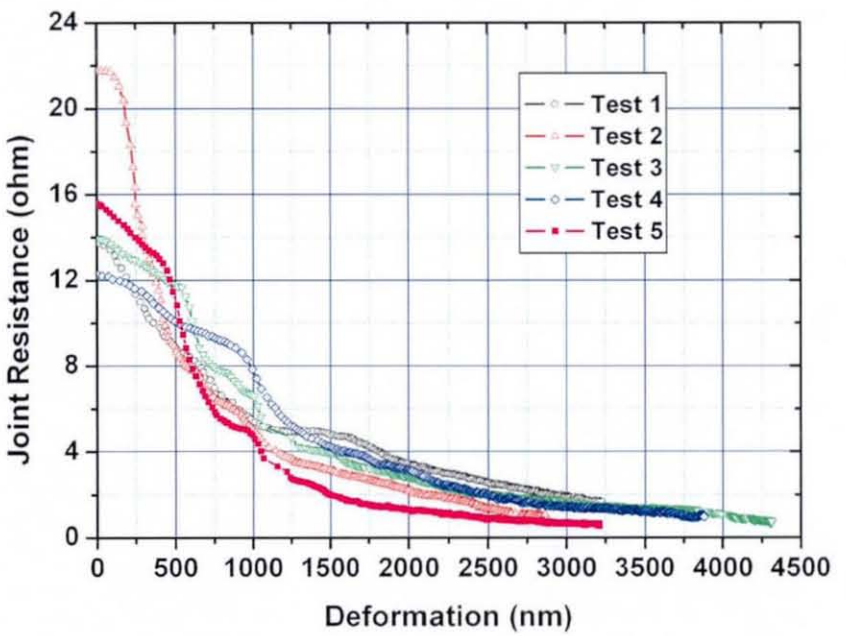

Figure 6.22: Five electrical results of electrical tests.

6.3.2 Electrical Results for Different Punches

In order to have a comparison between the punch material effects on the electrical performance of a single ACA joint. Tests using HSS punch were also performed, the typical results are plotted in Figure 6.23, where the left vertical axis is for the deformation and the right vertical axis is for the joint resistance. It was found that the joint resistance recorded in the deformation, as shown in the figure, was not as consistent as that using the W/Cu punch, as shown in Figure 6.20, at load rates of 1 mN/s. It is believed this is because the conductivity of HSS is not as good as W/Cu and also the polished surface of the HSS punch was much smoother than the W/Cu punch as shown in Figures 5.6 and Figure 5.7, resulting in a higher contact resistance. The relative rough W/Cu punch tip is considered better than the HSS one, because the small points on the rough surface can break the oxide layers more easily, thereby reducing the contact resistance.

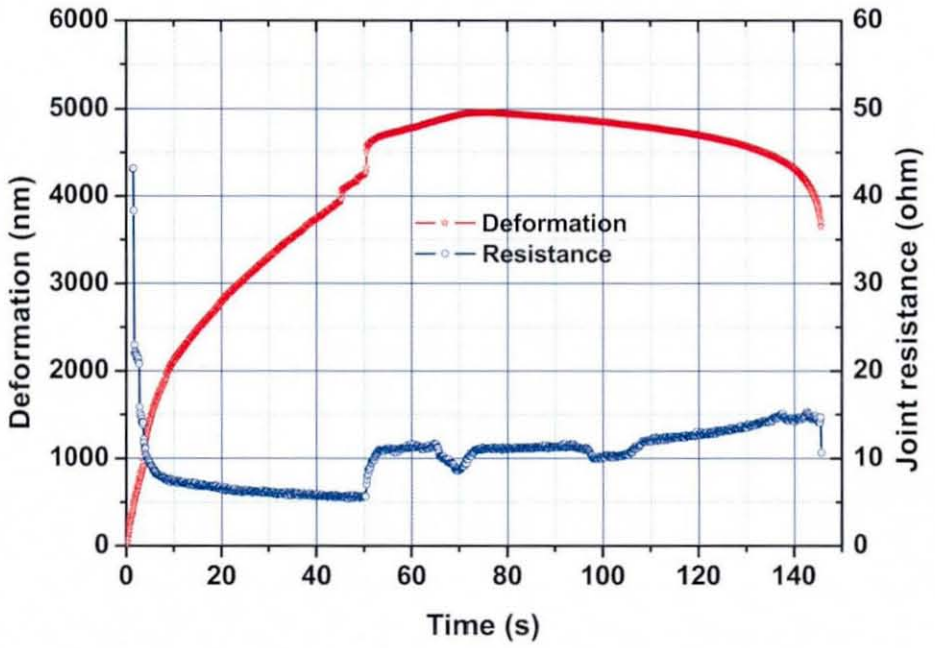

Figure 6.23: Joint resistance versus deformation at a load rate of 1 mN/s.

The joint resistance recorded using the HSS punch was found to be affected by the load rates. Therefore, two kinds of experiments were conducted to compare between the electrical results when the particles were undergoing deformation at load rates of 2 mN/s, and 0.5 mN/s and the results measured at load rates of 1 mN/s. In the tests,

the initial load was 0.35 mN, dwell time was 5 s, and the maximum load was 70 mN. The typical results are selected and plotted in Figure 6.24, where the left vertical axis is for the deformation and the right vertical axis is for the joint resistance. In Figure 6.24-a, the initial joint resistance varied around 40 Ω, and then jumped to about 10 Ω when the load time was about 10 s and the deformation was about 3300 nm. It is believed that some initial deformation was needed to acquire a good stationary contact between the punch and the particle, and between the particle and the base stage in load rates of 2 mN/s, possibly due to the need to penetrate on oxide film on the punch. After the sudden drop in contact resistance it remained stable as the load increased further. The situation was better for a 1 mN/s load rate, as shown in Figure 6.23, however there was still a sudden resistance drop, from more than 40 Ω to about 15 Ω, during the initial deformation stage. More stable joint resistances were recorded when a 0.5 mN/s load rate was used, as shown in Figure 6.24-b. No obvious sudden drop in resistance was found during the deformation before crushing at 4000 nm. The result was similar to the one shown in Figure 6.20 obtained using the W/Cu punch, but the joint resistance at 40% of deformation was about 7.5 Ω, much bigger compared than the 1.5 Ω achieved with the W/Cu punch.

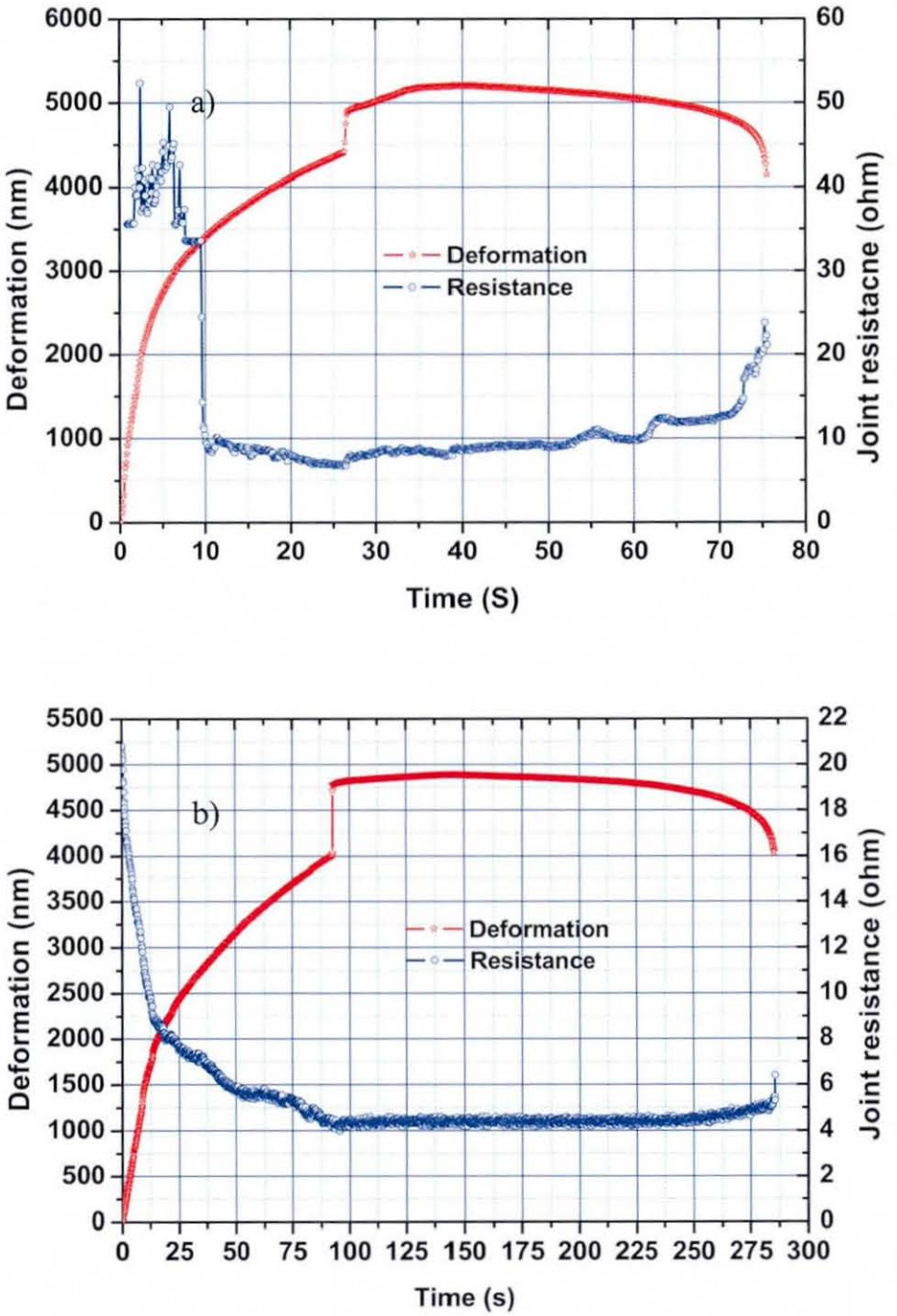

Figure 6.24: Joint resistance versus deformation at a load rate of a) 2 mN/s and b) 0.5 mN/s.

It can be seen that low load rate was needed to achieve consistent joint resistance in the deformation if the HSS punch was used. Therefore, five tests at a load rate of 0.5 mN/s using the HSS punch, as plotted in Figure 6.25, were selected to compare with the tests measured using W/Cu punch. In the figure, Test 2 is the typical result selected earlier. The electrical test results shown in the figure are similar to those for the W/Cu punch in Figure 6.22 except that the joint resistances measured using the HSS punch were higher than those for the W/Cu punch. Some vibrations were found in the tests as shown in Figure 6.25. One thing can be noted in these two tests is that not every test was found to have a distinct crushing event unlike these identifiable in the deformation versus time plots in Figure 6.20 and Figure 6.24-b. The absence of crushing is believed to be because the brass base stage was used instead of glass. The brass is much softer than glass, and the particles can indent into the base to some degree which in some cases may have prevented the stress from concentrating in the deformed particle to as high as that induced in the particles deformed on a glass base stage, thereby preventing them from crushing. This can also be used to explain the short cushing as shown in Figures 6.23 and 6.24-a, where crushing was found to start from about 4200 nm deformation and continued for about 500 nm, shorter than those deformed in the mechanical deformation experiments.

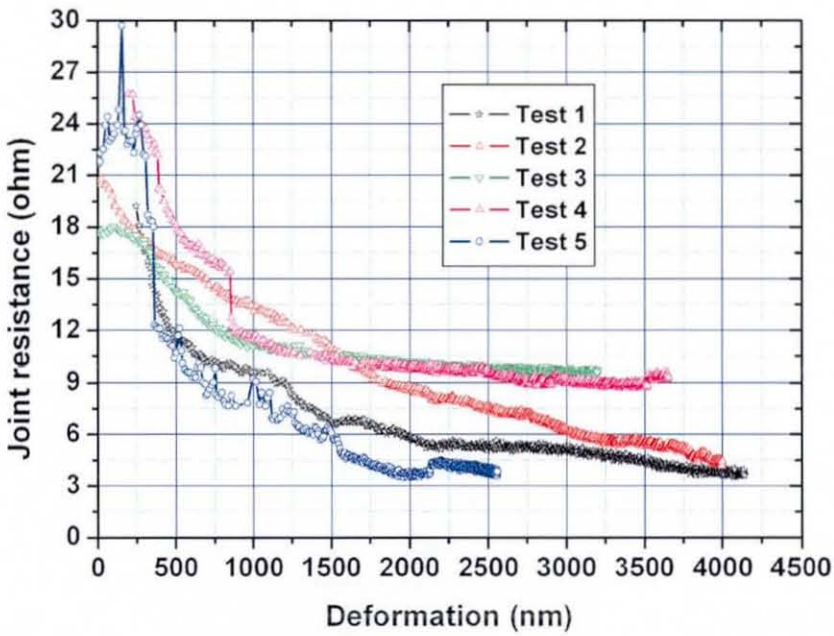

Figure 6.25: Five electrical test results using the HSS punch at 0.5 mN/s.

6.3.3 Resistance Stability Tests on Individual ACA Particles

When electronic components are assembled using an ACA, the conductor particles are deformed to a certain degree during the thermal bonding and then held between the bumps and pads by the cured adhesive. Additional shrinkage induced forces may also be induced by the curing of the adhesive during bonding. Therefore, it is very important to know if the electrical contacts are stable or not in an ACA joint. Experiments on the stability of the resistance of individual ACA particles were therefore designed and carried out by using an extended dwell time at maximum load. The experimental parameters are listed in Table 6.6.

Table 6.6: Experimental Parameters for the Resistance Stability Tests

Tests NO./ID	*Load rate* (mN/s)	*Maximum force* (mN)	*Initial force* (mN)	*Dwell* (s)	*S or F*
$ST-01$	0.5	10	0.3	60	S
$ST-02$	0.5	10	0.3	60	S
$ST-03$	2	10	0.3	60	S
$ST-04$	2	10	0.3	60	S
$ST-05$	1	10	0.3	60	F
$ST-06$	1	10	0.3	60	F
Note:	S:Experiment succeeded; F:Experiment failed.				

The W/Cu punch was used in the tests. The tests at load rates of 2 and 0.5 mN/s were succeed, however the tests at 1 mN/s were considered failed. There was no resistance recorded in ST-05, and there was crush event found in ST-06. Therefore, ST-05 was not presented. A typical result, ST-03, is selected to detail how the test worked in this study. The load force versus deformation for this test is shown in Figure 6.26, where the dwell started when the deformation was about 1600 nm and ended when the deformation was about 1700 nm, i.e. around 30% of the particle size. That is, further deformation occurred during the dwell period, and the deformation continued from reaching the maximum load time 5 s to 30 s, and then almost no more deformation was detected in the following dwell as the deformation versus time curve shown in Figure 6.27, where the left vertical line is for the deformation and the right line is for the joint resistance. However, almost no variation in the joint resistance was found during the dwell except in the first and last 5 s as shown in Figure 6.27.

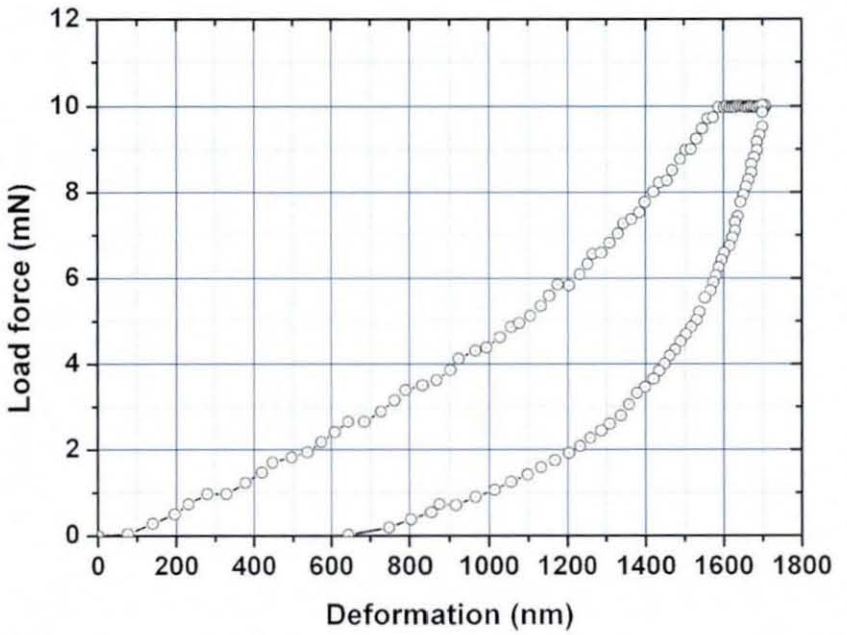

Figure 6.26: Load force versus deformation in electrical stability test.

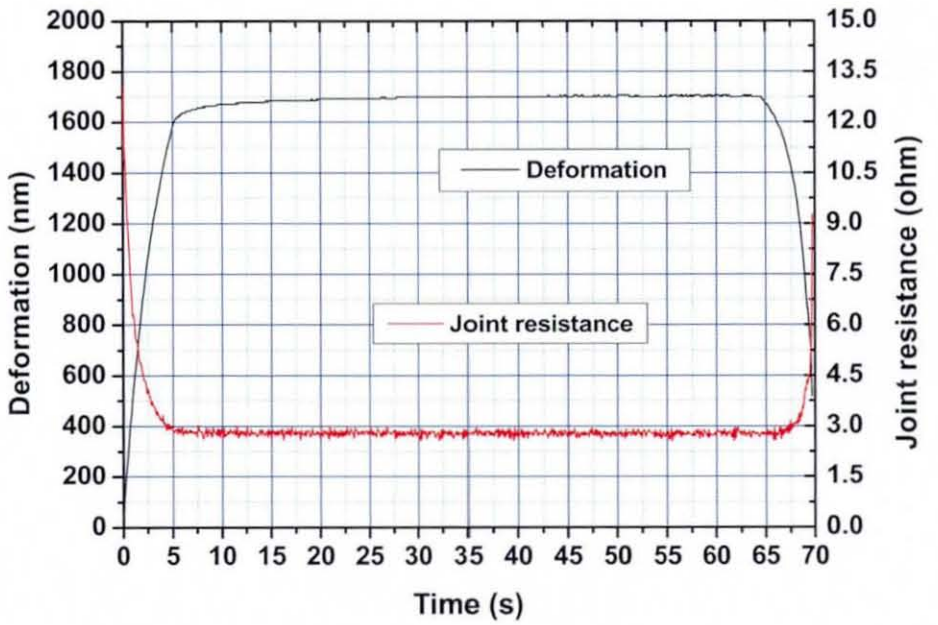

Figure 6.27: Joint resistance and deformation versus time.

These results indicate that the joint resistance was stable after no more deformation occurred in the dwell period, but the joint resistance does increase if the holding load is released, as shown for the unloading stage in the figure.

The successful and ST06 results for the experiments listed in Table 6.6 are plotted in Figure 6.28. The results show that the joint resistances were different when different load rates were used. Stable joint resistances were found during the dwell for all of the four successful experiments, but lower joint resistances were found in the high load rate tests (2 mN/s) than in those at a low load rate (0.5 mN/s).

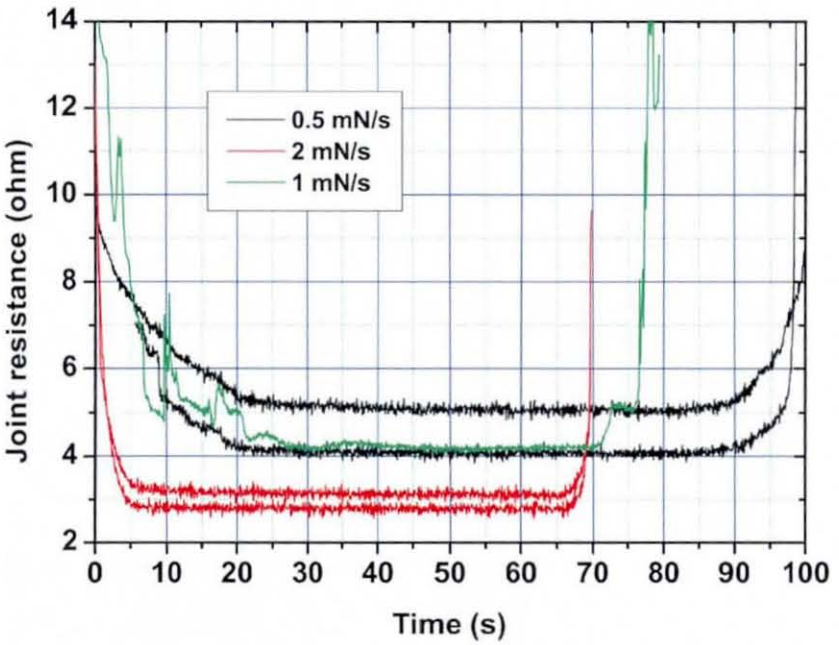

Figure 6.28: Joint resistance versus time.

6.3.4 Voltage and Current Properties of a Deformed ACA Particle

Voltage versus current (V/I) measurements on a deformed ACA particle were conducted in this research to study the V/I properties of individual ACA joints. A W/Cu punch, polished brass base stage and Type II particles were used in this study. A DATA PRECISION-8200 current source was used to supply the current and the Agilent data logger was used to monitor the experiment process. The experimental

setup is listed in Table 6.7.

Table 6.7: Experimental Parameters for V/I Experiments

Parameter	*Unit*	*Value*
Load rate	(mN/s)	1
Maximum load	(mN)	35
Initial force	(mN)	0.35
Dwell time	(s)	600
Start time	(s)	128
End time	(s)	438
Note:	The time of the first indenter record is 0	

The experimental procedure was that the particle was deformed up to maximum load 35 mN at a load rate of 1 mN/s, and then dwelled for 10 minutes, as shown in Figure 6.29. More deformation and some crushing events are found in the initial dwell as shown in the figure. The V/I measurement was performed during that part of the dwell between the two red vertical lines, from about 128 s to 440 s. The current, I, was applied using the current source and was manually switched in steps of 0.1 mA, approximately every 10 seconds from 0.1 mA to 1.6 mA, and then back to 0.1 mA,

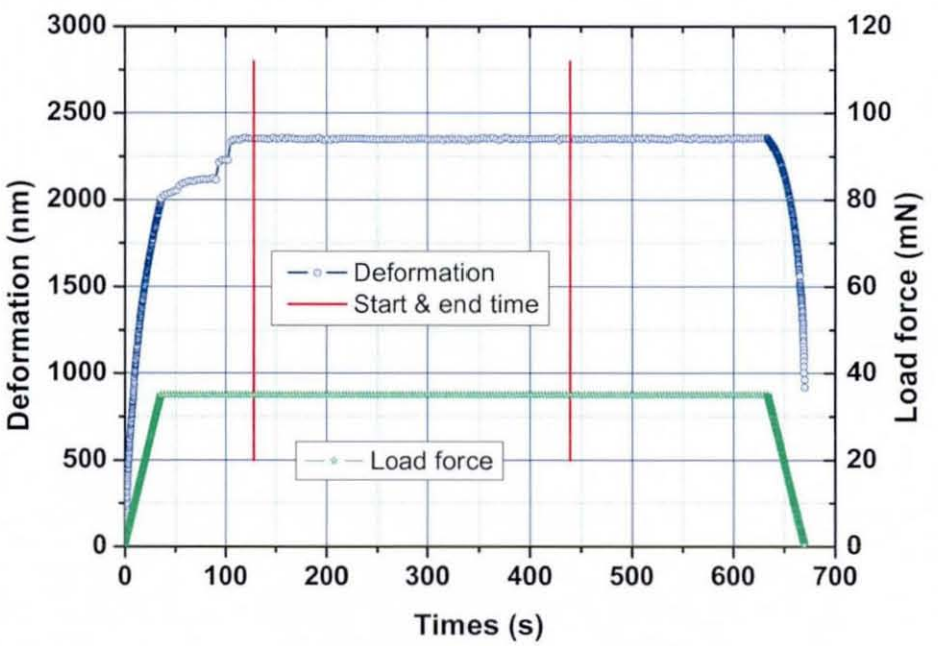

Figure 6.29: Deformation and load force versus time of V/I test.

as shown in Figure 6.30, which is plotted from data recorded by the data acquisition. The voltage as recorded by another channel of the data logger is shown in Figure 6.31. Compared to the applied current, there were significant random fluctuations in the measured voltage, which is believed to be due to noise picked up by the data acquisition system.

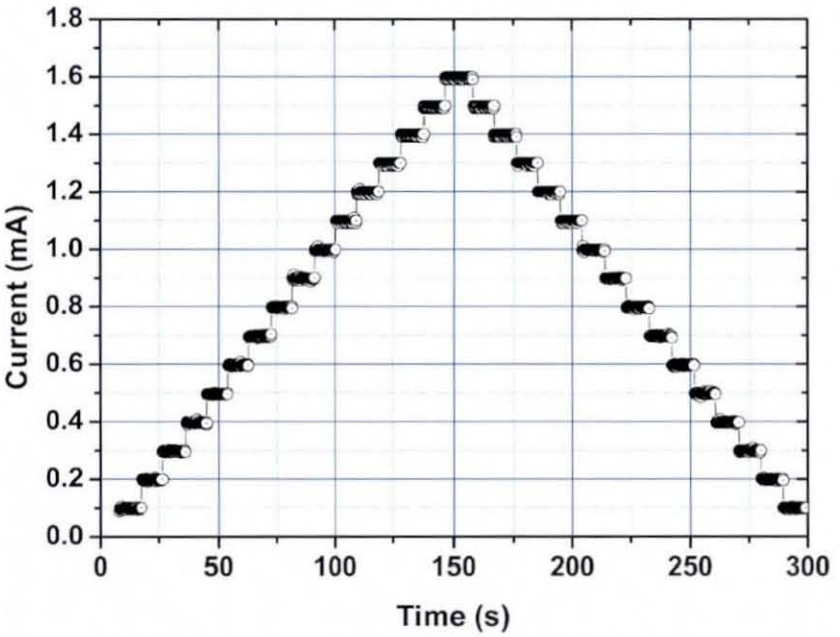

Figure 6.30: Current versus time.

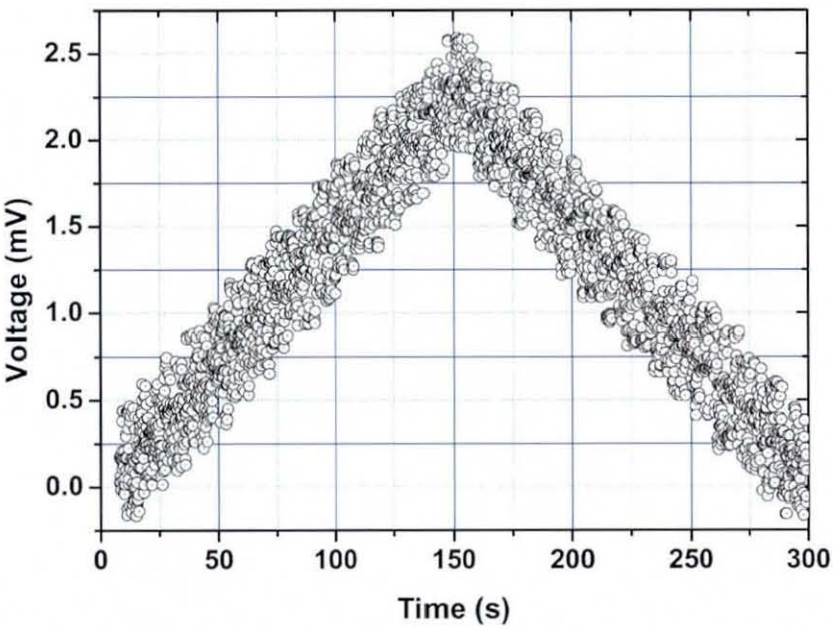

Figure 6.31: Voltage versus time.

Chapter 7

Analysis and Discussion of the Particle Deformation Results

7.1 Introduction

In this chapter, the particle deformation results as presented in Chapter 6 are analysed and discussed. In order to interpret and analyse the experimental results, mathematical and statistical methods are used and the discussion is illustrated in formulas or figures.

The analysis and discussion of the mechanical deformation of individual particles are presented firstly, including the strain versus stress analysis, load rate effects, visco-elastic deformation, and the effects of the presence of adhesive on the particle deformation. Then the mechanical deformation of multiple ACA particles is discussed.

Next, the typical electrical resistance of a single particle undergoing deformation is discussed, followed by the analysis and discussion of the resistance stability tests, the resistance tests with different punch materials, and the V/I behaviour tests.

At the end, the merits of the experimental results are summarized.

7.2 Mechanical Deformation of ACA Particles

The results of the loading and unloading experiments for single ACA particles suggest that the effects of the test parameters on the particle deformation is complex. This complex behaviour is believed to be a function of the size of the particles, their spherical geometry, and their materials. The particles are small, and the surface roughness

of the stage, the punch and the particles may have been large enough to affect the deformation process. Deformation of a ball is complex, since the strain is localized in very small areas of the particle when the compression starts, then the materials near the contact point begin to deform. Finally, the presence of the metal layers also increased the complexity. During deformation, perhaps the metal layers firstly stretch, then cracks initiate and grow in the metal layers, followed by the initiation and growth of cracks in the polymer, and finally the crushing of the particle. Simultaneously, plastic deformation occurs throughout the whole deformation process. Furthermore, the polymer materials used in the particle core have a visco-elastic nature [23], where the local strain rate (which is dependant on how fast the machine changes the deformation of the particle) is important. These effects are a combination of geometrical non-linearity (large displacements and structural contact), and material non-linearity (visco-elasticity, plasticity, fracture and hardening/softening properties of the polymer core during deformation). A typical particle stiffness variation with displacement curve is shown in Figure 7.1, where the slope of the load versus deformation curve indicates the particle stiffness at that deformation.

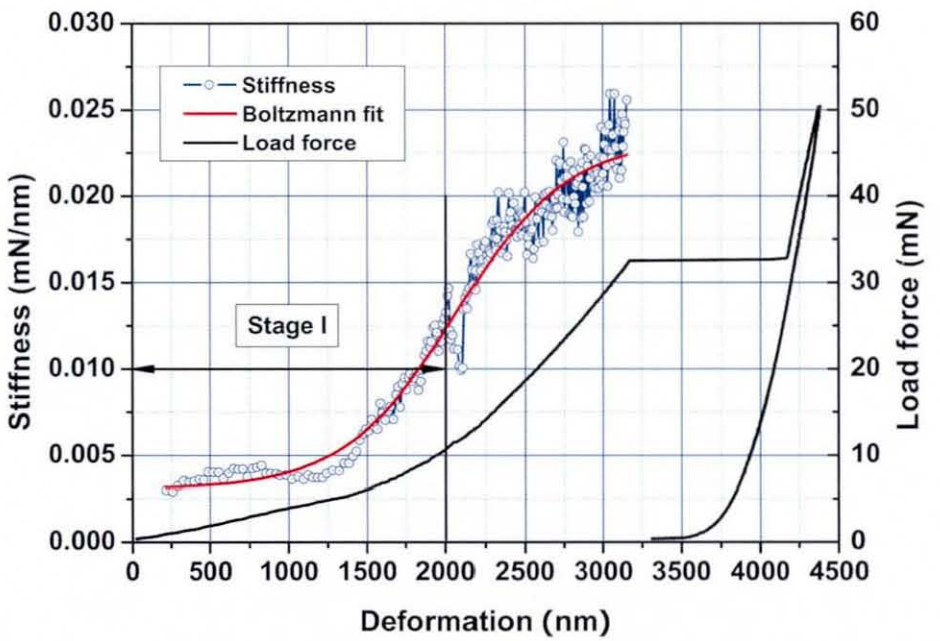

Figure 7.1: Stiffness of a typical ACA particle undergoing deformation.

This particle stiffness was calculated as a moving average over 7 data points in order to reduce short term fluctuations due to measurement noise. It can be seen that the stiffness increased as the deformation increased, but that at high levels of deformation the rate of increase dropped, indicating that changes in the material behaviour were starting to take place before crushing occurred.

A typical mechanical deformation of an individual ACA particle can be helpfully considered as occurring in four stages, as shown in Figure 7.2.

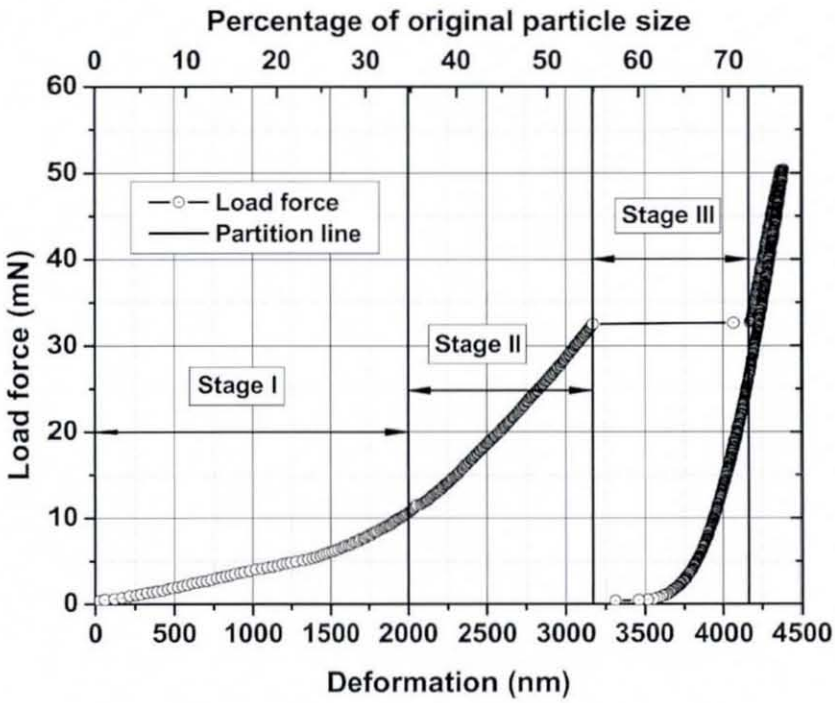

Figure 7.2: Stages of particle deformation.

Stage I (initial deformation): Initially the deformation is approximately proportional to the load force applied until the deformation degree reached approximately 25%. Then the particle stiffness was rising well before a deformation of 2000 nm, 35% of the original particle size, as shown in Figure 7.1, because the initial deformation started from a point, and then the point increased into a circular area and grew larger and larger as the load force increased, but was still small compared to the particle diameter. It can be concluded that the deformation was mainly concentrated in the contact area in this step.

Stage II (further deformation): This stage started at about 35% particle deformation, and continued until it reached about 55%. The stiffness increased significantly during this stage as shown in Figure 7.2, since the deformed contact area became larger compared to the particle. Therefore, the shape of the deformed particle became more like a deformed cylinder, rather than a sphere. However, the rate of increase in stiffness was getting smaller before the particle was crushed as shown in Figure 7.1. This is believed to be because small cracks initiated in the polymer before crushing.

Stage III (crushing): In this stage the deformation rapidly increased from about 55% to around 72%. The very low stiffness during this stage of deformation suggested that the particle was crushing in this step.

Stage IV (post crushing): In this stage, the load ramped up until the load reached the maximum force (50 mN), followed by the unloading process as shown in the figure. The particle had been crushed thoroughly, and the particle remains were very stiff and had almost no further plastic deformation as the unloading data shows. The unloading process is similar to the unloading of the indentation directly on glass, as was shown in Figure 6.2.

It was found that the particles were crushed after the experiment, as shown in Figures 7.3 and 7.4. Figure 7.3 shows five crushed particles imaged by SEM. It can be seen that the crushed particles had a similar pattern, however only the second one from the left clearly showed almost all of the crushed particle remains, while the others only showed some pieces of the crushed particles. It is believed that some crushed parts dropped from the base stage after the punch was removed from the deformed particles. A detailed image of the second from the left crushed particle in Figure 7.3 is shown in Figure 7.4.

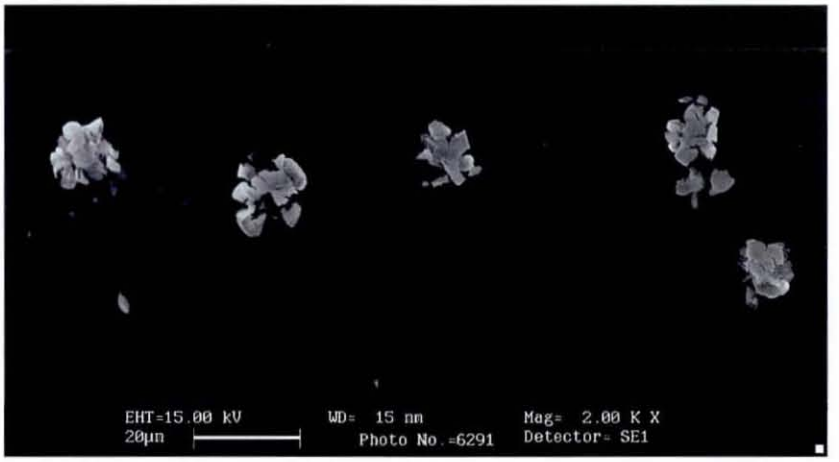

Figure 7.3: SEM of crushed ACA particles.

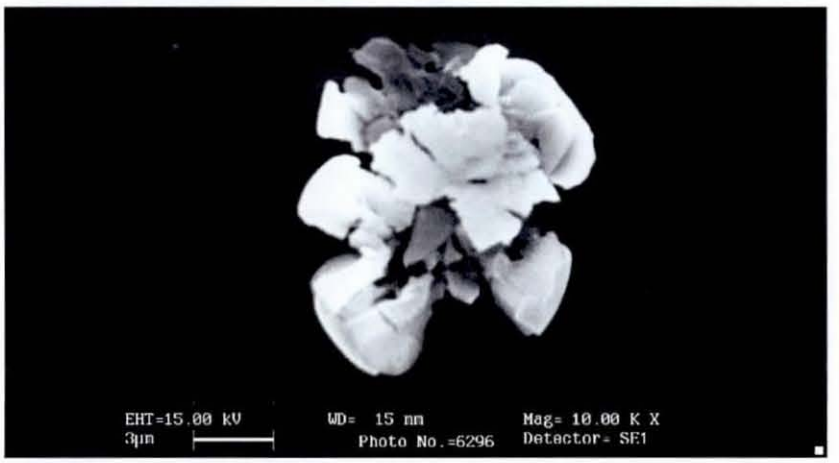

Figure 7.4: SEM of a typical crushed ACA particle.

7.2.1 Strain Versus Stress

It is very difficult to directly measure the strains and stresses within individual ACA particles undergoing deformation because they are so small (5.75 μm in diameter for Type II particle for example). Therefore methods to estimate the strain and stress in a deforming particle are introduced in this section. In the calculation, the stress in the contact area is taken as the stress within the deforming particle, and the particle deformation degree, $\Delta d/d$, is adopted as the average strain, as shown in Figure 7.5. These can only approximately represent the induced strain and stress in the particle

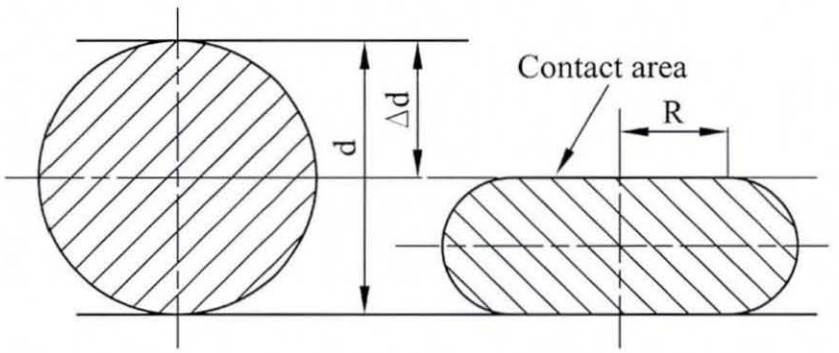

Figure 7.5: Deformed resin of an ACA particle.

undergoing deformation, because the real strain and stress distribution within the particle is uneven. The stress, σ, within the contact area can be defined as:

$$\sigma = \frac{F}{\pi R^2}, \tag{7.2.1}$$

where F is the load force and R is the radius of the contact circle area. The average strain, ε, throughout the particle can be defined as:

$$\varepsilon = k = \frac{\Delta d}{d}. \tag{7.2.2}$$

The radius of the contact area can be estimated if the particle deformation degree and the particle diameter are known. If it is assumed that the particle volume does not significantly change during the deformation process, then the original sphere volume, V_{sphere}, of the particle is equal to the deformed solid volume, $V_{deformed}$, of the deforming particle:

$$V_{deformed} = V_{sphere} = \frac{4}{3}\pi(\frac{d}{2})^3. \tag{7.2.3}$$

Figure 7.6-*a* shows a deformed particle, whose cross-sectional profile in the yz-plane is assumed to be as illustrated in figure 7.6-*b*. As the illustration shows, the cross-sectional profile consists of a rectangular area and two semi-circular areas. The length of the arc enclosing the right semi-circle is given by:

$$[y - R]^2 + z^2 = [\frac{h}{2}]^2, \qquad (y \geq R), \tag{7.2.4}$$

where $R(k, d)$ is the radius function of the circle contact area, and $h(k, d)$ is the height function of the deformed particle, as dimensioned in Figure 7.6-*b*. h is defined as:

$$h(k, d) = (1 - k)d. \tag{7.2.5}$$

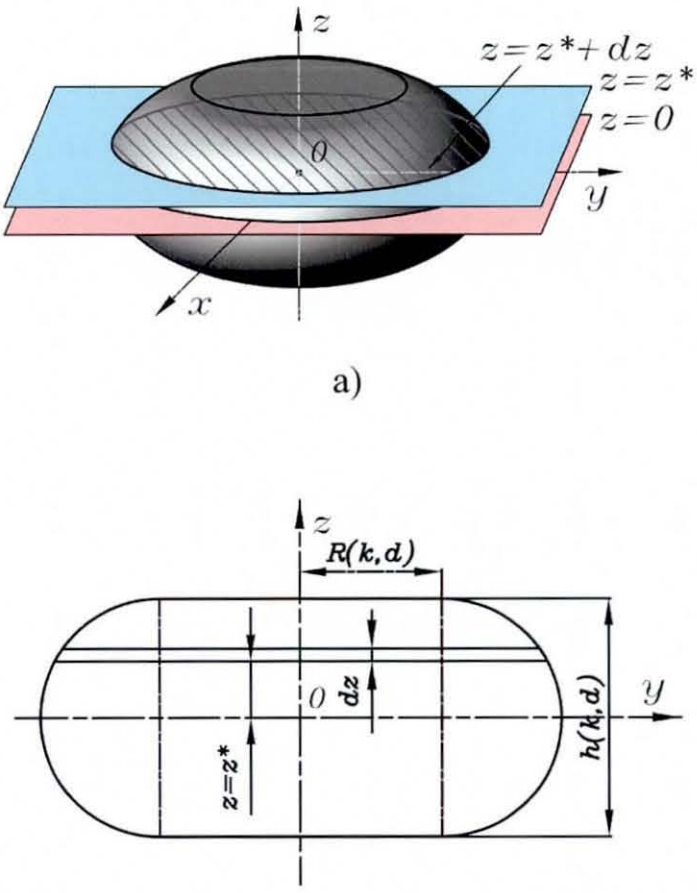

Figure 7.6: Geometry of a deformed ACA particle.

The cross-sectional profile of the deformed particle in the plane $z = z^*$ is a circular, where the circle radius is y^*, and whose area is therefore $\pi(y^*)^2$. Substituting $z = z^*$ in Equation 7.2.4 and simplifying it, we obtain $(y^*)^2$:

$$(y^*)^2 = \left[\sqrt{(\frac{h}{2})^2 - (z^*)^2} + R\right]^2 . \tag{7.2.6}$$

Thus, the circular area is:

$$S^* = \pi(y^*)^2 = \pi\left[\sqrt{(\frac{h}{2})^2 - (z^*)^2} + R\right]^2 . \tag{7.2.7}$$

As Figures 7.6-a and b show, the volume increment between $z = z^*$ and $z = z^* + dz$ is $V^* = S^* dz$, which is an integral unit of the whole deformed particle from $-\frac{h}{2}$ to

$+\frac{h}{2}$ along z axis. Substituting Equation 7.2.7 into $V^* = S^* dz$, we obtain:

$$V^* = S^* dz = \pi \left[\sqrt{(\frac{h}{2})^2 - (z^*)^2} + R \right]^2 dz \tag{7.2.8}$$

The volume of the deformed particle can therefore be expressed with an integral equation:

$$V_{deformed} = \int_{-\frac{h}{2}}^{+\frac{h}{2}} V^* = \pi \int_{-\frac{h}{2}}^{+\frac{h}{2}} \left[\sqrt{(\frac{h}{2})^2 - (z^*)^2} + R \right]^2 dz. \tag{7.2.9}$$

Applying Equation 7.2.9 and 7.2.5 in 7.2.3, an equation for $R(k,d)$ is obtained:

$$R(k,d) = \frac{-3\pi(1-k)^2 d + \sqrt{[3\pi(1-k)^2 d]^2 - 48(1-k)[2(1-k)^3 d^2 - 2d^2]}}{24(1-k)}. \tag{7.2.10}$$

Taking test $T10-10$ from Table 6.2 in Chapter 6 as an example, the calculated rate of strain $d\varepsilon/dt$ of this typical ACA particle undergoing deformation is shown together with the particle deformation in Figure 7.7, where the horizontal axis represents both the load force and the load time due to the 1 mN/s load rate used in the test, the left axis is for the strain rate and right line indicates the particle deformation.

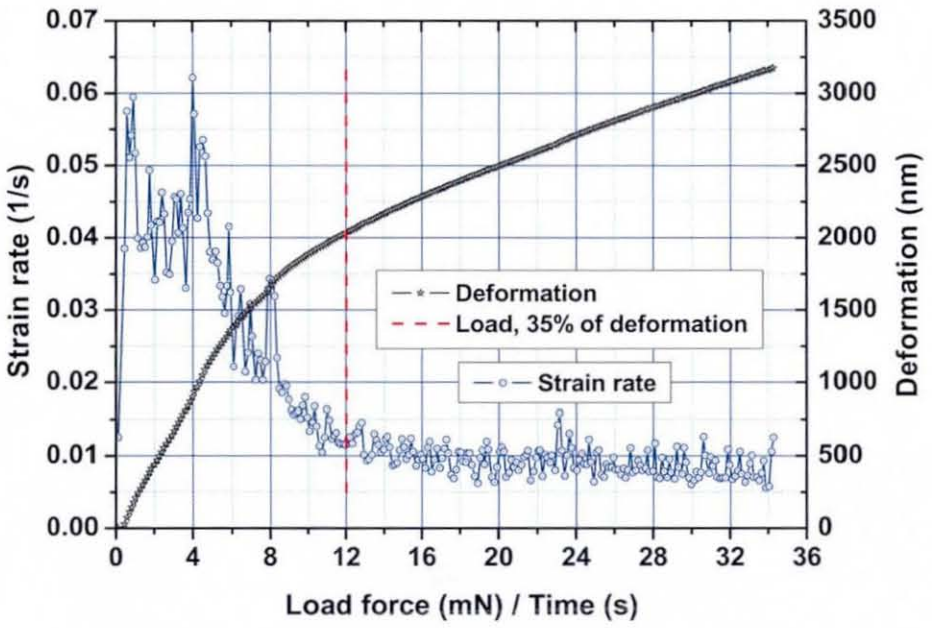

Figure 7.7: Strain rate during particle deformation.

The red dashed line in the figure is used to distinguish between deformation Stages I and II as discussed in the last section. The load force that this line indicates is 12 mN (12 s), at a deformation of about 2000 nm, or about 35% of the original particle diameter. The initial strain rate was quite noisy, but clearly decreased from about 0.04 $/s$ to 0.01 $/s$ during Stage I. Subsequently the strain rate was stable at around 0.01 $/s$.

The calculated strain versus stress for test $T10-10$ is plotted in Figure 7.8, where the horizontal axis represents the log stress, the left axis is for the strain and the right axis is for the particle deformation corresponding to the strain. It can be seen that the stress at the initial contact was much higher than subsequently and therefore it is not easy to interpret the deformation behaviour for this figure. Therefore the deformation is broken down into three steps as follows:

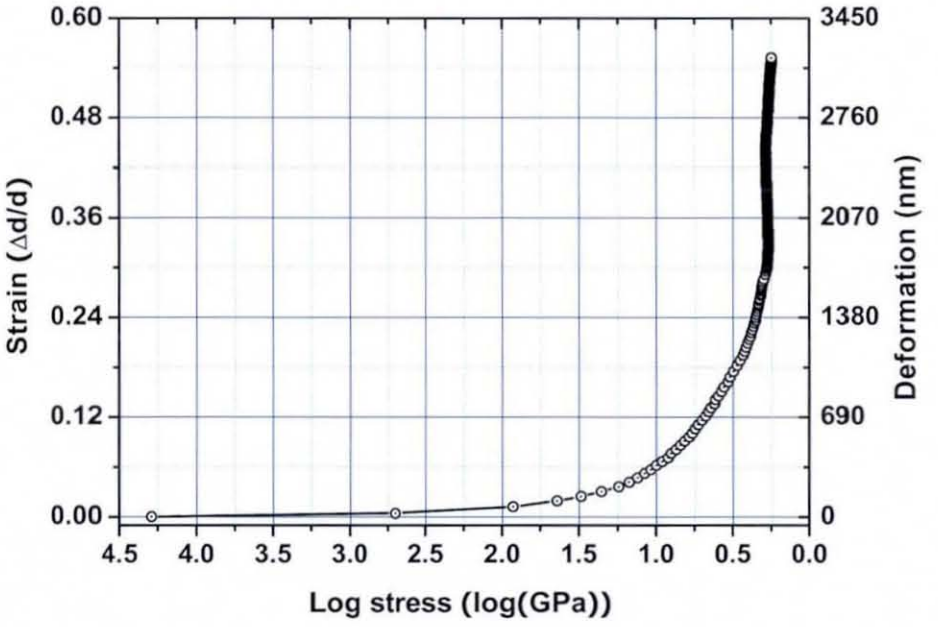

Figure 7.8: Full range of strain versus stress.

In the first step, only the first 11 points recorded in the experiment are used as plotted in Figure 7.9. In the figure, the plotted strain versus stress is from the first recorded test point to the 11th point. It can be seen that the calculated stress for the first point is extremely high, about 20×10^3 GPa, much higher than the stress at the second point, about 498 GPa. After point 2, the strain increased steeply. The high stress for point 1 indicates that the first touch of the punch on the particle resulted

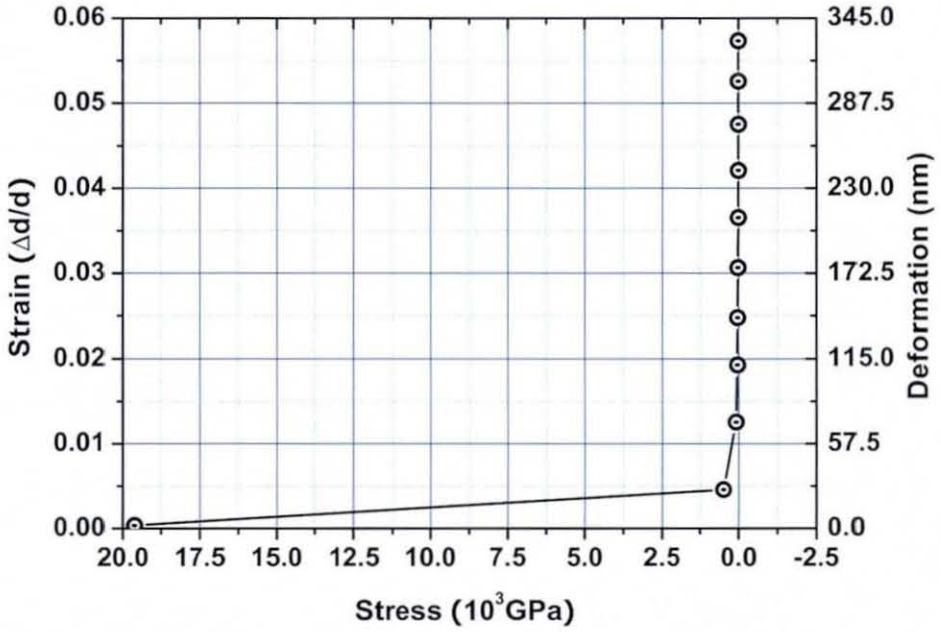

Figure 7.9: Strain versus stress for first 11 points.

in a very small spot, in theory a point. The stress after point 1 fell quickly as the contact area grew much bigger.

The second step includes the deformation to the end of Stage I. The calculated strain versus stress in Stage I after the first 2 points is plotted in Figure 7.10. The stress reduced quickly, but the rate of reduction dropped rapidly as the strain increased.

The third step covers the deformation during Stage II as shown in Figure 7.10. The detailed strain versus stress for the particle during this stage is shown in Figure 7.11, where the red circles are the results for $T10-10$ that follow on from the typical results in Stage I discussed above. It can be seen that there are two major changes (which are identified as the first turn and second turn) in the slope of the curves. One is just above a strain 0.3 and the other is at strains of about 0.45. This also happened in other tests, as the results for $T10-01$ and $T10-06$ show in the figure. It can be concluded that particle was harder between the first turn and second turn and then became softer again after the second turn. It is believed that the particle was harder after the first turn because the deformation was not concentrated in the contact areas only; i.e. the whole particle was deforming.

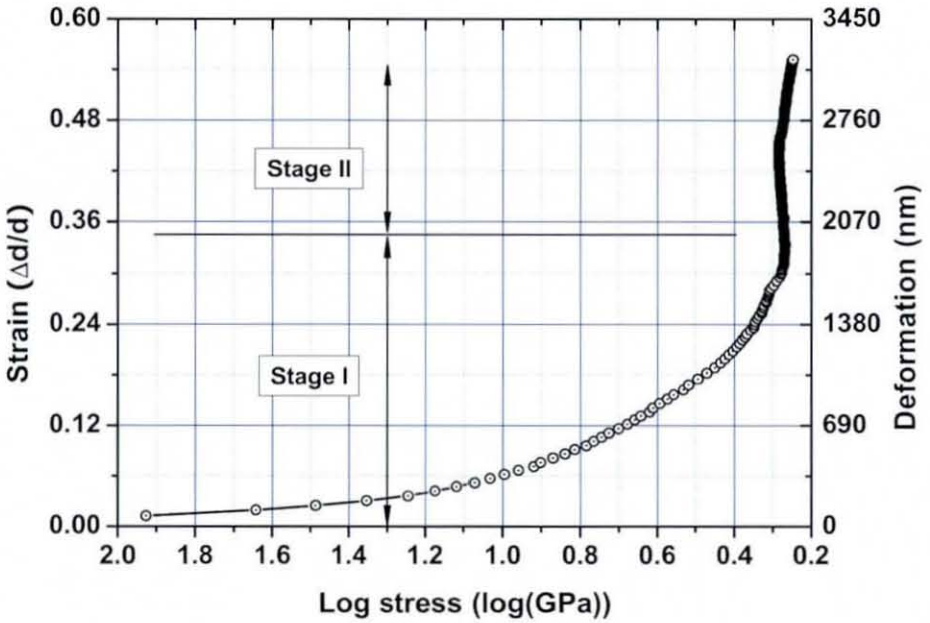

Figure 7.10: Strain versus stress after the first 2 points.

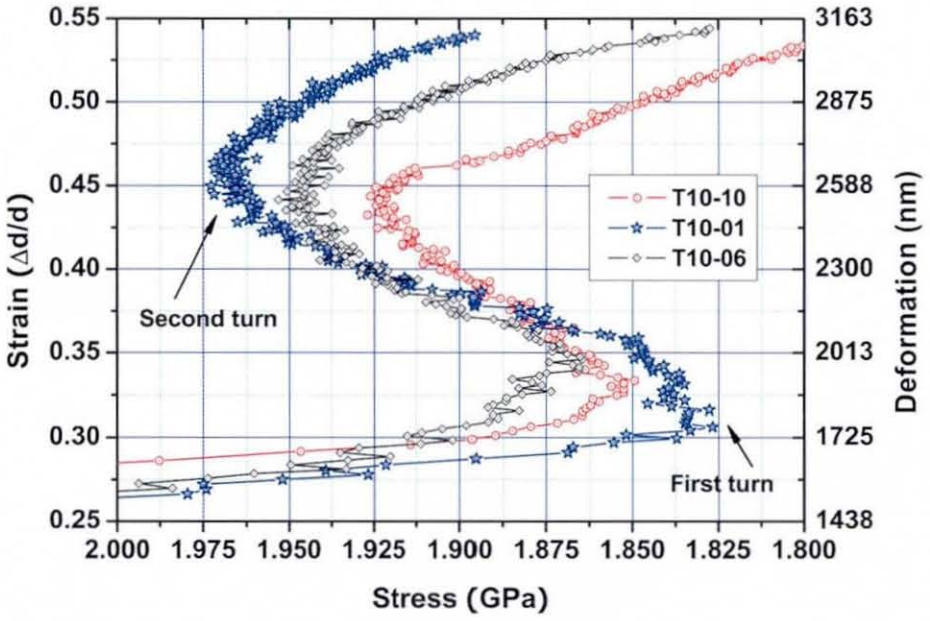

Figure 7.11: Strain versus stress in Stage II.

The particle appears to soften after the second turn is believed to be due to some small cracks initiating before the actual crushing event.

The strain versus stress behaviour at different stages may provide an explanation why joints where the particles are deformed to about 40% of the original particle size have been reported to have the best reliability [50][51]; because the deformed particles were in Stage II, where the well deformed particles had large contact areas between the particles and the component parts, yet were not deformed to a point where cracks initiated, reducing the particle strength as the stain-stress curves shown after the second turn in Stage II.

7.2.2 Effects of Load Rate on the Deformation of Particles

The results presented in Figure 7.12 are the mean values for the particle deformation at the crush point for load rates of 0.5 mN/s, 1 mN/s and 2 mN/s (as plotted in Figures 6.4-a, b and c).

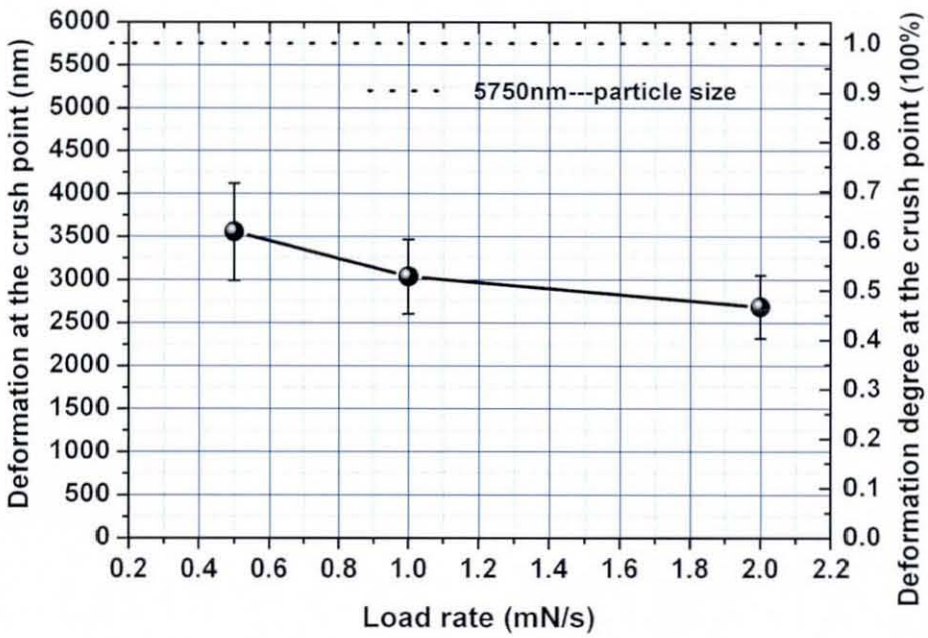

Figure 7.12: Particle deformation at the crush point.

Each value in the figure is the average (arithmetic mean) of the deformation when the particle started crushing. It shows that the particle deformation at the crush point was higher when the load rate was lower. At 0.5 mN/s, the particles could be

deformed by about 3500 nm, or around 60% of the particle size. However, the crush point deformation dropped to about 52% of the particle size, about 3000 nm, when the load rate was 1 mN/s. And there was a further small drop when the load rate was 2 mN/s to a deformation of around 2700 nm, or about 46% of the particle size. Therefore, it can be concluded that the load rate affected the particle deformation process, measurably delaying crushing at lower load rates. This is considered to be due to the visco-elastic properties of the polymer particles allowing more deformation at a lower load rate. The standard deviation error bars in the figure suggest that the lower the load rate, the more variable the crush point.

The results plotted in Figure 7.13 are the mean values of load at the crush point as tested at the load rates of 0.5 mN/s, 1 mN/s and 2 mN/s. Each value in the figure is the average (arithmetic mean) of the load force when the particle started crushing. It shows that the crush load was about 31 mN, when the load rate was 0.5 mN/s, but that it dropped a little, to less than 30 mN, when the load rate was 1 mN/s. Therefore, there was no major difference in the crush load force between load rates of 0.5 mN/s and 1 mN/s if only the mean load force was considered. When the load rate was 2 mN/s, the mean load force dropped to about 20 mN,

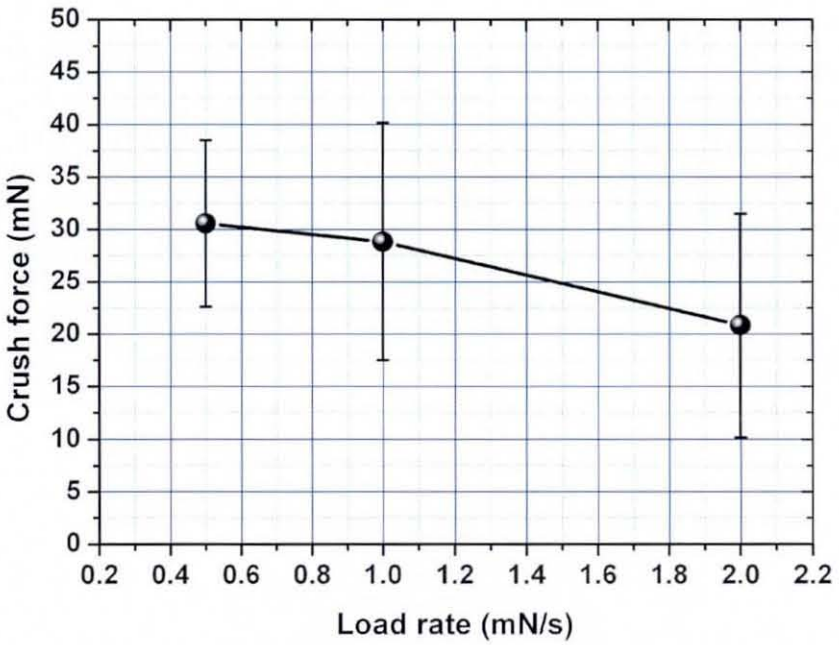

Figure 7.13: Crush force at crush point.

which is more significant than the drop for the load rate of 1 mN/s, and the standard deviation error bar was similar to that for the load rate of 1 mN/s. It can be seen that the crush load force was more variable at the higher load rate, since the variability of the results was bigger. However, more tests are needed to confirm if the crush force is more variable at higher load rates.

7.2.3 Visco-elastic Properties of Individual ACA Particles

As stated before, the ACA particles examined in this study were metal coated polymer spheres. Solid polymers are often viscoelastic materials [103]. In theory, general quantitative predictions of solid polymer behabiour are possible only in the case of linear viscoelasticity, for which the results of changing stresses or strain are simply additive, but the time at which these changes occur must be taken into account [104]. The typical response to a step change in the level of stress for a linear viscoelastic material is plotted in Figure 7.14, where the vertical line in a) is load and in b) is extension or strain. For the most general case of a linear viscoelastic solid the total strain e is the sum of three essentially separate parts:

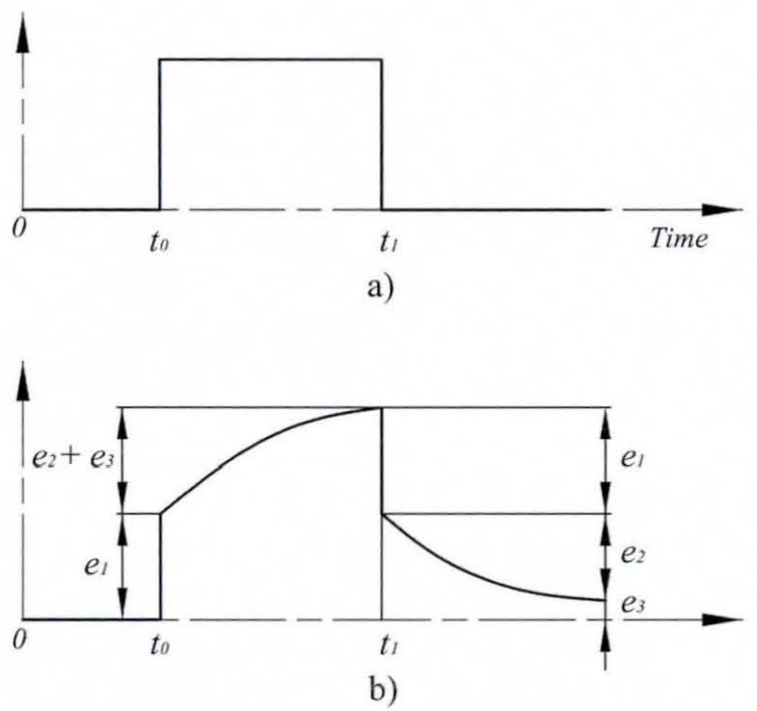

Figure 7.14: Deformation of a linear viscoelastic solid. a) Load; b) strain or extension.

e_1 the immediate elastic deformation, e_2 the delayed elastic deformation and e_3 the Newtonian flow, which is of the same form as the deformation of a viscous liquid obeying Newton's law of viscosity. It can be seen from the figure that deformation of a viscoelastic solid results in a time dependent change in strain following a step change in stress. This kind of deformation is sometimes called creep, but should not be confused with e.g. the time dependant plastic flow of metals at high temperatures and stresses.

If the material shows linear behaviour the magnitudes of e_1, e_2, and e_3 are exactly proportional to the magnitude of the applied stress, so that a creep compliance $J(t)$ can be defined, which is a function of time:

$$J(t) = \frac{e(t)}{\sigma} = J_1 + J_2 + J_3, \tag{7.2.11}$$

where J_1, J_2 and J_3 correspond to e_1, e_2 and e_3. It is found that cross-linked polymers do not exhibit a J_3 term [105].

In the load cycling experiments on ACA particles, a rapid change in load was applied similar to that illustrated in Figure 7.14 although not a step change. Figure 7.15 shows the results from the second load dwell of the typical load cycling test shown in Figure 6.6. It can be seen that the second load cycle started from a deformation of about 2450 nm, therefore the deformed particle was about 3300 nm in height. The deformation in the cycle was about 170 nm, so the cyclic strain can be calculated as 170/3300, or about 5%. During the dwell period, while subjected to a constant stress the deformed particle experienced a time-dependent increase in deformation. This phenomenon is known as viscoelastic creep. There was also a very small visco-plastic strain, e_3, as shown in Figure 7.15-b. This behaviour was unexpected because the particles are made from cross linked polymers for which the strain should be recoverable after unloading. It is believed that this strain is due to plastic strain in the metal coating of the particles. Just this creep deformation is plotted in Figure 7.16. A logarithmic function, $d(t) = A * ln(B * t + 1) + d(0)$, was used to fit the deformation as this has been shown to be a suitable model for differences in the rate and extent of polymer creep deformation, where A is an extensional term and B is a rate term [106]. A relates to the long term change in particle extension due to the load/stress and B relates to the deformation rate ($1/B$ is the time constant).

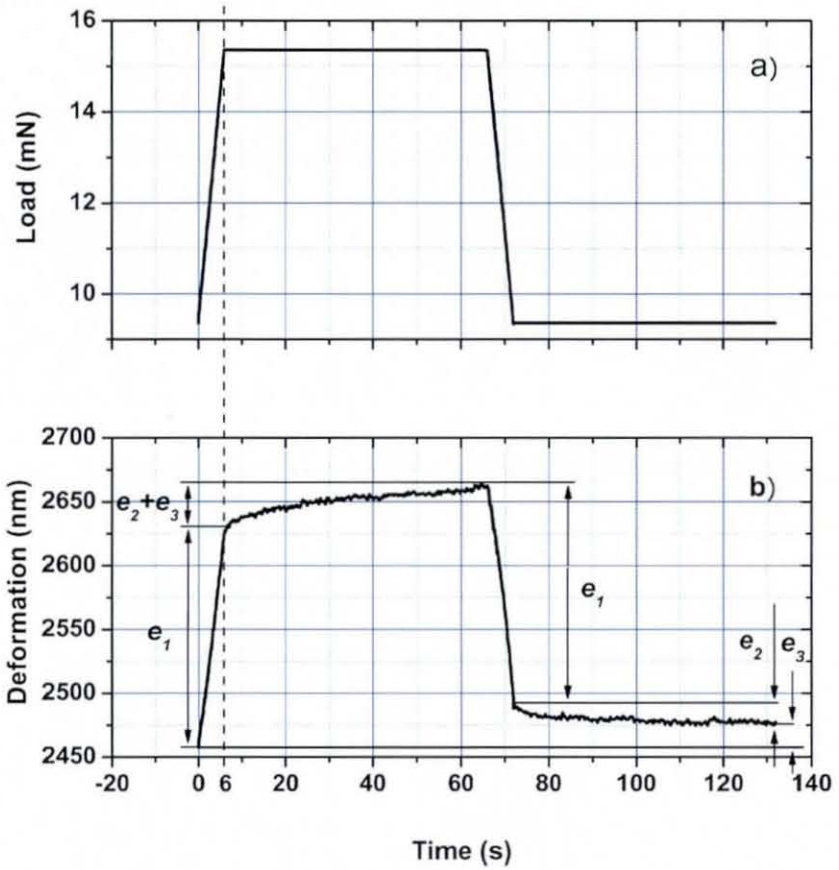

Figure 7.15: Deformation of a typical ACA particle. a) Load; b) deformation.

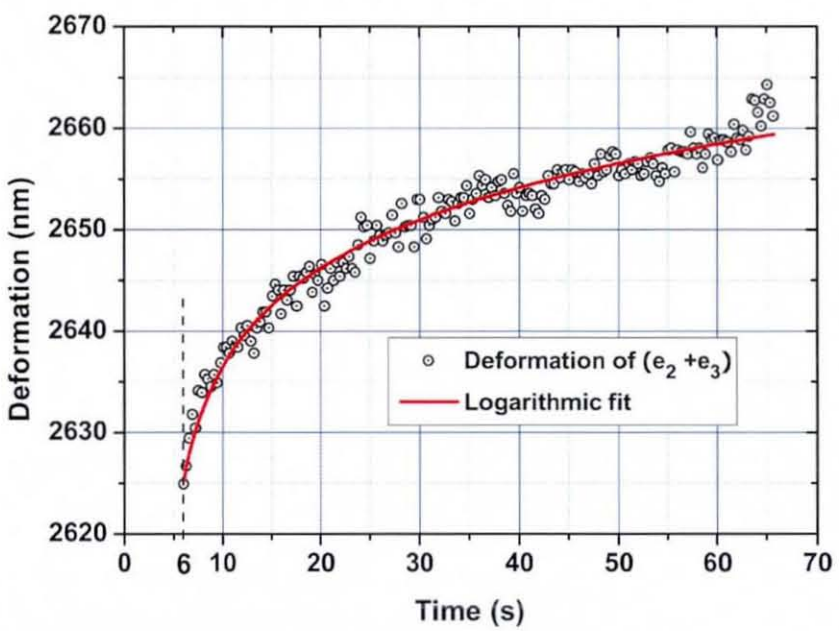

Figure 7.16: Second load dwell for a typical ACA particle.

Using a least squares fit, the formula obtained is:

$$d(t) = 9.79ln(5.68t + 1) + d(0). \tag{7.2.12}$$

All of the load cycling experimental results could be closely fitted by this logarithmic function. The fitted functions for the second dwell of the experiments unloaded to 40%, 60% and 80% are plotted in Figure 7.17, where $d(0) = 0$ is assumed in order to easily compare the three creep deformation curves. It can be seen the fitted curves are similar although different unloading percentages were used. This indicates that the creep deformation was not seriously affected by the unloading percentage.

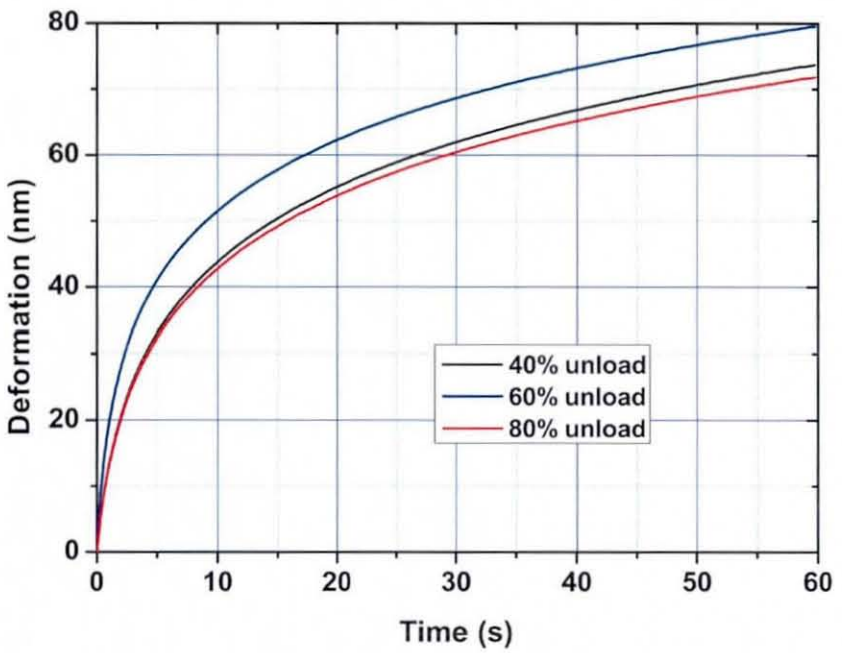

Figure 7.17: Logarithmic fits to second dwell in load cycling experiments.

7.2.4 The Effects of Adhesive on the Mechanical Deformation of ACA Particles

The results presented in section 6.2.4 suggested that the main effects of the presence of adhesive on the mechanical deformation of individual ACA particles are increases in the crush force and the crush displacement. They also showed that the chances of achieving successful deformation of an individual ACA particle was rare since the

particles were easily pushed out from under the punch in many of the experiments, resulting in only indentation on the glass bass stage being recorded. This suggests the lubricating effect of adhesive resins on particle movement during assembly may be an issue.

Statistical methods were used to establish how the adhesive affected the particle deformation process. The results of this analysis are plotted in Figure 7.18, where the left vertical line is for the deformation at crush and crush displacement and the right line is for the crush force. It can be seen that there was almost no difference between the deformation at the crush point with and without adhesive, both being about 3000 nm, although the variability in the experiments with resin was smaller than without. However, the average crush displacement of particles with resin was, at 1917 nm, significantly (about 20%) larger than without resin, which was 1600 nm. The crush force for the experiments with resin was also bigger than without resin, 37.11 mN compared to 28.84 mN, or about 30% higher. These results are believed to be due to the liquid adhesive reducing friction in the contact areas between the particle and the punch/base stage. The longer crush deformation in the experiments with resin also indicated that lower friction existed in the contact areas during the deformation, because the crushed particles can move more freely with resin than without.

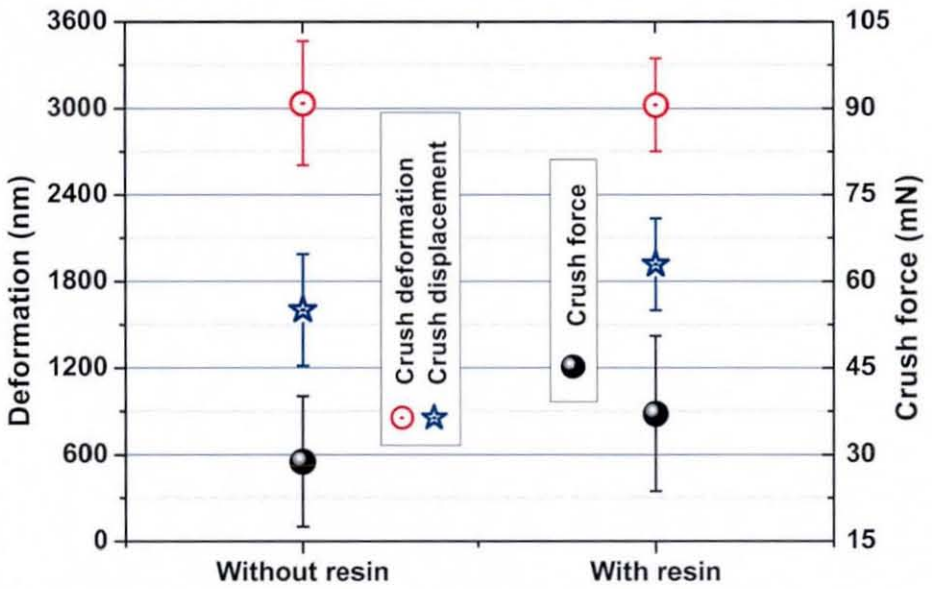

Figure 7.18: Particle crushing results without and with resin.

7.2.5 Mechanical Deformation of Multiple ACA Particles

ACA assemblies have been shown to have the highest reliability if the particles are deformed to about 40% of the original particle size [50][51]. And the best deformation degree was discussed as around 40%, as shown in Figure 7.11 in section 7.2.1. Therefore, 40% of the Type I particle size, or 1600 nm, was expected to be the optimum deformation degree for the test particles. The raw results for one, two, three and four particles from a deformation of 1200 nm to 2000 nm (30% to 50% of the original particle size) are plotted in Figure 7.19, where five results for each level of deformation are shown, except for the two particle deformation where only the three successful tests are included. The results show an increasing load force with deformation, however the results are randomly distributed, and difficult to interpret.

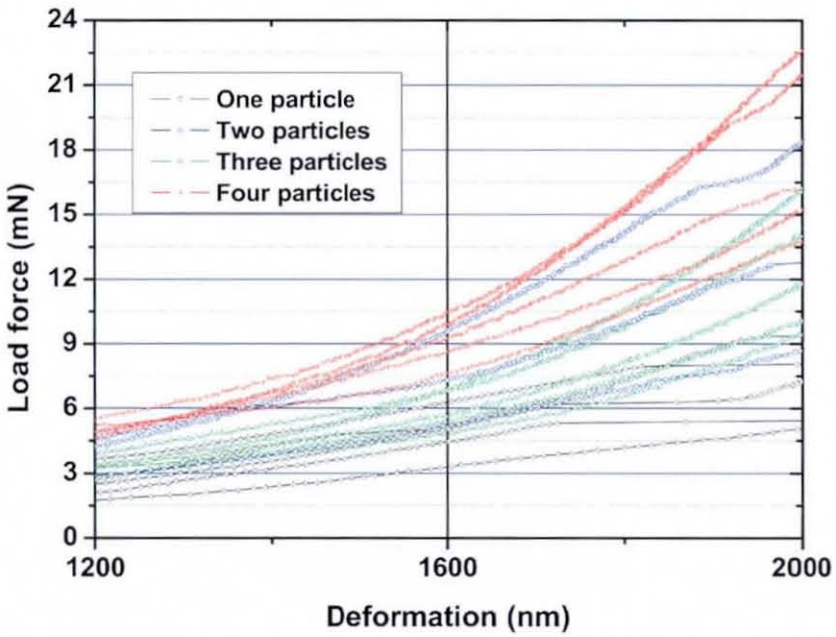

Figure 7.19: Deformation of multiple ACA particles around the optimum level of compression.

In order to understand how the load force affected the deformation, at between 30% to 50% of the original particle size, four deformation points were chosen to display the mean value of the tests at the deformation levels, 1200 nm, 1400 nm, 1600 nm and 2000 nm. The mean value, with one standard deviation error bars, are plotted in Figure 7.20. It can be seen from the figure that the relationship between load

force and deformation was similar in each kind of test. The load force increased as the deformation degree increased in each test or decreased as the particle numbers decreased in the tests except for the two particle tests. It shows that the mean load force was almost linear to the particle deformation degree in the one particle deformation test, but this is not true because the particles was found to be crushing at the deformation degree, 50%, in the four one particle tests as shown in Figure 7.19. Therefore the mean value for the one particle test at 50% degree should be higher than it is.

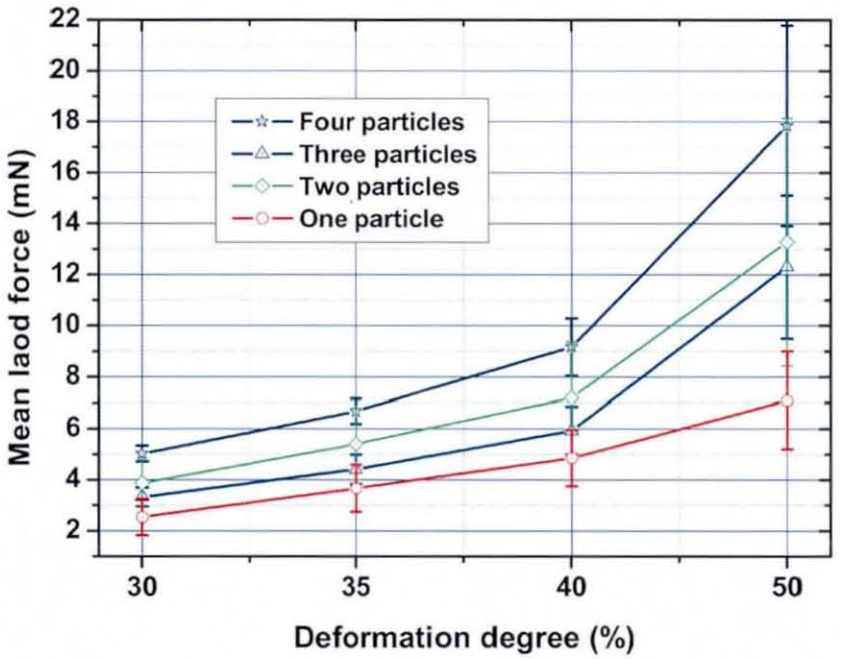

Figure 7.20: Deformation of multiple ACA particles to different deformation levels.

In order to gain a detailed understanding the effect of particle number on the load force, the load force and load force per particle versus number of particles at a deformation of 1600 nm, or 40% of the original particle size, is statistically analyzed as shown in Figure 7.21, where the horizontal axis is for the particle number deformed in each kind of experiment and the vertical line is for the load force. It can be seen that the mean load force increased as the particle number increased (two particle tests not considered), non-linearly. However, the load per particle was found to decrease as the particle number increased. The load per particle should be constant if the particles were of the same size and the punch tip and the base stage were perfectly

smooth and in two parallel planes. These possible reasons can be detailed as follows:

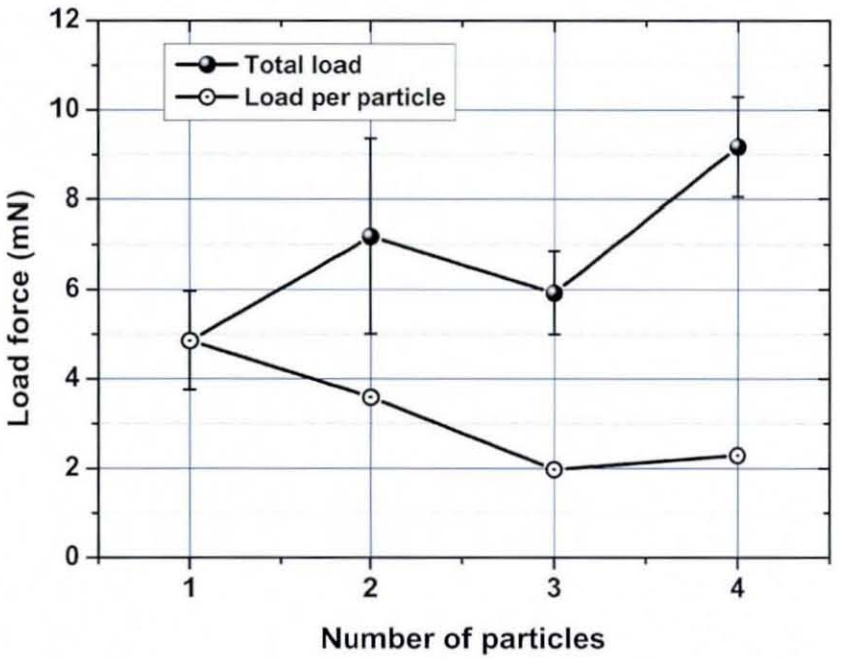

Figure 7.21: Deformation of multiple ACA particles at 40% of original particle size.

- *Particle finish*: The multiple particles may have different diameters due either to polymer particle core size variation or an uneven metal coating thickness. Therefore, the particles are not deformed to the same degree.

- *Punch and base stage roughness*: The punch tip and the base stage surfaces are not perfectly smooth and can not be aligned to be perfectly parallel. Therefore, the particles are not deformed to the same degree.

Therefore, the observed drop in load per particle for deformation of multiple ACA particles is considered to be due to one particle began to be deformed first, then the next and the next etc.. Therefore, the average deformation degree is actually smaller than that recorded. Occasionally the particles may also move under the punch due to the uneven surface of the contact surfaces. The worst situation was that some particles were pushed out during the deformation, as shown in the failed tests in the two particle deformation experiments.

7.3 Electrical Tests on ACA Particles

7.3.1 Typical Electrical Resistance of a Single ACA Particle Undergoing Deformation

In this section, experimental results obtained using a W/Cu punch, as shown in Figure 6.22, are analysed in more detail. The results of the electrical tests showed that the electrical properties of individual ACA particles undergoing deformation were variable, although the general shapes of the resistance curves were similar. An important finding is that the resistance increased when the particle began to crush, as shown in Figure 6.20. The reason for this is believed to be that the contact pressure between the particle and the metal surfaces dropped suddenly when the particle started crushing. The joint resistance kept steadily reducing up to the crush point (or the maximum load if no crushing occurred) although the crush points were quite variable, as shown in Figure 6.22. The initial joint resistances when the deformation started were also variable. Many factors can affect the initial contact resistance, such as the particle finish, the local topography of the contact surfaces, oxide or other insulating layers, and the micro structure of the contact metals.

Mathematical analysis is used to find the relationship between the joint resistance and the deformation. Test 2 is selected for analysis, as shown in Figure 7.22, where the left vertical axis is for the joint resistance and the right one is for a calculated constant as will be explained below. In the figure, the blue curve is smoothed using a moving average of 10 points on the raw resistance data. If the resistance as a function of deformation, x, is denoted as $r(x)$, then the expression, $\frac{1}{r(x)}\frac{dr(x)}{dx}$, can be calculated as:

$$\frac{1}{r(x)}\frac{dr(x)}{dx} = \frac{r(i+1) - r(i)}{[x(i+1) - x(i)]r(i)}, \tag{7.3.1}$$

where $r(i)$ is the ith measured resistance and dr is the deformation increment. The calculated values of $\frac{1}{r(x)}\frac{dr(x)}{dx}$ are also shown in Figure 7.22. It can be seen that these calculated results roughly follow a constant line as shown by the red line in the figure. Taking the constant as λ, Formula 7.3.1 can be written as:

$$\frac{dr(x)}{dx} = \lambda r(x). \tag{7.3.2}$$

It can be seen from Equation 7.3.2 that $r(x)$ is an exponential decay function, where the value of resistance decreases at a rate proportional to its current value. In Equation 7.3.2, $r(x)$ is the quantity and λ is a positive number called the decay constant. The standard solution of $r(x)$ can be written as:

$$r(x) = Aexp(-x/\lambda) + B, \tag{7.3.3}$$

where A is a coefficient and B is a constant. Therefore, it can be concluded that the experimental results for resistance versus deformation can be fitted reasonably well by the equation of exponential decay, as shown in Equation 7.3.3.

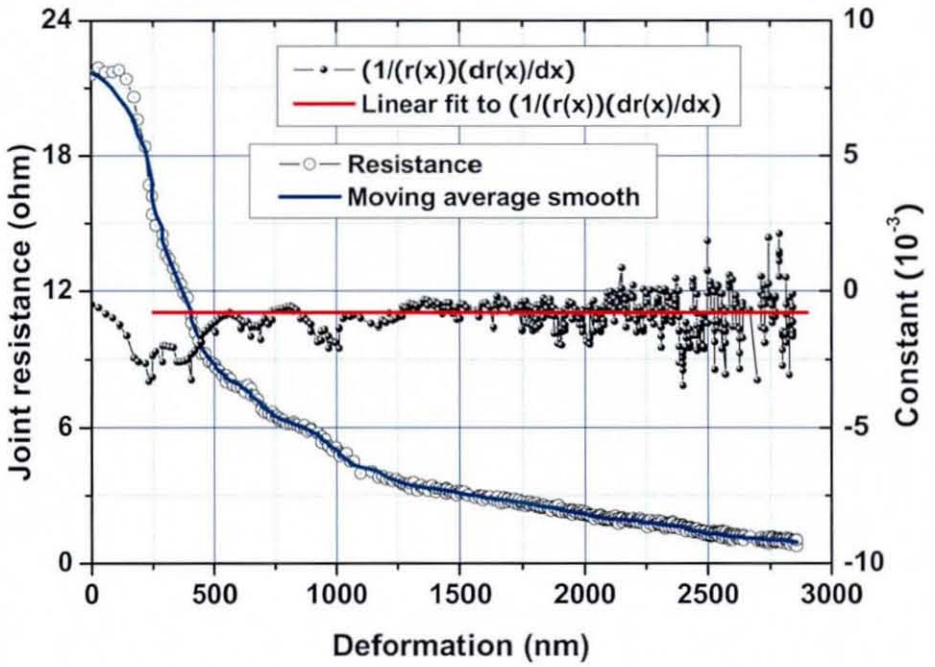

Figure 7.22: Fitting of a function to the resistance data.

For the five tests in one experiment, it can be seen that the outcome (dependent variable) shows substantial variation, even though all experimental parameters (independent variables) remain constant. Therefore, the method of least squares fitting was used to establish the parameters in Equation 7.3.3 using the raw data of the five tests as shown in Figure 7.23. The calculated value of the coefficients and the constant are:

$$A = 16.30,\ \lambda = 826.71,\ and\ B = 0.84. \tag{7.3.4}$$

Therefore, the fitted Equation 7.3.3 is:

$$r(x) = 16.30exp(-x/826.71) + 0.84. \tag{7.3.5}$$

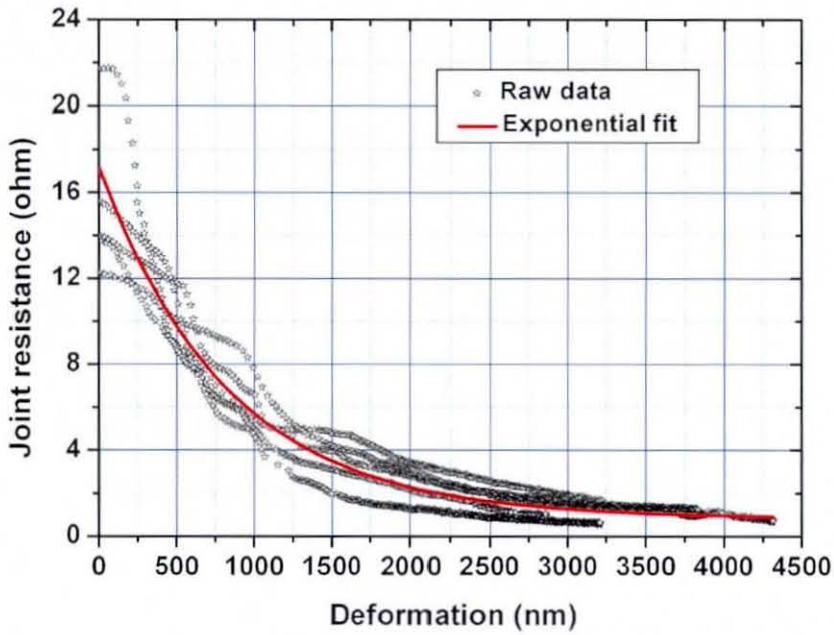

Figure 7.23: Joint resistance fit.

The coefficients and the constant of Equation 7.3.3 are different for each individual test as shown in Figure 6.22. Separately fitted curves for the five tests are plotted in Figure 7.24 together with the best fit to all five tests. The calculated values of the coefficients, A and λ, and constant B, for the exponential decay equation are listed in Table 7.1 for each of the experiments. It can be seen that they vary significantly between tests, even for the same punch, same base stage, and same particle type. These variations may be due to manufacturing variations between individual ACA particles or variations in the material properties of the area of the punch and base stage used to deform the particles. The initial resistance and the shapes of the curves are different, but are all roughly similar.

A is believed to be a material coefficient that is affected by the initial contact resistance, and the metal conductivity of the contact parts. It controls the resistance in the initial stages of compression/deformation. λ is believed to be a material coefficient that is affected by the electrical and physical properties of the conductive

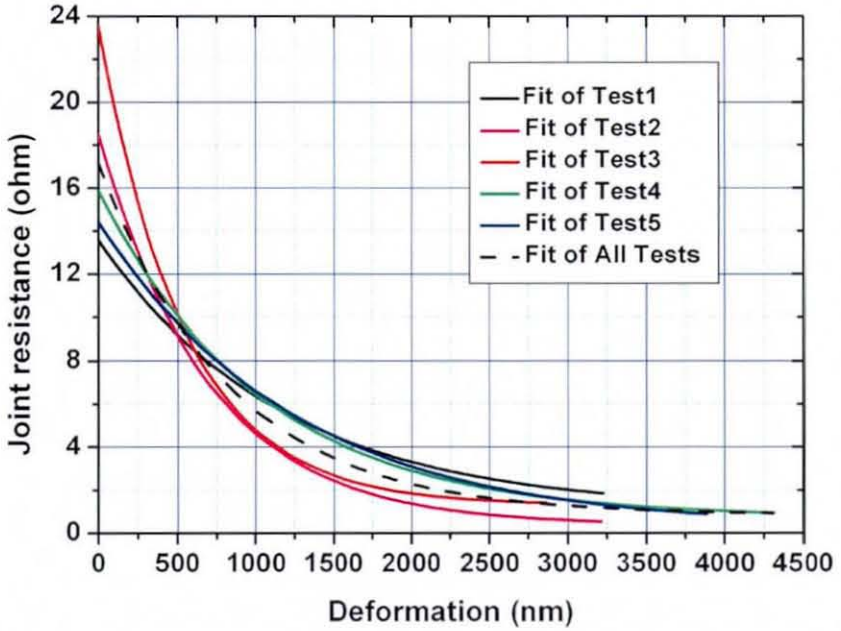

Figure 7.24: Comparison between different fits.

Table 7.1: Exponential Function Parameters for the Resistance Experiments

Test	A	λ	B
*Test*1	12.51	1168.43	1.05
*Test*2	22.26	538.84	1.30
*Test*3	15.17	1036.09	0.69
*Test*4	14.15	1247.75	0.24
*Test*5	18.13	689.88	0.374
TestAll	16.30	826.71	0.84
Note:	TestALL is the best fit to all five tests		

particle and the actual contact areas in the deformed contact area. It terminates the speed of decay for Equation 7.3.3. As for the constant B, the smaller it is, the smaller the joint resistance that can be achieved. This constant is considered to be affected by the metal conductivity of the particle, the punch and the base stage. It is around 1 for the contact metal parts, i.e. the W/Cu punch, the Type II particle and the brass base stage, used in this experiment. However, more research on the physical understanding of A, λ, and B is required before the formula found in this research can contribute to the understanding of the electrical properties of individual ACA particles.

7.3.2 Electrical Stability Tests on Individual Particles

Stable joint resistances were found in the electrical tests on individual particles if the load was constant during the dwell. The joint resistance measured during the dwell was smaller if a higher load rate had been used. For example, the smallest stable resistance was about 2.9 Ω when a 2 mN/s load rate was used, less than the smallest, about 4.2 Ω, measured when 0.5 mN/s was used, as shown in Figure 6.28. The final resistances of individual particles in an actual ACA assembly may not be the same resistance as the resistances measured here, since the deformation locked in by the curing of the adhesive will not be the same as the bonding force applied during the assembly process. Normally, this holding force would be expected to be smaller than the applied force during the final stage of the bonding process [107]. Therefore, the joint resistance of individual particles increases to some degree due to the load force switching from the bonding force to the force supported by the shrinkage stresses. These stresses are affected by the temperature and becomes stable in room temperature after the cooling process is finished and the following applied bonding force was released in the final bonding process.

7.3.3 Electrical Resistance Tests with Different Punch Materials

The results show that the joint resistance was significantly higher when a HSS punch was used rather than a W/Cu punch. These differences in resistance are because the stationary contact resistance in the contact area between the particle and the punch or the base stage is highly dependant on the conductivity of the contact metals and the contact surface finish of the contact parts.

The fitting method as used in last section is used to obtain a detailed comparison between these two kinds of tests. Their joint resistance versus deformation are shown in Figure 7.25, and the values of the coefficients and constants are listed in Table 7.2. It can be seen in the figure that the shape of the decay curve is similar, as the coefficients A and λ are similar. The initial resistance in the tests using a HSS punch was slightly higher than those tests using a W/Cu punch. Compared to the other

coefficients, the constant B for the HSS punch results is much bigger than for the W/Cu punch. This suggested that the shape of the resistance versus deformation relationship for the same type of particle is similar, although the initial resistance and the stable resistance are quite different, as shown in the figure, for different test punch materials. This is further confirmation that constant B is affected by the metal conductivity, since B for the tests using the W/Cu punch was much smaller than for the tests using the HSS punch.

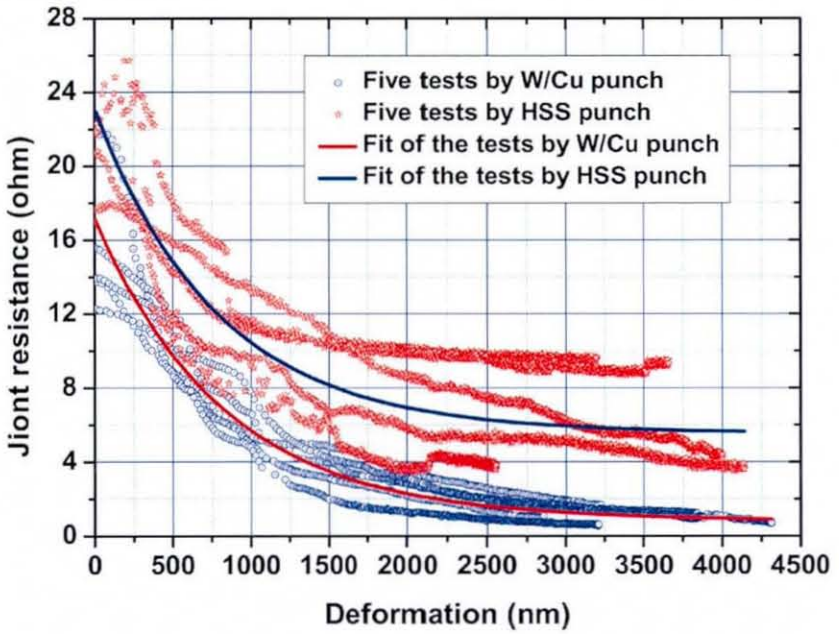

Figure 7.25: Exponential curve fits to experiments using different punches materials.

Table 7.2: Best Fit to the Five Experiments for Each Punch Type

Test	A	k	B
W/Cu punch	16.30	826.71	0.84
HSS punch	17.53	786.55	5.55

7.3.4 V/I Properties of a Deformed ACA Particle

The voltage measured for each current increment is presented in Figure 7.26, where the vertical axis is the mean value of measured voltage. Ohmic conduction was found

in the range of the applied current (0.1 to 1.6 mA) with a resistance of about 1.41 Ω as the green linear fit shown in the figure. Normally, there are at least 20 particles trapped in each joint of an actual electronics package, therefore this individual particle resistance of 1.41 Ω would result in a joint resistance of 70 $m\Omega$, which is of a similar magnitude to the joint resistance of an actual assembly, for example, about 40 $m\Omega$ for the experimental results in the Chapter on Co-planarity (section 4.3.1).

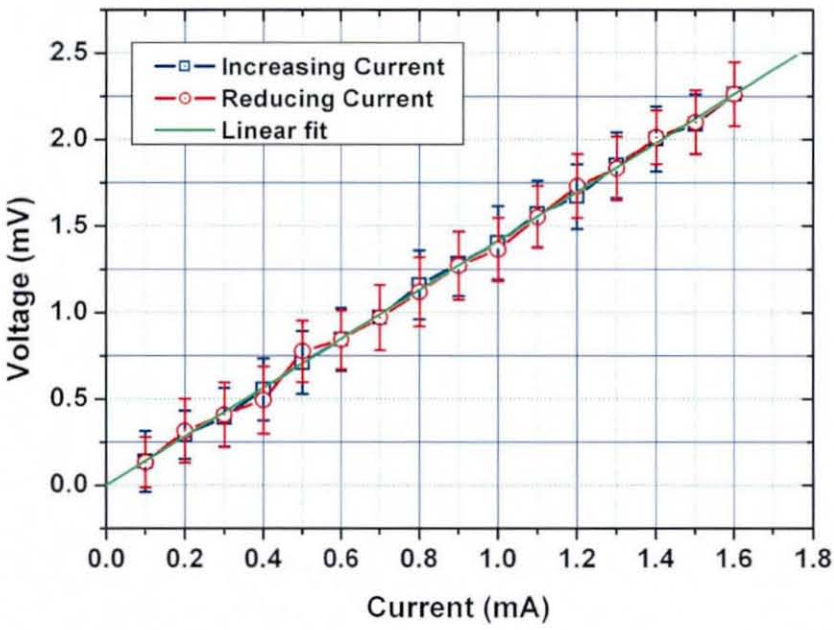

Figure 7.26: V/I behaviour of a single particle.

The results from this experiment fit well with the experimental linearity measurements previously reported by Oguibe et al. [21], where it was found that low resistance joints exhibited ohmic behaviour for currents up to 200 mA. In their experiments ACA joints with multiple particles (the number of particles in the joints is not known) were used, rather than only one particle as used in this research. This V/I measurement for individual ACA particle joint further confirms that ACA joints exhibit ohmic behaviour.

7.4 Summary

The results from the mechanical deformation and electrical tests on individual ACA particles have been analysed and discussed in this chapter using mathematical and statistical methods. This research will contribute to the fundamental understanding of the use of ACA materials in electronics packaging. The novel experimental methods used in this research delivered a new way to test small particles mechanically and electrically, and can also be used in other research area where the particle size is similar to ACA particles.

Significant Findings include:

- Detection of changes in the particle behaviour starting to take place before crushing occurred.
- The mechanical deformation of individual ACA particles was found to be affected by the load rate, confirming the ACA particles tested had Linear viscoelasticity properties.
- It was found that the presence of resin during the mechanical deformation of individual ACA particles affected the deformation process, the deformation with resin required a higher crush force although the crush deformation was as same as in the experiments without resin.
- The electrical tests showed that the joint resistance increased when the particle began to crush or the load was released and the relationship between the joint resistance and deformation was fitted well by an exponential decay function.
- Joint resistance was affected by loading rate and a stable resistance was measured if the holding force was kept unchanged during a dwell period.
- It was confirmed found that the conduction of individual ACA particles was Ohmic up to a significant level of applied current.

Chapter 8

Conclusions and Future Work

The research presented in this thesis has advanced the fundamental understanding of ACA technology in electronics packaging in a number of areas. The conclusions from the work and a number of avenues for future work are summarized in this chapter.

8.1 Thesis Conclusions

The conclusions from the research work presented in this thesis are grouped into three parts in this section: the effects of planarity variations on ACA assembly, the experiments on individual ACA particles and a comparison of the resistance versus deformation results for these two types of experiments.

8.1.1 Effects of Planarity Variations on ACA Assembly

Deliberate chip rotation was used to simulate co-planarity variation in an ACA assembly. The actual bond thicknesses, i.e. the height of the deformed particles in ACA joints with rotation were measured. The measured bonds were thinner in the less compressed sides and thicker in the highly compressed sides than the calculations. This indicates that the actual rotations were smaller than planned. This research has led to the following conclusions:

Three stages of particle deformation were identified from the rotation experiments. In stage I, at low rotation angles, low and uniform resistances were found. In stage II, the joint resistances of the less compressed side increased, due to the decreased deformation of the ACA particles. In contrast to the less compressed side, the lower

conductivity joints in the highly compressed side resulted from crushed particles and the reduced area of mechanical contact between the particles and the pads. In stage III, highly variable ACA joints were found in the less compressed side, because the ACA particle deformation was dramatically decreased and the mechanical contact between the particles and bumps/pads were very limited. It suggests that the joint resistances in the highly compressed sides are more stable compared those in the less compressed side, however such joints may suffer reliability problems in service, since that ACA particles were crushed in this stage and stationary contacts between the bumps and pads may be initialled between the pieces of the crushed particles. It was found that the joint resistance reduced as the bond thickness reduced by 55% of the original particle diameter, but then the joint resistance had relatively little further change for greater deformations, although there is some evidence of a slight increase in resistance. On the other hand, the results suggest that the joint resistances are getting more consistent after the particles were deformed by more than half of their original diameter.

8.1.2 Experiments on Individual ACA Particles

A novel methodology for the mechanical and electrical testing of individual ACA particles has been developed in this research. A number of significant findings have resulted from these experiments. The technique could be used to test any kind of micro particles that are of a similar size to the ACA particles tested. The most significant conclusions from these tests are listed in the following sections.

Mechanical Deformation

- *Typical mechanical deformation of individual ACA particles*: The typical load versus deformation behaviour of individual ACA particles was established. Four stages were identified in this process. In the initial deformation (Stage I), the deformation is approximately proportional to the load force applied until the deformation degree reached approximately 25%. Then the particle stiffness was rising well before a deformation degree of 35%. During further deformation (Stage II), the stiffness increased significantly, but the rate of increase in stiffness

reduced before the particle was actually crushed. In Stage III, the particles were crushed experiencing a large deformation with no increase in load. In the post crushing process, Stage IV, the load ramped up to the maximum load, followed by a unloading process.

- *Strain versus stress*: The strain versus stress behaviour was estimated from the load experiments. In Stage I, the stress was initially localised and very high, but reduced quickly. However the rate of reduction dropped rapidly as the strain increased. There are two turns in the slope of the curves of strain and stress in Stage II. It can be concluded that in Stage I and up to the first turn the particle was soft, but the particle became significantly harder after the first turn until becoming soft again after the second turn.

- *Load rate*: The mechanical deformation of individual ACA particles was found to be affected by the load rate. The lower the load rate was, the higher the crush force and the deeper the particle deformation before crushing.

- *Visco elasticity*: The ACA particles tested in this research showed linear visco-elastic behaviour where the deformation increased with time. Non-recoverable stain was also found in the experiments. It was found that the deformation during the load dwells closely fitted to a logarithmic function. The deformation was almost unaffected by the size of the unloading cycle.

- *Resin effects*: The presence of an adhesive resin during the mechanical deformation of individual ACA particles affected the deformation process. Deformation with resin resulted in a higher crush force, although the crush deformation was the same as in the experiments without resin. The crush displacement with resin was also found to be longer than without. This is believed to be due to the liquid adhesive lowering the friction in the contact areas between the particle and the punch or base stage.

- *Multiple ACA particle deformation*: Experiments on mechanical deformation of multiple ACA particles showed that the load force was higher if more particles were deformed together up to the same deformation degree, however the increase was not proportional to the number of particles. Particle non-uniformity, punch

and base stage roughness and non-planarity are believed to be the main reasons for this.

Electrical Tests

- *Typical electrical resistance of a single ACA particle*: The joint resistance of a single particle reduced as the load increased until the particle began to crush at which point it increased slightly. The relationship between joint resistance and deformation was found to closely fit an exponential decay function. The parameters of the function were calculated and their physical significance was postulated.

- *Electrical stability*: Stable joint resistances were found in the electrical tests on individual particles if the load was constant during the dwell. The joint resistance measured during the dwell was smaller if a higher load rate was used.

- *Punch materials*: It was found that the shape of the resistance versus deformation relationship for the same type of particle is similar, although the initial resistance and the stable resistance are quite different for different punch materials.

- *V/I behaviour*: From the voltage versus current behaviour of a deformed ACA particle it can be concluded that the conduction of ACA particles is Ohmic within the range of the current applied.

8.1.3 A Comparison of the Resistance versus Deformation Results for These Two Type of Experiments

In order to compare the resistance versus deformation results for these two type of experiments, the raw data for the five tests using the W/Cu punch as shown in Figure 6.22 and the raw data of resistance versus bond thickness for the co-planarity experiments as shown in Figure 4.13 are compared as shown in Figure 8.1, where the left axis is for the single particle resistance and the right is for the resistance of ACA

joints measured in the rotation experiments. Exponential decay function fits to these two sets of data are used to aid the comparison as also shown in the figure. It can be seen that the variation in resistance of individual ACA particles is smaller than that for the actual ACA joint resistances.

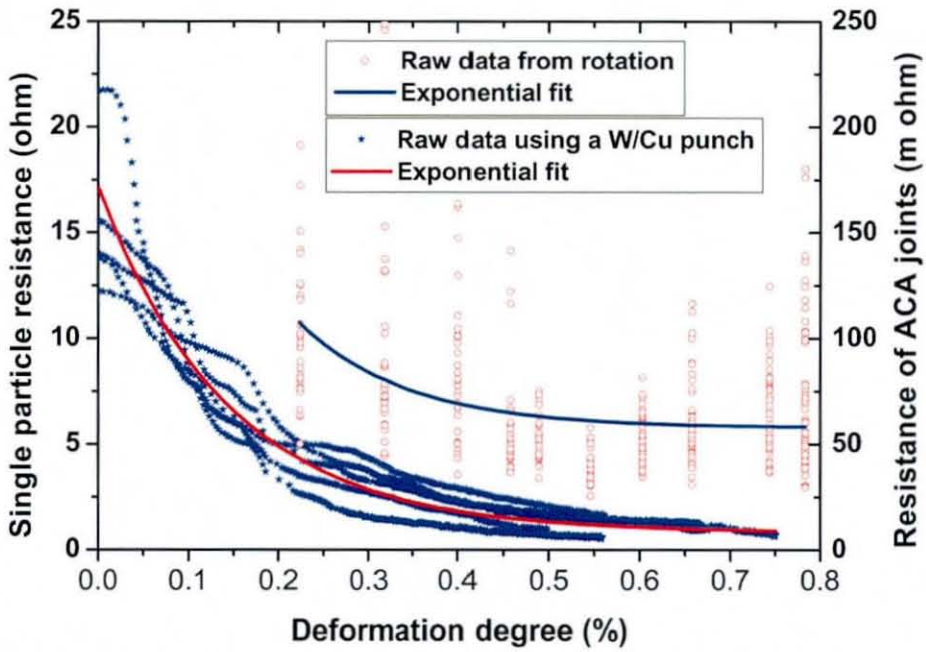

Figure 8.1: Resistance of individual ACA particles and ACA joints.

Figure 8.2 shows the comparison between the fitted exponential curves for the individual ACA experiments and the estimated resistance per particle in the rotation tests, where 20 particles per joint is assumed for each of the individual joints, as discussed in the last chapter. It can be seen that they obey almost the same relationship between the resistance and the deformation, and although the joint resistance per particle for a deformation degree less than 20% is not available; for deformations of more than 20%, they have a similar decay rate and value even though the experiments did not use exactly the same type of ACA particles. This further confirms that the experimental techniques for measuring the behaviour of individual ACA particles as discussed in this thesis can be used to determine information relevant to the performance of actual ACA assemblies.

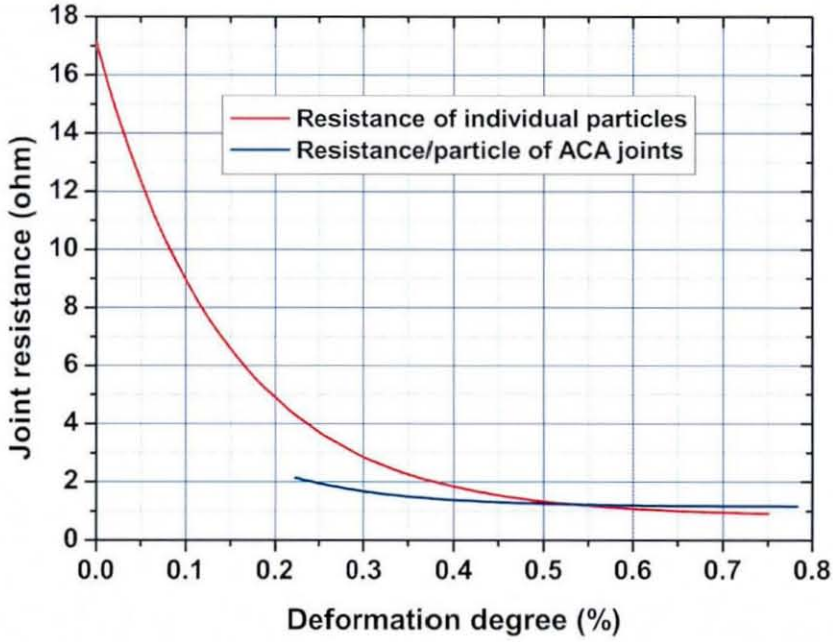

Figure 8.2: Comparison between single particle resistance and resistance/particle of ACA joints.

8.2 Future Work

The research carried out in this thesis has given rise to a number of ideas for future work on the performance of ACA conductor particles:

- The behaviour of ACA assemblies with other types of bond pad non-planarity, as detailed in section 3.4.1, are of interest, particularly those chip bump and substrate pad geometries that can be manufactured. Such a study might include computational analysis, such as FEM modelling, particularly where experiments are difficult or impractical.

- In the co-planarity experiments, it was found that the smallest joint resistance was for the unrotated samples. In other words, any planarity variation in an ACA assembly will result in an increased joint resistance even where the joint thickness is reduced. More research is required to investigate this finding and whether it is due to particle displacement from the bond pads.

- Further development of the experimental technique for testing of individual ACA particles is likely to include a ruby or diamond punch for the mechanical

deformation of individual ACA particle and a ceramic punch coated by gold or platinum for the electrical test. The methodologies used in this research are ready to be tried on other kinds of materials. Such as amorphous particles, fine solder balls and any other particles that are of similar size.

- As for the mechanical deformation of individual particles, tests on different types of particles are of interest including particles with or without coating. This will help to further improve the fundamental understanding of ACA technology. It would be ideal if the particles could be tested within a layer of melted adhesive where the temperature is controlled in the same way as in the actual assembly process.

- Analysis using computational modelling will be another valuable work to be undertaken in this area. This could include, for example, more detailed modelling of individual ACA particle deformation, the effect of adhesive present in the joint, the visco-elastic deformation, load rate effects on the particle deformation, etc...

- More work is also needed on the electrical testing of individual ACA particles to further understand the conduction mechanisms for the ACA technology. An exponential decay function was found to be a good fit to the electrical test results for the particles used in this research. Testing of different kinds of ACA particles could be undertaken to see if all particles show the same behaviours. Analytical and computational modelling could also be used to investigate the physical basis for this relationship.

- The new technique provides a basis for research to determine the optimum particle deformation parameters to improve the performance of ACA assembly and their long term reliability.

- Some additional research is required to check the possible effects of residues on the punch tip and to verify whether there is any deflection of the sample base stage used in the individual particle deformation.

References

[1] Rao R. Tummala, "Fundamentals of Microsystems Packaging," *McGraw-Hill*, New York, 2001, pp. 5.

[2] Viswanadham P. and Singh P., "Failure Modes and Mechanisms in Electric Packages," *Springer*, New York, 1998.

[3] Lau J. H., "Low Cost Flip Chip Technologies for DCA, WLCSP, and PBGA Assemblies," *McGraw-Hill*, New York, 2000, pp. 1-17.

[4] Ulrich R. K. and Brown W. D., "Advanced Electronic Packaging," *John Wiley & Sons, Inc. ISBN: 13978-0-471-46609-X*, 2006, pp. 1-28.

[5] Liu J., "Conductive Adhesive for Electronics Packaging," *Electrochemical Publications Ltd, Port Erin, Isle of Man, British Isles, ISBN 0901-150-37-1*, 1999, pp. 2.

[6] Liu J., "Life time prediction of anisotropic conductive adhesive joints during temperature cycling for electronics interconnect," *First International IEEE Conference on Polymers and Adhesives in Microelectronics and Photonics*, Potsdam, Germany, 2001, pp. 209-212.

[7] Liu J., "Conductive Adhesive for Electronics Packaging," *Port Erin, Isle of Man, British Isles: Electrochemical Publications Ltd. ISBN 0901-150-37-1*, 1999, pp. 234-248.

[8] European Union, "DIRECTIVE 2002/96/EC OF THE EUROPEAN PARLIAMENT AND OF THE COUNCIL of 27 January 2003 on waste electrical and electronic equipment (WEEE)," *Official Journal of the European Union*, 13, February 2003, pp. 19-23.

[9] European Union, "DIRECTIVE 2002/95/EC OF THE EUROPEAN PARLIAMENT AND OF THE COUNCIL of 27 January 2003 on the restriction of the use of certain hazardous substances in electrical and electronic equipment," *Official Journal of the European Union*, 13, February 2003, pp. 24-38.

[10] Liu J., "ACA Bonding Technology for Low Cost Electronics Packaging Applications-Current Status and Remaining Challenges," *Soldering & Surface Mount technology*, Vol. 13, No. 3, 2001, pp. 39-57.

[11] Mannan S. H., Oguibe C. N., Whalley D. C. and Williams D. J., "Effects of Gap Height on Conduction within Anisotropic Conducting Adhesive Assemblies," *Journal of Electronic Manufacturing*, Vol. 7, No. 3, September 1997, pp. 211-224.

[12] Dou G., Whalley D. C. and Liu C., "Electrical Conduction Characteristics of Solid Metal Anisotropic Conductive Adhesive Particles," *IEEE 4th International Conference on Polymers and Adhesives in Microelectronics and Photonics*, Portland, Oregon, USA, 12-15 September 2004, pp. 132-136.

[13] Dou G., Whalley D. C. and Liu C., "Electrical Conductive Charateristics of ACA Bonding: A Review of the Literature, Current Challeges and Future Prospects," *Proceedings of 6th IEEE Conference on High Density Microsystem Design and Packaging and Component Failure Analysis (HDP'04)*, Shanghai, China, 2004, pp. 264-276.

[14] Dou G., Whalley D. C. and Liu C., "The effect of co-planarity variation on Anisotropic Conductive Adhesive assemblies," *Proceeding of the* 56^{th} *IEEE Electronic Components and Technology Conference*, Vol. 1, San Diego, USA, May 2006, pp. 932-938.

[15] Dou G., Whalley D. C. and Liu C., "Deformation Property Measurement for Single Anisotropic Conductive Adhesive Particles," *Proceedings of 1st Electronics Systemintegration Technology Conference (ESTC), 2006*, Vol II, Dresden, German, September 2006, pp. 840-847.

[16] Dou G., Whalley D. C. and Liu C., "Mechanical and Electrical Characterisation of Individual ACA Conductor Particles," *8th International Conference on Electronic Materials and Packaging (EMAP2006)*, Hong Kong, pp. 667-675.

[17] Williams D. J., Whalley D. C., Boyle O. A. and Ogunjimi A. O., "Anisotropic Conducting Adhesive for Electric Interconnection," *Soldering & Surface Mount Technology*, No. 14, June 1993, pp. 4-8.

[18] Hu K. X., Yeh C. P., and Wyatt K.W., "Electro-thermo-mechanical Responses of Conductive Adhesive Materials," *IEEE Transactions on Components, Packaging, and Manufactering Technology*, Part A, Vol. 20, Dec. 1997, pp. 470-477.

[19] Yim M. J, Paik K. W., "Design and Understanding of Anisotropic Conductive Films (ACF's) for LCD Packaging," *IEEE Transactions On Components, Packaging, and Manufacturing Technology*, part A, Vol. 21, No. 2, June 1998, pp. 226-234.

[20] Shi F. G., Abdullah M., Chungpaiboonpatana S., Okuyama K., Davidson C. and Adams J. M., "Electrical Conduction of Anisotropic Conductive Adhesive: Effect of Size Distribution of Conducting Filler Particles," *Materials Science in Semiconductor Processing* Vol. 2, 1999, pp. 263-269.

[21] Oguibe C. N., Mannan S. H., Whalley D. C. and Williams D. J., "Conduction Mechanisms in Anisotropic Conducting Adhesive Assembly," *IEEE Transactions, Packaging, and Manufacturing Technology*, Part A, Vol. 21, No. 2, June 1998, pp. 235-242.

[22] Fu Y, Willander M. and Liu J., "Stastics of Electric Conductance Through Anisotropically Conductive Adhesive," *IEEE Transactions on Components and Packaging Technology*, Vol. 24, No. 2, June 2001, pp. 250-255.

[23] Liu J., "Conductive Adhesive for Electronics Packaging," *Port Erin, Isle of Man, British Isles: Electrochemical Publications Ltd. ISBN 0901-150-37-1*, 1999, pp. 1-14.

[24] Lau, J. H., "Flip Chip Techonologies," *McGraw-Hill*, New York, 1996, pp. 2-3.

[25] Liu J., "Conductive Adhesive for Electronics Packaging," *Port Erin, Isle of Man, British Isles: Electrochemical Publications Ltd. ISBN 0901-150-37-1*, 1999, pp. 6.

[26] Liu J., "Conductive Adhesive for Electronics Packaging," *Port Erin, Isle of Man, British Isles: Electrochemical Publications Ltd. ISBN 0901-150-37-1*, 1999, pp. 36-37.

[27] Liu J., "Conductive Adhesive for Electronics Packaging," *Port Erin, Isle of Man, British Isles: Electrochemical Publications Ltd. ISBN 0901-150-37-1*, 1999, pp. 3.

[28] Holloway M. J., Ward M. B. and Scully L. V., "Novel Anisotropically Conductive Film for Area Array Packaging," *Advances in Electronic Packaging, Proceedings of ASME International Electronic Packaging Conference*, Vol. 2, 1999, Hawaii, pp. 1699-1704.

[29] Williams D. J., Whalley D.C. and Boyle O. A., "The Effects of Conducting Particle Distribution on the Behaviour of Anisotropic Conducting Adhesives: Non-niform Conductivity and Shorting Between Connections," *Journal of Electronic Manufacturing*, Vol. 3, No. 2, 1993, pp. 85-94.

[30] Liu J., "Conductive Adhesive for Electronics Packaging," *Port Erin, Isle of Man, British Isles: Electrochemical Publications Ltd. 2*, 1999, pp. 5.

[31] Liu J., "Conductive Adhesive for Electronics Packaging," *Port Erin, Isle of Man, British Isles: Electrochemical Publications Ltd. 2*, 1999, pp. 185, 257-261.

[32] Liu J., "Conductive Adhesive for Electronics Packaging," *Port Erin, Isle of Man, British Isles: Electrochemical Publications Ltd. 2*, 1999, pp. 10-12.

[33] Liu J., "Conductive Adhesive for Electronics Packaging," *Port Erin, Isle of Man, British Isles: Electrochemical Publications Ltd. 2*, 1999, pp. 120-122.

[34] Solvolainen P. and Kivilahti J., "Electrical Properties of Solder Filled Anisotropically Conductive Adhesives," *Journal of Electronics Manufacturing*, Vol. 5 No. 1, 1995, pp. 19-26.

[35] Kivilahti J., and Solvolainen P., "Anisotropic Conductives for Flip-chip Bonding," *Journal of Electronics Manufacturing*, Vol. 5 No. 4, 1995, pp. 245-252.

[36] Solvolainen P. and Kivilahti J., "A solder Alloy Filled Z-aix Conductive Epoxy Adhesive," *Journal of Adhesives*, Vol. 49, 1995, pp. 187-196.

[37] Whalley D. C., Glinsky G., Bailey C. J. and Liu J., "Computational Modelling of the Anisotropic Conductive Adhesive Assembly Process," *Proceedings of the 3rd International Symposium on Electronics Materials and Packaging*, November 2001, Jeju, Korea, pp. 393-398.

[38] Dudek R., Meinel S. and Schubert A., "Flow Characterization and Thermo-Mechanical Response of Anisotropic Conductive Films," *IEEE Transactions on Components and Packaging Technology*, Vol. 22, No. 2, June 1999, pp. 177-185.

[39] Holm R., "Electric Contacts, Theory and Application," *Springer-Verlag, Berlin*, New York, 1967.

[40] Whalley D. C., Kristiansen H. and Liu J., "Characterization of Anisotropic Conductive Adhesive Compression During the Assembly Process," *Proceedings of the IMAPS MicroTech 2003 Microelectronics and Medicine and Polymers for Advanced Microelectronics Conference*, 2003, Stratford, UK, pp. 1-7.

[41] Fan, S. H. and Chan Y. C., "Effect of misalignment on the electrical characteristics of anisotropic conductive adhesive joints," *Proceeding of the* 52^{th} *IEEE Electronic Components and Technology Conference*, San Diego, 2002, pp. 1605-1612.

[42] Yeung N. H., Chan Y. C. and Chan C. W., "Effect of Bonding Force on the Conducting Particle with Different Sizes," *Journal of Electronic Packaging, ASME*, Vol. 125, Issue 4, December 2003, pp. 624-629.

[43] Dou G., Chan Y. C. and Liu J., "Electrical Conductive Characteristics of Anisotropic Conductive Adhesive Particles," *Journal of Electronic Packaging, ASME*, Vol. 125, Issue 4, December 2003, pp. 609-616.

[44] Määttänen J., "Contact Resistance of Metal-coated Polymer Particles Used in Anisotropically Conductive Adhesives," *Soldering & Surface Mount Technology*, Vol. 15, Issue 11, 2003, pp. 12-15.

[45] Chan, Y. C. and Luk D.Y., "Effects of bonding parameters on the reliability performance of anisotropic conductive adhesive interconnects for flip-chip-on- flex packages assembly I.Different bonding temperature," *Microelectronics Reliability*, 2002. Vol. 42, No. 8, pp. 1185-1194.

[46] Chan, Y. C. and Luk D. Y., "Effects of bonding parameters on the reliability performance of anisotropic conductive adhesive interconnects for flip-chip-on- flex packages assembly II. Different bonding pressure," *Microelectronics Reliability*, 2002. Vol. 42 No. 8, pp. 1195-1204.

[47] Seppala, A. and Ristolainen E., "Study of adhesive flip chip bonding process and failure mechanisms of ACA joints," *Microelectronics Reliability*, 2004. Vol. 44, No. 4, pp. 639-648.

[48] Seppala, A., Aalto K., and Ristolainen E., "Reducing bonding cycle time of adhesive flip chip process," *Soldering & Surface Mount Technology*, 2003. Vol. 15 Issue 1, pp. 16-20.

[49] Ogunjimi A. O., Mannan S. H., Whalley D. C. and Williams D. J., "The Assembly Process for Anisotropic Conductive Joint—Some New Experimental and Theoretical Results," *Journal of Electronic Manufacturing*, Vol. 5, No.4, 1995, pp. 263-271.

[50] Shiozawa N., Isaka K. and Ohta T., "Electric Properties of Connections by Anisotropic Conductive Film," *Journal of Electronic Manufacturing*, Vol. 5, No. 1, March, 1995, pp. 33-37.

[51] Liu J., "Conductive Adhesive for Electronics Packaging," *Electrochemical Publications Ltd, Port Erin, Isle of Man, British Isles, ISBN 0901-150-37-1*, chapter 8, 1999, pp. 189.

[52] Lee K. K., Ng K. T., Tan C. W.; Chan Y. C., Cheng L. M., "Fabrication of Smart Card Using UV Curable Anisotropic Conductive Adhesive (ACA.) Part I: Optimization of the Curing Conditions," *International Conference on Business of Electronic Product Reliability and Liability*, Shanghai, 2004, April 2004, pp. 134-139.

[53] Tan C. W., Siu Y. M., Lee K. K., Chan Y. C. and Cheng L. M., "Fabrication of Smart Card Using UV Curable Anisotropic Conductive Adhesive (ACA) Aart II: Reliability Performance of the ACA joints," *International Conference on Business of Electronic Product Reliability and Liability*, Shanghai, 2004, pp. 140-144.

[54] Shiming L. and Liu, J., "Development and Characterization of Single Mode Microwave Cured Adhesives for Electronics Packaging Application," *Proceeding of the* 52^{th} *IEEE Electronic Components and Technology Conference*, San Diego, 2002, pp. 1147-1150.

[55] Fu Y., Wang T.; Liu J., "Microwave-transmission, Heat and Temperature Properties of Electrically Conductive Adhesive," *IEEE Transactions on Components and Packaging Technologies*, Part A, Vol. 26, Issue: 1, March 2003, pp. 193-198.

[56] Lee C. H., "Anisotropic conductive flip chip-on-glass technology," *Flip Chip Technology*, Ed. Lau J. H., McGraw-Hill, New York, 1996, pp. 317-339.

[57] Groh U., Meinel S. and Meyer A., "On the numerical simulation of coupled transient problems on MIMID parallel system," *Fast Solvers for Flow Problems (Series Notes on Numerical Fluid Mechanics)*, W. Hackbusch and G. Wittum, Eds. Berlin, Germany: Braunschweig, 1995, Vol. 49, pp. 109-120.

[58] Mannan S. H., Whalley D. C., Ogunjimi A. O. and Williams D. J., "Modelling of the Initial Stages of the Anisotropic Adhesive Joint Assembly Process," *Proceedings of 1995 Japan International Electronic Manufacturing Symposium*, Omiya, 1995, pp. 142-145.

[59] Mannan S. H., Whalley D. C., Ogunjimi A. O. and Williams D. J., "Assembly of the Planar Array Components Using Anosptropic Conducting Adhesive—a Benchmark Study," *IEEE Transactions On Components, Packaging, and Manufacturing Technology*, part C, Vol. 19, No. 4, 1996, pp. 264-269.

[60] Whalley D. C., Chen L. and Liu J., " Modeling of the Anisotropic Conductive Adhesive Assembly Process," *Proceedings of of 4th IEEE International Symposium on Electronic Packaging Technology*, August 2001, Beijing, pp. 319-324.

[61] Wu C. M. L., Liu J. and Yeung N. H., " The Effects of Bump Height on the Reliability of ACF in Flip-Chip," *Soldering & Surface Mount technology*, Vol. 13, Issue 1, 2001, pp. 25-30.

[62] Wang Y., Chen G., Liu J. and Lai Z., "The Contact Characterization of Conductive Particles in Anisotropically Conductive Adhesive Using FEM," *Proceedings of*

2nd IEEE International Symposium on Polymeric Electronics Packaging, Sweden, 1999, pp. 199-206.

[63] Buratynski E. K., "Thermomechanical Modelling of Direct Chip Interconnection Assembly," *Journal of Electronic Packaging*, Vol. 115, 1993, pp. 382-391.

[64] Chiang K. N., Chang C. W. and Lin J. D., "Analysis of ACA/ACF package Using Equivalent Spring Mehtod," *Proceedings of 3rd Electronics Packaging Technology Conference*, Singapore, 2000, pp. 110-116.

[65] Gustafsson K., Mannan S. H., Lai Z., Liu J. Whalley D. C. and Willliams D. J., "The Effect of Temperature Ramp Rate on Flip-Chip Joint Quality and Reliability Using Anisotropic Conductive Adhesive on FR-4 Substrate," *Proceeding of the* 47^{th} *IEEE Electronic Components and Technology Conference*, San Jose, 1997, pp. 382-391.

[66] Wu S. S., Hu K. X. and Yeh C., "Contact Reliability Modelling and Material Behaviour of Conductive Adhesive under Thermal-mechanical Loads," *Chapter 6 in Conductive Adhesive for Electronic Packaging*, Ed. Liu J., Electrochemical Publication Ltd, Isle of Man, June, 1999.

[67] Pinardi K., Lai Z. H., Vogel D., Kang Y. L., Liu J., Liu S., Huang R. and Willander M., "Effect of Bump Height on the Strain Variation during the Thermal Cycling Test of ACA Flip-Chip Joints," *IEEE Transactions on Components and Packaging Technologies*, Vol. 23, No. 3, 2000, pp. 447-451.

[68] Chiriac V. A. and Lee T. T., "Transient Thermal Analysis of an ACF Package Assembly Process," *IEEE Transactions on Components and Packaging Technologies*, Vol. 24, No. 4, December 2001, pp. 673-681.

[69] Chin M., Iyer K. A. and Hu S. J., "Prediction of Electrical Contact Resistance for Anisotropic Conductive Adhesive Assemblies," *IEEE Transactions on Components and Packaging Technology*, Vol. 27, No. 2, June 2004, pp. 317-326.

[70] Smith J. R., "Chapter of Thermal and Mechanical Modelling of Electronic Interconnections for Automotive Environment, Mathematics in the Automotive Industry," *Clarendon Press, Oxford*, New Series Number 36, The Institute of Mathematics & its Applications Conference Series, 1992, pp. 290-291.

[71] Johson K. L., "Contact Mechanics," *Cambridge University Press*, Cambridge, 1985, pp. 93.

[72] Kristiansen H., Gullisken N., Haugerud H. and Friberg R., "Characterisation of Electrical Contacts Made by Non-conductive Adhesive," *Proceedings of 3rd International Conference on Adhesive Joining and Coating Technology in Electronics Manufacturing*, Binghamton, 1998, pp. 345-350.

[73] Kristiansen H., Bjøneklett A., "Fine Pitch Connection to Rigid Substrates using Non-Conductive Epoxy Adhesvie," *Journal of Electronics Manufacturing*, Feburary 1992, pp. 7-12.

[74] Constable J. H., "Analysis of ACA Contact Resistance," *Proceedings of IPACK03 International Electronic Packaging Technical Conference and Exhibition*, Hawaii, 2003, pp. 1-8.

[75] Wu, S. X., Hu, K. X. and Yeh, C. P., "Contact Reliability modelling and material behaviour of conductive adhesvie under thermomechanical loads," *Conductive Adhesive for Electrics Packaging, Chapter 6*, Ed. Liu J., Electrochemical Publication Ltd, Isle of Man, pp. 121.

[76] Adebayo O. Ogunjimi, Samjid H. Mannan, David C. Whalley and David J. Williams, "Assembly of Planar Components Using Anisotropic Conducting Adhesives-A Benchmark Study: Part I—Experiment," *IEEE Transactions On Components, Packaging, and Manufacturing Technology*, Part C, Vol. 19, No. 4, October 1996, pp. 257-263.

[77] Samjid H. Mannan, David C. Whalley, Adebayo O. Ogunjimi, and David J. Williams, "Assembly of Planar Components Using Anisotropic Conducting Adhesives-A Benchmark Study: Part II—Theory," *IEEE Transactions On Components, Packaging, and Manufacturing Technology*, Part C, Vol. 19, No. 4, October 1996, pp. 264-269.

[78] Kristiansen H. and Liu J., "Overview of Conductive Adhesive Interconnection Technologies for LCD's," *IEEE Transactions On Components, Packaging, and Manufacturing Technology*, part A, Vol. 21, No.2, 1998, pp. 208-214.

[79] Chan Y. C., Hung K. C., Tang C. W. and Wu C. M. L., "Degradation mechanisms of anisotropic conductive adhesive joints for flip chip on flex applications," *Proceedings of 4th International Conference on Adhesive Joining and Coating Technology in Electronics Manufacturing*, Espoo, Finland, 2000, pp. 141-146.

[80] Ogunjimi A. O., Boyle O. A., Whalley D. C. and Williams D. J., "A Review of the Impact of Conductive Adhesive Technology on Interconnection," *Journal of Electronic Manufacturing*, Volume 2, No. 3, September 1992, pp. 109-118.

[81] Zhang J. H., Chan Y. C., Zeng Z. M. and Chiu Y.W., "Research on the Interfacial Reaction Between Anisotropically Conductive Film and Bumpless Die," *Proceeding of the* 52^{th} *IEEE Electronic Components and Technology Conference*, San Diego, 2002, pp. 1569-1574.

[82] Mercado L. L., White J., Sarihan V. and Lee T. T. "Failure Mehcnism Study of Anisotropic Conductive Flim (ACF) Packages," *IEEE Transactions on Components and Packaging Technologies*, Vol. 26, No. 3, September 2003, pp. 509-516.

[83] Mannan S. H., Williams D. J., Whalley D. C. and Ogunjimi A. O., "Models to Determine Guidlines for the Anisotropic Conducting Adhesives Joining Process in," *Liu J. (Ed.), Conductive Adhesive for Electronics Packaging, Electrochemical Publications Ltd*, Port Erin, Isle of Man, 1999, chapter 4, pp. 92-97.

[84] Wong E. H., Teo Y. C. and Lim T. B., "Moistrue Diffusion and Vapour Pressure Modelling of IC Packaging," *Proceeding of the* 48^{th} *IEEE Electronic Components and Technology Conference*, Washington, 1998, pp. 1372-1378.

[85] Tee T. Y. and Ng H. S., "Whole Field Vapour Pressure Modelling of QFN during Reflow with Coupled Hygor-mechanical and Thermal-mechanical Stresses," *Proceeding of the* 52^{th} *IEEE Electronic Components and Technology Conference*, San Diego, 2002, pp. 1552-1559.

[86] Wong E. H., Chan K. C., Rajoo R., Lim T. B., "The Mechanics and Impact of Hygroscopic Swelling of Polymeric Materials in Electronic Packaging," *Proceeding of the* 50^{th} *IEEE Electronic Components and Technology Conference*, Las Vegas, 2000, pp. 576-580.

[87] Wei Z., Waf L. S., Loo N. Y., Koon E. M., Kuang M., "Studies on moisture-induced failures in ACF interconnection," *Proceedings of* 4^{th} *Electronics Packaging Technology Conference 2002*, Singapore, 2002, pp. 133-138.

[88] Teh L. K., Teo M., Anto E., Wong C. C., Mhaisalkar S. G., Teo P. S. and Wong E. H., "Moisture-induced failures of adhesive flip chip interconnects," *IEEE Transactions on Components and Packaging Technologies*, Part A, Sept. 2005. pp 506- 516.

[89] Lou S. and Wong C. P., "Moisture Absorption in Uncured Underfill Materials," *IEEE Transactions on Components and Packaging Technologies*, Vol. 27, No. 2, 2004, pp. 345-351.

[90] Peter J. O., "Anisotropic Conductive Film for Flip-chip Applications: An Introduction," *The Tutorial 05 on website: http://www.flipchips.com/tutorial05.html.*

[91] Yin C. Y., Alam M. O., Chan Y. C., Bailey C. and Lu H., "The effect of reflow process on the contact resistance and reliability of anisotropic conductive film interconnection for flip chip on flex applications," *Microelectronics Reliability*, Vol. 43, No.4, 2003, pp. 625-633.

[92] Yin C. Y., Lu H., Bailey C. and Chan Y. C., "Experimental and Modeling Analysis of the Reliability of the Anisotropc Conductive Films," *Proceeding of the* 53^{th} *IEEE Electronic Components and Technology Conference*, New Orleans, 2003, pp. 698-702.

[93] Yin C. Y., Lu H., Bailey C. and Chan Y. C., "Effects of Solder Reflow Process on the Reliability of Flip-Chip on Flex Interconnections Using Anisotropic Conductive Adhesives," *IEEE Transactions on Electronics Packaging Manufacturing*, Vol.27, No.4, 2004, pp. 254-259.

[94] Yeung N. H., Chan Y. C., Tan S. C., Lee K. K. and Chan K. K., "Effect of Void in the Anisotropic Conductive Assembly," *Proceeding of the* 53^{th} *IEEE Electronic Components and Technology Conference*, New Orleans, 2003, pp. 1378-1382.

[95] Fu Y., Wang Y., Liu J., Lai Z., Chen G. and Willander M., "Experimental and Theoretical Characterization of Electrical Contact in Anisotropically Conductive

Adhesive," *IEEE Transactions on Advanced Packaging*, Vol. 23, No. 1, February 2000, pp. 15-21.

[96] Kwon W. S. and Paik K. W., "Experimental Analysis of Mechanical and Electrical Characteristics of Metal-Coated Conductive Spheres for Anisotropic Conductive Adhesives (ACAs) Interconnection," *IEEE Transactions on Components and Packaging Technologies*, 2006, 29(3): pp. 528-534.

[97] Rao R. Tummala, "Fundamental of Microsystems Packaging," *McGraw-Hill*, New York, 1998, pp. 928-930.

[98] "Department of Electronic Engineering, City University of Hong Kong," *http://www.ee.cityu.edu.hk.*

[99] "Hong Kong University of Science and Technology," *http://www.ust.hk.*

[100] "Compass Technology Company Limited," *http://www.compass-flex.com.*

[101] Fan S. H. and Chan Y. C., "Effect of misalignment on electrical characteristics of ACF joints for flip chip on flex applications," *Microelectronics Reliability*, vol. 42, no. 7, July 2002, pp. 1081-1090.

[102] "Data Sheet of Keithly 580 Micro-ohmmeter," *http://www.keithley.com.*

[103] Ward I. M. and Hadley D. W., "An Introduction to the Mechanical Properties of Solid Polymers," *John Wiley & Sons Ltd, Chichester, ISBN 0 471 938878 4*, 1993, pp. 45.

[104] Ward I. M. and Hadley D. W., "An Introduction to the Mechanical Properties of Solid Polymers," *John Wiley & Sons Ltd, Chichester, ISBN 0 471 938878 4*, 1993, pp. 47.

[105] Ward I. M. and Hadley D. W., "An Introduction to the Mechanical Properties of Solid Polymers," *John Wiley & Sons Ltd, Baffins Lane, Chichester, West Sussex PO19 1UD, England. ISBN 0 471 938878 4*, 1993, pp. 48.

[106] Beake B., "Modelling Indentation Creep of Polymers: a Phenomenological Approach," *Journal of Physics D: Applied Physics*, vol. 39, 2006, pp. 4478-4485.

[107] Chin M., Barber J. R. and Hu S. J., "Effect of Elastic Recovery on the Electrical Contact Resistance in Anisotropic Conductive Adhesive Assemblies," *IEEE Transactions on Components and Packaging Technology*, Vol. 29, No. 1, 2006, pp. 137-144.

Appendix 1

Experimental Results for α-rotation.

Table 8.1: α-rotation.

Joint	Less compressed side, R ($m\Omega$).										
Sample	0	1	2	3	4	5	6	7	8	9	10
1	38.4	45.9	55.1	59.8	67.1	61.5	50.9	53.4	70.1	72.7	74.8
2	57.9	39.2	58.8	34.4	43.1	51.4	47.1	58.3	70.8	60.5	100.5
3	51.8	45.7	53.8	50.1	65.5	53.9	67.0	81.8	73.7	62.1	95.7
4	39.9	35.2	63.7	47.0	60.0	49.6	35.8	46.5	44.6	52.4	63.2
5	35.6	28.2	45.3	53.1	60.6	50.3	50.7	51.7	51.1	49.2	80.3
6	53.4	42.2	71.7	50.2	116.7	50.9	69.4	71.7	56.8	75.6	106.2
7	40.9	33.8	43.0	41.5	71.2	50.3	67.8	62.4	56.8	69.8	118.9
8	35.9	35.3	43.5	40.1	44.8	66.2	63.7	100.8	59.3	73.1	77.6
9	42.6	34.1	54.2	46.8	122.2	49.7	74.5	76.2	76.4	60.8	97.9
10	30.3	31.0	52.7	50.1	141.5	65.0	100.1	77.8	70.8	69.7	76.7
11	38.7	45.0	75.2	58.7	65.7	100.2	161.9	85.5	102.5	136.6	150.8
12	30.7	45.3	58.9	65.4	43.6	74.9	101.5	51.1	86.6	124.7	63.9
13	48.3	29.4	68.7	81.6	51.7	83.2	93.0	89.5	131.4	98.5	101.3
14	37.7	39.8	73.6	59.6	55.5	102.6	163.5	124.5	246.2	176.4	141.7
15	34.3	55.8	58.6	69.4	51.9	116.5	110.7	66.4	137.4	103.6	140.1
16	53.4	47.6	51.2	47.5	52.9	112.7	147.3	85.6	248.9	118.2	191.4
17	50.2	69.6	55.0	53.1	55.4	88.8	97.7	85.6	152.8	139.4	172.2
18	43.8	44.5	59.2	55.4	48.8	88.1	84.0	56.9	105.7	76.1	88.9
19	33.5	44.1	54.8	61.7	57.2	64.4	87.2	54.2	59.5	72.6	82.6
20	35.4	44.9	44.3	72.3	49.5	61.2	104.7	97.1	132.2	127.5	125
21	32.4	27.5	46.2	62.8	39.5	50.7	77.8	68.8	87.2	101.2	120.1
22	25.7	32.3	40.1	66.2	37.3	55.3	72.9	64.6	69.8	78.9	66.2
23	32.3	41.4	45.2	60.0	39.4	63.2	129.9	99.0	88.5	103	85.8
24	31.1	36.3	49.2	73.6	44.5	58.1	80.5	92.8	78.6	99.3	106.7
25	37.6	50.5	53.0	63.2	60.7	50.3	80.7	103.9	72.2	108.2	76.2
26	25.6	32.5	39.6	58.2	36.7	48.8	101.1	79.5	72.6	73.3	102.3
27	35.5	34.8	34.0	53.5	36.7	50.4	45.3	75.7	59.1	66.7	81.1
28	34.5	43.7	60.1	53.4	46.8	59.4	50.4	72.6	65.1	180.4	125.9
29	38.4	30.0	54.9	55.6	46.8	47.3	43.2	38.5	45.7	40.6	49.8
30	40.7	47.1	52.6	64.0	47.6	61.1	55.7	80.1	66.7	114.6	118.3

Table 8.2: β-rotation.

Joint	Highly compressed side, R ($m\Omega$).										
Sample	0	1	2	3	4	5	6	7	8	9	10
1	36.2	55.3	57.2	53.5	61.7	66.1	64.6	52.3	56.8	41.0	52.9
2	47.3	45.1	71.3	45.3	52.4	56.1	91.5	39.4	56.8	46.2	54.3
3	61.3	39.2	43.6	50.3	64.8	47.6	46.7	55.9	56.8	60.4	88.3
4	34.0	38.2	45.7	40.9	39.1	39.8	42.3	59.2	56.8	35.2	40.7
5	38.2	37.0	40.4	52.2	49.4	51.6	40.1	48.5	49.8	30.2	31.9
6	43.3	37.5	50.1	43.2	44.3	46.8	47.6	76.5	49.8	46.9	62.3
7	41.6	36.4	56.8	38.0	36.9	58.7	44.7	56.4	49.8	44.2	41.4
8	40.6	36.4	34.5	41.0	50.1	42.4	41.7	48.6	49.8	30.9	35.8
9	33.6	41.0	45.5	47.3	56.5	41.2	45.4	36.8	41.4	30.2	45.8
10	32.6	35.5	44.2	41.0	43.1	46.1	47.1	41.6	56.8	41.9	37.3
11	32.9	51.1	68.9	44.7	50.6	52.9	64.0	54.1	52.1	56.3	63.0
12	37.6	44.5	41.3	48.6	47.1	41.2	39.8	49.8	47.0	47.6	46.2
13	35.9	32.5	45	47.8	46.6	44.8	58.5	47.9	58.3	40.3	33.8
14	34.7	32.2	35.1	50.2	40.4	34.5	42.7	38.3	59.3	29.8	45.3
15	34.2	35.6	44.5	45.6	38.5	42.5	46.8	50.1	40.7	45.0	37.4
16	38.2	31.7	36.3	55.3	39.5	45.2	38.1	42.3	45.5	51.6	38.2
17	36.8	29.8	37.6	54.7	61.3	40.2	46.3	37.5	40.1	38.1	43.8
18	39.2	33.3	39.5	55.6	68.1	50.6	69.8	41.3	46.0	47.2	43.8
19	48.1	42.9	40.8	65.2	41.2	52.8	71.6	54.3	53.3	42.1	58.4
20	59.6	55.4	55.8	36.8	36.4	56.8	88.9	81.5	48.9	50.4	52.2
21	39.8	35.4	78.0	38.9	43.6	40.4	72.5	55.7	53.4	49.3	50.6
22	38.1	33.9	42.8	36.8	37.4	31.1	43.1	49.8	41.5	42.4	69.4
23	42.4	31.5	48.0	65.2	37.8	45.7	56.2	49.3	42.1	54.7	64.4
24	38.8	40.3	48.1	37.4	48.3	38.8	67.1	59.3	53.8	45.1	46.4
25	57.1	55.8	72.2	41.2	43.6	66.6	76.9	71.4	79.2	60.7	52.2
26	34.9	40.0	43.4	48.3	34.7	44.3	95.2	50.4	44.7	38.9	53.2
27	40.4	28.9	58.8	51.7	45.6	54.4	51.7	52.8	47.2	55.6	48.2
28	40.2	49.7	90.8	54.4	72.3	76.2	80.1	75.9	81.1	78.1	90.1
29	54.5	43.4	58.2	44.3	60.8	59.9	62.3	48.6	71.0	70.9	84.6
30	43.8	42.3	61.2	48.3	51.2	80.3	60.3	57.8	71.7	72.1	54.1

Appendix 2

Drawings of indenter components manufactured for particle experiments

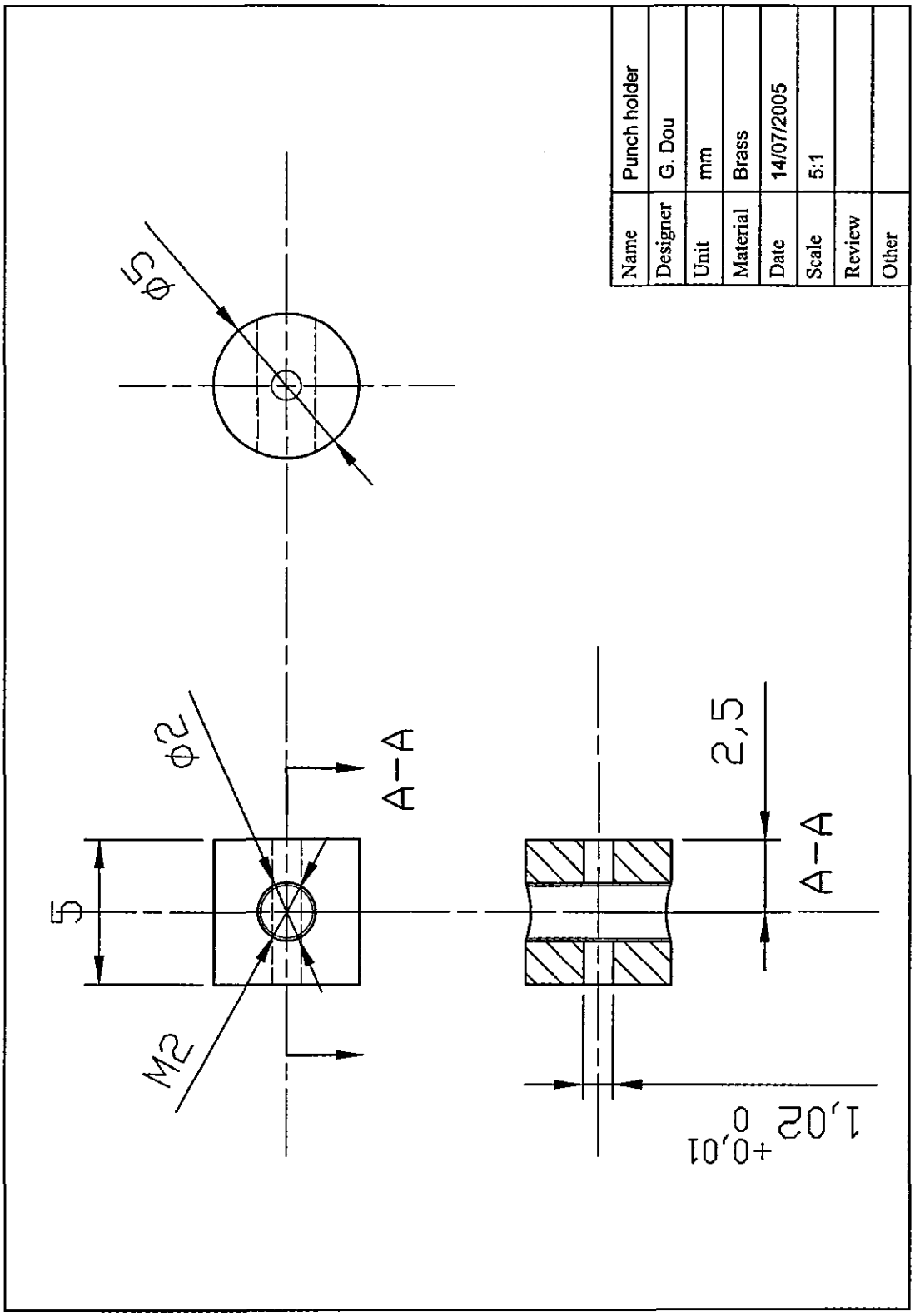

Figure 8.3: AutoACD design of indentor holder.

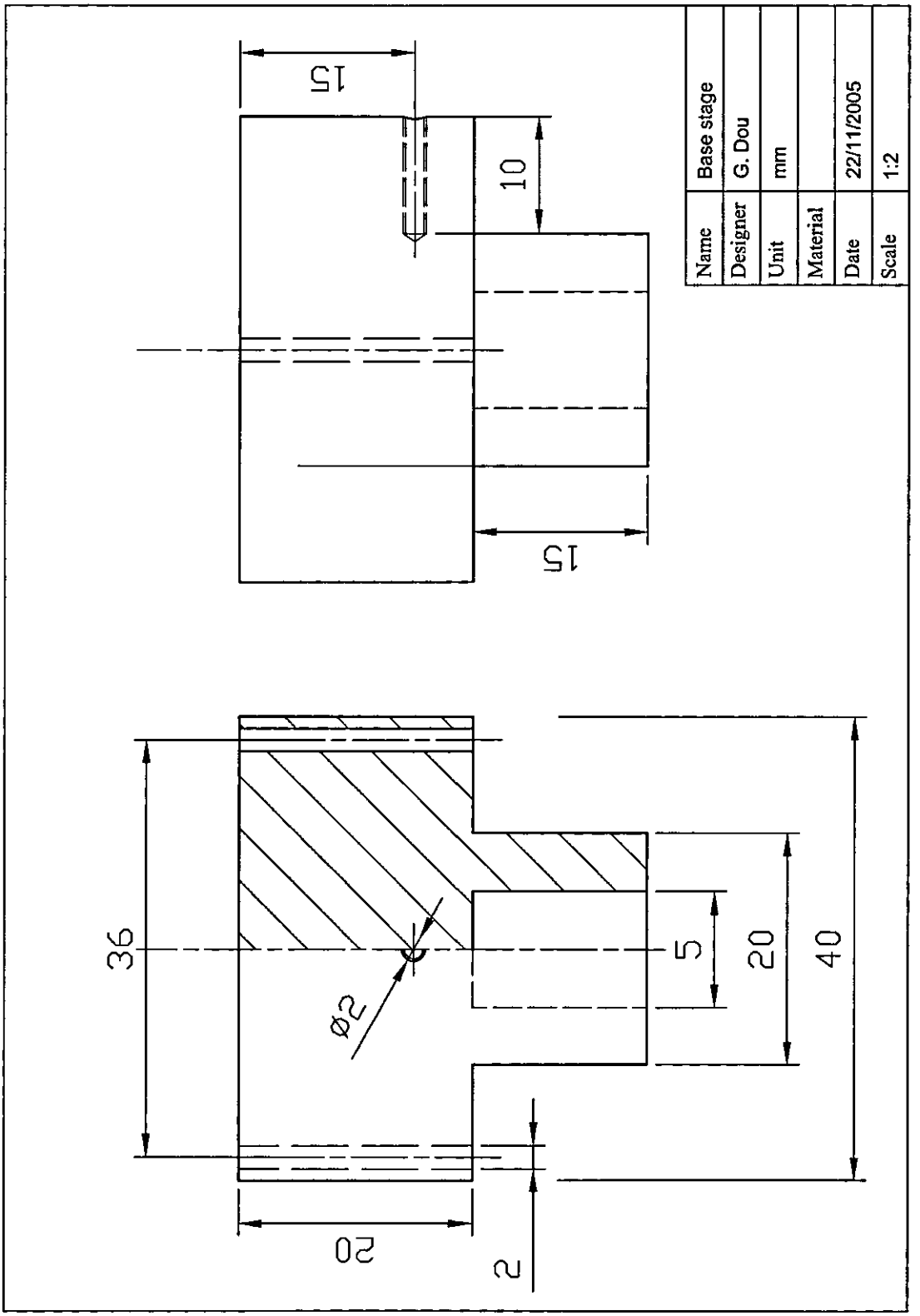

Figure 8.4: AutoACD design of base stage.